CZECH TECHNICAL UNIVERSITY IN PRAGUE

Faculty of Nuclear Sciences and Physical Engineering

DOCTORAL THESIS

Spectator Response to the Participant Blast

Prague 2005 Vladimír Henzl

The doctoral thesis was produced at GSI Darmstadt in Germany and in collaboration with the Nuclear Physics Institute of Academy of Sciences of Czech Republic in Řež

Supervisors:

RNDr. Andrej Kugler, CSc., NPI ASCR, 250 68 Řež, Czech Republic
Dr. Karl-Heinz Schmidt, GSI, Planckstr. 1, 642 91 Darmstadt, Germany

October 2005 Darmstadt

to Charles Payne who planted the seed,
and to Martina Kučerová and Miloslav Jireš who took care of the seedling

Content:

1. Introduction

1.1 Search for the equation of state of the nuclear matter

The equation of state (EOS) of nuclear matter, ruling how nuclear pressure responds to temperature and density, belongs to the key topics of nuclear physics. It also constrains the nucleon-nucleon interactions in the nuclear medium [Wir88] represented by the mean-field (MF) potential, and it remains an important ingredient for a detailed understanding of astrophysical and cosmological phenomena such as supernovae explosions [Lie01], stability of neutron stars under gravitational pressure [Pra97], and the evolution of the early Universe [Boy01].

The determination of the nuclear equation of state with use of high-energy heavy-ion reactions turned out to be more difficult than was initially anticipated. Thus, early on, it seemed to be possible to describe early single-particle observables using the cascade model [Yar79, Cug81] with an ideal gas EOS, where the potential energy term needed for binding nuclei was missing. Only the failure to describe the results from the first 4π experiments [Gus84, Ren84, Dan85, Dos86] drew the attention to the importance of including the mean-field potential felt by the nucleons in the reaction dynamics. Meanwhile, the [Ber75] hydrodynamic approach predicted newly observed collective effects [Sche74] and yielded in the beginning at least qualitative agreement with the data [Buch84]. In addition, the need for the inclusion of compressional energy was suggested by the study of entropy production by measuring light fragment formation cross sections [Dos85].

During the same time, several theoretical papers were published that described the collective effects from a semiclassical microscopic viewpoint, emphasizing either the importance of the short-range nature of the nuclear force [Mol84] or the density-dependent mean field aspect [Kru85]. However, after a short period of optimism, when the results of transport model calculations have exhibited the sensitivity of the pion yields [Kru85, Stö85], subthreshold kaon yields [Aich85], and collective flow [Kru85, Stö85, Mol85a, Mol85b] to the nuclear EOS, it was suggested to test whether this sensitivity to the EOS might be distorted by introducing momentum-dependent interactions into the theory [Ain87]. Later it had been demonstrated [Gal87, Aich87, Wel88, Had95] that the effects of the soft EOS with included momentum-dependent MF are comparable with the effects of a stiff EOS with a static mean field. Although the nonlocality of the optical potential has long been known from elastic nucleon scattering [Bet56, Wya60], it has been difficult to demonstrate this nonlocality in heavy-ion collisions. Further ambiguities were associated with the effective NN cross sections which have been expected to be lower in the nuclear medium [Jeu76, Jia91] than those in free space.

This complex puzzle of heavy-ion reactions, where many effects related to different properties of matter compete in generating observables, calls for the search of experimental observables or their combinations which would be reasonably sensitive only to individual features of nuclear matter rather than their interconnected manifestations. Joint effort of more and more elaborate comparisons of theoretical predictions with systematical results of (not only) new generation full-acceptance detectors has led to a significant progress. The stopping observables, such as linear momentum transfer, balance energy and ERAT, i.e. the ratio of the transverse and longitudinal energy, respectively, have been linked to the in-medium cross section reduction [Col98, Schu97, and Schn98]. The giant monopole resonance excitation [Bla80, You01], the sideward flow [Pan93], and strangeness production have been shown to be connected to the nuclear incompressibility [Bro91, Scha97]. On the other hand, the elliptic flow seems to exhibit preferential sensitivity to the momentum dependence of the mean field [Dan00], and the shadowing effects of the spectator on the particle emission anisotropy are

suggested as the timer of the nuclear collision, especially when looking at the energy dependence of created secondary particles [Wag00,Dan02a].

Unfortunately, as can be found in all recent articles [Rei97, Rich01, Rei02, Dan02b], despite the steady progress due to the enormous amount of experimental results as well as new theoretical approaches, the final conclusion on the nuclear EOS cannot be made. Until that is possible still a large systematic effort delivering data of higher diversity and better quality to constrain many unknown parameters, (not forgetting independent confirmations of already established knowledge) will be required. However, due to the enormous complexity of physical processes involved in heavy-ion collisions, the understanding of the experimental results and their interpretation is very difficult and has been often possible only due to detailed comparison to theoretical predictions.

For this very reason stated above, this work has been intending to address the characteristics of the momentum-dependent nuclear mean field with a recently established experimental probe – **the spectator response to the participant blast** [Ric03,Shi01].

1.2 Spectator response to the participant blast

1.2.1 Theoretical background

Although the influence of the large spectator fragments on the evolution of the participants decompression has long been considered [Stö86, Dan98], it has not been until very recent times that the heavy reaction residues have been investigated in terms of sensitivity to the nuclear equation of state [Shi01].

When nucleons of a projectile are decelerated in the participant region (region of overlap with the target nuclei), the longitudinal kinetic energy brought in by the initial colliding nuclei is converted into thermal and potential compression energy. In the subsequent rapid expansion, the collective transverse energy develops [Dan92, Dan95, Pak96, Rei97], and many particles from the participant zone get emitted in the transverse directions. The particles emitted towards the reaction plane can encounter the cold spectator pieces and, hence, get redirected or absorbed. On the other hand, since the spectators serve to deflect particle emissions toward the reaction plane, their properties may be significantly changed.

Therefore it can be argued, that the very same fundamental properties of the nuclear matter which rule the dynamic evolution of the participant explosion also predetermine the way in which the properties of the spectator may be affected by the blast. Careful investigation of the spectator properties then may serve as a sort of mirror, with which one can take an indirect look into the participant zone, i.e. into the place of the most extreme conditions in the heavy-ion collision being ruled by the nuclear equation of state.

The analysis of Shi et al. [Shi01] utilizes a set of BUU transport equations in order to demonstrate the sensitivity of the spectator observables to the compressibility and momentum dependence of the nuclear MF. The most interesting quantity turned out to be the average center-of-mass momentum change per nucleon of the surviving spectator $\Delta|\langle \mathbf{P}/A \rangle|$. In **Fig.1.1**, taken from the work of Shi [Shi01], the calculated net momentum change is plotted as the function of the impact parameter for two symmetric systems differing by the mass at comparable incident beam energies, for four different types of the EOS, including soft and hard with and without momentum dependent MF. In the figure, we can see the clear sensitivity of $\Delta|\langle \mathbf{P}/A \rangle|$ to the momentum dependence of the MF contrasted by the very weak sensitivity to the stiffness of the EOS.

Moreover, the most striking feature of the calculations carried out with the momentum-dependent (MD) MF is the leveling off of the residue velocities with decreasing impact parameter in the system $^{124}Sn+^{124}Sn$ (in contrast to the non MD cases) and even rising to

positive values for the heavier system ^{197}Au+^{197}Au. This means that the surviving spectator emerges from the reaction even with higher net average momentum per nucleon than it have had before the collision still as the original projectile.

Considering the absolute values of the $\Delta|\langle \mathbf{P}/A \rangle|$ being in order of 1% of the initial momentum per nucleon, one should not be surprised that only few indications of such effect (called longitudinal re-acceleration) had been found in the past studies [Kau80, Lov88, Mor89].

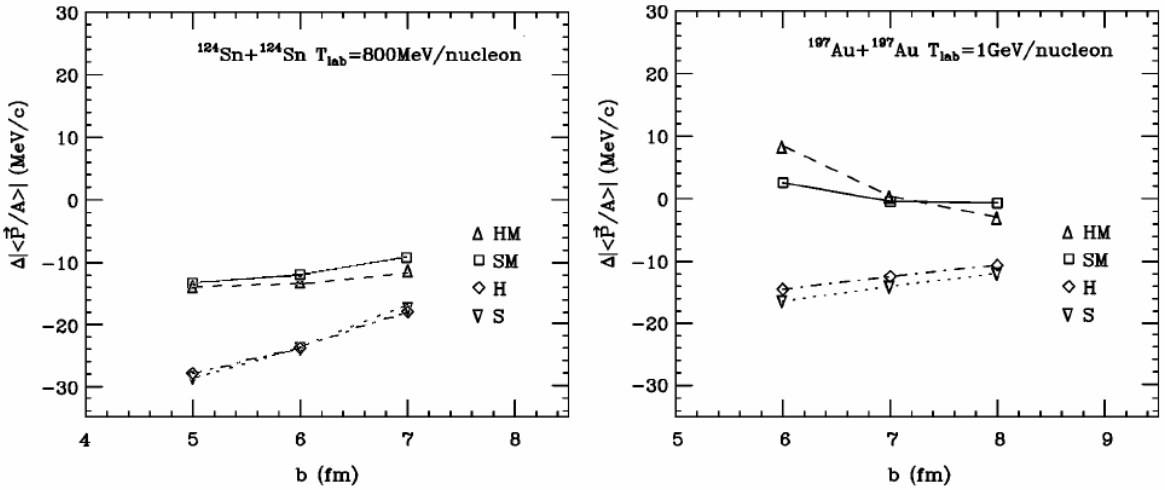

Fig. 1.1: Change in the average net c.m. momentum per nucleon $\Delta|\langle \mathbf{P}/A \rangle|$ as a function of the impact parameter for four representative EOS: hard momentum-dependent (HM), soft momentum-dependent (SM), hard momentum-independent (H), and soft momentum-independent (S) for the spectators of the system ^{124}Sn+^{124}Sn at 800 *A* MeV (left) and ^{197}Au+^{197}Au at 1 *A* GeV. Results of the BUU calculation reprinted from [Shi01].

1.2.2 Experimental evidence and possibilities

Although the "unusual" momenta of some fragmentation residues have been reported in previous works of [Cum86, Lov88], the first clear evidence of the re-acceleration phenomenon has appeared in the uranium fragmentation on lead, where the use of the inverse kinematics in combination with the high-precision magnet spectrometer FRS allowed for complete identification of the reaction residues and measurement of their momentum distribution [Enq99]. However, as there was still no suitable theoretical explanation available, this feature of that experimental observable has been left without interpretation.

The situation changed when the similar re-acceleration of the fragments with their decreasing mass has been observed in the uranium fragmentation on titanium under very similar experimental conditions [Ric01, Per03, Ric03]. As can be seen in **Fig. 1.2**, with the increasing mass loss, the mean velocities of the final reaction residues first decrease with the established systematic [Mor89] reflecting the friction undergone in the initial stage of the collision. But around the mass ~160 the mean velocities level off and finally increase again. Light fragments become even faster than the projectiles. The results have been interpreted [Ric03] as the recently postulated spectator response to the participant blast [Shi01]. According to our understanding, the ground for a new experimental approach has been laid.

The unique possibilities at the FRS allow for precise determination of the longitudinal momentum of all measured final reaction residues. The TOF resolution of 100ps on 36m allows determining $\beta\cdot\gamma$ with a relative uncertainty of $2.5\cdot10^{-3}$. Combining this with the $B\rho$ measurement, which is performed with a relative uncertainty of $5\cdot10^{-4}$, a mass resolution of $(A/\Delta A) \sim 400$ is obtained, resulting in an unambiguous identification of all detected fragments in *A* and *Z*. A recursive calculation of $\beta\cdot\gamma$ from the known $B\rho$, *A*, and *Z* eliminates the

influence of the TOF resolution and provides the $\beta\cdot\gamma$ value with a relative uncertainty of $5\cdot10^{-4}$. The correlation of the final fragment mass and the impact parameter of the initial collision are generally known and have been demonstrated in several experiments, e.g. [Hub91]. Therefore, the magnitude of the fragment re-acceleration as the function of the residue mass can be a measure of the strength of the MD effects as a function of impact parameter, or in other words as a function of the energy deposited in the participant region.

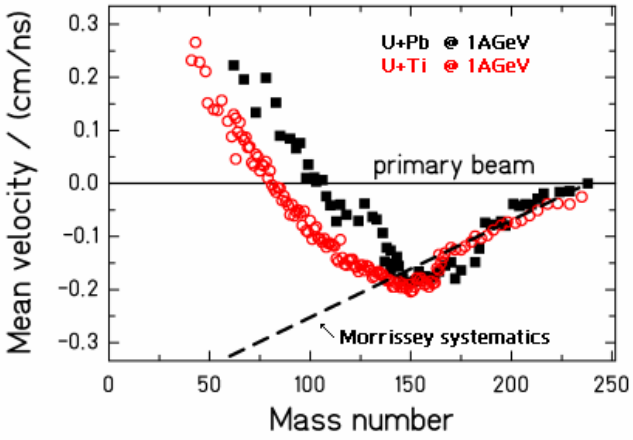

Fig. 1.2: Mean values of the velocity distributions of reaction residues, excluding fission, produced in ^{238}U+Pb (full squares [Enq99]) and ^{238}U+Ti (open points [Ric03]) at 1 *A* GeV in the frame of the projectile. The absolute uncertainty amounts to less than 0.05 cm/ns for each system, ^{238}U + Pb and ^{238}U+Ti, independently. The dashed line marks the Morrissey systematic [Mor89].

1.3 Proposed experiment

In the view of the arguments given in the previous section, we have been convinced that a systematic exploration of the longitudinal re-acceleration phenomenon can possibly lead to the determination of fundamental properties of the nuclear mean field. The unprecedented precision of the measured residue momenta can also serve as a reliability test of the used transport codes based on different approaches or using different potentials and parameterizations. By complementing the results obtained by different methods, such as measurements of the particle production or collective observables, the dedicated experimental study on re-acceleration of the reaction residues can help to improve our knowledge on the equation of state.

The data obtained by [Enq99,Ric03], see Fig.1.2, showed a new way to investigate the nuclear mean field in terms of heavy-ion collisions, but, unfortunately, these data alone cannot be used to extract any finer details on the characteristics of the MFs momentum dependence. Mainly it is the complexity of the heavy-ion collision itself that hinder the detailed analyses.

The re-acceleration magnitude is surely ruled not only by the strength of the MD effects, but presumably also by the time the spectator spends in the reaction zone. This time is on the other hand ruled by the incident velocity of the projectile and the size of the reaction zone and cannot be properly accounted for from measurements performed at the same beam energy. It is related to emission times derived from shadowing effects of secondary particles by the spectator fragments [Wag00,Dan02a]

Finally it is also the high fission cross section of uranium, which pollutes the desired observables. Since the fission occurs only in the collisions with very high impact parameter,

its products do not carry any information on the compression and expansion dynamics that occurs for lower impact parameters. However, the masses of fission products are similar to the fragmentation products, which are the direct witnesses of the participants explosion. Due to different kinematical properties of the fission and fragmentation products it is possible to separate both reaction mechanisms, but nevertheless the cost to be paid is the precision of the mean momenta for individual isotopes.

Therefore, it was proposed to perform a sequel of dedicated experiments, where two fundamental features of the reacceleration phenomenon will be studied; the dependence of the reacceleration on the incident-beam energy and the isospin composition of the participant zone.

The first part of the proposed experimental program forms the backbone of this thesis. The systems to be studied were chosen as ^{197}Au+^{197}Au at 500 and 1000 *A* MeV. The advantages of this reaction system are manifold.

Both, the experimental data (see Fig.1.2) and theoretical calculations (Fig.1.1), suggest stronger MD MF effects for rather heavy systems. Gold is a very good candidate, taking into account the very low fission cross section in comparison to other heavier nuclei, such as Pb or U. Neglecting the effects of the neutron skin for very peripheral collisions, the symmetry of the system assures a constant N/Z of the participant zone, given by the isospin of gold, for all possible impact parameters. Since the system is symmetric, the measurement of projectile residues also determines the target residues and their kinematical properties, what allows for an easier relativistic correction on relative projectile-participant-target motion, in contrast to strongly asymmetric systems. Choosing a wide range of incident beam energies offers the possibility to investigate the dynamics of the participants' decompression evolution and its strength. According to the abrasion model [Gai91], different incident energies of a projectile do not have a crucial influence on the fragmentation production in the proposed energy range. Therefore, the proposed incident beam energies would reveal pronounced effects of the compression/expansion dynamics as, on one hand, the spectator spends different time close to the participant zone and, on the other hand, there is a difference in the energy deposited by the projectile, in the rate and in the magnitude of the density build-up. Yet another crucial aspect is also the available amount of data on Au on Au collisions, which has been taken almost as "a standard" in heavy-ion collisions. The rich database of experimental as well as theoretical studies of this isotope using many different approaches or aiming at various quantities will offer a unique possibility for comparisons and validity crosschecks.

The second part of the original proposal suggests systems ^{112}Sn+^{112}Sn and ^{124}Sn+^{124}Sn at the incident beam energy E_{beam}= 1 *A* GeV as the best candidates for studying the possible isospin influence on the strength of the spectator response. However, at the time of writing this thesis, this part of the proposed experimental program still has not been carried out, and thus will not be anymore addressed within this work.

The proposal of the above described experimental program named "**Investigation of the nuclear mean field by precision measurements of the spectator response to the participants blast"** has been formulated during summer 2003, and approved by the GSI Program Advisory Committee in January 2004. With respect to the number assigned to the accepted proposal, the collaboration S276 has been formed.

The first experimental run with the beam of ^{197}Au at 1000 *A* MeV was carried out in April 2004. The second experimental run with the same beam, this time with lower incident energy of 500 *A* MeV, then took place in August of the same year. Due to exceptionally favorable beam conditions, the opportunity to extend our measurements by one additional system was taken. With respect to that time beam conditions (in terms of energy and intensity) the target of aluminum has been chosen. In combination with gold projectiles, the geometric asymmetry of the system allowed to investigate the reacceleration phenomenon in terms of the number of participating nucleons, while keeping the size of the spectator same as in the symmetric

system of ^{197}Au+^{197}Au. Since within the frame of the abrasion-ablation model, the final size of the reaction residue is given by the excitation energy introduced to the spectator by the abrasion process, which is proportional to the number of the abraded nucleons. These abraded nucleons on the other hand form the participant zone, which is during the reaction being compressed and subsequently explodes. Thus one can argue, that while in the symmetric system Au+Au the contribution to the participant zone is same from the projectile and the target nuclei, in the case of Au+Al system is the contribution of smaller nucleus significantly lower, although the final product may be the same as in the case of the symmetric system.

This thesis is therefore dedicated to the analysis of the results of the performed experiments and their comparison to the theoretical predictions by the same dynamical model as was used in the work of Shi et al [Shi01], where the possibilities of the spectator response to the participant blast as a novel approach to access the nonlocal properties of the nuclear mean field were for the first time identified. The thesis is organized as follows:

In chapter 2 the experimental set-up is described. The unique possibilities of the combination of powerful heavy-ion accelerator and high resolution magnetic spectrometer, the Fragment Separator are discussed, as well as the function of individual detectors and the main principles of the employed data acquisition system.

Chapter 3 is dedicated to the data analyses. It is demonstrated how a charge and mass identification of the detected fragments can be performed and how this essential knowledge may be used to improve the resolution of the measured velocity by almost an order of magnitude with respect to the direct measurements of the time of flight. At the end of this chapter, the procedure of reconstructing the full velocity distribution of individual isotopes is described.

Chapter 4 presents the main experimental results of this work, i.e. the velocity distributions of the surviving spectator residue, their mean values and their dependencies on the residue mass, as well as on the incident beam energy and the size of the reaction system. The characteristics of the reacceleration phenomena and its most direct implications are discussed toward the end of this chapter.

Chapter 5 presents the procedure how to deduce the impact parameter of the reaction in which a particular isotope was on average produced in case of the highly inclusive measurements, such as those performed within this study.

Chapter 6 presents the essential features of the model used for the calculations which helped not only to identify the spectator response as a high-profile observable with respect to the momentum dependent properties of the nuclear mean field, but which also are to be used for comparison with the experimental results in this work.

In chapter 7 the experimental results are confronted with the theoretical predictions. It is demonstrated, how different scenarios of the spectator response or various model assumptions may influence the degree of agreement between theory and experiment.

Chapter 8 concludes this thesis. It summarizes the implications from the experimental results itself, as well as those from the comparison of the experiment to the theory. Within this chapter it is attempted to highlight progress of understanding the phenomenon of reacceleration, but also to identify the reasons of incomplete agreement.

2. The experiment

In the present work, the velocities of the fragmentation residues produced in the reactions ^{197}Au+^{197}Au at 0.5 and 1.0 *A* GeV, and ^{197}Au+^{27}Al at 0.5 *A* GeV were studied. The complexity of these measurements, along with high expectations concerning the precision of the measurements required extraordinary experimental conditions.

Taking into account the above requirements, the most suitable choice of the experimental approach is the use of the "inverse kinematic technique" (see **Fig.2.1**) and the in-flight detection facility. With respect to the nuclear reactions in the so called "classical kinematics", where the beam impinges on the target and the products of the target nuclei are investigated, in case of the inverse kinematics, those are the reaction products of the projectile nucleus which leave the target and enter the detecting apparatus. In our case it is a magnetic spectrometer, where the projectile remnants are detected in-flight. If the incident beam energy is sufficiently high and the thickness of the target properly chosen, basically all projectile fragmentation residues can escape the target and be detected before their radioactive decay.

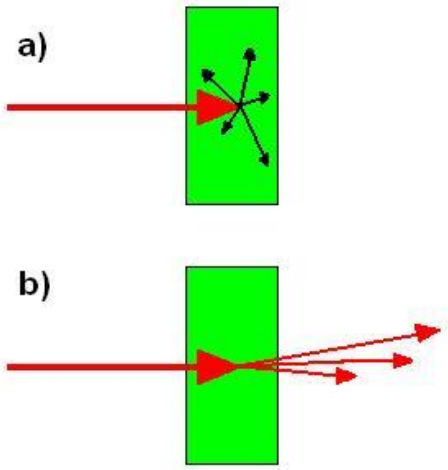

Fig. 2.1: a) schematic view of the classic reaction kinematics; b) schematic view of the inverse kinematics

The present experiments were performed during the year 2004 at Gesellschaft für Schwerionenforchung (GSI) in Darmstadt, Germany, using its accelerator complex consisting of the linear accelerator UNILAC serving as an injector of the SIS heavy-ion synchrotron, and the high-precision magnetic spectrometer, the Fragment Separator (FRS) (**Fig.2.2**).

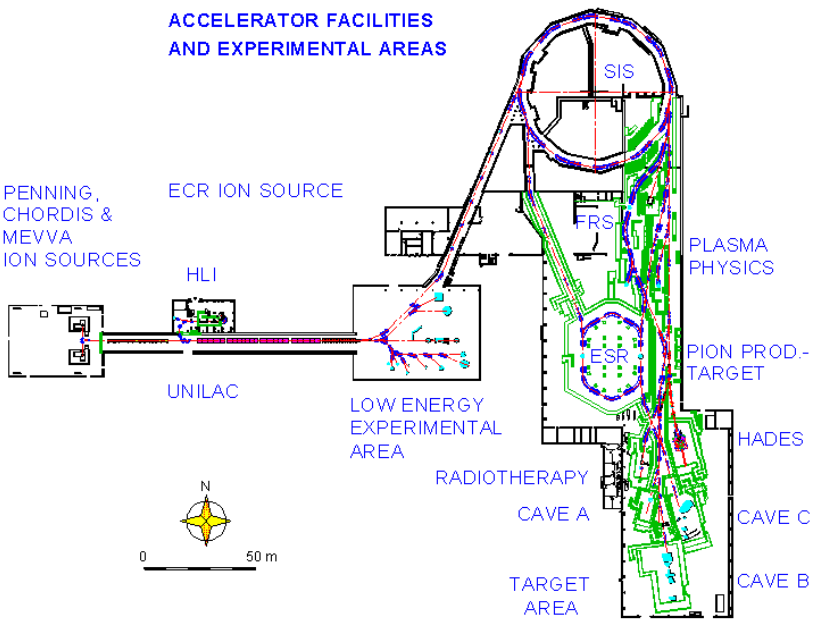

Fig. 2.2: The accelerator facilities and experimental areas at GSI- Darmstadt

2.1 The experimental set-up

In all three experiments, the ^{197}Au beam delivered by the SIS was, in part of the measurements, monitored by the Secondary Electron Transmission Monitor (SEETRAM) and focused on the production target, consisting of the self-supporting thin metal foils of either gold or aluminum. Most of the projectile-like fragments, due to their high momenta, leave the target while being focused forward. The fragments which were emitted in smaller angles than is the angular acceptance of the Fragment Separator can enter the detection device. But only fragments satisfying certain kinematical condition set by the magnetic fields of the first two dipoles of the FRS can be transmitted to the intermediate focal plane S2. All the other, including the beam projectiles which did not interact in the target, exit the vacuum line from the side, and end up most frequently absorbed in the matter of the first magnetic dipole, see **Fig.2.3**. The transmitted fragments pass in S2 through the first scintillator detector, where the horizontal position of the incoming fragments can be deduced, and optionally through the additional degrader. These layers of matter induce energy losses of the transiting fragments, thus slowing them effectively down. Then, depending on the magnetic fields of the third and fourth dipole, only a certain group of fragments can pass further and be brought to the final focal plane S4 at the end of the Fragment Separator. Subsequently, these fragments pass through two multiple sampling ionization chambers (MUSICs) and the second scintillator detector. In the ionization chambers, based on the suffered energy losses, the charge of the fragments can be deduced, and in addition the drift times of the induced charge can serve for determination of the horizontal position of the incoming fragments. The signal from the second scintillator and its time difference with respect to the similar signal from the first scintillator serves as a measure of the time of flight of the fragments on the way through the second half of the FRS. With the knowledge of the horizontal positions in intermediate and final focal plane and the applied magnetic field, it is possible to determine the radius of the fragments trajectory, which combined with the information on the velocity and charge of the fragment leads to the determination of the mass, thus allowing for an identification of the detected fragment, as will be describe in detail in chap.3.

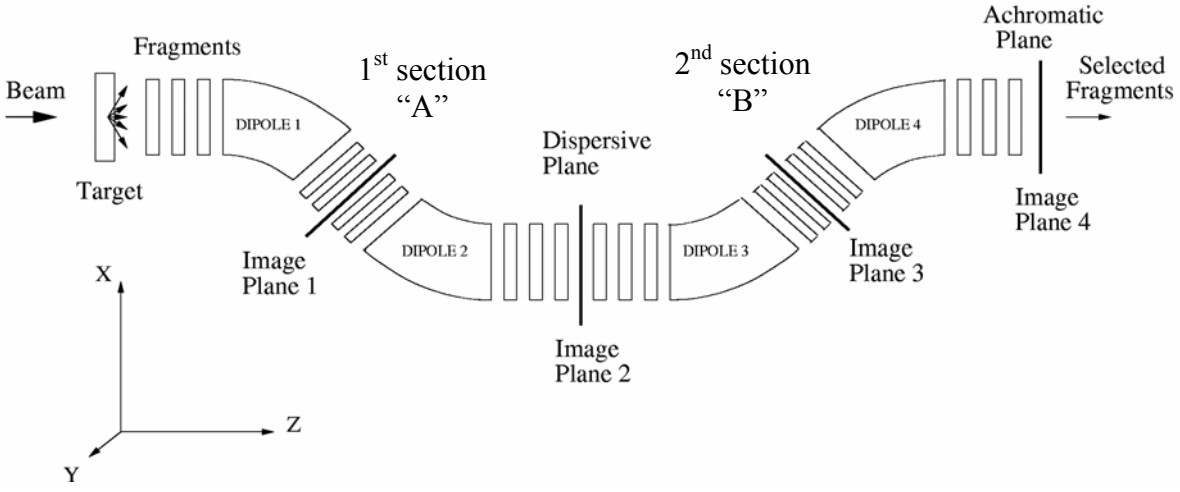

Fig.2.3: Schematic view of the Fragment Separator as an ion-optical system. Quadrupoles are placed before and after each dipole to define the ion-optical conditions at each image plane.

2.2 The production of the beam and its monitoring system

In this section, it is intended to provide general information about the employed experimental facility, concerning the preparation and acceleration of the primary beam, and its delivery to the experimental area of the Fragment Separator. In the second part, the attention will be focused on the system of detectors allowing for precise direction of the beam on the production target and piloting the beam through the detection apparatus. In the third part, the brief description of the beam profile and intensity monitor SEETRAM will be given.

2.2.1 Accelerator system

The accelerator facility at GSI can, in principle, deliver any ion beam consisting of stable nuclei from hydrogen up to uranium, with energies up to 1-4.5 GeV per nucleon, depending on the accelerated ion. The accelerator complex consists of three different stages [Acc95]: the linear accelerator UNILAC, the heavy-ion synchrotron SIS, and the storage ring ESR.

The ions used as the beam particles can be generated and extracted from several ion sources: the Penning ion source (PIG) at the South injector, the Metal-Vapor Vacuum-Arc ion source (MEVVA) alternating with a Multi Cusp Ion Source (MUCIS) at the North injector, both injectors located at the beginning of the beam path, and an Electron Cyclotron Resonance ion source (ECR) source located in the High Charge Injector (HLI), i.e. injecting directly into the second stage of the UNILAC.

The gold ions used as beam particles in our experiments were generated in the Penning Ion Source, where a high-current gas discharge bombards the selected atoms to ionize to the ionic charge state of 4+, i.e. 4 electrons have been stripped off, in order to allow for their extraction and pre-acceleration through a potential difference of 150kV.

The first stage of the UNILAC is the high current injector. It consists of three accelerating structures, the first one being the radio frequency quadrupole and the next two the IH drift tube linacs with an inverting-polarity frequency of 36 MHz. In order to guide the beam along the 30-meter-long axis of the accelerator, some of the electrodes contain additional magnetic lenses. On the way, the accelerated ions pass through a supersonic gas beam to get more electrons stripped off. At the end of the first stage of the UNILAC, the gold ions acquire energy of 1.4 *A* MeV with an average charge state of 25+, i.e. so far 25 electrons have been stripped off. The additional ionization is the necessary condition for reaching the desired final energy within the length of the linear accelerator, before the injection in the SIS.

The second stage of the UNILAC is accelerator of the Alvarez design. It totals 55 meters in length and contains four 13-meter-long tanks with 150 drift tubes. The polarity between the electrodes of the drift tubes can be reversed three times faster than the high current injector, i.e. with a frequency 108 MHz. The gold ions leave the Alvarez stage with energy of 11.4 *A* MeV.

The last stage of the UNILAC consists of fifteen single resonators, which allow for adjusting the ion velocity by accelerating or decelerating the ion beam by +/- 1.5 *A* MeV. Afterwards, the beam is injected into SIS over a period of app.100 μs in the regime of the multi-turn injection, i.e. each filling of the SIS consists of 10 or 20 individual injections from UNILAC.

Before entering the synchrotron ring accelerator SIS, which provides the final stage of the accelerating process, the beam passes through a thin carbon foil in the transfer channel responsible for stripping off several additional electrons. Thus, the charge state of the gold ions in our experiment was increased from 25+ to 65+, which allowed for reaching high energies necessary for the experiment. The SIS itself consists of 12 identical cells placed consecutively along a circumference perimeter of 216 meters. Each of these cells consists of

two dipoles, a focusing quadrupole triplet and a set of sextupoles correcting for the chromatic aberrations. The acceleration of the passing ions can be in SIS induced by two radio-frequency structures, situated diametrically on the ring, opposite to each other. However, due to the limitation in the ramping time of the SIS magnets, which is 1.3 T/s, only one accelerator structure is used. The passing ions are then accelerated during each revolution by means of a potential difference of 9 kV. With increasing velocity of the beam after each cycle, the frequency of the structure rises from 800 kHz to 5.6 MHz. The time needed for acceleration of the gold ions by SIS from the initial energy delivered by the UNILAC to 1 *A* GeV, i.e. the time between two subsequent spills was app. 3 seconds.

The maximum energies achievable by most of the synchrotrons are determined by the maximum bending power of the magnets they consist of. In case of the SIS it is 18 Tm. For various accelerated beams, this can mean different maximum energies, depending on the injected charge state and the N/Z ratio. The magnetic rigidity of $^{197}Au^{65+}$ accelerated to 1 *A* GeV with a charge state 65+ is 17.103 Tm, what is thus very close to the limits of the SIS.

As can be found in reference [Ste92], the transversal beam emittances were determined with the help of the FRS. The typical values from the standard deviations of the position and angular distributions $\varepsilon = \pi\sigma_{position}\sigma_{angle}$ are $\varepsilon_{xx'} = (1.8\pm0.1)\ \pi$ mm·mrad, and $\varepsilon_{yy'} = (4.0\pm0.2)\ \pi$ mm·mrad, with beam widths of 3.0 and 3.9 mm in x and y respectively. Under stable conditions, the beam momentum spread $\delta p = \Delta p/p$ is below 10^{-3}.

In order to investigate also the most exotic reaction products, the GSI accelerator facility is able to deliver beams of very high intensities. While the value of the maximum technically achievable intensity is determined by the space-charge limit of the SIS, in case of very heavy ions such as gold it is not usually reached. The actual intensity is then influenced by several other factors, including the type of the accelerated ions, the isotopic composition of the material used for the ion production, type of the used ion source, location of the experimental area and actual tuning of the whole accelerator system. In the experiments analyzed within this work, the highest beam intensity reached was about $2.8\cdot10^8$ particles per spill.

2.2.2 Beam-position monitors before the FRS

Once the beam is extracted from the SIS, it is directed to the FRS experimental area by two dipoles and sets of quadrupoles and sextupoles (see Fig. 2.3). The precise centering of the beam on the production target is performed with two so-called "current grids", which are in fact beam-profile monitors with gas amplification and current readout.

Each current grid can be moved into and out of the nominal beam position by means of a compressed-air activated feed-through. The mechanical layout of the wire planes, the electrodes and the mounting inside the gas chamber is based on experience gained at GANIL [Baz84, Ann85]. For measuring the horizontal (x) and vertical (y) intensity distribution of the beam, two planes of parallel wires (77 wires/plane, 1 mm distance) are used, being mounted between metal-foil cathodes in a gas chamber. The most important information on the mechanical layout of the current grids is compiled in **Fig.2.4.**

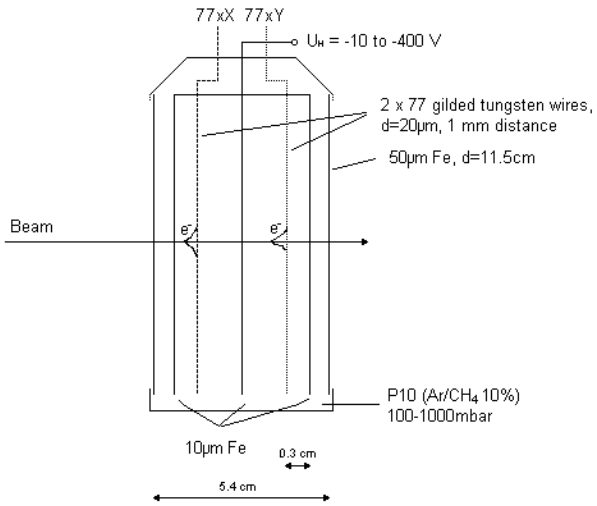

Fig.2.4: Schematic view of the beam position monitors before the FRS

After determining the actual *x* and *y* position-profile of the beam with the current grids, it is possible to correct for any angle or unwanted offset of the beam by tuning the magnets on the path from the SIS to the target area. The precise values of corrected magnetic fields are determined by a dedicated software named Mirko [Fra83].

2.2.3 Beam structure and intensity monitor

Although the measurement of the absolute production cross sections of the reaction has not been the main intention of this experiment, the information on the total flux of the beam particles is essential in order to properly reconstruct full velocity distributions of individual isotopes, which due to the limited angular and momentum acceptance of the FRS have to be measured in several steps. However, such beam-intensity monitor has to be able to withstand very high beam intensities up to the order of 10^9 beam particles per second without saturation, i.e. responding linearly to the beam intensity. Moreover, it should not disturb the quality of the beam before it hits the target neither it should contribute to the overall fragment production by nuclear interactions of the beam particles with atoms of the detector itself.

With respect to these requirements, a specific apparatus, Secondary Electron Transmission Monitor (SEETRAM), which is capable to correctly monitor the intensity of heavy-ion beams with high intensities, was developed at GSI [Zie92].

The monitor consists of three aluminum foils of app. 10µm thickness (~10 mg/cm^2), mounted on rings of 11.5 cm in diameter, placed in a vacuum, perpendicular to the beam. The inner foil is insulated from the rest of the detector and grounded via a current integrator. The outer foils are connected to the voltage of +80 V. When then a beam particle passes through the monitor, the inner foil of the detector may release some electrons close to the surface. Driven by the potential difference, these electrons are collected by the outer foils, resulting in a positive current in the central layer. This current, together with the pedestal current is added by purpose to the entrance current of the digitizer in order to avoid "negative" frequencies, creating together a background signal, which is transformed into the voltage signal by the current integrator. The intensity of this current depends on the beam particle species and their energy, and can range from 10^{-10} to 10^{-4} A. Therefore seven levels of sensitivity can be adjusted through a choice of the proper resistance, which can be varied by an order of magnitude in range of 10^4 to 10^{10} Ω. The resulting voltage signals are then filtered, digitized and accumulated in a time spectrum. The fast analogue output of the signal can be used for real-time monitoring of the extraction profile.

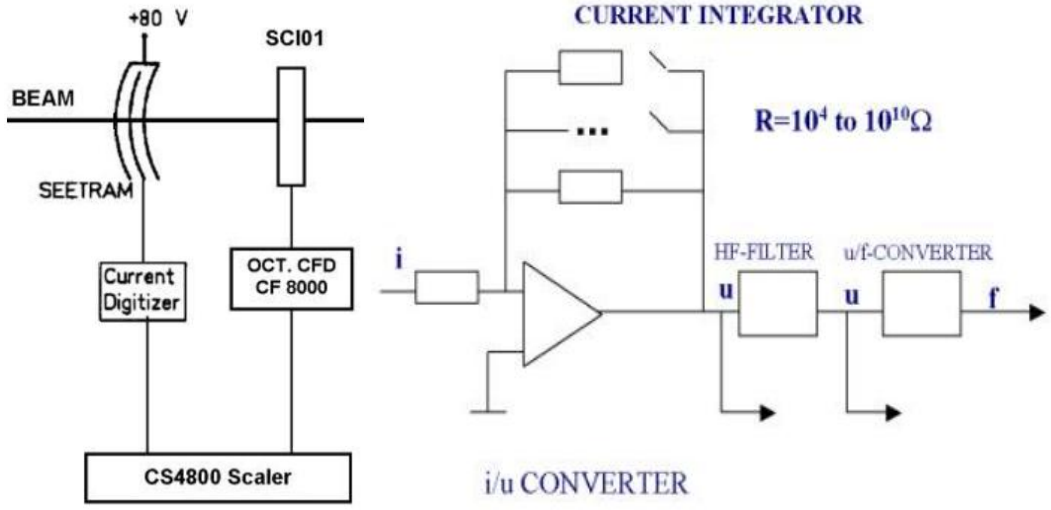

Fig.2.5: Schematic view of the SEETRAM detector (*left*) and the current digitizer (*right*).

The calibration of the SEETRAM monitor is a necessity for determination of the absolute beam intensities, however in our experiments, the absolute yields were of no significant importance and therefore the SEETRAM output has been used only for relative normalizations without any explicit calibration, as described in chap.3.4.3.

Although the SEETRAM has been developed with best intentions not to influence the results of the physical experiment itself, the thickness of the SEETRAM can cause a nuclear reaction with app. 0.1% probability. This is very often negligible with respect to the production targets used in the experiments at the FRS. But, as will be reiterated later in the next chapter, such nuclear reaction rate is comparable especially with the nuclear-reaction rate in our gold production targets, which thickness were chosen as the best compromise in order to manifest the effects of the nuclear collision on the dynamical evolution of the fragmentation residue.

Therefore the beam monitor could not been used throughout the whole experiment, but was always inserted into the beam only for an initial part of the measurements after the change of the magnetic field settings. Thus, under certain assumptions discussed in chap.3.4.3, the ratio of the reaction yields in the measurements with and without SEETRAM and the absolute yields in the measurements with the SEETRAM could be used to normalize to the same beam dose also the yields of the measurements without the SEETRAM. Details of this procedure are given in chap.3.4.3.

2.3 The production targets

The material of the production target has been determined with respect to the physical interest, and has been already discussed in the introductory chapters of this work. However, facing the experimental challenge, another feature of the target which can have a detrimental influence on the final results is its thickness.

When estimating the thickness of the target, one has to assume all possible interactions of the beam particles with the target material and the effects of this interaction on the characteristics of the desired reaction products. In case of the nuclear reactions, which are the wanted events, in the first approximation the collision event can be seen as a 2-stage process: abrasion and evaporation.

In the peripheral collision of the high energy projectile with the target nucleus the participant nucleons are stripped off, leaving the remaining nucleons almost unaffected. The residual prefragment (spectator) is excited and moves roughly in the direction of the projectile. In the abrasion stage the spectator acquires certain momentum shift, which according to [Mor89] increases with the number of abraded nucleons (ΔA). The momentum after the abrasion stage is not sharp but it exhibits a certain momentum distribution, which is according to [Gol74] given by the Fermi motion of the remaining nucleons. This gives rise to a Gaussian momentum distribution of the spectator, which depends on the number of nucleons abraded. A more detailed description of the abrasion stage is based on the idea of stripping off the nucleons from the different particle levels. This gives rise to the excitation energy of the spectator, which increases with the number of nucleons abraded, and therefore with decreasing impact parameter. The excited prefragment then decreases its energy via evaporation of particles or light clusters. The emission is assumed isotropic in the rest frame of the spectator, and the evaporation process thus causes a broadening of the momentum distribution, but it does not change the mean velocity.

Generally unavoidable competing phenomena accompanying the nuclear reactions are non-nuclear reactions, namely the interactions with the atoms or atomic electrons of the target material. As a consequence, the beam particles or products of already induced nuclear reactions undergo additional energy losses and angular straggling. This is the case for the

inelastic scattering, when the beam ion may excite or ionize the target atoms via interactions with their electrons. Since such interactions in the target material are really numerous, the total energy loss as well as its straggling may be significant and comparable to the effect of the nuclear reactions itself. Similar influence have the elastic interactions, however, in this case, the projectiles or fragments are elastically scattered from the target atom. The energy remains virtually unaltered, but the process can result in a sizeable angular straggling.

Another process of deserved importance is the possible capture or loss of electrons by the traversing beam particle or reaction product. This results in different charge states of the fragment at the exit of the target material, causing thus problems due to their different deflections in the magnetic field of the spectrometer and possible false identification of the nuclear-charge based on the energy loss in a corresponding detector. The process basically depends on the velocity of the fragment and the velocity of the electrons on its orbits, and follows the Bohr criterion, which says that the orbital electrons are stripped off if their orbital velocity is less than the velocity of the fragment, and attached in the opposite case. Moreover, there is even a slight dependence of the process on the target material.

Moreover, the fragments may undergo secondary reactions in the target itself. This gives the upper limit on the percentage of the primary nuclear reactions in the target, which now cannot be too high not to allow the secondary reactions in the target to become too important.

In conclusion of these ideas, when we want to optimize the target thickness in order to achieve the most favorable experimental conditions for the detection and identification of the fragmentation products, we should respect the following criteria:

- ***Narrow and well defined momentum distribution of the produced fragments***
- ***Small energy straggling of the produced fragments***
- ***Optimum percentage of the primary nuclear reactions in the target***
- ***Optimum charge-state distribution of the reaction product***

The effects of the first two processes, together with the secondary reactions in the target would be minimized with a very thin target. But the necessity to get the incoming projectiles fully stripped, and the desire to achieve as high as reasonably affordable statistics, prevents the target to be too thin. Therefore, if the optimum target thickness is to be found, one has to quantitatively evaluate the relative contributions of the mentioned effects for a given target and projectile and thus choose the most reliable target thickness.

In the present work the main emphasis was put on the requirement of minimizing the energy loss and energy straggling of the reaction products in the target, in order to study kinematic properties of the final residues ruled predominantly by the nuclear reaction process and not by the inelastic collisions with the atomic electrons. Quantitatively, our aim was to keep the ratio of straggling due to inelastic non-nuclear reactions (δE_{ion}) to the one according to Goldhaber model (δE_{Gold}) at level $\delta E_{\mathrm{ion}}/\delta E_{\mathrm{Gold}} = 0.1\text{-}0.2$.

In case of the incident beam energy of 1000 *A* MeV the chosen Au target thickness was then 100 mg/cm^2, in case of the lower beam energy, i.e. 500 *A* MeV, we decided for the thickness of the Au target of 50 mg/cm^2. The thickness of the aluminum target was ruled by the availability of the already mounted targets; therefore, we chose the thickness of 160 mg/cm^2, i.e. the thinnest target available. The expected number of nuclear reactions in these targets and the various charge state contributions behind them are summarized in **Tab. 2.1**.

Tab.2.1: Basic characteristics of the targets used in the experiments as predicted by [AMA].

Target	thickness	E_{beam}	nucl. react.	charge states [%]		
	$[mg.cm^{-2}]$	*[A MeV]*	*[%]*	***0e***	***1e***	***2e***
Al	160	500	1.424	73	24.9	2.1
Au	50	500	0.112	60.4	34.6	5
Au	100	1000	0.223	90.1	9.7	0.3

2.4 The Fragment Separator

The Fragments Separator is an achromatic zero-degree in-flight separator [Gei92]. Its main components are four 30º dipoles and sets of quadrupoles and sextupoles, all based on non-superconducting technologies and grouped into four stages.

The vacuum line is separated from the ultra-high vacuum of the SIS by a titanium window. Specially adapted for our experiments in order to minimize the number of nuclear reactions on the window, a little aperture in the window of app. 30 mm diameter around the beam axis has been covered by a thin carbon layer (30µg/cm^2). The vacuum line passes then through the FRS from the entrance to the exit along a distance of app. 70 m. Transversal apertures range from ±10-18 cm in horizontal direction and ±5-15 cm in vertical direction. These geometrical parameters together with the ion-optical properties result in a limited acceptance of the device, which accounts for ±1.5% in momentum and 15 mrad in angle around the beam axis.

The curvature of the magnets with radius of 11.25 m and the maximum magnetic field of 1.6 T achievable by the individual dipoles results in a maximum accepted magnetic rigidity of 18 Tm, which is the same as that of the SIS. The magnetic fields are controlled by the Hall probes with a precision and stability of about 10^{-4}.

In our experiments, as an ion-optical system, the FRS can be represented by two symmetric sections separated by a layer of matter, which acts as a velocity degrader, while four dipoles act as dispersive elements, and the quadrupoles as the focusing elements, and the sextupoles as correctors of chromatic aberrations. However the dispersive effect of the last two dipoles is just inverse to that of the first two, making the overall system achromatic at the final image plane S4.

The motion of the charged particles (i.e. ions) inside the magnet is determined by the Lorenz force, being proportional to the vector product of the particle's velocity and the magnetic field. Since the magnetic fields inside the dipoles are uniform and perpendicular to the trajectory of the ions, the field curves the flight-path of the ions. The action of the magnetic field upon the charged particle, with ionic charge q and momentum p, can be thus described by the following equation:

$$B\rho = \frac{p}{q} = \frac{m \cdot v}{q} \tag{2.1}$$

where B is the magnetic field inside the magnet, ρ is the radius of the trajectory, v is the velocity and m the mass of the ion. In relativistic regime $m=\gamma \cdot m_0$ with m_0 being the rest mass and γ the relativistic kinematical factor $\gamma = \sqrt{\left(1-\beta^2\right)^{-1}}$ with $\beta=v/c$ (c being velocity of the light). Further assuming fully stripped ions, i.e. $q= Z \cdot e$, with Z as the atomic number and $-e$ as the charge of the electron, and rewriting the rest mass into atomic units as $m_0=A \cdot u$, (A is the mass number, u is the atomic mass unit) the eq.2.1 can be rewritten into form:

$$B\rho \approx \frac{u}{e}\frac{A}{Z}\beta\gamma c\,, \tag{2.2}$$

which directly shows the main principle of the magnetic fragment separator, i.e. the correlation of the radius of the trajectory with the isotopic composition and the velocity of the detected fragment. The ratio *p/q*, i.e. the quantity $B\rho$, is *the magnetic rigidity*, and is characteristic of every particle determined by its mass, charge and velocity.

Because the dipoles act as dispersive elements, two ions entering the FRS with different magnetic rigidities, but under the same angle, will pass through the S2 area (called the dispersive image plane) in different horizontal positions. Their displacement Δx is proportional to their relative difference in magnetic rigidity, $\Delta B\rho/B\rho$, through quantity *dispersion* and defined as follows:

$$D = \frac{\Delta x}{\Delta B\rho / B\rho}\,. \tag{2.3}$$

In our experiments, the dispersion at the intermediate image plane was app. ~ 6.5 cm/%. Thus, due to above mentioned mechanical constrains and physical dimensions of the FRS, if two ions differ in magnetic rigidities too much (i.e. more than ±1.5%), they cannot be transmitted by the device at the same time, i.e. the same magnetic setting. Therefore, by applying a certain magnetic field on the first two dipoles, one selects a specific group of ions within a limited range of magnetic rigidity.

As the fragments at the intermediate image plane pass through a layer of matter (the scintillator detector and optionally additional degrader) they suffer a loss of energy according to Bethe equation:

$$\frac{dE}{dx} \approx f(v, I, Z_M)\cdot Z^2 \tag{2.4}$$

where Z and v are the charge and the velocity of the fragment, and I and Z_M the ionization potential and the atomic number of the medium, i.e. the degrading material. As a consequence of the suffered energy loss, every fragment is slowed down and its magnetic rigidity is lowered according to its nuclear charge and velocity. In terms of the magnetic rigidity, this means smearing off of the sharp interval of magnetic rigidities accepted by the first stage of the FRS, from which only a limited part can be further transmitted through the second stage of the FRS, i.e. through the 3rd and 4th dipole, according to the applied magnetic field.

In conclusion, the magnetic field of the first two dipoles selects fragments within a certain range of magnetic rigidity, from which only a specific interval of nuclear charges is chosen by the field of the last two dipoles (see **Fig. 2.6**).

The result of the limited acceptance is thus the inclusive nature of the measurement and the necessity to combine many different magnetic field settings of both FRS-stages in order to map full range of magnetic rigidities and charges of all the reaction products.

The identification of the produced fragments is performed by measuring the time-of-flight, over the flight path of the second stage of the FRS, together with the magnetic rigidity determined from the applied magnetic field and the horizontal positions in the S2 and S4, which altogether allow deducing A/Z of the fragment, according to eq.2.2. The charge of the fragments was deduced from the energy losses in dedicated detectors placed at the exit of the FRS, allowing determining mass A of the detected fragment.

.

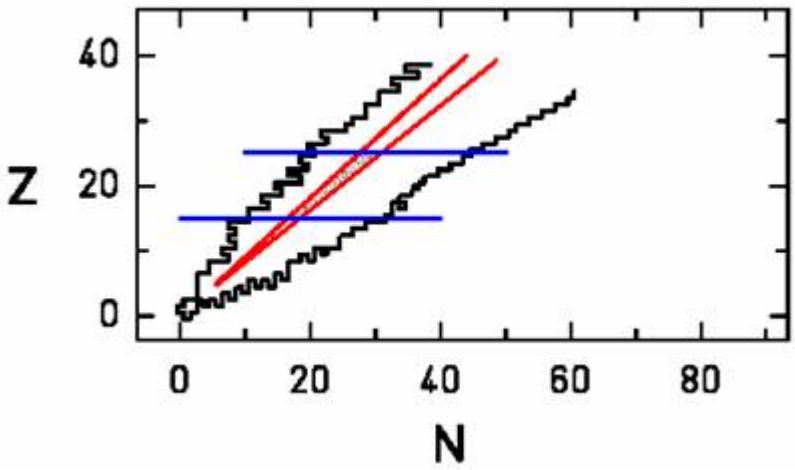

Fig.2.6: Simplified schematic view of the isotope selection according to the magnetic rigidity in the first stage (red) and according to their nuclear charge in the second stage (blue) of the FRS.

In order to measure the fragment velocity behind the production target, and bypass the corrections for particle slow-down in the degrader material at S2 and S4, the first stage of the FRS can be used in principle independently of the time-of-flight measurement. This is however possible only after successful unambiguous identification of the detected fragment with the second stage of the FRS, as described above. Once the *A* and *Z* of the fragment are determined, their values, now being integers without any uncertainty, can serve as input to the modified eq.2.2 where the fragment velocity is treated as the unknown variable. Knowing the horizontal position of the fragments at S2 and the strength of the magnetic field in the first FRS-stage, i.e. the magnetic rigidity, the fragment velocity can be determined with even significantly higher precision than with the time-of-flight method itself, as will be further re-iterated and discussed in chap.3.4.1.

The description of the FRS in this section concentrated only on those features of the device, which were utilized during the experiments within this work. The details of the ion-optical characteristics and various working modes can be found in dedicated publications, such as [Geis92].

2.5 The detectors

Fig.2.7 schematically displays the FRS with its standard detection equipment as it was used during the experiments described within this work. The beam monitor (SEETRAM) in front of the target was optionally used to determine the intensity of the primary beam and to monitor the spill profile. Two scintillator (SCI21 and SCI41) detectors were used at the intermediate and final focal planes to measure the horizontal position of the produced fragments. At the same time the time deference between their two signals served as the measure of the time-of-flight through the second stage of the FRS. Two ionization chambers (MUSIC1, MUSIC2) at the exit of the fragment separator measured the energy losses of the incoming fragments, thus allowing for the nuclear-charge determination. Drift times of the induced charge in the MUSIC detectors served to deduce the horizontal position of the detected fragments, even with better precision than the position determined by SCI41. Moreover, they were also used for determination of the flight angle of the detected fragments. The Hall probes inside each of the four dipoles continuously monitored the strength and stability of the magnetic field.

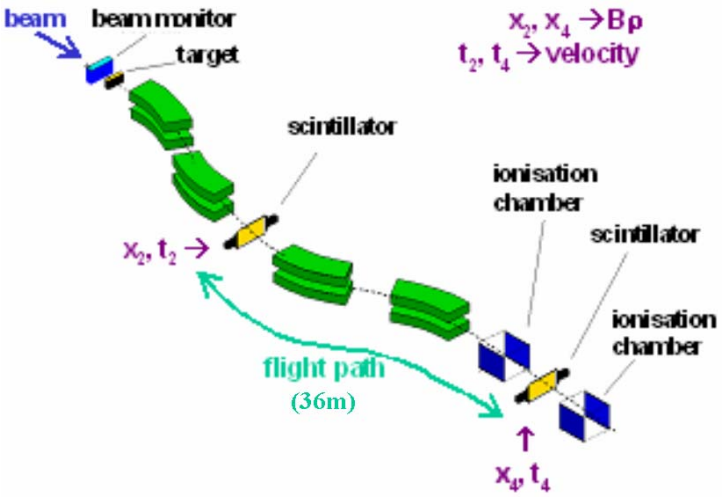

Fig.2.7: Schematic view of the FRS and its standard detection equipment.

Additionally to the above mentioned detectors, during several calibration procedures two multi-wire proportional chambers at S2 and S4 (MW22 and MW41) were used. The first detector served for the calibration of the SEETRAM signal, the later for the calibration of the corresponding scintillators at S2 and S4; in case of MW42 also for the calibration of the MUSIC drift times.

2.5.1 The Hall probes

The magnetic field inside the dipoles is measured by the Hall probes. The working principle of these detectors is based on the Hall Effect. If an electric current flows through a conductor in a magnetic field, the magnetic field exerts a transverse force on the moving charge carriers which tends to push them to one side of the conductor. A buildup of charge at the sides of the conductors will balance this magnetic influence, producing a measurable voltage between the two sides of the conductor. Since both values of the current and voltage can be accurately measured, the Hall probes are able to return the values of the magnetic field with a relative error of $\sim 10^{-4}$. At the FRS, the magnetic field of every dipole is continuously measured by a corresponding Hall probe.

2.5.2 The scintillators

The experimental requirements of high resolving power of the FRS, in order to separate and identify the detected fragmentation products, set strict demands on the detection device responsible for the measurement of the position and the time of flight of the incoming fragments. The detectors should provide fast and precise measurements on the event-by-event basis and at the same time preserve the ion-optical quality of the magnetic system. In order to secure the absence of heterogeneities of the detector together with uniform thickness and fulfill the requirements on the quality of the detector response, a detector system composed of two fast scintillator detectors has been developed [Vos95].

The scintillators are produced from a BC240 plastic material, characterized by a high efficiency of the light production, and by a very fast signal rise time (~0.5 ns). The sensitive area is 210x80 mm2 and 200x80 mm2 in case of SCI21 and SCI41, respectively. The nominal thickness of both detectors is 5mm. The scintillation light is transported by total internal refection and driven through light guides to the fast photomultipliers where it is being

registered and transformed to a electrical signal. There are two photomultipliers mounted on each scintillator, on the left and right side with respect to the axis of the FRS.

The horizontal position x_2 and x_4 is then determined by the time difference of the signals arriving at the two photomultipliers. The same signals, but now the difference of left or right sides of two different scintillators, were used to measure the time-of-flight of the fragments, as schematically displayed in **Fig.2.7**. The signals coming from the photo-multipliers are first treated with the constant-fraction discriminators (CFD) and subsequently used as a start and stop of the time-to-amplitude converter (TAC). The analog signal of the TACs was then read and digitized by the analog-to-digital converter (ADC). The threshold of the CFDs was set to app. 10 mV in order to discriminate the noise and light particles, since the main interest of the performed experiments lied in the region of rather higher nuclear charges ($Z \geq 10$).

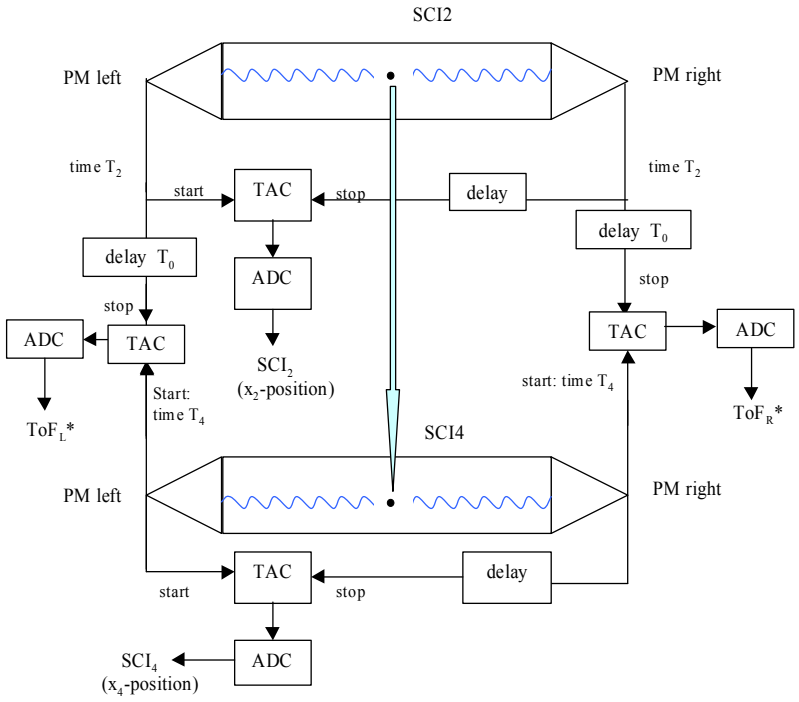

Fig.2.8: Schematic usage of the two scintillators for the measurements of the *x*-position at S2 and at S4 and of the time-of-flight of the fragment.

The time-of-flight of the fragment is considered as the difference of the times at which the ion passes through SCI21 and SCI41 at times t_2 and t_4 respectively. Since the signal from the left (optionally also right) side of the SCI41 has been used as the master trigger of the whole electronics, the signals from this detectors had to be read by the corresponding TACs before the arrival of the signals from SCI21. Therefore, the delay t_0 has been chosen in such a way, that $t_2+t_0 > t_4$. The measured time-of-flight ToF^* was than taken as the average of the times ToF_L^* and ToF_R^* deduced from left and right sides separately. Transforming the measured times from channels to seconds with calibration factors α_L and α_R its possible to write:

$$ToF^* = \frac{ToF_L^* \cdot \alpha_L + ToF_R^* \cdot \alpha_R}{2} = t_2 + t_0 - t_4 , \qquad (2.5)$$

and considering the real time-of-flight ToF as being defined also by the ratio of flight-pat s_0 and the fragment velocity v:

$$ToF = \frac{s_0}{v} = t_4 - t_2 , \tag{2.6}$$

we arrive at the concluding equation

$$ToF = t_0 - ToF^* = t_0 - \frac{ToF_L^* \cdot \alpha_L + ToF_R^* \cdot \alpha_R}{2} \quad . \tag{2.7}$$

The position resolution of the detector Δx = 4mm, with respect to the speed of light inside the scintillator being c_{SCI} = 20 cm/ns, corresponds to the time resolution of Δt = 40 ps [Vos95, Schw98], and assuming dispersion at S2 of app. 6.5 cm/% to the magnetic rigidity resolution of $\Delta B\rho \approx 6 \cdot 10^{-4}$.

The quantitative details of the time-of-flight calibration and the methods how to precisely determine the calibration factors and the value of the ToF offset t_0 are introduced in a dedicated chapter 3.2.3.

2.5.3 The multiple sampling ionization chambers (MUSICs)

In order to satisfy the experimental requirements of unambiguous charge identification which is the necessity for subsequent identification in mass, two identical multiple-sampling ionization chambers (MUSICs) were placed at the exit of the FRS.

The schematic drawing of the MUSIC is displayed in **Fig.2.9**. Although the anode is segmented into six parts, only the middle four are used for actual measurements, and the outer two served only to avoid border effects. The advantage of dividing the active anode into several parts results is the higher number of independent measurements (samples), thus allowing for precise determination of the fragment's charge. When a fragment traverses the chamber, it excites and ionizes atoms of the gas along its flight-path, creating thus a cloud of electrons and positively charged ions. The charge-carriers, driven by the uniform electric field between anodes and the cathode drift in the corresponding direction, i.e. electrons to the anodes, and the ions to the cathode. Because the drift velocity of the electrons is app. by 3 orders of magnitude higher (~5 cm/µs) than for the ions, the charge collected on the anodes is used in the analyses, whose magnitude is app. proportional to the energy loss and thus to the square of the fragment's charge, as described by the Bethe's equation (2.4).

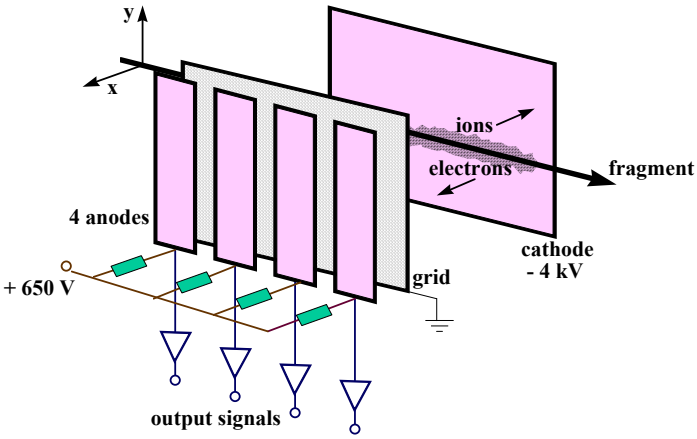

Fig.2.9: Schematic drawing of the MUSIC; the outer protection anodes are not displayed.

The role of the Frisch grid placed in front of the anode is to make the signal induced by the drifting electrons independent on the distance of the ion trajectory from the anodes, and to screen off the influence of the produced positive ions. The active volume of the chamber is 406 mm in beam direction and 276x150 mm^2 in x and y directions. The entrance and exit windows are made of 25 µm Kapton foils covered by 40 µg/cm^2 aluminum layer. The filling gas is P10, i.e. mixture of argon (90%) and methan (10%), at atmospheric pressure and

temperature. During the experiment, the gas is continuously being renewed just by the pressure in the gas supply.

While the signals from the MUSIC anodes were used to measure the charge of the passing ions, the same signal was also used to measure the drift-time of the produced electrons. The signals from the SCI41 were used as the start and the anode signal as the stop signal brought to the time-digital-converter (TDC). The drift times track the path of the fragment in the *xz*-plane and allow for reconstruction of the effective flight-path of the fragment.

The calibration of the energy losses measured by the MUSICS as well as the description of the drift-time calibration is given in the dedicated chapter 3.3.

2.5.4 The multiwire proportional chambers

The multiwire proportional chambers (MW) at the FRS have been primarily designed for precise measurements of the transversal positions in *x* and *y*, and were thus used for initial centering of the beam. Moreover, their technical construction allowing for independent absolute calibration predestines them for calibration of other detectors, such as scintillators and MUSICs. MWs are installed at all image planes of the FRS, i.e. in S1, S2, S3 and S4, and in order to allow even for measurements of the flight-angles and tracking, at S2 and S4 are installed even two MWs.

All the chambers, except the manually-mobile MW42, are housed in hermetic containers, which are optionally insertable into the beam line. Entrance and exit windows of 100 µm titanium shield them from the vacuum. The MW42 uses two 25 µm Kapton windows to separate the chamber from the surrounding air.

The MW detectors employ five sets of wires organized in parallel planes. The first two planes are spatially separated from the other three, which are close to one another. With these two planes, the detector can be operated in a two-stage operation mode, which however has not been used in our experiments, and therefore this description of MW functionality will be limited only to the one-stage mode, employing three wire planes, i.e. cathode X and Y and the anode 45°, see **Fig.2.10**.

The central plane from these three is the anode. It consists of 20µm tungsten wires separated from each other by a distance of 2mm, aligned in a 45° transverse direction, with respect to the *x* and *y* axes. The voltage of the central anode has to be properly adjusted with respect to the nuclei to be measured; the typical values are around 2500V. The first and third planes (*x* and *y* plane, respectively) are grounded cathodes and consist of 50 µm tungsten wires in vertical, resp. horizontal direction, with a 1 mm pitch, and connected to the delay lines. Each side of the delay line is connected as an independent stop input of a TDC, while the signal from the anode provides a common start. The wire planes are housed in a container filled with mixture of Argon, CO_2 and alcohol at atmospheric pressure.

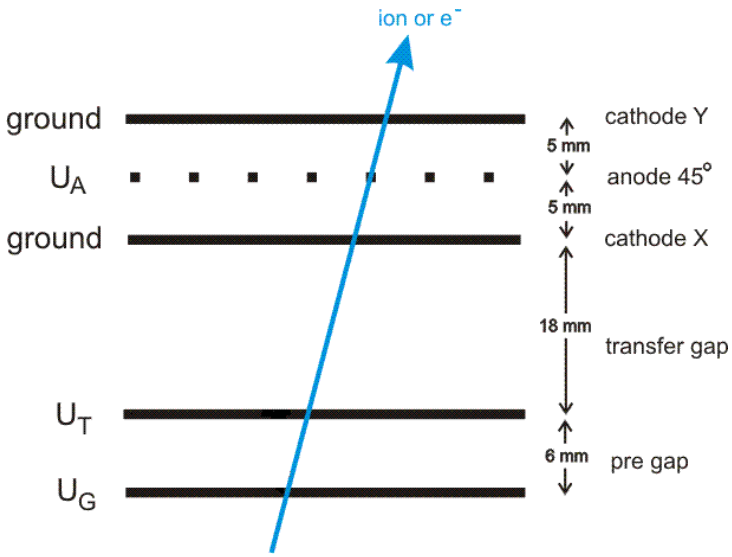

Fig.2.10: Schematic view of the multi-wire proportional chamber.

The ion, passing through the MW, produces a track of ionized gas particles. Driven by the electric field, the electrons drift toward the nearest anode-wire. This results in a current induced in the closest wires of the x- and y-plane, that adjure the anode. Due to a certain delay between the closest wires, signals from different wires need different time to arrive to the TDC as the stop signals. The time difference between arrival of signals from opposite sides of the same wire (x_L, x_R, y_U, $y_{D)}$ provide the information on the position of the traversing ion:

$$\begin{aligned} x_{MW}(mm) &= a_x \cdot (x_L - x_R) + b_x \\ y_{MW}(mm) &= a_y \cdot (y_U - y_D) + b_y \end{aligned} \tag{2.8}$$

where a_x, a_y, b_x and b_y are determined from an independent calibration performed with help of a radioactive source. Additionally, since all the wires have the same length, the sum of signals from opposite sides, i.e. x_R+x_L and y_U+y_D, should be constant, thus allowing to discriminate good events from the ones cause by a multiple hit.

The active area perpendicular to the beam axis is 200x200 mm^2 and the achievable resolution about 1 mm.

Since the wire-structure introduces transversal heterogeneities strong enough to spoil the achromaticity of the FRS, the detectors were removed from the beam during the production measurements.

3. Data Analysis

The main aim of the experiments has been to measure the longitudinal velocities of the fragmentation residues produced in three different reactions, i.e. ^{197}Au+^{197}Au at 0.5 and 1.0 *A* GeV, and ^{197}Au+^{27}Al at 0.5 *A* GeV. Since the physical interest was to study the evolution of this dynamical property with respect to the size of the participant blast, being ruled by the impact parameter, our measurements were done systematically for all isotopes of all elements with significant production cross sections, which were effectively identifiable by the FRS. In case of the system at the highest reaction energy, the measurements covered essentially all elements from charge 10 up to the charge of the projectile. In case of the systems with lower reaction energy, our measurements scanned a bit limited region of nuclear charges $10<Z<65$, since in this energy domain, due to stronger population of different charge states of the same element, the separation of different isotopes of the heaviest elements could not be achieved with the necessary resolution.

The velocity of the individual fragments was basically measured by determining the transversal position at the intermediate focal plane, measured by the scintillator SCI21, and by the magnetic fields in the first stage of the FRS (see eq. 2.2). However, the necessary condition for the proper velocity determination is the knowledge of the mass and charge of the fragment. Therefore, a complete identification had to be performed prior to the velocity determination.

In order to better understand all the steps of the data analysis needed to finally extract the longitudinal velocities of the fragmentation residues, we have to recall that the FRS is a forward spectrometer with limited momentum and angular acceptance, as discussed in chap. 2. This feature of the FRS affects both the analysis of the measured data as well as the interpretation of the final results, since only inclusive measurements could be performed; meaning that only one product of any single nuclear reaction could be measured, provided this fragment fulfilled the conditions of momentum and angular acceptance.

The impact of the limited momentum acceptance has also its technical aspect. Once the magnetic fields are set, only fragments with magnetic rigidities fitting into a window set by the magnets can be transmitted and detected. Thus, in order to measure the full range of all magnetic rigidities populated by the reaction products, we had to systematically scan a wide interval of $B\rho$ of the first FRS-stage, and moreover, for each of these settings use several different tunings of the second FRS-stage, in order to scan all elements produced with the magnetic rigidities accepted by the first stage. In order to provide best transmission conditions for all fragments, the scanning steps, by which the spectrometer was tuned, were of 1.5%.

In case of all three experiments, this meant several hundred different magnetic-field settings. The task of the data analysis is to "glue" all the pieces, represented by the results measured in individual settings, together, and reconstruct the full velocity distribution for every single isotope.

The main difficulties connected to the limited angular acceptance were the loss of transmission efficiency and the necessity to perform additional corrections, especially for the fragments with lower nuclear charges. On the other hand, this limitation resulted in a possibility to distinguish two different reaction mechanisms, namely fragmentation and fission, as is explained in chap.4.1.

In this chapter, the procedures of the data analysis leading to the determination of the velocity of the fragmentation residues will be described.

Note: *As will be seen in the following sections, many calibrations and data analysis procedures are connected to the fact that the three experiments were organized in two separate experimental runs, and thus the two with the lower incident-beam energy share some of those analysis procedures, without any dependence on the utilized target. Therefore, for the sake of clarity and simplification, at the places where one can exclude any confusion, the*

experiment with the ^{197}Au beam at 1000 A MeV will be referred to as Run121, and the experiment with ^{197}Au beam with energy of 500 A MeV will be referred to as Run123, no matter whether the gold or the aluminum target was used.

3.1 General overview

The performed data analysis can be divided into three main parts and schematically summarized in the following way:

I. Initial Fragment Separator calibrations
- *determination of the dispersions at S2 and S4*
- *measurement of the thicknesses of the layers of matter in the beamline (SEETRAM, target, SCI21, degraders)*
- *measurement of the effective radii of both stages of the FRS*
- *ToF calibration*
- *SEETRAM calibration*

II. Identification of the detected fragments
- *correction of energy losses in MUSIC on ToF, position, temperature and pressure*
- *calibration of the scintillator SCI21*
- *calibration of the MUSIC drift-times*
- *determination of A/Z of the fragments*
- *identification of the fragments*

III. Reconstruction of the velocity distributions
- *normalization of the yields (beam dose, dead-time)*
- *correction for angular transmission*
- *reconstruction of the velocity distributions by superposition of different magnetic settings*

In the first part of the data analysis, it is necessary to measure the "inner characteristics" of the FRS, such as the effective radii of the dipoles or dispersions at S2 and S4, and calibrate the ToF detectors by measuring the thicknesses of all layers having impact on the measurements of the fragments velocities, i.e. those in the beam line at the target area and the intermediate focal plane. These measurements (with the only exception of the TAC calibration) can be performed only with a well defined beam of known magnetic rigidity.

The aim of the second part of the data analysis is the identification of the detected fragments. Therefore, the main effort is invested into calibrations of detectors essential for fragment identification such as SCI21 and MUSICs, including-energy loss as well as drift-time calibration. Often the most efficient way to perform these calibrations is to use the reaction products which populate a large volume in phase space, and thus can interact within the whole active area of the detectors. Afterwards, an identification of every detected fragment can proceed.

In the last stage of the data analysis, the velocity distributions of every individual isotope are reconstructed. Pieces of those distributions from different magnetic-field settings are superimposed on one another. At the same time, the results have to be normalized to the same beam dose and corrected for the dead-time and the angular transmission. Only then, one can receive correct shape, magnitude and mean value of the velocity distribution for any measured isotope.

3.2 Initial Fragment-Separator calibrations

As pointed out in chap. 2, the key equation of the data analysis is eq. 2.2, from which one would like to extract A/Z of the fragments. However, this assumes the knowledge of the applied magnetic fields, radius of the fragments trajectory, and velocity of the fragments. Moreover, since the magnetic field of the dipoles is homogenous, two fragments with the same velocity but different magnetic rigidities will flight on trajectories with different radii and traverse S2 or S4 at different positions. The relation between the difference of these two positions and the magnetic rigidities is ruled by the dispersions in the individual FRS stages, which also have to be determined experimentally.

3.2.1 Determination of dispersions at S2 and S4

The most efficient way to measure the dispersions at the intermediate and final focal planes is the use of a spatially well defined beam of ions with known magnetic rigidity. The fully stripped beam of ^{197}Au at 500 A MeV has $B\rho$ = 9.0414 Tm; the ^{197}Au at 1000 A MeV has $B\rho$ = 14.0744 Tm. After aligning the beam in the whole FRS, we insert the MW22 into the beam line at S2. We measure the position of the beam and increase the magnetic field of the whole stage by a factor of 1.003, i.e. we increase the magnetic rigidity corresponding to the central trajectory by +0.3%. Since the bending power of the dipoles is now stronger, the position of the beam at S2 is shifted. After recording the new position of the beam, we perform the same procedure several times in order to sweep the beam through the whole momentum acceptance window, monitoring the magnitude of the beam-position shifts to determine the dispersion and its dependence on the position at S2.

The results of the measurement of the dispersion at S2 for the beam of ^{197}Au at 1 A GeV is summarized in **Tab.3.1**, which is graphically represented in **Fig. 3.1**. When assuming the error of the position measurement in order of 1 mm, the measured dispersion has then the value of D_2 = -6.38 ± 0.03 cm/%.

Analogical procedures were performed in order to determine the dispersion at S4 and the dispersion at S2 and S4 in case of the ^{197}Au beam at 500 A MeV, i.e. in Run123. The resulting dispersions were having values of D_4 = 8.42±0.07 cm/% in Run121, and D_2 = -6.34±0.04 cm/% and D_4= 8.22 ± 0.06 cm/%. in Run123.

In conclusion of this section, we can state that the dispersion has been found linear in all of our experiments in the whole range of the intermediate and final focal plane.

ΔB [%]	B_{12} [T]	x_2 [mm]
-1.4	1.2277	88.8
-1.1	1.2313	70.6
-0.8	1.2352	51.0
-0.6	1.2381	35.1
-0.3	1.2413	18.4
0.0	1.2449	-0.2
0.3	1.2488	-19.7
0.6	1.2527	-39.3
0.9	1.2563	-58.4
1.2	1.2600	-76.8

Tab. 3.1: Summary of the measurements of the dispersion D_2 at S2 during Run121. ΔB is the change of the magnetic field with respect to the position of the centered beam, B_{12} is the average magnetic field in the first FRS-stage and x_2[mm] is the beam position at MW21, i.e. at S2.

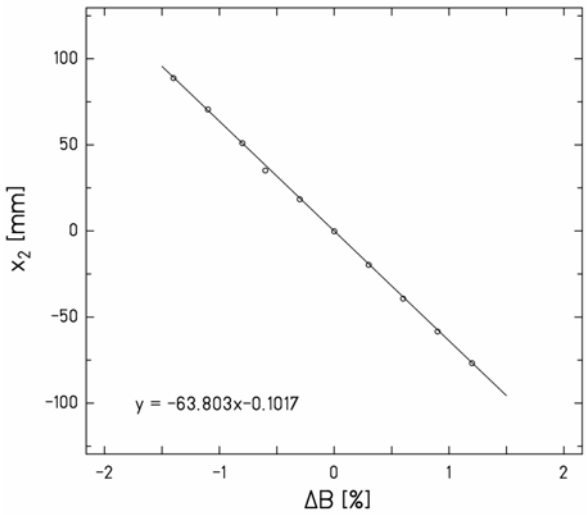

Fig. 3.1: Measurement of the dispersion at S2 in Run121. The line is a linear fit of the measured values; its slope defines the dispersion. Uncertainty in the x_2 determination is around 1 mm

3.2.2 Measurement of the thicknesses of the layers of matter in the beam-line

The ions passing through a layer of material in the FRS, such as the target or the SCI21 detector, suffer energy losses and are effectively slowed down. Their magnetic rigidities generally decrease, and therefore the fields of the magnets behind this degrading material have to be adapted, in order to be able to transmit the passing ions through the rest of the fragment separator. In order to correctly predict the magnetic rigidities of the reaction products or the beam, and thus properly plan the various tunings of the FRS magnets, the precise knowledge of the thicknesses of the materials put into the beam line is essential. To account for the individual characteristics of different beams (velocity, Z) and to avoid possible uncertainties due to uncertainty of the value of nominal thicknesses, the thicknesses of all the materials present in the beam line are measured experimentally from the energy loss of the beam.

In our experiments, the materials involved in the beam line were the SEETRAM, two gold and one aluminum target in the target area (S0), and scintillator and various degraders at S2. The layers of matter at S4 do not influence the settings of the FRS; therefore the knowledge of only nominal thicknesses is satisfactory.

The measurement is again most efficiently performed with the beam of known magnetic rigidity. First we record the position of the beam at S2 with help of the multiwire proportional chamber MW22 when SEETRAM and gold or aluminum target is in the beam line. Then the SEETRAM is taken out and we record the shift of the beam position at S2. Afterwards the target is taken out and the SEETRAM inserted back.

With the knowledge of the dispersion at S2, we can convert the shift of the beam position into the change of the magnetic rigidity corresponding to the individual material:

$$\Delta(B\rho)[\%] = \frac{\Delta x[cm]}{D_2[cm/\%]} \tag{3.1}$$

where $B\rho$ is the magnetic rigidity, x the horizontal position at S2, and D_2 the dispersion at S2.

Then utilizing the program AMADEUS [AMA], we can calculate the thickness of the material, which would result in the observed decrease of the magnetic rigidity.

Analogical procedures were performed in order to determine the thicknesses of various materials in the beam line at S2. The results of the measurement of the thickness of the involved material at S0 and S2 for the beam of ^{197}Au at 1 *A* GeV are summarized in **Tab. 3.2**.

Analogical procedures were performed in order to determine the thicknesses of various materials at S0 and S2 also in the case of the ^{197}Au beam at 500 *A* MeV. From these results the most important are the thicknesses of the production targets which were 51.2 mg/cm^2 in case of the gold target and 158.3 mg/cm^2 in case of the aluminum target.

Assuming the uncertainty in x_2 determination of 1 mm and the uncertainty of the calculation by [AMA], then the overall relative uncertainty of the thickness determination is around 1-2%.

Tab. 3.2: Summary of the measurements of the thicknesses of various objects at S0 and at S2 during Run121. B_{12} and B_{34} are the average magnetic field in the first and second FRS-stage, respectively, x_2 [mm] and x_4 [mm] the beam positions at MW21 and MW42, respectively, and $\Delta B\rho$ is the change of the magnetic rigidity with respect to the primary beam. Concerning the layers of matter, *Au* stands for the gold target, *See* for the SEETRAM detector, while *hom* and *S2 disc* stand for various types of degraders and their combinations with different nominal thicknesses 300, 4200 and 4600 mg/cm^2 of aluminum equivalent.

S0:						
layer	B_{12} **[T]**	x_2 **[mm]**	$\Delta B\rho$ **[%]**	**object**	**thickness**	
Au+See	1.24495	-0.2	0.000			
Au	1.24505	2.7	0.053	**Au target**	***105.8***	***mg/cm^2 Au***
See	1.24505	18.4	0.300	**Seetram**	***12.9***	***mg/cm^2 Al eq.***
S2:						
layer	B_{34} **[T]**	x_4 **[mm]**	$\Delta B\rho$ **[%]**	**material**	**thickness**	
-	1.24503	-0.5	0.000			
SCI21	1.21410	6.4	-2.401	**SCI21**	***583.1***	***mg/cm^2 Al eq.***
300mg hom	1.19840	-1.6	-1.388	**300mg hom**	***325.1***	***mg/cm^2 Al eq.***
S2 disc	1.17470	-0.3	-3.325	**disc S2**	***774.0***	***mg/cm^2 Al eq.***
S2disc+4200	0.93988	-1.2	-22.677			
S2disc+4200	0.93985	-1.8	-22.686	**4200mg + disc**	***4905***	***mg/cm^2 Al eq.***
S2disc+4600	0.91418	-4.6	-24.834			
S2disc+4600	0.91415	-5.5	-24.847			
S2disc+4600	0.91415	-5.3	-24.845	**4600mg + disc**	***5320***	***mg/cm^2 Al eq.***

3.2.3 Measurement of the effective radii of both stages of the FRS

As indicated by eq. 2.2 and discussed in chapter 2, the magnetic rigidity, the main characteristic of the fragment, is determined by the radius ρ of the fragment trajectory in a magnetic field of given strength B. Since the output voltages of the Hall probes, which measure the magnetic-field strength, are subject to long-term variations, e. g. due to radiation damages, the product of B_{Hall} as given by the Hall probes and ρ for an ion following the central trajectory along the FRS need to be calibrated with a beam, whose magnetic rigidity is known independently. For this purpose, the primary beam with its nominal energy as measured in the SIS accelerator by its revolution frequency is passed on the central trajectory. That means, the magnetic fields are adjusted in a way that the beam with known magnetic rigidity $B\rho_b$ hits the detectors MW22 at S2 and MW42 at S4 in the central horizontal position. As a technical procedure, we still use the value of B_{Hall} given as an output of the read-out hardware of the Hall probes, which is based on an initial calibration, and determine the effective radius ρ_{eff} in such a way that the product $B_{Hall}\cdot\rho_{eff}$ is exactly equal to the known

magnetic rigidity $B\rho_b$ of the primary beam. Since only the product $B_{Hall} \cdot \rho_{eff}$ enters into our analysis, this procedure is equivalent to calibrating the output of the Hall probes. It is also clear that the effective radius ρ_{eff} of the same FRS stage is generally not the same in different experiments, although the geometry of the separator was not changed.

The measurement of the effective radius of the first stage of the FRS is performed by insertion of various layers of matter, with known effective thickness, into the beam line and monitoring the shift of the beam position with the MW22 at S2. Such a procedure is necessary since the beam provided by SIS is not yet fully stripped. For this case, we can utilize the already performed measurements from the measurements of the thicknesses of layers of matter in the beam line in the previous section. According to the equation:

$$\rho_{eff} = \frac{(B\rho)_{calc}}{B_{12} + (x / D_2) \cdot 100} \tag{3.2}$$

we determine the effective radii for each of the involved matter and take the average value. We assume $(B\rho)_{calc}$ as being the calculated magnetic rigidity of the fully stripped beam after passing the given layer of matter, B_{12} the average magnetic field of the first and second dipole, i.e. the first FRS-stage, x the horizontal position at S2 measured by the MW22, and D_2 the dispersion at S2.

Determination of the effective radius of the second FRS-stage is possible without involvement of any additional material at S2, provided the beam traverses through the center of the intermediate focal plane.

The results of the measurements of the effective radii of the first and second FRS-stage are summarized in the **Tab.3.3**. Analogical procedures were performed in order to determine the effective radii of the first and second FRS-stage also in the case of the ^{197}Au beam at 500 A MeV.

Tab.3.3: Summary of the measurement of the effective radii ρ_1 and ρ_2 of the first and the second FRS-stage during the Run121. B_{12} and B_{34} are the average magnetic fields in the first and the second FRS-stage, respectively, x_2 [mm] and x_4 [mm] are the beam positions at MW21 and MW42, respectively, and $\Delta B\rho$ is the change of the magnetic rigidity with respect to the primary beam. $B\rho$ is then the magnetic rigidity of the beam behind the corresponding layer of matter. The layers of matter and their acronyms are the same as in Tab.3.2.

layer	B_{12} [T]	x_2 [mm]	$\Delta B\rho$ [%]	$B\rho$ [Tm]	*rho* [m]
beam	-	-	0	14.074	-
Au+See	1.2449	-0.2	0.35250	14.025	11.266
Au	1.2450	2.7	0.29973	14.032	11.267
See	1.2450	18.4	0.05277	14.067	11.272
				rho $_1$=	**11.268**
layer	B_{34} **[T]**	x_4 **[mm]**	$\Delta B\rho$ **[%]**	$B\rho$ **[Tm]**	*rho* **[m]**
-	1.2450	-0.5	0	14.025	11.265
				rho $_2$=	**11.265**

3.2.4 Time-of-flight calibration

The time-of-flight detectors at the FRS consist of two scintillators at S2 and S4, as described in detail in chap.2.5.2. They measure the time the fragments need to pass through the second stage of the FRS, i.e. over the flight path of app. 36 meters. This velocity

determination is necessary in order to perform the identification of the fragments, however, should not be confused with the procedure of more precise velocity determination, which is the object of this study, and which would not be possible without a prior identification, as is described in chap. 3.4.1.

Since the velocity of the beam particles with energy 1000 *A* MeV is app. 26.26 cm/ns in the laboratory frame, and for the ions with energy 500 *A* MeV it is app. 22.76 cm/ns, the time needed to cover the total distance between both scintillators is app. 137 ns in case of higher beam energy, and 158 ns for the lower beam energy. But it is necessary to consider, that due to nuclear reactions of different fragment species in target and degrading material at S2, the fragments arriving at the end of the FRS can have velocities significantly different than the primary beam, and that the fragments of the same charge and mass can also populate a rather broad range of velocities. Therefore, the time delay of the signal from the SCI21 has to be properly adjusted in order to come after the signal from the SCI41, which is the master-trigger of the whole data acquisition system, within the range of the TAC. Moreover, these ranges of the corresponding TACs have to be adjusted, in order to cover all possible times, when the reaction products can arrive.

The necessary range of the TACs was determined to be app. 30 ns, based on the model calculations performed with the Goldhaber model [Gol74] and Morrissey systematic [Mor89], and later confirmed by the real fragments. The actual absolute calibration of the TACs is then performed without the beam with help of a pulse generator, which is able to deliver signals with known period that is shorter than the set TAC range. The result is a spectrum with three sharp peaks, such as is displayed in **Fig. 3.2** for the calibration of the left side of the ToF in Run121, where the distance between two neighboring peaks corresponds to the period of the signal, i.e. 10ns. Determination of the number of channels corresponding to 1ns of real time is then a straightforward task as summarized in **Tab. 3.4**. This calibration factor is exactly the factor α_L in eq.2.5. With the analogical procedure, we calibrated also the right side of the ToF and both sides of the ToF in Run123.

The delay, which is necessary to bring the signals from SCI21 after the triggering signal from the SCI41 has to be adjusted with the beam and later confirmed with the real fragments, which should arrive within the gate generated by the trigger signal. In order to measure the absolute value of this delay, the so called time-of-flight offset being denoted as t_0 in eq. 2.5, we inserted different layers of matter of known effective thicknesses into the beam line at S2, since within this equation also the value of s_0, i.e. the total length of the flight-path, is an unknown quantity.

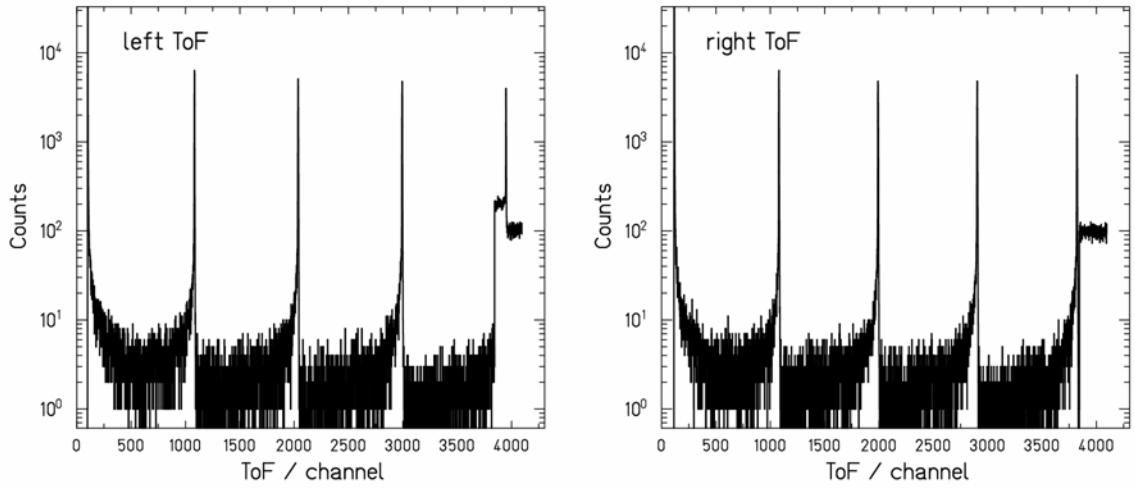

Fig.3.2: Calibration of the TAC range for the left and right side of the time-of-flight detector performed in the Run123. The distance between two peaks corresponds to a period of 10ns.

Tab. 3.4: Summary of the time-of-flight TACs calibration performed in Run123. SCI21L-SCI41L stands for the TAC of the time-of-flight determined from the left sides of the scintillators, SCI21R-SCI41R then corresponds to the right side.

time [ns]	SCI21L-SCI41L [chn]	SCI21R-SCI41R [chn]
10	1083±3	1079±3
20	2037±3	1991±3
30	2994±4	2904±4
40	3949±5	3822±5
factor (chn/ns)	**95.55±0.09**	**91.41±0.09**

As the result of the inserted material the beam got slowed down and arrived at S4 at later time, but since the delay of the S2 signal is kept constant, that meant that the corresponding signal from S2 arrived earlier with respect to that from S4, came two signals closer to one another. By measuring the corresponding ToF and using laboratory velocities v of the beam after passing through the various layers of matter at S2 calculated with the AMADEUS program [AMA], the dependence of $1/v$ on the measured ToF^* according to the following equation could be established:

$$\frac{1}{v} = \frac{t_0}{s_0} - \frac{ToF^*}{s_0} = a + b \cdot ToF^* \tag{3.3}$$

where $a=t_0/s_0$ and $b=1/s_0$, and ToF^* is the time measured directly by the TACs, as defined in eq.2.5. From eq. 3.3, it may be seen that by fitting the linear dependence shown in **Fig.3.3** and summarized in **Tab. 3.5,** the parameters a and b could be obtained, from which the determination of s_0 and t_0 is a straight forward task. In the Run121, taken as the average value of the left and right side, the time-of-flight offset has been t_0=164.2±0.2 ns and the flight-path s_0=36.79±0.08 m. With the same procedure we determined the ToF offset in Run123 as t_0=187.4±0.6 ns and the flight-path s_0=36.56 ±0.10 m.

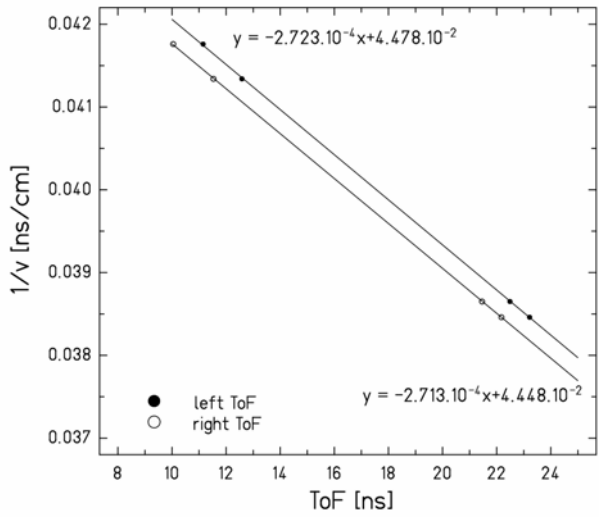

Fig. 3.3: Determination of the time of flight delay t_0 and total flight path s_0 performed in Run121. The linear fits indicated in the figure have the form of eq.3.3

Tab. 3.5: Summary of the time-of-flight offset calibration performed in Run121. The layers of matter and their acronyms are the same as in Tab.3.2, calc. ($1/v$) stands for the inverse of the beam velocity behind the corresponding material calculated with [AMA], and the last two columns are the measured values of ToF* for each side of the detector separately. ToF*-left, ToF*-right.

layer	thickness [cm/mg^2]	calc. ($1/v$) [ns/cm]	ToF*-left [ns]	ToF*-right [ns]
disc+4600	5320.5	0.0418	11.15	10.04
disc+4200	4905.0	0.0413	12.59	11.53
300mg hom	325.1	0.0385	23.22	22.17
disc S2	774.0	0.0387	22.49	21.46

3.3 Identification of the detected fragments

To identify a fragment means to know its nuclear-charge number Z and mass number A. While the charge can be directly measured by the multiple sampling ionization chambers (MUSICs), the mass can be determined only by measuring the magnetic rigidity of the fragment and utilizing the eq.2.2, provided the charge Z and velocity v of the fragment is already known:

$$\frac{A}{Z} = \frac{e}{u} \cdot \frac{B \cdot \rho}{\beta \gamma c} \tag{3.4}$$

where B is the magnetic field, ρ is the radius of the trajectory, $\beta=v/c$ with c being the speed of light, $-e$ the charge of the electron and u the atomic mass unit. Since also the magnetic field is directly measured by the Hall probes, the remaining task is the determination of the correct radius of the fragments trajectory. Measuring the position at S2 by the SCI21 and at S4 by the drift-times of the MUSICs, and keeping in mind that the magnetic field is homogeneous, we can determine the ρ_{frag} of the fragments in the second FRS-stage by applying a correction to the radius of the central trajectory ρ_{eff}, which is given by the deviation of the fragment trajectories, i.e. by the position at S2 and S4 and the ion-optical properties of the system:

$$\rho_{frag} = \rho_{eff} \cdot \left(1 + \frac{x_4 - x_2 \cdot M}{D_4} \cdot \frac{1}{100}\right), \tag{3.5}$$

where x_2 and x_4 are the horizontal positions of the fragment at S2 and S4, D_4 is the dispersion at S4 and M is the ion-optical magnification of the second FRS-stage given by $M=D_4/D_2$.

Therefore, in this section the emphasis is put on the calibration of the detectors, which directly measure the characteristics of the fragments, such as the charge and magnetic rigidity via the horizontal position at the intermediate and the final focal plane. The common feature of these calibrations is that they can be performed only with the produced fragments, such that the response of the detectors can be obtained from any place of their active volume, contrary to the well localized primary beam utilized for the initial calibration of the Fragment Separator.

3.3.1 Correction of energy losses in MUSIC

The fragments passing through the MUSIC detector leave behind the track of ionized gas composed of individual electrons and positively charged ions. As explained in detail in chap.2.5.3 the created cloud of electrons drifts to the anode of the detector, where it is being collected. The magnitude of the specific energy loss is according to the Bethe formula directly proportional to the square of the nuclear-charge of the fragment and inversely proportional to the square of its velocity:

$$\left(\frac{dE}{dx}\right)_{theory} = \mathrm{f}(Z,v) \propto \frac{Z^2}{v^2}\mathrm{L}(v,Z) \cong \frac{Z^2}{\mathrm{f}(v)} \tag{3.6}$$

The amplitude of the MUSIC signal also depends on the density of the filling gas, which ruled by the atmospheric pressure and temperature, does not stay constant during the experiment, and moreover, also on the position of the fragment's transit, since with increasing distance the electrons have to drift to the anode, the probability to recombine increases. Therefore

$$\Delta E_{measured} = f(Z,v,x_4,t) \propto Z^2 \cdot \frac{d(t)\cdot g(x_4)}{f(v)} \tag{3.7}$$

In the equation above, we assume that different dependencies of the energy loss can be separated. Therefore we can write:

$$Z^2 \propto \Delta E_{correct} = \Delta E_{measured} \cdot \frac{f(v)}{d(t)\cdot g(x_4)} \tag{3.8}$$

implicating, that in order to deduce the charge of the detected fragment, we have to first find, and then remove the dependence on the velocity *f(v)*, dependence on the position $g(x_4)$ and the dependence on the density of the gas, i.e. on atmospheric conditions *d(t)*. The procedures leading to determination and removal of these dependencies are described within this section, divided into the following three parts.

- ***Correction of the MUSIC energy losses for the velocity of the fragment***
- ***Correction of the MUSIC energy losses for the position dependence***
- ***Correction of the MUSIC energy losses for the density of the gas***

In principle, all of these corrections can be treated independently on one another, and the final result should not be influenced by the order of the execution. For practical reasons, the correction for the velocity was performed before the correction for the position. The correction for the density of the gas is the smallest of all three, and therefore is performed as the last one.

Correction of the MUSIC energy losses for the velocity of the fragment

Each of the MUSICs provides 4 independent measurements of the energy loss of the fragment. The magnitude of the signals from individual anodes is given by the main amplifier and generally does not have to be the same for all anodes. However, since the measurements by individual anodes are independent of one another, the resolution in charge of the signal, which is taken as the mean value of all four signals within one chamber, is by a factor of 2

higher, provided the amplitudes of the signals from the four anodes are approximately the same. Moreover, due to the same gas conditions within each MUSIC, we can apply the same type of corrections for all four signals, or more efficiently, correct directly the mean signal.

As an example, in the top-left subset of **Fig.3.4** displays the energy losses measured in part of the Run123 in MUSIC1. The resolution is rather limited; however, when displaying the same energy loss as the function of the ToF in the top-right subset of Fig.3.4, i.e. as the function of the velocity of the fragment, one clearly sees the source of the limited resolution, which is just the projection of the first figure on the horizontal axis. The observed ridges correspond to different charges of the fragments. However, if one orders the ridges in vertical direction, the resolution in terms of the projection on the horizontal axis, i.e. in charge, significantly improves, as is demonstrated in the bottom subsets of Fig.3.4.

Since the slope of each charge-ridge is different, we had to fit each of them separately by a linear function. The slope of these fits turned out to be a function of the energy losses, as seen in **Fig.3.5,** establishing the basis for a proper analytical correction:

$$\Delta E^{1}_{cor} = f(\Delta E_{uncor}) \cdot (ToF_{ref} - ToF) + \Delta E_{uncor} \tag{3.9}$$

where ΔE^{1}_{cor} is the corrected energy loss, $f(\Delta E_{uncor})$ is a polynomial function given by the slope of the individual charge ridges, as displayed in Fig.5, ΔE_{uncor} is the energy loss before

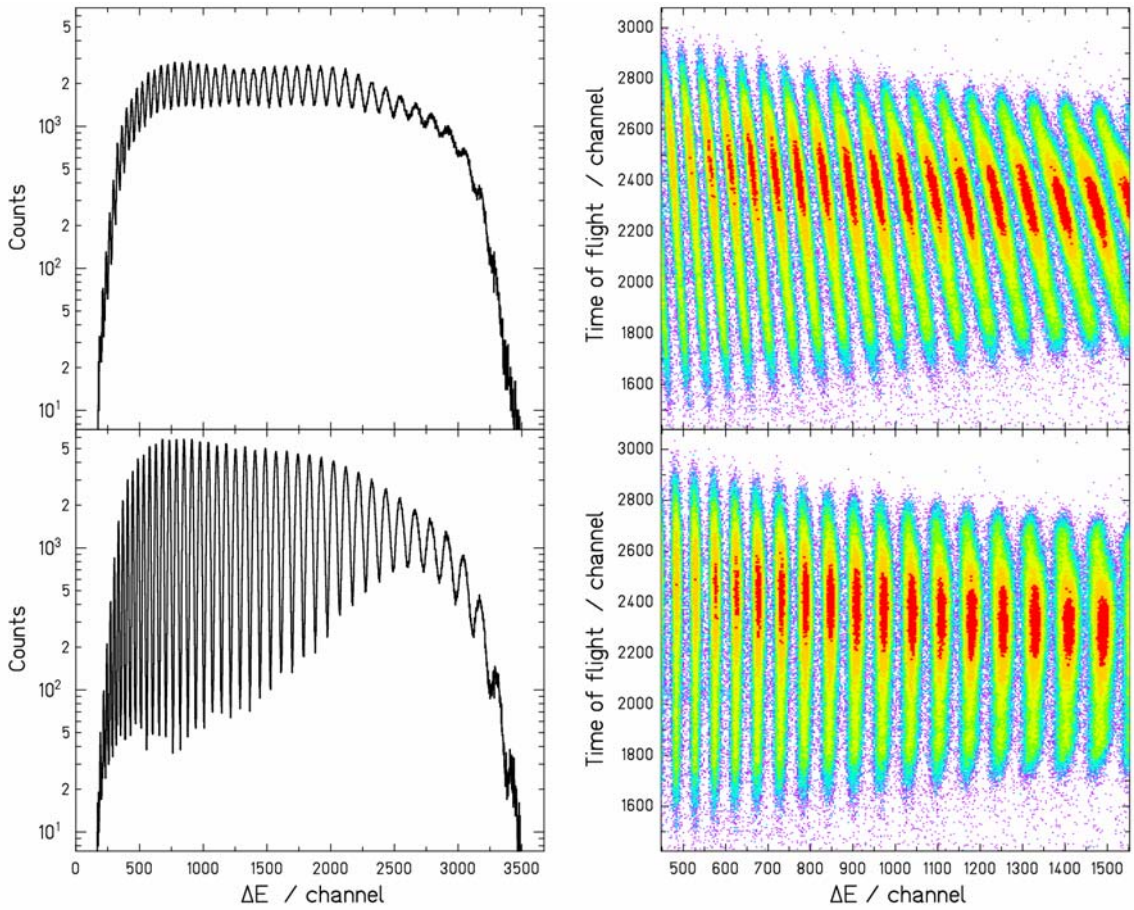

Fig.3.4: *Left:* Spectrum of the average energy loss in MUSIC1 as measured in part of the Run123 before (*top*) and after (*bottom*) the correction of energy losses on the velocity of the passing fragments. Each peak corresponds to different fragment's charge. *Right:* The dependence of the average energy loss on the fragment's time-of-flight, i.e. the velocity, as measured in part of the Run123 before (*top*) and after (*bottom*) the correction on the ToF dependence. Each ridge corresponds to a different fragment charge.

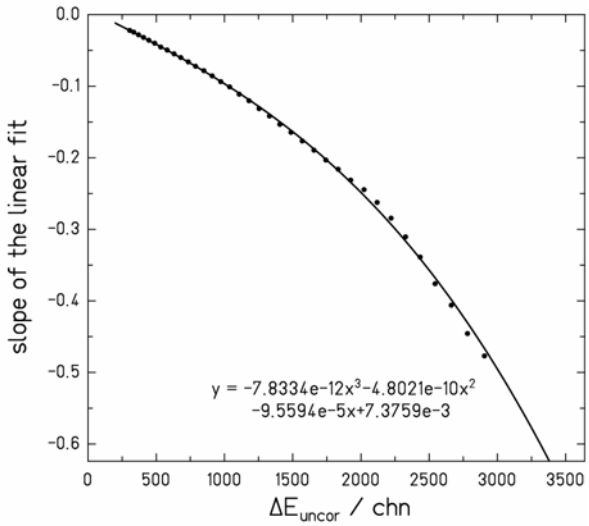

Fig.3.5: The slopes of individual uncorrected charge ridges as the function of the energy loss. The cubic fit is the correction function *f(ΔE)* from the eq.3.9.

the correction, *ToF* the measured time-of-light, and ToF_{ref} the reference time-of-flight to which all the charge-ridges are corrected (usually chosen as the app. average time-of-flight within a set of measurements).

Correction of the MUSIC energy losses for the position dependence

The dependence of the measured energy loss on the position in the MUSICs is caused by the partial recombination of the created electrons. Their recombination follows an absorption law, meaning that the number of electrons traversing a certain distance dx_4 is reduced each time by the same fraction. Therefore one would expect the function *g* from eq.3.8 to be exponential.

However, since in reality we correct for the position dependence the data which were already corrected for the dependence on Tof, and since there is a correlation between the position at S4 and the velocity, the resulting correction function is not an exponential, but rather follows a power law.

In the top-left subset of **Fig.3.6** we observe the energy losses measured in part of the Run123 in MUSIC1 and already corrected for the dependence on the time-of-flight. In fact, these data and figure is identical as bottom left plot in Fig.3.4 of the previous section. However this time, the figure can be obtained as the projection of the 2D spectra displaying the energy losses as the function of the position in the MUSIC1 (see top-right plot in Fig.3.6), given by the drift time. It is again possible to observe various ridges corresponding to different elements, which are tilted by the position dependence. In the analyses, each of these ridges was fitted by a power function $g=a(E)x_4^{b(E)}$, with its power and argument being functions of the energy losses. Thus it was possible to correct the measured energy losses in the following way:

$$\Delta E^2_{cor} = \frac{\Delta E^1_{cor}}{x_4^{\,b(\Delta\tilde{E}=a(\Delta E))}} \tag{3.10}$$

where x_4 is the position in MUSIC given by the drift-times, $b=b(\Delta\tilde{E}=a(\Delta E))$ is the function given by the dependence of the power of the fitted power function on the energy loss, which is however also dependent on the factor of these power functions, see **Fig.3.7**, in order to

correct the energy losses with respect to the same frame of reference. As the consequence, the spectrum of the resulting energy losses is stretched wider, than the uncorrected spectrum, as is clearly evident from the comparison of the left plots in Fig.3.6, but significantly increases the charge resolution especially in the region of higher charges, as displayed in bottom-right plot of Fig.3.6 and compared to the top-right plot of the same figure.

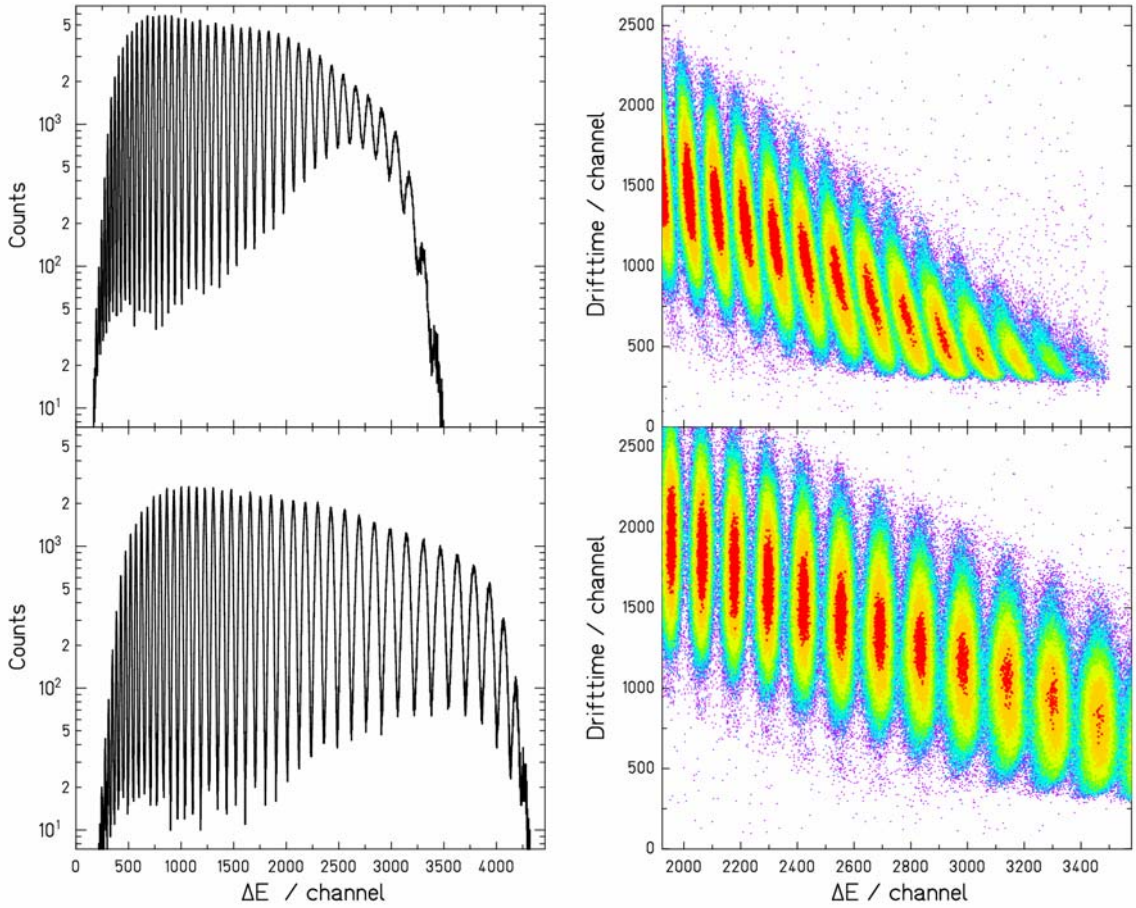

Fig.3.6: *Left:* Spectrum of the average energy loss in MUSIC1 as measured in part of the Run123 before (*top*) and after (*bottom*) the correction of energy losses on the position at S4 of the passing fragments. Each peak corresponds to different fragment's charge. *Right:* The dependence of the average energy loss on the fragment's position at S4, i.e. the drift-time, as measured in part of the Run123 before (*top*) and after (*bottom*) the correction. Each ridge corresponds to different fragment's charge.

Correction of the MUSIC energy losses for the density of the gas

The density of the gas influences the magnitude of the energy loss which the fragment suffers while traversing the MUSIC. The denser is the gas, the more of its atoms the fragment meets and can thus ionize, consequently inducing higher charge than in less dense environment. Since the density of the filling gas is ruled by the atmospheric conditions, such as pressure and temperature, and both of our experiments took place during a course of app. 9 days, when the data were taken virtually 24 hours a day, one can expect significant changes of the atmospheric conditions, varying by day and night, as well as changing with development of the overall weather conditions. As the result of the density dependence, the MUSIC response to the fragments of the same element varied from measurement to measurement.

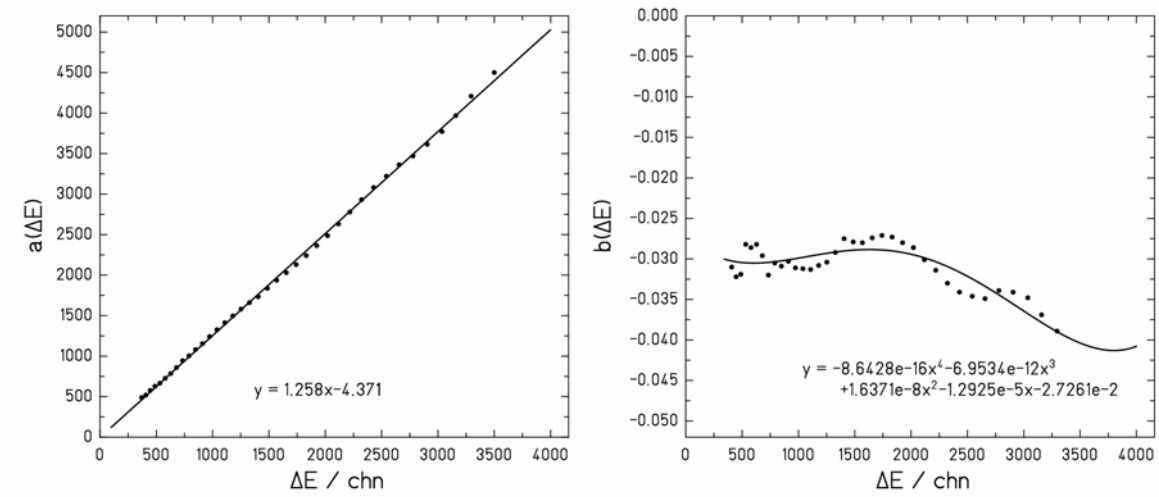

Fig.3.7: *Left:* the factors of the power fits of the individual uncorrected charge ridges as the function of the energy loss. The polynomial fit is the correction function $a(\Delta E)$ from the eq.3.10. *Right:* The powers of the fits of the individual uncorrected charge ridges as the function of the energy loss. The polynomial fit is the correction function $b(\Delta E)$ from the eq.3.10.;

In order to correct for this effect we assume that the atmospheric conditions did not change during one measurement, which took typical between 15 and 60 minutes. Then the charge spectrum for each file, i.e. the individual measurement, was fitted, and the positions of peaks, such as in **Fig.3.8**, determined. The positions of these peaks were then compared to an arbitrarily chosen reference file and corrected by a polynomial function $d_{file}=d_{file}(\Delta E)$, which was determined for each file individually:

$$\Delta E^3_{cor} = \Delta E^2_{cor} - d_{file}(\Delta E^2_{cor})\,. \tag{3.11}$$

The consequence of the correction for the density of the filling gas is an improvement of the overall resolution in the nuclear charge by app. 10%.

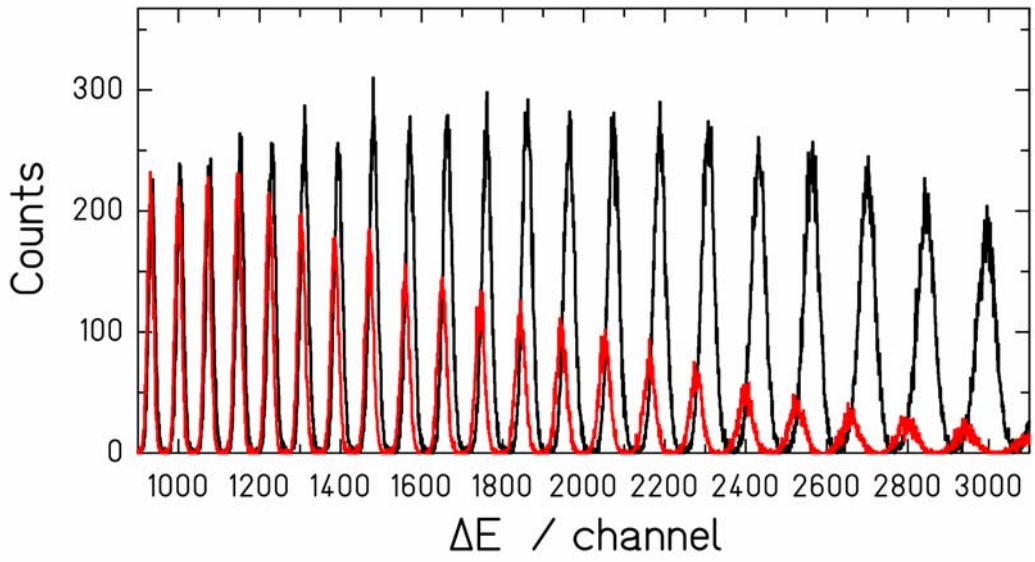

Fig.3.8: Charge spectra measured by MUSIC1 during Run123 in two different files corrected for position and velocity dependence. The shift between the two spectra is caused by the different atmospheric conditions during the measurements and has to be corrected by means of eq.3.11.

Once the resolution of the MUSICs has been restored, one can in principle calibrate the nuclear charge *Z*. In certain measurements it is particularly easy; one can identify the primary beam on the charge scale, and count by one-unit steps, thus identifying all the charges. However in measurements without the primary beam, this is not possible, and one has to rely on various different approaches. But these depend on the ability to determine the fragment's *A*/*Z* as will be seen in later sections. Therefore, at this phase of the data analyses, it is more convenient to perform just an "arbitrary calibration", using the advantage of the approximate square dependence of the energy losses on the nuclear charge of the fragment such that:

$$Z_{temp} \approx z\left(\sqrt{\Delta E_3^{cor}}\right) \tag{3.12}$$

where $z \approx z(\sqrt{\Delta E})$ is the pseudo-calibration function, which is in reality determined by correlation of positions of different charge-peaks of a corrected MUSIC spectrum with integer numbers. The introduced error of several charge units is at this stage unimportant.

3.3.2 Calibration of the scintillator SCI21

The scintillator at S2 is one of the key detectors. It is one of the time-of-flight detectors and it measures the horizontal position of the fragment's transit through S2. Especially the later information is not only important for the identification of the fragment itself, but is also essential in the later stages of the data analyses, when the precise velocity for the already identified fragment is to be determined. Therefore, special attention was invested into the calibration of this detector.

Although the general calibration procedure consists of a direct correlation of the absolutely calibrated signal from the multi-wire chamber MW21 and the signal from SCI21, prior to that a special treatment of the SCI21 signal has to be performed, which takes into account the influence of the walk of the constant fraction discriminator (CFD), making the SCI21 response sensitive to the charge of the passing fragment. The left plot of **Fig.3.9** displays the 2D spectrum of the SCI21 signal, i.e. horizontal position, with respect to the charge of the passing fragment. In the figure, we can observe individual ridges corresponding to the different charges, which position is however slightly shifted with respect to one another. The severity of the effect grows with the decreasing charge of the fragment. Recalling the physical dimensions of the active area of the scintillator, as described in chap.2.5.2, we have to consider, that these dimensions are constant for all passing fragments regardless of their charge, and moreover, that this active area is app. equally populated by all fragments.

Defining the borders of each ridge, given by the extremes of he SCI21 active area, as the channels corresponding to the half of the height of the ridge-plateau on each side, such as demonstrated in the left plot of **Fig.3.10**, we can perform the correction of the scintillator signal, such that the effects of the CFD are compensated:

$$x_2^{cor} = A(Z_{temp})x_2^{uncor} + B(Z_{temp}) \tag{3.12}$$

where x_2^{uncor} is the raw position signal from the SCI21, $A(Z_{temp})$ is a stretching factor determining how much should the ridge be compressed or extended, and the $B(Z_{temp})$ is the shifting parameter, pushing the ridge to the same reference position, in this case to channels from 2700 to 3200. The results of this procedure are displayed in the right subset of Fig.3.9.

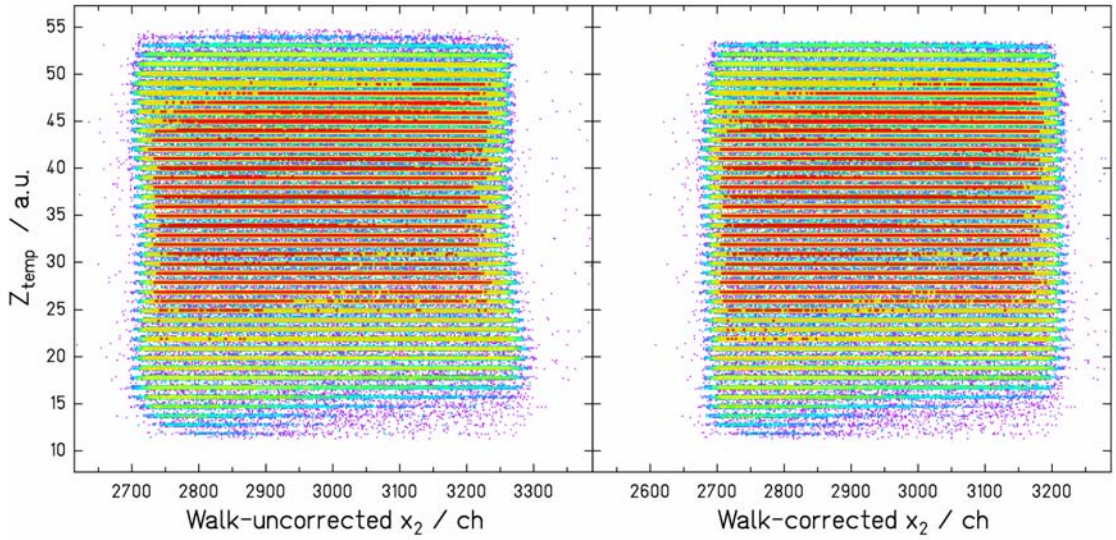

Fig.3.9: The average energy loss in MUSIC1 vs. position at S2 before (*left*) and after (*right*) the correction for the walk of the constant fraction discriminator, as measured during part of the Run123. The applied correction corresponds to the one described by the eq.3.12.

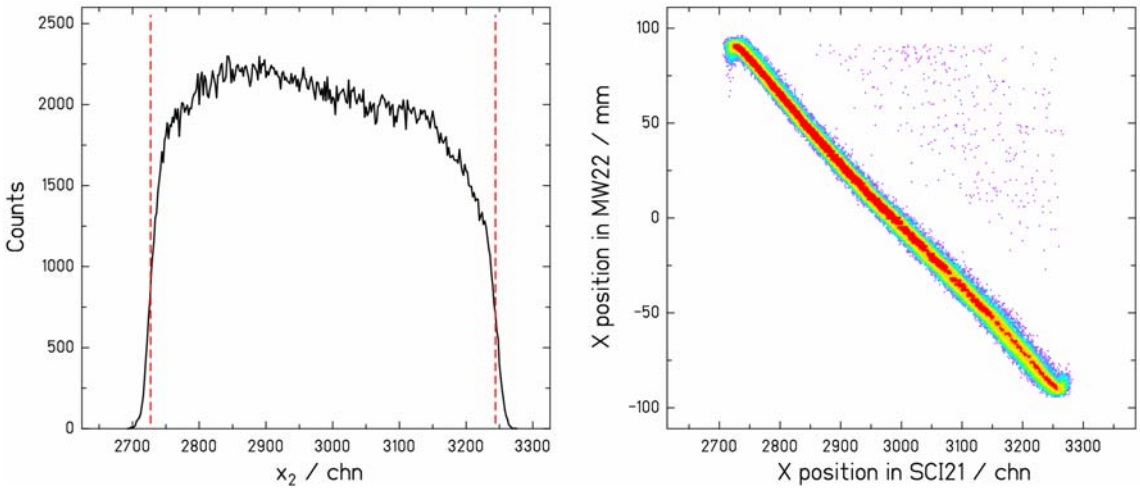

Fig.3.10: *Left:* Position spectrum from the scintillator SCI21 as measured during part of the Run123. The channels of the red borders of the distribution correspond to extremes of the sensitive range of the scintillator. *Right:* An example of the calibration of the SCI21 by a MW22 as performed during the Run123.

After the signal from the scintillator is corrected, it is possible to proceed with its calibration by MW22. In praxis, this is done for such a setting of the magnetic fields of the first FRS stage, that the produced fragments more-or-less uniformly populate the whole S2 area, i.e. the full sensitive range of the scintillator, as well as the MW22, which is temporarily inserted into the beam.

The calibration of the SCI21 detector is usually performed several times during the course of the experiment, in order to assure, that the detector response had not changed; for example due to degradation of its scintillating properties caused by a radiation damage, as may be the danger especially when the scintillator is directly hit by a primary beam of high intensity.

The right plot of Fig.3.10 then displays one of the calibrations of the scintillator SCI21 performed by the MW21 during the course of the Run121. The correlation is approximately linear; however slight influence of the borders is visible. Therefore such calibration curves were fitted with up to the sixth degree polynomial.

3.3.3 Calibration of the MUSIC drift-times

The position of the fragments transit through the final focal plane S4 is another essential quantity in order to determine the proper radius of the trajectory and perform the fragments identification. In principle, there are several possibilities how to deduce this position. The most natural choice may be the SCI41, since this detector should be positioned directly in the final focal plane. However, in case of this scintillator, the fragments do not populate the full active range of the detector and thus the possible influence of the walk of the corresponding CFD remains hardly correctable, or even undetected.

Another possibility may be a pair of multi-wire proportional chambers, which additionally to their good resolution and absolute calibration would even allow for determination of the fragments flight angle. But the rather low detection efficiency for the elements with low $Z<30$ prevented them from being used for this purpose.

Yet another possibility is the use of the drift times of the MUSIC detectors, since these signals do not suffer from the loss of efficiency for low Z's, and the resolution in the position determination is even superior to that of the multi-wire chambers. The only technical complication is the necessity to calibrate individually each of the drift-time signals coming from eight different anodes (four anodes per MUSIC).

In the real experiment, the constant-fraction discriminators (CFDs) processing the drift-time signal have a limited dynamic range corresponding to the set threshold. Thus, the output signal has the correct value/shape only for a certain charge range. Therefore, the thresholds of four CFDs of one MUSIC are set in such a way, that the full charge range is covered by four overlapping "windows"; e.g. the first anode is set to be sensitive to the lowest charges, the fourth to the highest charges. The thresholds of corresponding CFDs are arranged in the same way in both MUSICs, thus the drift-time of the charge induced by each fragment is properly processed at least by one pair of anodes, each from one MUSIC. Therefore also in the case of the S4 position determination by the MUSICs one is able to deduce the flight angle of every passing fragment.

However, the consequence of different thresholds at MUSIC CFDs is that only the drift-times from anodes "sensitive to the highest" charges can be calibrated directly by the multi-wires. The anodes sensitive to the lowest charges do not see properly the signal seen by the MWs, and on the other hand, the signal seen by these anodes is not detectable by the MWs. Therefore, these anodes (usually 1st and 2nd) are calibrated with help of the other anodes, already calibrated by the MWs.

The procedure is similar in both types of calibrations, and takes into account the possible flight angle of the incoming fragment. Therefore, the not-yet-calibrated position-signal is correlated with a signal tracked from two calibrated positions into the physical position of the anode which is to-be-calibrated, such as displayed in the **Fig.3.11** and described by the following relation:

$$x_{M1}^{an4} = b = \frac{(c-a)\cdot e}{e+f} + a \tag{3.13}$$

where a, b, and c are the positions of the fragment read by the MW41, anode of the MUSIC and MW42, respectively, e and f are the distances between MW41, anode of the MUSIC and the MW42, respectively. The calibration of any other MUSIC anode by MWs or pair of other anodes is ruled by an analogical relation. In principle, the calibration can be performed with any magnetic setting in which the S4 area is fully populated by the produced fragments. The example of the calibration of the 2nd anode of the MUSIC1 performed by the 2nd and 4th anode of the MUSIC2 is displayed in **Fig.3.12**.

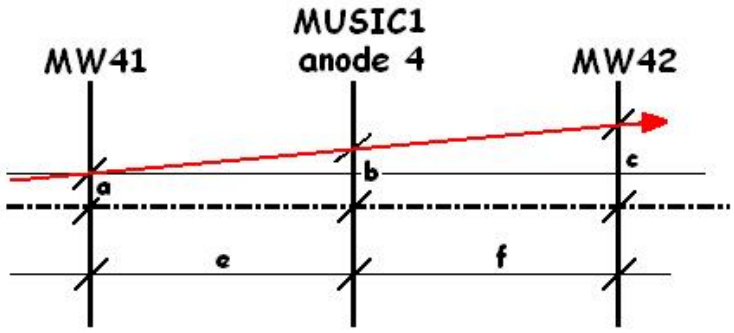

Fig.3.11: An example scheme of the calibration of the anode 4 of the MUSIC1 by tracking its position with help of two multi-wire proportional chambers MW41 and MW42. Red arrow indicates the trajectory of the transiting fragment, *a*, *b*, and *c* are the positions of the fragment read by the corresponding detectors, *e* and *f* are the distances between MW41, anode of the MUSIC and the MW42.

After calibrating all drift-times from the individual anodes, one is able to read the horizontal position of the transiting fragment, depending on its charge, at different positions along the beam axis, which correspond to the different physical position of the suitable anode. This of course is not desirable, and trajectories of every fragment, read by (at least) one pair of anodes have to be extrapolated to a common reference position along the beam axis. As this reference position, due to the practical reasons, the location of SCI41 is chosen. The trajectory of the fragment is then tracked with help of two known positions at two MUSIC anodes into the position of the SCI41 in the same manner as described by eq.3.13 and Fig.3.12, although this detector is not directly used for the position determination.

The resolution in the extrapolated S4 position determined by tracking the trajectory of the fragment with known transit positions in the MUSICs is around 1 mm, which is in general better than that of the scintillator alone, which is known to be around 3-4 mm.

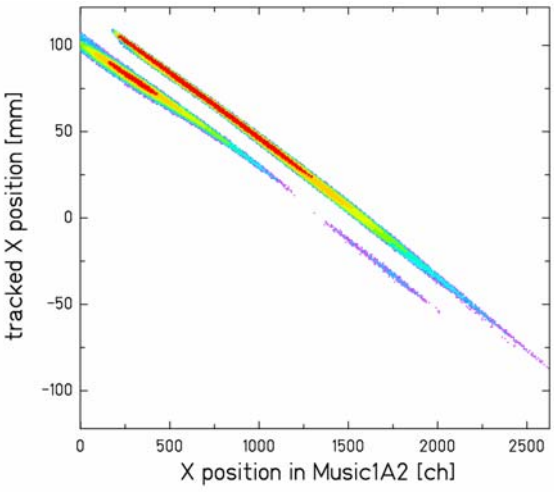

Fig.3.12: Calibration of the drift-times from the 2nd anode of MUSIC1 by tracking its position by already calibrated 2nd and 4th anode of MUSIC2 as performed during Run121. The weaker correlation in lower channels of the 2nd anode of the MUSIC1 corresponds to signals produced by fragments which are actually above the dynamic range of the CFD of this anode or the 2nd anode of the MUSIC2, but are within the charge window of the CFD of the 4th anode of the MUSIC2. For the purpose of this calibration, only the upper correlation corresponding to proper signals from all three anodes is taken.

3.3.4 Determination of *A*/*Z* of the fragments

Let's recall that at this stage of the data analyses, the charge of the detected fragment is determined with the best possible resolution, yet it's not absolutely calibrated, the time-of-flight detector has been calibrated, and the positions of the fragment's transit at S2 as well as at S4 can be determined from the SCI21 and the drift-times of the MUSICs, respectively. According to eq.3.4 and eq.3.5, all necessary information for the determination of the fragment's *A*/*Z* is available. However, in the spirit of maximizing the mass resolution, in order

to deduce the A/Z of the detected fragments with the best possible precision, we adopt the method of Ricciardi [Ric05] to increase the precision of various calibration parameters.

According to this method, one of the critical points is the determination of the fragments velocity, since the calibration of the time-of-flight had been performed with the primary beam. Thus we could determine the length of the flight path s_0. However the flight path s of a real fragment may be slightly different due to two reasons. One is that the fragment can acquire a transversal momentum in the nuclear reaction, or caused by the straggling in the scintillator SCI21, and enters the second stage of the FRS with an angle α_x. The second reason is that the fragments with different rigidities than the one corresponding to the central trajectory enter the second section at different x_2-position and thus follow a different path along the FRS which is effectively longer by Δs. Although the real path inside the FRS depends on the detailed ion-optical properties of the spectrometer, in the first approximation we can consider the dependence of the flight path on the angle as linear and Δs as a quadratic function of the position of transit at S2. Thus the original eq.3.3 has to be modified in the following way:

$$v = \frac{s}{ToF} = \frac{s_0 \cdot (1 + c_\alpha \cdot \alpha_x) + \Delta s}{t_0 - ToF^*} \tag{3.14}$$

where ToF is the time-of-flight and s_0 the distance between two scintillators measured along the central trajectory as introduced in chap.3.2.4.

Therefore in order to remove these additional dependencies, we further follow the idea of Ricciardi and take into consideration that:

- the A/Z-ratio, determined according to eq.2.2, forms a characteristic pattern given by the integer nature of the nuclear charge and mass when plotted against the nuclear charge (see Fig.3.14)
- the measured data must give values of the A/Z that must coincide with the expected values, e.g. fragments with $N=Z$ have to form a vertical line in Fig.3.19
- for any given isotope, the A/Z-ratio must not depend on the values that measured quantities (B_{34}, x_2, x_4, α_x, ToF,) assume.

These considerations then allow us to investigate the correlations of A/Z of fragments of one certain element with position at S2, S4, ToF and measured angle α, as is displayed in **Fig.3.13a-d)**. Removal of these dependencies, usually one by one, by tuning the calibration parameters such as c_α, Δs or fine adjustments of t_0, as displayed in **Fig.3.13e-f)** results in an increased mass resolution, correct A/Z determination and obtaining the corresponding characteristic pattern in **Fig.3.14**, displaying the nuclear charge of the fragments vs. their A/Z.

3.3.4 Identification of the detected fragments

Once the A/Z of the fragments has been determined and the characteristic pattern of the measured data, such as Fig.3.14, obtained, it is possible to proceed with the identification of individual fragments, since due to the integer values of the fragment nuclear-charge and mass numbers, the lines formed in this pattern correspond to fragments with constant neutron deficiency or excess, i.e. constant N-Z. But it is needed to remind, that due to the nature of the experiment, when all reaction products where measured in several scans according to their nuclear charge (see chap.2), there are generally three kinds of characteristic patterns when three different identification approaches have to be utilized.

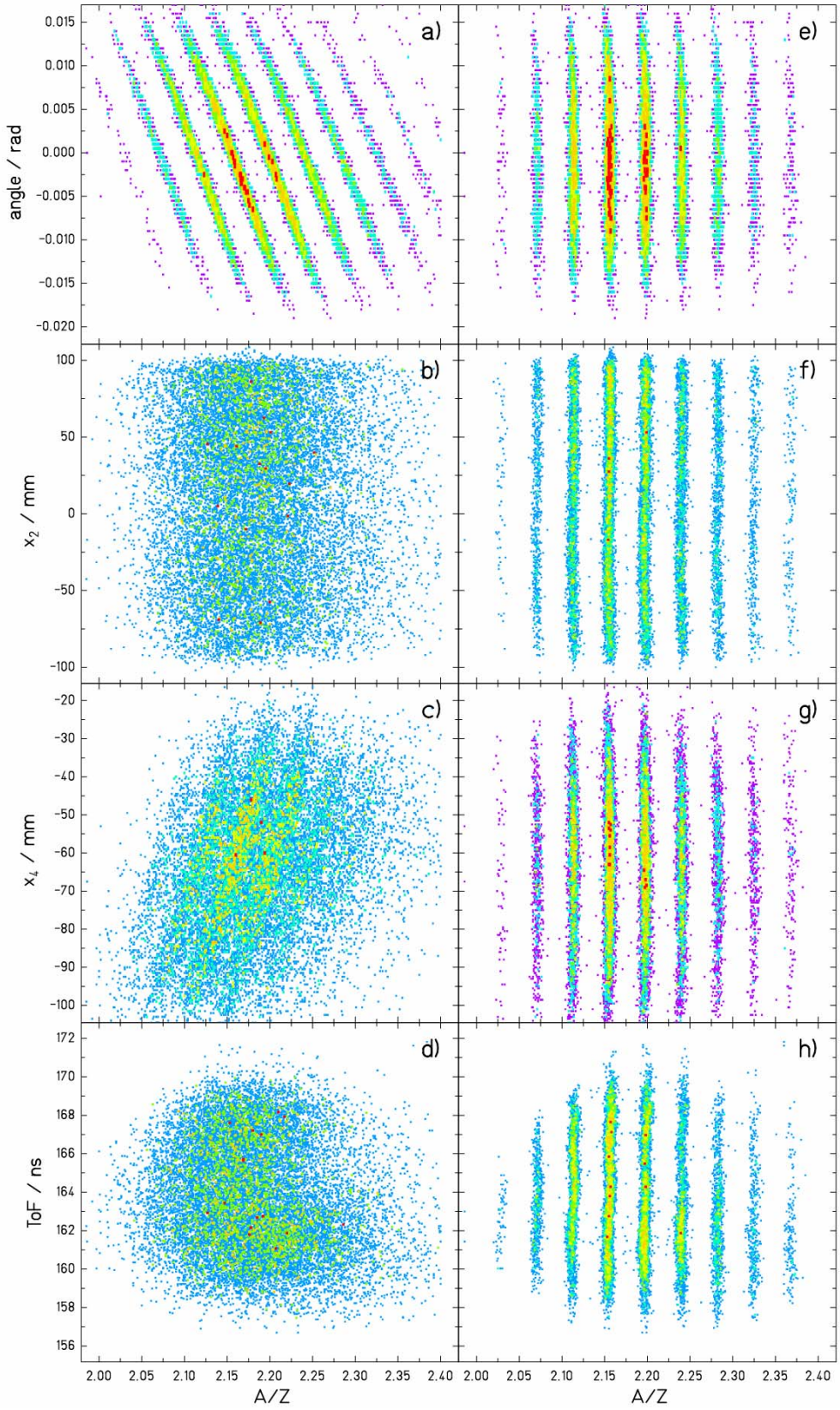

Fig.3.13: Investigation of the A/Z dependence on various measured quantities for one element before (***a-d***), and after (***e-h***) precise determination of the calibration parameters according to the method of Ricciardi [Ric05]. In the figures, each resolvable line corresponds to an individual isotope. Before the correction, the dependence of A/Z on the angle is so strong (*a*), that it effectively destroys all resolution in A/Z with respect to the position at S2 (*b*) and to the ToF (*d*). After the correction on the angle (*e*) it is usually still necessary to perform slight corrections on the position at S2, S4 and ToF offset t_0 in order to improve the resolution to the quality of figures *e-h*).

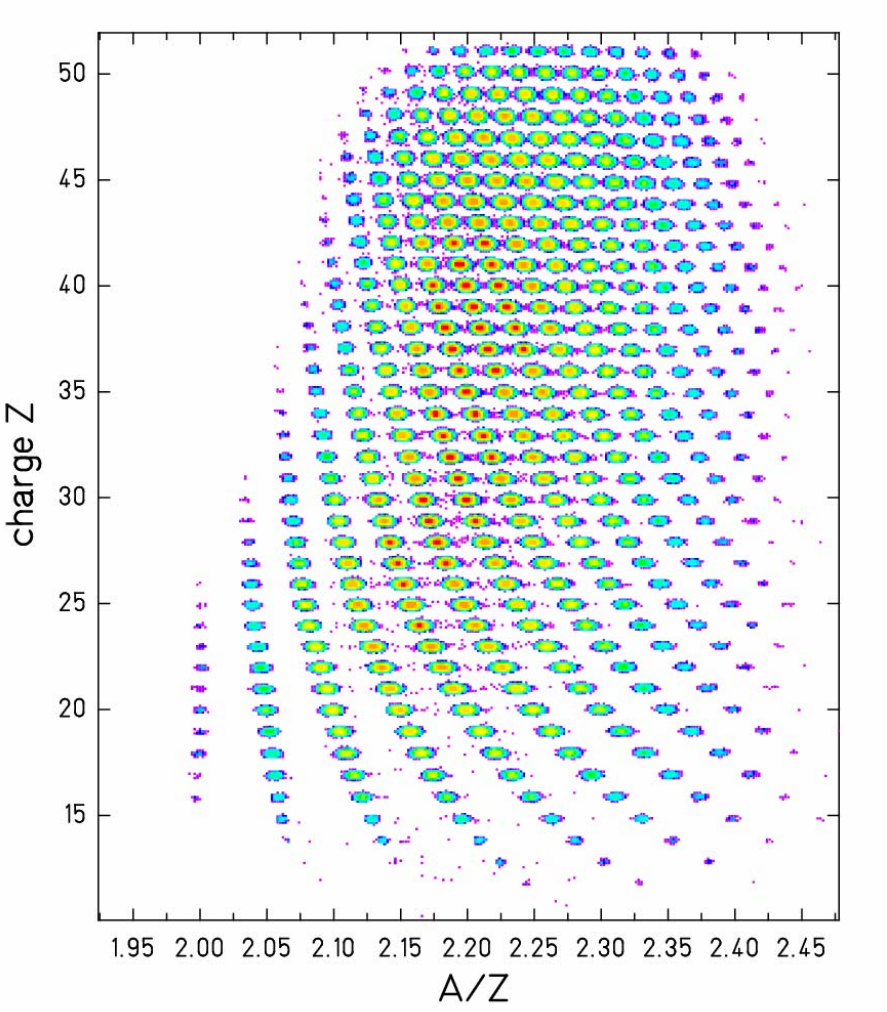

Fig.3.14: Characteristic pattern of isotopes measured in part of the experiment with ^{197}Au beam on ^{27}Al target at 500 *A* MeV. Color scale is logarithmic.

The ***first type*** of the pattern is obtained in the measurement concentrated on the lower part of the chart of the nuclides. The identification of fragments from these measurements is particularly easy, since we can take the advantage of the vertical line formed by the fragments with *N*=*Z* and easily identify a "hole", as in the left subset of **Fig.3.15**, which corresponds to an isotope which is unbound and cannot be detected, and therefore is absent in the final plot. The marked hole in Fig.3.15 belongs to the isotope with *N*=*Z*-2. Since there are no other "missing isotopes" with greater charge and *N*=*Z*-2, comparing to the chart of the nuclides, this hole has to be ^{16}F. The isotope next to the right from the identified one has the same charge but one more nucleon, i.e. neutron, and is therefore ^{17}F. Next to it is ^{18}F with *N*=*Z*=9. Just below ^{18}F is ^{16}O, since we made one step along the line with *N*=*Z*. In an analogical way, it is possible to proceed step by step and to identify all the fragments one by one.

The ***second type*** of the identification pattern stems from the measurements of the heaviest fragments, in which also the primary beam or several neutron-removal channels are present. These reaction channels leading in case of the ^{197}Au beam to the production of $^{194\text{-}196}$Au, and particularly the beam itself, are so intense, that during the magnetic setting in which these can be transmitted through the whole FRS, they have to be geometrically shadowed by thick metal slits in order not to overload and possibly destroy the detectors. But this limitation means also direct identification of the small remnants of these isotopes which are still being detected, allowing in a similar way as for the case of lower charges to go step by step, identifying one by one the fragments in direction away from the identified position of the primary beam.

The most difficult identification is the one of the fragments in the middle of the mass range, i.e. the ***third type*** of the identification pattern, when neither the primary beam, nor the light charges with easily identifiable $N=Z$ line are present in the measurement. However also in this case we take the advantage of the integer nature of the fragment's mass and charge and the fact that all measurements were performed in such a way that although different charge regions were measured separately, there exist significant overlaps. Therefore the $\langle N \rangle / Z$ of different produced elements with some best-guessed identification is determined and compared to the same quantity deduced in case of the already properly identified elements in lower and higher charge regions. Since the $\langle N \rangle / Z$ can assume only discreet values, the equity with the values for already identified elements can be achieved only if also the fragments from intermediate charge regions are properly identified. The right plot of **Fig.3.15** demonstrates the effect of an error in identification by 1 neutron and/or 1 proton on the agreement of the $\langle N \rangle / Z$ between two separately measured charge regions.

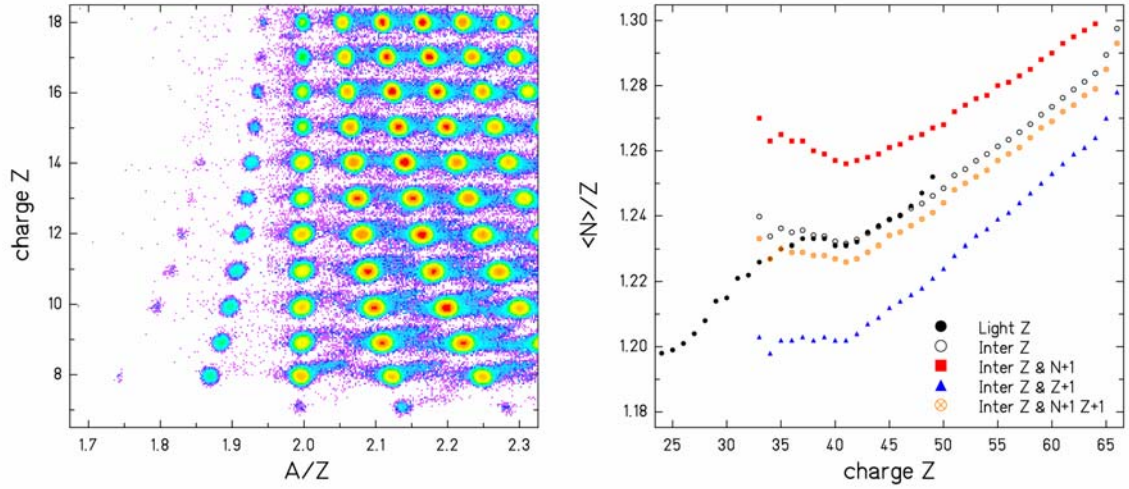

Fig.3.15: *Left:* Characteristic pattern of isotopes measured in part of the experiment with ^{197}Au beam on ^{27}Al target at 500 A MeV which can be directly used for the fragments identification. The red circle indicates the absence of ^{16}F isotope, which is unbound and cannot be thus measured, the vertical line then isotopes with $N=Z$. Color scale is logarithmic. *Right:* Identification of the detected fragments with the help of the $\langle N \rangle / Z$ in part of the Run123. The points denotes as "Light Z" correspond to measured $\langle N \rangle / Z$ of the independently identified lighter elements. The points denoted as "Inter" correspond to $\langle N \rangle / Z$ of the elements for which no direct identification was possible, but the agreement of $\langle N \rangle / Z$ in Z=38-48 proves that the "guessed" identification is correct. The other curves with notation "N+1", "Z+1" or "N+1, Z+1" manifest how different would the values of $\langle N \rangle / Z$ be, if there was an error in identification by 1 neutron, 1 proton or 1 proton and neutron, respectively.

3.3.5 Ionic charge states of the residual nuclei

After the reaction takes place, the residual nuclei can pick-up or strip-off some electrons due to the atomic interactions with the different layers of matter, leading to a change of its atomic charge Q. Since the variation of the A/Q value of the transmitted nuclei makes their identification with use of the FRS difficult, the analyses was limited only to fully stripped ions, i.e. those without any electrons and for which their nuclear charge $Z=Q$. The left plot of **Fig.3.16** displays the charge state distributions of the reaction residues after traversing the target in each of our experiments for the bare, hydrogen-like and helium-like ions.

The charge-state distribution behind the target is which enters the first FRS-stage is altered at S2 by the transit through the SCI21 and other possible degrading materials. This induces a strong correlation between the position of the ions at the exit of the FRS and their ionic charge state making it possible to discriminate the fragments which change their charge-

state during the transit of S2. The right plot of **Fig.3.16** displays the energy loss signal measured in the first MUSIC versus the positions measured by the MUSIC drift-times. The different groups of diagonal bands in the figure correspond to nuclei with different charge-state configurations at both stages of the FRS.

However, this did not exclude from the analysis the hydrogen-like or helium-like ions which acquired their charge state in the target and did not change it during the transit of S2. But the extremely low probability ~1% makes their contribution negligible.

Apart from the mechanism described above, an ion which is fully stripped during its whole way through the FRS can pick-up an electron in either of the MUSIC detectors and be thus also falsely identified, without being recognizable by the different ΔE vs. x_4 correlation as was the earlier case. In the experiments we made therefore use of the independent signal on the ionic charge of the fragment produced in both MUSIC detectors separately. In the subsequent analyses we accepted only events with same charge measured by both MUSICs. In case of the heaviest fragments in the 1 *A* GeV beam with masses close to the projectile, as well as for the heaviest fragments detected in the experiments with 500 *A* MeV beam with A~140, the probability for a fully stripped ion to pick-up an electron in the MUSIC chamber is in order of 10%. If that happens, it has then app. 90% probability to loose its electron in the second MUSIC. Therefore, the above mentioned condition assures for contribution of wrongly identified nuclear charge due to this second mechanism in order of ~1%, decreasing with the mass of the fragment. We assume that such a contribution can be also neglected.

Generally if one would intend to reconstruct the absolute yields of the fragmentation residues, a special correction for losses due to the incompletely stripped-ions would need to be applied. However, in this study the main interest lies in the velocities of the fragmentation residues for which the absolute yields are not necessary, and therefore such losses did not need to be compensated.

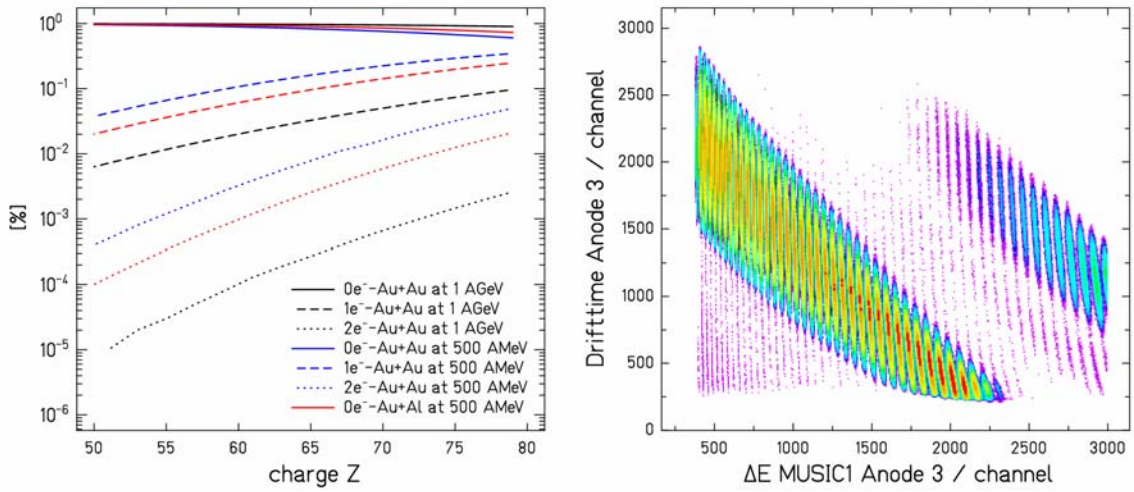

Fig.3.16: *Left:* Relative contribution of different charge states of the reaction residues behind the target in the corresponding experiment as the function of the nuclear-charge of the residue. *Right:* The energy loss signal measured in MUSIC1 anode 3 versus the position measured by the MUSIC drift-times. The different groups of diagonal bands in the figure correspond to nuclei with different charge-state configurations at both stages of the FRS. The most intensive band corresponds to the ions which were fully stripped in both stages of the FRS. The color scale is logarithmic.

3.4 Reconstruction of the velocity distributions

Due to the limited acceptance of the Fragment Separator, the measured yields of various isotopes do not exactly correspond to their actual production rate in the reaction. Therefore, if we want to reconstruct the full velocity distribution of any individual isotope we have to take into account the loss of efficiency caused by the finite dead-time of the detection system, different beam doses in individual measurements with different magnetic field settings as well as the loss in transmission due to the limited angular acceptance. In the following paragraphs the detailed description of the precise determination of the fragment velocity and of the individual corrections leading to the reconstruction of the realistic isotope yields will be discussed.

3.4.1 Precise determination of the fragment velocity

After the identification, the velocity of the fragment can be deduced from its position at S2 which is transformed to the corresponding magnetic rigidity in the first FRS stage

$$(B\rho)_1 = B_{12}\rho_{eff}^1\left(1+\frac{x_2}{D_2}\cdot 100\right) \tag{3.15}$$

where B_{12} is the magnetic field of the first FRS stage, ρ_{eff}^1 is its effective radius, x_2 the position of the transit at S2 measured by the SCI21 and D_2 is the dispersion at the intermediate image plane S2. This value of the magnetic rigidity then serves as the input to the analog of eq. 3.4; however, we also take into account the variation of the nuclide mass with the binding energy:

$$A_{cor} = \frac{\left(m_N N + m_P Z - E_{bind}\right)}{u} \tag{3.16}$$

where E_{bind} is defined as [Mye67]:

$$E_{bind} = \left(15.4941\cdot A - 17.9439\cdot A^{2/3}\right)\cdot\left(1-1.7826\cdot\frac{(A-2Z)^2}{A}\right) - Z^2\cdot\left(0.7053\cdot A^{-\frac{1}{3}} - \frac{1.1529}{A}\right) \tag{3.17}$$

then the energy of the fragment in the laboratory frame can be calculated as (which is the analog of eq. 3.4.):

$$E_{LAB} = u\cdot\left(\sqrt{\left(\left(\frac{(B\rho)_1\cdot Z}{uA_{cor}/c}\right)^2+1\right)}-1\right) \tag{3.18}$$

and consequently its velocity can be determined according to:

$$v_{LAB}^{*} = c\cdot\sqrt{\left(1-\frac{1}{\left(1+\left(E_{LAB}/u\right)\right)^2}\right)} \tag{3.19}$$

where, considering eq. 3.15-19, c is the speed of light, u is the atomic mass constant, m_P and m_N the mass of the proton and neutron, respectively, and A, Z, and N being the mass, charge and neutron number of the considered nuclide.

However, the velocity determined in this way is not the real velocity of the fragment right after the reaction, but due to the finite thickness of the target material it is rather the velocity of the fragment ruled by the reaction in combination with the effects of the fragment's energy loss in the target.

In order to correct for this effect we assume that the target is so thin, that the beam itself is not attenuated by the means of the nuclear reactions. And since the reaction cross section does not vary appreciably with the small variation of energy that the beam can experience, the position where the fragment is formed is thus on the average in the middle of the target. Moreover, we assume that the number of secondary reactions of the already produced fragments with the nuclei of the target is negligible. Taking into account the probability of a nuclear reaction for a beam particle in the target (~0.1-0.2 % in case of gold target and 1.5% in aluminum target), and its average energy loss one can observe that both assumptions are very reasonable. Therefore, it is only necessary to correct the measured velocity of the fragment to the one in the middle of the target:

$$v_{LAB} = v^{*}_{LAB} + \Delta v \tag{3.20}$$

as is schematically displayed in **Fig.3.17**, where Δv is the correction of velocity due to the energy loss of the fragment in the target calculated with help of [AMA], and recalculate the fragment's velocity with respect to the projectile velocities, i.e. in the reference frame of the beam, utilizing the Lorenz transformation as follows:

$$v_{PF} = \frac{v_{LAB} - v_{beam}}{\left(1 - \frac{v_{LAB} - v_{beam}}{c^2}\right)} \tag{3.21}$$

where v_{beam} is the velocity of the projectile particles in the middle of the target in the laboratory frame.

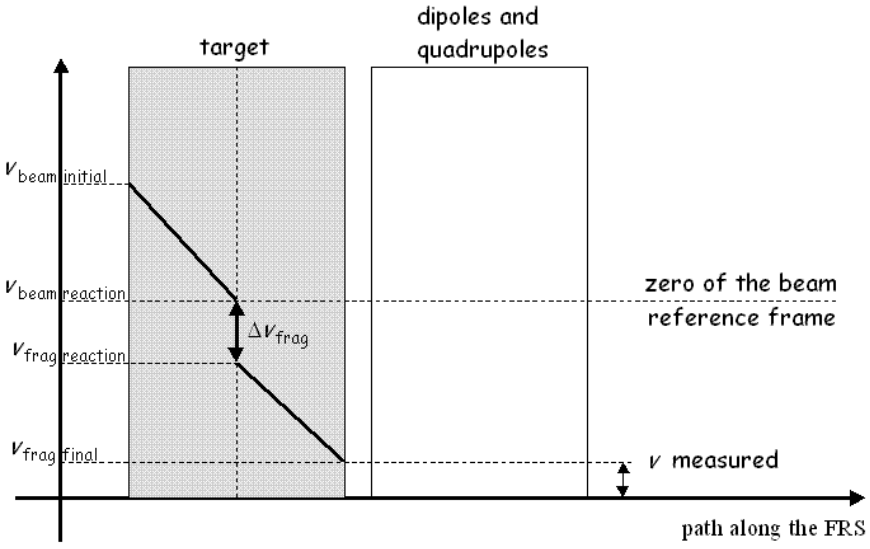

Fig.3.17: Schematic diagram (not to scale) for the variation of the beam and fragment velocity v as a function of their path along the layers and the target.

At this stage, the fragment velocities are finally properly determined. However, in order to combine results from different measurements and reconstruct the full velocity distribution, we still have to normalize the yields from individual measurements.

3.4.2 Dead-time correction

By definition, the dead time of the detector is the time after each event detected by the detector in which the detector is not able to reveal another event if it happens. In the experiments discussed within this work, with typical fragment intensities at S4 in the order of ~1-2·10^3 particles per second, we consider the dead time of the whole detection device rather than the dead time of the individual detectors. The reason is the processing time of one good event by the DAQ system which is by orders of magnitude longer than the processing time of any individual detector itself.

Therefore, after the signal from the master trigger (which is usually the signal from SCI41) is accepted, the DAQ is closed for accepting any other signal before this one is fully processed what takes on average ~100 μs, while the "intrinsic dead time of the scintillator is ~100 ns. During the time the DAQ system processes the "good event", the scintillator signals from other passing fragments are fed into scalers, which are not subject to a dead-time, in order to count how many other fragments have been missed while the system was busy with the previous ones. Thus, when approximating the intrinsic dead-time of the SCI41 as zero, the ratio of the free triggers, i.e. all signals, and the accepted triggers, i.e. the fully processed ones, serves as the measure of the overall dead-time of our detection system t_{dead}:

$$t_{dead}[\%] = \frac{N_{free}^{trig} - N_{acc}^{trig}}{N_{free}^{trig}} \cdot 100 \tag{3.22}$$

where N_{free}^{trig} is the number of the free triggers and the N_{acc}^{trig} the number of the accepted triggers. Since the overall dead time depends primarily on the rate of the fragments reaching S4, it may vary from setting to setting with respect to the tuning of the magnetic fields. Therefore, the overall yields in each individual measurement, i.e. setting, are corrected for the effects of the dead-time by the following factor C_{dead}:

$$C_{dead} = \frac{1}{1 - (t_{dead}/100)}. \tag{3.23}$$

The typical dead-time during our measurements was below 30%.

3.4.3 Correction for the beam dose

The total beam dose in individual measurements was not generally the same. Firstly the time of various measurements varied for practical reasons, and the intensity of the beam itself was often modulated in order to maximize the efficiency of the data acquisition. Therefore, in order to make the measurements from different settings compatible, it is necessary to normalize the measured yields to the same beam dose.

The precise beam intensity can be measured with use of the SEETRAM described in chap.2.2.3. However, since its effective thickness is quite similar to that of the production targets, the "unwanted" yields of nuclear reactions taking place within this monitor would be

comparable to the "wanted" yields from the gold or aluminum target itself. Therefore, the SEETRAM could not be directly used in any measurement. Instead of that we utilized an indirect method of the beam-intensity determination.

In each measurement we first inserted the SEETRAM into the beam line and measured the yields of all fragments produced in combination by the fragmentation of the beam projectiles on the nuclei of the SEETRAM as well as on the nuclei of the target itself. After an acquisition of sufficient statistics, the SEETRAM was removed from the beam line and the measurement continued. In this way, only the fragments produced in reactions of the beam projectiles with nuclei of the target were acquired.

The measurements with the presence of the SEETRAM could be straightforwardly normalized to the same beam dose by a correction factor C_{SEE}:

$$C_{SEE} = \frac{1}{N_{SEE} \cdot f_{SEE}^{cal}} \tag{3.24}$$

where N_{SEE} is the number of the measured SEETRAM counts in the individual measurement and the f_{SEE}^{cal} is the SEETRAM calibration factor as described and determined in chap.3.2.5.

In order to normalize also the measurements when no beam intensity monitor was present and which in a fact are of the primary interest we have to assume that:

1. the average energy loss of the beam projectiles in the SEETRAM is negligible, thus it does not affect the final magnetic rigidity of the produced fragments
2. the differential production cross section is approximately the same or differs by a constant factor for the fragmentation of the beam projectiles on the material of the SEETRAM, i.e. Al+Ti, and on gold or aluminum, which is the material of the target.

The first point means that the window of magnetic rigidities open by the specific magnetic field setting is same for measurements with SEETRAM and those without it. In reality the effective thickness of the SEETRAM causes an energy losses of the beam projectile equivalent to the loss of 0.05% and 0.1% of its magnetic rigidity in Run121 and Run123 respectively, which changes the transit of the fragment through S2 by app 3 mm, resp. 6 mm. With respect to the total aperture at S2 being app. 200 mm we can assume that the fragments seen by our detectors in the settings with and without SEETRAM are practically the same.

The second point assumes similar or at least slowly changing magnitude of the production cross section of various fragments with respect to their charge and mass. If this would be precisely true, then the fraction of the fragments produced by reactions in the SEETRAM would be same in all measurements, and the ratio of the total yield within one setting with and without SEETRAM would be given only by the ratio of the total beam intensity in each of these two measurements. Based on the studies of fragmentation of the same projectile on different targets [Enq99, Ric03] we can observe that indeed for a constant Z and varying N this assumption is true, while the production cross section is a function of Z slightly varying with the target. However, in case of an intermediate and large size nuclei such as aluminum and titanium in the SEETRAM and gold in the production target, the variation with Z is not so drastic and therefore in the good approximation we can assume the contribution of the fragmentation in the SEETRAM to that in the target to be constant in the full charge range. This allows us to normalize the beam dose even for the yields from the measurements without the direct beam intensity monitoring, provided the same setting had been measured also with the SEETRAM:

$$C_{NOSEE} = \frac{Y_{NOSEE} \cdot t_{dead}^{NOSEE}}{Y_{SEE} \cdot t_{dead}^{SEE}} \cdot C_{SEE} \tag{3.25}$$

where the total yield Y_{SEE} and Y_{NOSEE} in one measurement with and without SEETRAM, respectively, is corrected for the corresponding dead-time.

In this work we are aware of the possible systematic uncertainty generated by the above described normalization procedure and especially its impact on the evaluation of the absolute cross-sections. However, they do not stand in the center point of our attention. The main intention is merely just to provide a consistent ground for any arbitrary normalization, since it is just the relative magnitude of the production yields which is necessary for the proper reconstruction of the velocity distribution and determination of its center which is the measure of the relative momentum changes of the spectator residues as the possible response to the participant blast. The effects of the correction for beam dose, with respect the data corrected only for the dead-time, are schematically displayed in **Fig.3.18**.

3.4.4 Angular-transmission correction

In order to correct for the limited angular acceptance of the FRS, the method of Benlliure et al. [Ben02] has been utilized. In reactions of relativistic projectiles the projectile-fragmentation leads to residues with a velocity close to that of the primary beam and a distribution of transversal angles that can be described by a Gaussian function:

$$\frac{dI}{d\Omega} = \frac{1}{2\pi\sigma_\theta^2} \exp\left(-\frac{\theta^2}{2\sigma_\theta^2}\right) \tag{3.26}$$

where σ_θ is the width of the angular distribution. The angular transmission for a given nuclide can be calculated by integrated the eq.3.19 within the angular range defined by the effective acceptance map of the spectrometer according to the positions of the considered nuclide at both image planes, i.e. S2 and S4, :

$$T = 1 - \exp\left(-\frac{\alpha_{eff}^2}{2\sigma_\theta^2}\right) \tag{3.27}$$

where α_{eff} is the effective acceptance angle and $\alpha_{eff}=\alpha_{eff}(x_2,x_4)$. The width of the angular distribution is the result of the combination of several effects, namely the angular distribution introduced by the reaction mechanism, angular straggling in the target and the emittance of the primary beam.

The effective acceptance angle α_{eff} has been determined by a dedicated Monte Carlo code as described in [Ben02]. Then the factor correcting the measured yields for the effect of the angular transmission can be defined as:

$$C_{ang} = \frac{1 - \exp\left(\frac{\alpha_{eff}^{\max}}{2\sigma_A^2}\right)}{1 - \exp\left(\frac{\alpha_{eff}}{2\sigma_A^2}\right)} \tag{3.28}$$

where α_{eff}^{max} is the maximum effective acceptance angle for a given ion-optical setting, and σ_A is the width of the angular distribution for a given mass of the corrected nuclide.

In practice, the angular transmission correction is an iterative process. In the first step the widths of the angular distributions as the function of the fragments mass are determined from the yet not-fully corrected data or from empirical parameterizations like the one of Morrissey [Mor89]. In the second step, the widths are fitted from the corrected data and included into the re-correction of the original data. Usually only one iteration is necessary to converge to unique values of the widths of the angular distributions. The effects of the correction for the angular transmission are schematically displayed in the lowest subset of Fig.3.18.

Since we are not interested in the determination of absolute cross-section, the elimination on x_2 and x_4 is sufficient, and no further correction for the absolute transmission has been applied.

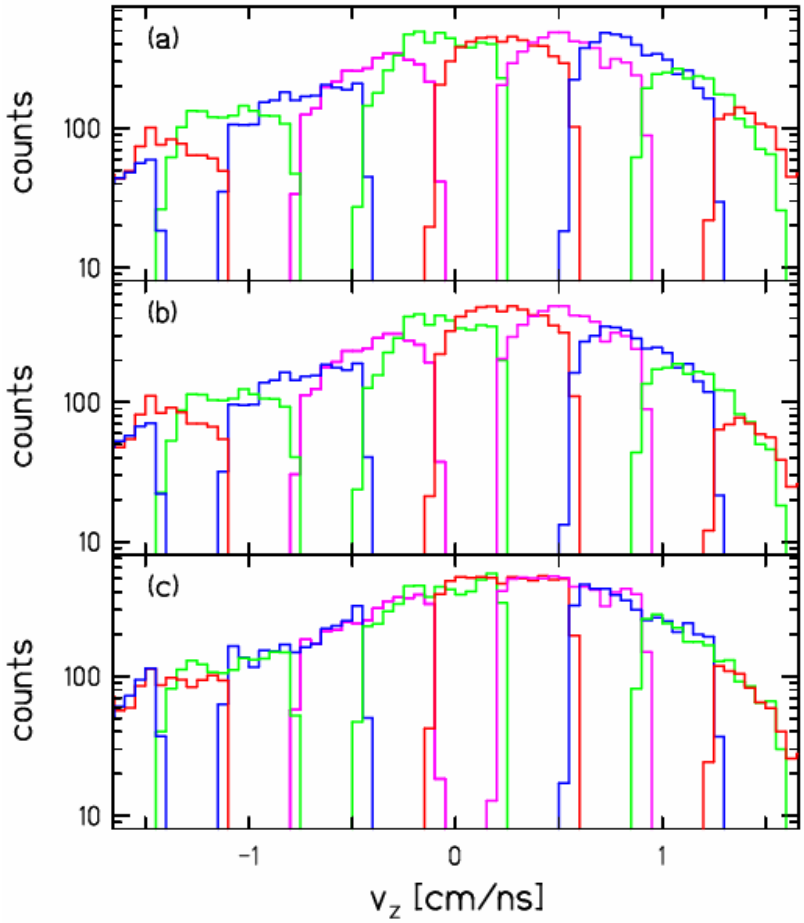

Fig.3.18: Reconstruction of the velocity distribution of ^{43}Ca (Z=20, N=23) in experiment ^{197}Au+^{27}Al at 500 A MeV. Different colors correspond to intervals of velocities measured in different magnetic field settings after the correction on dead-time (*a*), normalization to the beam dose (*b*) and correction for the angular transmission (*c*)

3.4.5 Reconstruction of the velocity distributions

As the consequence of the limited momentum acceptance of the FRS, it is generally possible that the full velocity distribution of an individual produced isotope cannot be measured in a single magnetic setting. Therefore in order to reconstruct the full velocity distribution it is necessary to combine corresponding pieces of the velocity distributions together, as is already apparent from the Fig.3.18.

During the experiment, the magnetic rigidity of the second FRS-stage was tuned by steps of 1.5% in $B\rho$. Thus, when considering the total momentum acceptance of app. ~3%, each region or interval of possible magnetic rigidity, i.e. interval of velocities of produced fragments, was measured twice, each time in a setting differing by 1.5% in the strength of the magnetic field. The main advantage of this procedure was the possibility to avoid the border effects by allowing only central regions of $B\rho$ (±1.2% with respect to the central trajectory) in each measurement to be considered for the final reconstruction of the velocity distribution. In the region of the overlap of the pieces of the velocity distributions from the neighboring settings the mean value of the normalized differential yield was taken. This procedure leads to a reconstruction of the shape of the velocity distribution and was performed for each individual isotope in all three experiments.

4. Velocities of the fragmentation residues

In this chapter the results of three experiments dedicated to the investigation of the longitudinal momentum of the fragmentation residues in the reactions ^{197}Au+^{197}Au at 0.5 and 1.0 *A* GeV and ^{197}Au+^{27}Al at 0.5 *A* GeV will be presented.

The **Fig.4.1** displays the relative abundances of various isotopes detected in the experiments. It can be seen that in each of the experiments we could observe basically all reaction products within 4-5 orders of magnitude of the relative production cross sections with nuclear charge ranging from Z~8 to that of the projectile in the experiment with higher energy, and to Z~65 in the two experiments with the lower incident beam energy.

At the first sight, despite the incident-energy difference and the varying size of the target nuclei all three reactions seem to lead to approximately the same distribution of the fragmentation residues. This qualitative feature is in agreement with the previous observations that the isotopic composition of the fragmentation products is independent of the target [Summerer-limiting fragmentation], provided a sufficiently high excitation energy is introduced in the abrasion stage of the reactions that can lead up to the complete disintegration of the projectile remnant. In other words, due to the interval of possible excitation energies, isotopes of all masses below the mass of the projectile can be created. The quantitative comparison is not yet possible, since the determination of the absolute reaction cross sections has not been the priority of this work, and it was not yet performed.

In principle it would be possible to expand the measurements up to the charge of the projectile even in the experiments ^{197}Au+^{197}Au, ^{27}Al at 500 *A* MeV. However, in case of this lower incident-beam energy the probability for such a heavy ion to pick up one or two electrons when passing through some layer of matter in the FRS grows significantly, thus making a consistent identification extremely difficult. Anyway, as will be shown later in this chapter, the kinematical properties of such heavy ions are well known and easily predictable, and therefore the loss of information by the absence of the measurement in this charge region is not important for the purpose of this thesis

On the other side, the measurement and proper identification of fragments with charges down to lithium (Z=3) would require only minor technical modifications and would be feasible. However such small fragments seem to be produced in several competing processes [Nap04] which together hinder extracting information on the impact parameter. Therefore neither they stand in the center of our interest.

4.1 Velocity distributions – global characteristics and trends

The direct output of the experiment, as described in detail in Chap.3, is the identification of every single detected nuclide, i.e. determination of its nuclear-charge Z and mass A, and measurement of its longitudinal velocity v_z. Therefore, the most natural way to sort out the experimental results is to construct the velocity distribution for every detected isotope. Taking into account only the isotopes with sufficiently high number of recorded events (≥100), the base of our experimental results consists of several thousands velocity distributions. As a representative example, **Fig.4.2** displays the velocity distributions of nine isotopes as they were measured in all three experiments.

Setting aside the area of the distributions which represents the relative yield of the isotope, the main property of any distribution is its overall shape, width and position. On the example of Fig.4.2 we can observe the evolution of these properties and will therefore dedicate the following sections to the discussion of these observations.

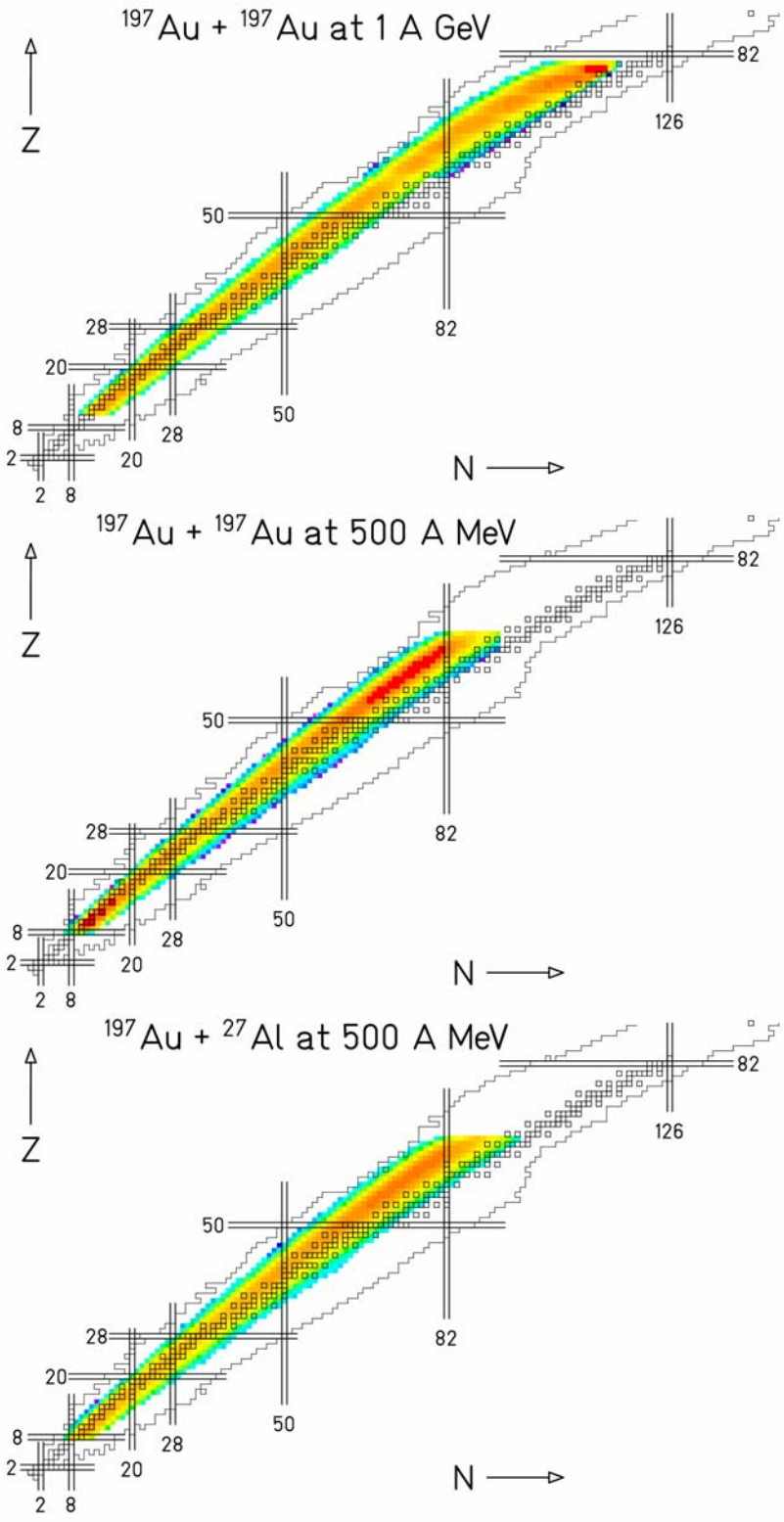

Fig.4.1: The relative abundances of the isotopes detected in the three experiments, plotted over the contours of the chart of the nuclides. The empty squares indicate the stable isotopes; the color scale is logarithmic and is for illustrative purposes adjusted for each plot separately. The experiments performed at 500 *A* MeV did not cover residues with Z_{res}>67.

4.1.1 Shape of the velocity distribution

Investigating Fig.4.2 in the direction of decreasing mass, we can generally observe that the shape of the distribution evolves from a single-peak structure to a structure which appears to be a convolution of three Gaussians to end up for the lightest masses as a structure appearing as composed of two Gaussian-shape distributions.

In order to understand the observed structure, we have to take into account the possible mechanisms of the residue production and the geometrical limits of the detection apparatus, i.e. the FRS. Concerning the possible reaction mechanism, which may lead to the production of such heavy residues in the range of relativistic energies, only fragmentation and fission can play a significant role. But while both these processes may at the end lead to the same reaction product, the course of the reaction is completely different. Moreover, since the probability for detection of its product is ruled by the finite angular acceptance of the FRS, it is not the same for both reaction mechanisms due to their different kinematical properties.

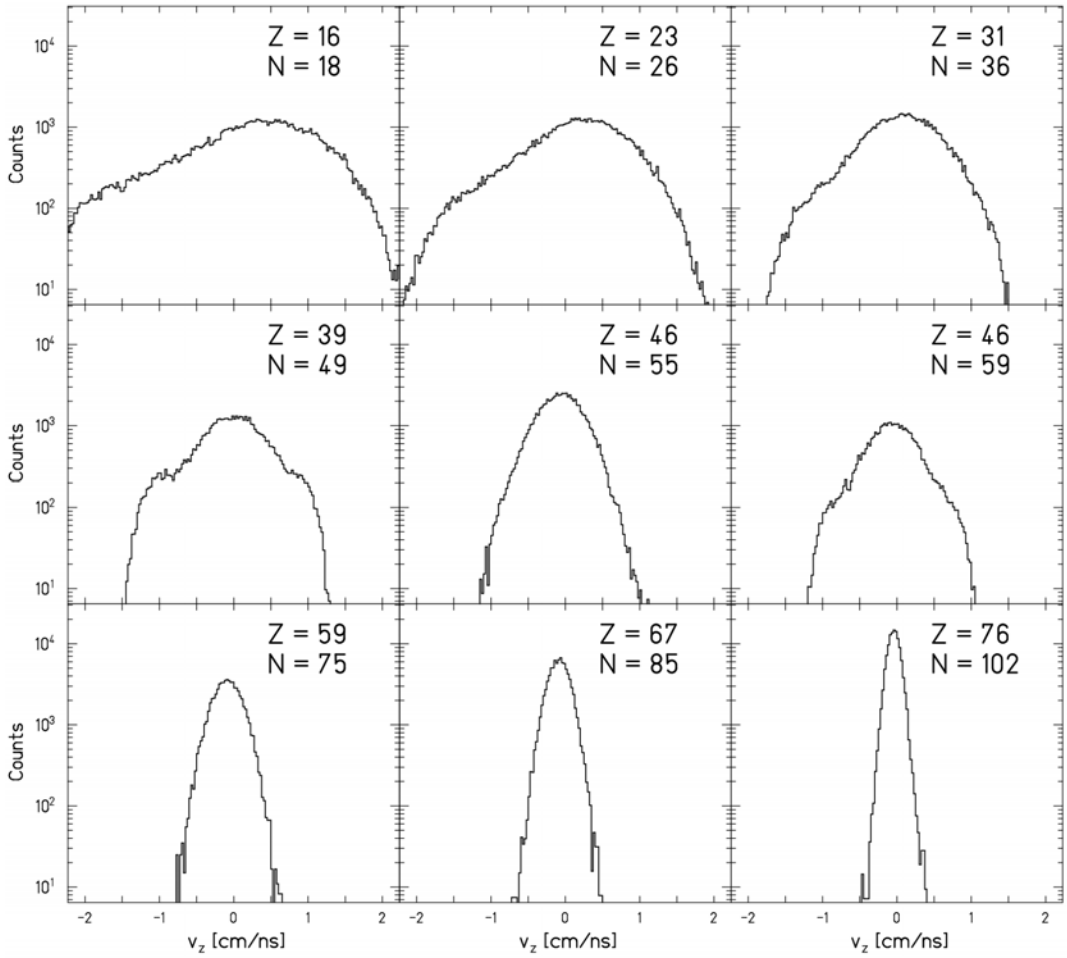

Fig.4.2: Example of longitudinal velocity distributions for nine isotopes measured in experiment ^{197}Au+^{197}Au at 1 *A* GeV.

The effects of the finite angular acceptance can be best demonstrated with help of **Fig.4.3**, where the acceptance can be displayed as a cone in the velocity space. Let us then consider a typical ***fragmentation event***: After an initial abrasion phase, the projectile remnant is excited by the interaction with the target nucleus. A three-dimensional Gaussian-shape momentum distribution is induced by the Fermi momentum of the abraded nucleons [Gol74]. The projectile remnant subsequently de-excites by an evaporation of individual nucleons or light clusters, and the evaporation is expected to be isotropic [Mor89]. The very limited recoil of

the evaporated particles leads to a slight broadening of the momentum distribution of the final residues. Generally, the size of the transversal momentum distribution of the fragmentation products is comparable with the limits of the angular acceptance of the FRS and, therefore, most of the fragments will be transmitted and detected. In terms of the measured longitudinal-velocity distribution we will observe a Gaussian-shape peak positioned close to the velocity of the primary beam, which is the projection of the 3-dimensional velocity distribution on the longitudinal velocity axis.

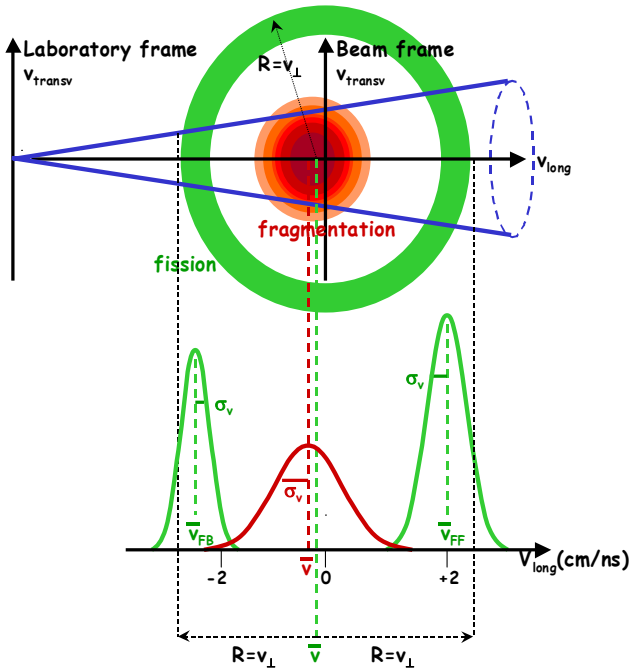

Fig.4.3: Schematic representation of the FRS angular acceptance, presented in the velocity space, and the projection of the transmitted events on the longitudinal axis.

But in the case of ***fission*** the situation is completely different. In such kind of process, the initial beam particle may also loose a few nucleons in the initial abrasion stage of the reaction, however, thereafter it fissions into two basically equal-sized fragments. Although also few individual nucleons may be emitted in addition, the dominant dynamical effect in fission is the Coulomb repulsion of the two highly charged pieces of matter, which drives them from one another in opposite directions. Therefore, in the velocity space the fission fragments will not populate a Gaussian-like cloud, but rather a shell of relatively large diameter. Since the size of this shell is generally greater than the limits set by the angular acceptance of the FRS, only the forward and backward parts of the fission shell may be accepted. Thus, when projecting the accepted fission events on the longitudinal velocity axis, we can expect two separated peaks almost equidistantly spaced from the velocity of the primary beam. Moreover, the acceptance of the forward component is, due to geometrical arguments, slightly enhanced compared to the backward component. Therefore, the faster peak will be slightly larger than the slower one, i.e. the one representing the backward fission events.

In conclusion, due to the limited angular acceptance of the FRS the structure of the final velocity distribution reflects the nature of the process which leads to the production of the individual fragment and therefore ***allows for distinguishing fragmentation from fission.*** In Fig.4.2 the single peak structure of the velocity distribution of the heaviest fragments can be attributed to a fragmentation process. On the other hand in the intermediate-mass region (A~100) both fission and fragmentation may contribute to the fragment production as is manifested in Fig.4.2, but can be separated from one another by a decomposition through a fit of three Gaussians. For the more neutron rich isotopes the contribution of fission is greater,

while the less neutron rich isotopes, even of the same element, may be produced by fission only inconsiderably, see the isotopes with Z=46 in Fig.4.2.

A special case appears in the lightest fragments where a double-Gaussian like structure can be present. Such a structure has been first observed by [Ric03] and later also by [Nap04] who explained it as result of a fast break-up dominated by very asymmetric partitions of the disassembling system, which leads to a formation of one or more light fragments together with one heavy residue.

In fact also the velocity distributions of fragmentation residues may get so broad, that they do not fully fit within the acceptance of the FRS. The angular transmission is larger for heavier fragments and reactions with higher initial beam energy. When the velocity distribution is not fully accepted, the forward component is enhanced with respect to the backward one in a similar way as in the case of fission. The result of this is a slight shift of the centre of the velocity distribution toward higher values. In order to evaluate the magnitude of this effect we have used a dedicated program which simulated the effect of the limited angular acceptance on a 3-dim Monte-Carlo generated Gaussian with width and mean value in the projectile frame dependence on the mass according to the measured data. The results are summarized in App.A, and show that such an effect is only minor for masses A<65 and practically negligible for any heavier residues.

4.1.2 Width of the velocity distribution

Fig.4.2 reveals also the evolution of the width of the individual velocity distributions. When turning our attention away from the fission and concentrating only on the central fragmentation peak, we observe that the distribution width is the smallest for the heaviest residues and increases with decreasing mass, as is summarized in **Fig.4.4**, where the FWHM of the velocity distributions of individual fragmentation isobars are plotted as measured in all three experiments.

Considering the common understanding of the course of the nuclear fragmentation reaction, the width of the nuclear distribution may serve as the measure of the "average violence" of the reaction leading to the production of the considered isotope.

According to the Goldhaber model [Gol74], it is the abrasion stage of the reaction which has the most detrimental influence on the momentum, i.e. the velocity, of the surviving projectile remnant. Since the individual nucleons within the nucleus posses their own individual momentum (being on average zero in the rest frame of the nucleus), the momentum of the projectile spectator after the abrasion phase is equal to the difference of the total momentum of the nucleus before the collision and the sum of the momenta of individual nucleons which where abraded.

Since the abrasion of the nucleons from the mother nucleus is a stochastic process, in the Goldhaber model the average momentum per nucleon lost by the abrasion is in the frame of the projectile equal to zero, yet the width of the distribution of the final momentum per nucleon reflects the possible fluctuations, which grow with the number of the abraded nucleons, i.e. with the decreasing impact parameter corresponding to an increasing violence of the collision.

Generally the width of the velocity distribution which we observe is not the pure consequence of the abrasion process alone. Another contributing process is of course the evaporation through which the hot prefragment releases its excitation energy. But comparing the possible recoil as the result of the evaporated neutron with the width of the momentum distribution of the nucleons within the nuclei, we would observe that its contribution to the momentum width is rather small. But in any case, the average excitation energy induced by the abrasion is directly proportional to the number of the abraded nucleons, thus leading to a

broadening of the momentum or velocity distribution of the final residue due to evaporation which is also correlated with the violence of the reaction.

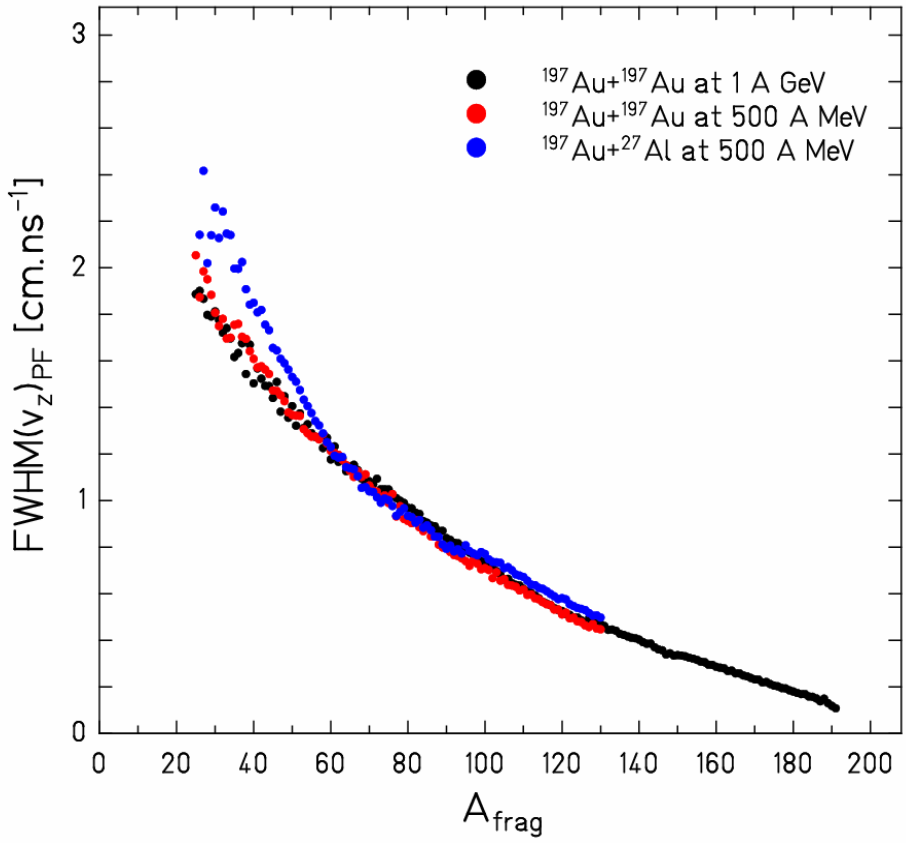

Fig.4.4: Widths of the velocity distributions of the fragmentation residues as a function of their mass A_{frag} in the reference frame of the corresponding primary beam. For discussion concerning the errors see chap.4.3.

The last significant processes possibly influencing the width of the velocity distributions are the energy and location straggling of the beam projectile and subsequently produced fragment in the target. While the straggling of the energy loss is not really significant at the relativistic energies, the location straggling due to the different specific energy-loss of the projectile and its residue combined with the with the possible reactions along the target may be an important issue. However as discussed already in chap.2.3 the thicknesses of the targets were chosen in such a way that this effect is significantly lower than those caused by nuclear processes.

Looking back on Fig.4.4, it is therefore no surprise that the widths of the velocity distributions are practically the same for both systems Au+Au although they differ in incident beam energy, because in this relativistic energy regime the abrasion phase is almost independent of the energy of the projectile and the violence of the collision from the point of view of the spectators is ruled only by the impact parameter, i.e. by the number of the abraded nucleons. The same is true for the case of the reactions with gold projectiles on the aluminum target except the region of the low residue masses (A_{frag}<50) where the widths are higher than in the two gold-on-gold systems. It may be suspected that this is the consequence of the asymmetry of the system, where the smaller aluminum target can abrade the same number of nucleons like gold nucleus but causing greater dynamical instabilities of the hot pre-fragment since the cylindrical volume abraded by a smaller nucleus has a more distorted shape.

To conclude this section, let be reiterated that the width of the velocity distribution increasing with the decreasing mass of the residue on average reflects the violence of the

reaction in which the residue was formed, and according to Fig.4.4, the fragments with same mass were formed in collisions with comparable violence in all three experiments.

4.1.3 Mean value of the longitudinal velocity distribution

The shape of the longitudinal velocity distributions of the fragmentation products can very well be approximated by a Gaussian distribution. In the projectile frame, which is the most suitable for comparison of the velocity distributions with respect to the mass of the corresponding fragment and which has been adopted also in Fig.4.2, the mean value of the velocity distribution reflects the mean overall effect of the dynamics of the reaction on the velocity of the surviving residue. We can observe that the distributions are positioned very close to zero, i.e. that the overall change of the velocity in the reaction is not really dramatic, at least with respect to the width of the distribution manifesting the strength of the stochastic abrasion process.

However, when taking a closer look at the centers of the displayed velocity distributions it is already visible that, when starting with the heaviest fragment, the average velocity decreases with decreasing mass. This can be understood in terms of the friction-like nature of the abrasion, when the two nuclei while abrading nucleons from one another also slightly decelerate each other. Such behavior of the fragments with masses close to the original mass of the projectile has been often observed and well described by the semi-empirical model of Morrissey [Mor89], which states that until a certain relative mass loss the deceleration of the fragmentation residue is directly proportional to the number of nucleons it lost. Let us have a closer look to the two quantities related by this systematics: The mean momentum is induced in the first abrasion step of the reaction, only, because the subsequent evaporation is expected to be isotropic. In contrast, the final mass of the fragmentation residues is given by the total mass loss in both the direct abrasion and, even to a greater part, in the subsequent particle-emission stage. However, since the mean excitation energy introduced by the abrasion, which determines the length of the evaporation chain, is also directly proportional to the number of abraded nucleons [Gai91], evaporation is not expected to weaken the strong correlation between the mass of the final fragments and their mean momentum, which has been established by Morrissey to be essentially linear.

Therefore; it is no surprise that the fragments we observe have generally lower mean velocities than the original projectile. But after these considerations, it is not expected to see the mean values of the velocity distributions shifted back from negative toward positive values as can be observed when a taking closer look at the intermediate and lighter fragments in Fig.4.2. This is the first trace of the phenomenon of reacceleration of the fragmentation residues as observed in the work of [Enq99], and later by [Ric03] linked to the predicted spectator response of the participant blast, formulated by [Shi01], what altogether served as the main motivation for the present experiments.

To the end of this section, let us summarize that the velocity distributions of the fragmentation residues reflect not only the nature of the reaction mechanism leading to the production of the considered isotope, but also the violence of the process and its correlation with the overall dynamical evolution of the projectile remnant.

4.2 Mean longitudinal velocities of the fragmentation residues

As discussed in the previous section, the mean value of the longitudinal velocity distribution of the fragmentation residues is the observable ruled by the overall dynamical evolution of the projectile remnant. Therefore, it is this observable which stands in the focus of this work. But for the sake of clarity and simplicity, it will not be investigated by means of

individual isotopes, i.e. determining the mean velocity for every fragment specie, but rather for the group of isotopes with constant mass A_{res}, in other words for the various isobars. This simplifying picture can be further supported by the insensitivity of the abrasion phase to the kind of nucleon which is abraded except for the case of very small mass losses [Han93], which however are not in the focus of this work.

In the following sections it will be then often referred to the mean longitudinal velocity $\langle v_z \rangle$ of the fragmentation residues which were determined as the mean value of the velocity distribution for a whole isobar, such as schematically displayed in **Fig.4.5,** taking into account only fragmentation events and excluding fission. The complete review of all longitudinal velocity distributions measured for different isobars can be found in App. B.

Fig.4.6 displays a full compilation of all measured data in all three experiments. It consists of 2-dim cluster plots of the longitudinal velocities as the function of the mass of the final residue in the reference frame of the primary beam. In the uppermost figure, representing the system ^{197}Au+^{197}Au at 1 *A* GeV, it is possible to observe the complete evolution of the residue velocities with its mass. The main ridge representing the dominating fragmentation events gradually broadens in direction of decreasing mass with the overall width of the distribution boosted by the onset of fission in the intermediate mass region and again in the region of the lowest masses (A_{res}~40) by the onset of yet another contributing process, most probably by the extremely asymmetric fission or break-up process as discussed in chap.4.1.2.

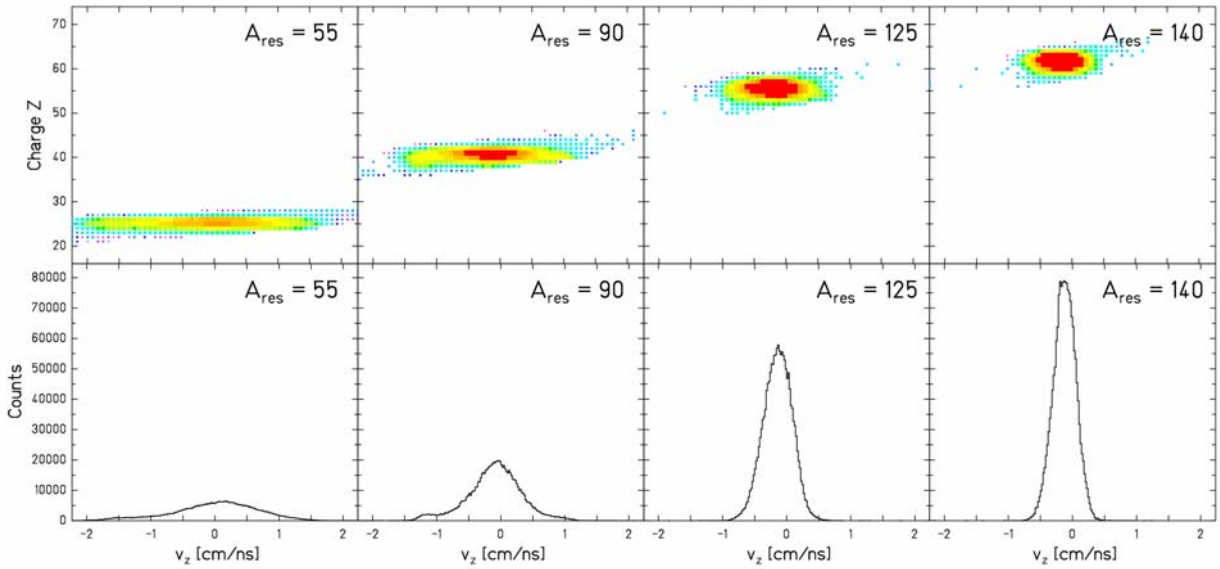

Fig.4.5: Four examples of a 2-dim representation of a velocity distribution for fragments with constant mass A_{res} but different nuclear-charge *Z* measured in the experiment ^{197}Au+^{27}Al at 500 *A* MeV (*upper row*), and its projection on the velocity axis in the reference frame of the incident beam (*lower row*). The color scale is logarithmic and represents the relative abundances of various velocities for individual isotopes of a corresponding isobar.

(*Note: the local depletion of the velocity distribution in the uppermost figure at A_{res}~130 is caused by the border effects in two subsequent measurements scanning the region of the highest and the intermediate nuclear charges. Unfortunately, the overlap of these two measurements in the mass range A_{res}≈125-135 was not sufficient to avoid the manifestation of the border effects on the yields of the affected isotopes. However, the smooth behavior of the mean longitudinal velocities over this mass range, as seen in Fig.4.7, indicates that they have not been affected.*)

Concentrating now on the position of the fragmentation ridge as a function of the residue mass A_{res}, we can see that it first follows the slightly declining trend with the decreasing mass, however starts recovering already around A_{res}~120. Then, despite the geometrically triangular

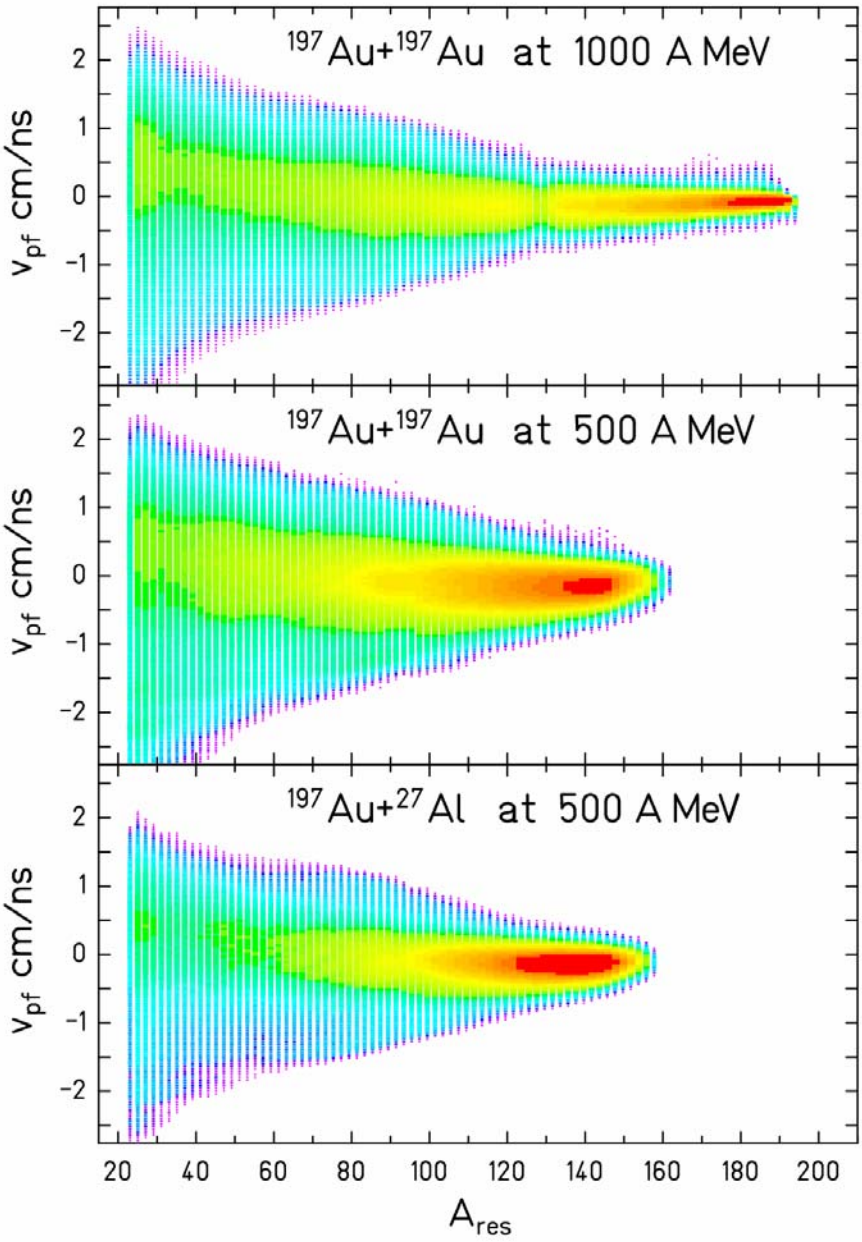

Fig.4.6: Velocities of the projectile residues as a function of their mass A_{res} in the reference frame of the primary beam. The color scale is logarithmic and represents the relative abundances of various velocities for fixed mass of the residue A_{res}. For illustrative purposes it is adjusted for each plot separately. The local depletion of the velocity distribution in the uppermost figure at A_{res}~130 is caused by border effects in two subsequent measurements (*see text*). The experiments performed at 500 *A* MeV did not cover residues with A_{res}>160.

shape of the total distribution, which is more or less symmetric around the zero velocity, the fragmentation ridge inevitably shifts its position to the positive velocity region with further decreasing mass.

Very similar trends can be observed in the other two systems displayed in the middle and the lowest subset of the Fig.4.6. However, here it has to be considered that the information on the velocity of the residues with masses close to the projectile is absent, and that the most intensively populated area of the plot around A_{res}~120-140 corresponds already to the velocity plateau. But the increasing trend of the dominant fragmentation ridge in the region of the lower masses remains evident.

As much as Fig.4.6 is illustrative in order to get the complete overview of the general kinematical properties of the projectile residues, it does not reveal any significant differences between the three compared systems caused by the varying incident beam energy or the size of the target nuclei. Therefore, to gain more insight into these fine differences it is necessary to simplify the overall picture by comparing the mean longitudinal velocities restricted to the fragmentation events. **Fig.4.7** displays the mean longitudinal velocities of the fragmentation residues $\langle v_z \rangle$ as a function of their mass A_{frag} in the reference frame of the projectile.

At the first sight, Fig.4.7 reveals a smooth variation of $\langle v_z \rangle$ with the mass of the fragmentation residues A_{frag}, in accordance with the discussion of Fig.4.6, and clearly displays the reacceleration phenomenon in all three systems studied. Moreover, it makes also visible the fine differences caused by the different beam energies and collision geometries.

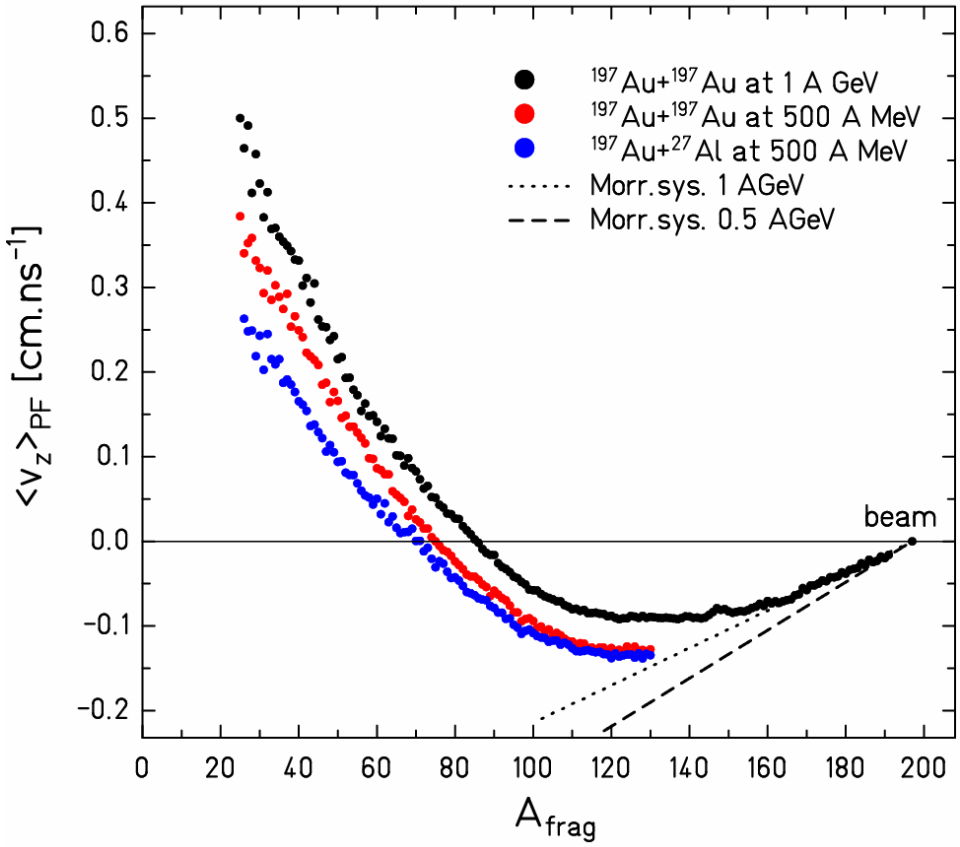

Fig.4.7: Mean longitudinal velocities of the fragmentation residues as a function of their mass A_{frag} in the reference frame of the corresponding primary beam. The black line represents the Morrissey systematic [Mor91]. For discussion concerning the errors see chap.4.3

The mean velocities measured in the experiment ^{197}Au+^{197}Au at 1 *A* GeV are the only ones which can be directly compared to the Morrissey systematic in the almost full relevant mass range, and the agreement in the region close to the mass of original projectile is very good. However, already at around $A_{frag} \sim 160$ the mean velocities begin to deviate and level off, until they start to recover around $A_{frag} \sim 120$, and finally reach positive values at $A_{frag} \sim 85$. This means that the fragments with masses $A_{frag} \leq 85$ are on average faster after the reaction than they were in the form of the projectile before. Therefore, this effect has been named ***reacceleration of the fragmentation residues***.

In comparison to the above discussed system, the mean longitudinal velocities $\langle v_z \rangle$ measured in the other two experiments are available only below $A_{frag} \sim 130$. However, it seems that around this mass the mean velocities just leveled off, and although the experimental data are absent, it is reasonable to assume that extrapolating to the higher masses they would reach

and closely follow the corresponding line of the Morrissey systematic as in the case of the higher energy data. In any case, interestingly enough, both systems, i.e. ^{197}Au+^{197}Au and ^{197}Au+^{27}Al at 500 *A* MeV, reach the velocity plateau with approximately the same $\langle v_z \rangle$, that is, however, significantly lower than the mean velocities measured in the 1 *A* GeV experiment. Also the recovery starts for both systems in the same mass region around A_{frag} ~120, but its pace is already different. The gold-on-gold system recovers faster and reaches positive values of $\langle v_z \rangle$ at A_{frag} ~75 practically copying the trend of the analog data from the higher-energy experiment. The magnitude of this negative offset stays with the further decreasing mass of the fragments down to A_{frag}~80 almost constant at the value of $\Delta\langle v_z \rangle$ ~ 0.04 cm/ns, indicating only a slight gradual increase below this mass.

Although the mean velocities measured in the experiment with the aluminum target share the same starting point as those from the experiment with the gold one, due to the different recovery pace they gradually deviate from their gold-target analogs, resulting in reaching the positive mean velocity region first at A_{frag} ~70. The mean velocity difference with respect to the Au+Au system at the same energy is at this mass region around $\Delta\langle v_z \rangle$ ~0.04 cm/ns and continues to grow further up to $\Delta\langle v_z \rangle$ ~0.10 cm/ns for the lowest masses included in the analysis, i.e. A_{frag} ~25.

4.3 The uncertainty of the measurement

The velocities of the individual fragments which form the base of the experimental data presented in the previous chapter are determined with help of eq.3.15-19 as discussed in Chap.3.4.1. Taking into account the negligible uncertainty of the constants such as the velocity of the light *c*, atomic mass unit *u*, mass of the neutron and proton m_n and m_p, respectively, the uncertainty of the final velocity may be influenced by the incorrect mass number *A* or nuclear charge *Z* determination, and measurement of the field of the magnetic dipoles B_{12}, effective radii ρ_{eff}, dispersion D_2 in the intermediate focal plane S2, and finally the measurement of the fragment's transit position x_2 through the scintillator SCI21. The following section therefore discusses the contribution of the individual quantities to the overall uncertainty of the longitudinal velocity and its mean value measured in the experiment.

Nuclear charge *Z*: The nuclear charge is by default an integer number, therefore when correctly determined it does not have any uncertainty at all. The general possibility to incorrectly determine the charge of an individual fragment is given by the charge resolution of the MUSIC detectors, which has been discussed and manifested in chap.3.3. Since it accounts to app. $\Delta Z/Z$ ~1/200 the contributions of incorrectly identified charge is virtually negligible. However, severe problems may be caused by various ionic charge states of the same element, what is discussed in chap.3.3.6, and what prevented the measurement of the heaviest residues in the experiments with 500 *A* MeV beam, but did not significantly affect any fragments measured in any of the three experiments.

Nuclear mass number A: The nuclear mass number *A* is by default an integer number, therefore when correctly determined it does not have any uncertainty at all. The general possibility to incorrectly determine the fragments mass number is given by the mass resolution of the FRS, which accounts for $\Delta A/A$ ~1/300-1/400, depending slightly on the charge and mass of the residue. Therefore, we consider the contribution of incorrectly determined mass-number as practically negligible.

Magnetic field B_{12} and effective radius ρ_{eff}: The magnetic field is measured with the Hall probes with a relative uncertainty of ~10^{-4}. The possible systematic error caused by the radiation damage or long-term variation is compensated by the determination of the effective radius ρ_{eff} with a similar relative uncertainty, as discussed in chap.3.2.3. Therefore, also the

error caused by the determination of the magnetic rigidity of the central trajectory for an individual magnetic field setting, which is given by the product of B_{12} and ρ_{eff} can be considered as inconsiderable, amounting for the $\langle v_z \rangle$ the order of ± 0.005 cm.ns^{-1}

Dispersion D_2: The dispersion is carefully measured by detecting the position of the beam by the MW21 when a magnetic field is changed by discrete relative steps. Since the position of the beam can be, with help of the multi-wire, detector determined with a precision of ~ ±1 mm, the slope of the linear fit determining the dispersion as introduced in chap.3.2.1 suffers from only a minor error in the order of 1%.

Position x_2 at S2: The position of the fragments transit through S2 is determined with help of the SCI21. The calibration by a MW21 can introduce an offset of the order of 1-2mm, additionally to that the achievable position resolution of the scintillator is in order of ~ ±2 mm. Another uncertainty is caused by the walk of the constant fraction discriminator which demands an additional correction discussed in chap.3.3.2. We assume that such a correction can induce an additional uncertainty of 3-4 mm being more pronounced close to the borders and the smallest in the center of the scintillator. The last considered effect influencing the position determination of the scintillator is the observed slight change in the response of the scintillator, causing an overall shift of the sensitive range. Such effect results in an observable offset with respect to the absolute calibration of the scintillator performed by the MW21, but can be corrected for by controlling the position of the borders of this sensitive range. This procedure contributes by an additional systematic error which we estimate to be up to ~ ±5 mm.

In the paragraphs above we have considered the influences of various uncertainties on the determination of the velocity of a single fragment. But since our interest lies in the full velocity distributions and their mean values, and we perform a scan of a great range of magnetic rigidities to cover the greatest possible part of the reaction products, many of the uncertainties mentioned above cancel out or can be explicitly corrected for.

Certainly the greatest error in the measurement of the fragments velocity is caused by the position determination. The offset in the position determination caused already by the calibrating MW can be determined and corrected for by use of a centered primary beam, since its velocity in the projectile frame has to be by default equal to zero.

The possible position-dependent error in the x_2 determination can be also controlled by the mean velocities of the heaviest fragmentation residues. While the widths of their velocity distributions are so narrow, they fully fit within the momentum-acceptance window of a particular setting. We then take the advantage of the overlap of the neighboring settings which differ by 1.5% in the magnetic rigidity what means that, with the full acceptance of 3%, each interval of covered magnetic rigidities was in a fact measured twice. That means that each of the distributions was also measured twice, but each time with the corresponding isotope traversing through different position at S2. If the calibration of the SCI21 is correct, the mean velocities of the same isotope measured in two different settings have to be equal. With this procedure, it is possible to increase the precision of the absolute calibration up to less than ±2 mm.

However, since the widths of the most of the velocity distributions correspond to several percent in magnetic rigidity, they have to be reconstructed by a superposition of several magnetic settings, and the procedure described in the last paragraph is no more possible. Nevertheless, also these velocity distributions are effectively measured twice, thus canceling out the effects connected to the position-dependent errors. Moreover, recalling the absolute sensitive range of the SCI21 being ~200 mm, neither the resolution of the SCI21 plays any significant role with respect to the width or with respect to the mean value of the velocity distribution. Then the remaining uncertainty connected to the position is the possible offset caused either by the changed response of the SCI21 or its calibration, which could not be verified by the primary beam. Such an offset then affects velocities of every measured

residue. But taking into account that a systematic error of 5mm, what is a realistic estimate of a possibly still undetected offset, corresponds to error of velocity ±0.02 cm.ns^{-1} in the projectile frame. Looking at Fig.4.7, it can be observed that such an error is negligible with respect to the overall magnitude of the reacceleration phenomenon, however may be significant in comparison of the results for different systems with one another. But it needs to be kept in mind that the results of one system are composed of several different scans covering limited ranges of charges, and that each of these charge scans was performed with slightly different tuning of the electronics and in different times. Yet no trace of discontinuity of the above mentioned size is visible, giving us confidence that the systematic errors in position determination were even below the mentioned limit. For explicit illustration, the small "bump" around A_{frag} ~165 in the data for 1 *A* GeV beam experiment can serve as the measure of the systematic discrepancy caused by a slightly different conditions for the position determination between two neighboring charge scans, since only the measurements above this mass could profit from a direct calibration by means of the narrow velocity distributions compared for individual isotopes as described above.

Moreover, while the systematic uncertainty can cause a certain small shift between the results of experiments with 1 *A* GeV and 500 *A* MeV beam, it cannot account for the difference between the two experiments within the same run with the lower incident-energy beam, because they have been measured under exactly the same conditions, when the gold and aluminum targets were alternated several times during the experiment.

On the other hand, a comparable uncertainty as the determination of the velocity itself brings in the reconstruction of the velocity distribution. This does not count for the heaviest residues, which are fully transmitted within one setting, but creates sizable effect for the intermediate and the light fragments. The first mentioned with masses A_{frag}~60-150 suffer the most by the normalization of the yields in the individual settings, which, with the method described in chap.3.4.3, can result in up to 5% errors in normalization of different pieces of the distribution, what for those spanning across only few settings can cause a slight shift of the mean value. On the other hand, since the mean velocities in Fig.4.7 are averaged over several isobars, this effect to a great extent cancels out, as it does also for the lightest residues, where the canceling effect is caused by a higher number of settings which need to be joined together for the full-distribution reconstruction.

The most detrimental effect on the uncertainty of the mean values of the velocity distributions of the lightest fragments (A_{frag}~25-70) is the angular transmission. Setting aside the absolute transmission efficiency correction which is not important for our purposes, the uncertainty in the correcting factor *T* defined by eq.3.27 is ruled by realistic values of the calculated α_{eff}. This effective acceptance angle is also position dependent, and not only on the position at S2, but additionally also at S4. As a consequence of the systematic error in α_{eff}, the *T* can overcorrect the relative yields toward one side of the physical borders of the FRS and under correct on the opposite side, resulting in overall distorted shape of the velocity distribution (see velocity distributions for A~30 in App.B). While the angular correction dependence on x_2 can be in a way controlled by the requirement that the parts of the velocity distributions measured in different settings should join smoothly (see Fig.3.23), such a grip of dependence on x_4 is not possible and results in a greater systematic error. Since the position at S4 is correlated with the nuclear charge, then the systematic error caused by the angular transmission results in a possibly less smooth connection of the measured mean velocities or widths of the velocity distributions as the function of *Z* reaching an uncertainty of 10% in the transmission for the fragments transiting S4 closest to the borders. However, in the experiment such a systematic error seemed to have only very limited effect as can be seen on the smooth variation of the mean velocity results around A_{frag}~65 and ~95 where in the case of the 500 *A* MeV beam three subsequent scans of the light, intermediate-light and intermediate

heavy fragments join. The systematic error in these masses is seen only in Fig.4.4 on the slight discontinuities of the corresponding widths.

In order to demonstrate the influence of the above discussed systematic uncertainties and their evolution with decreasing mass of the fragmentation residue, we have performed polynomial fits of the 3rd degree to all three data sets displayed in Fig.4.4 and calculated the deviation of the individual data points with respect to the corresponding fit. The resulting deviations as the function of A_{frag} are displayed in **Fig.4.8** for all three investigated systems. The scattering of the points thus represents the statistical [(*)] uncertainties with respect to the individual velocity distributions or their mean values; including also the "purely statistical" error of the fit as well as the systematic uncertainties discussed above.

Concluding this section, we can state that the standard deviations of the measured mean longitudinal velocities of the fragmentation residues account for ±0.010-0.015 cm/ns, for $A_{frag}\leq 50$, ±0.004-0.006 cm/ns for $51\leq A_{frag}\leq 100$, and ±0.002-0.003 cm/ns for $101\leq A_{frag}$ in all three investigated systems. More significant can thus be a systematic shift of the mean-velocities caused by an offset in the position calibration which we assume not to be greater than ~ ±0.02 cm/ns, however, the smooth course of the data in Fig.4.4, and rather small oscillations of $\Delta\langle v_z\rangle_{PF}$ visible in Fig.4.8, which are of the order of ±0.005 cm/ns, suggest that in reality it is probably lower.

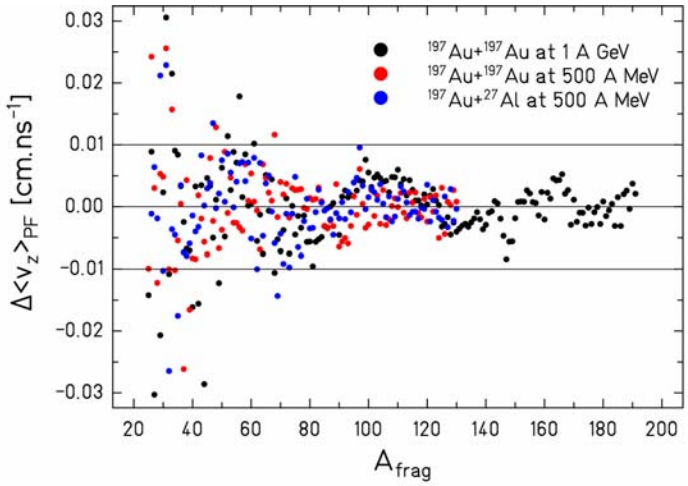

Fig.4.8: Deviations of the mean longitudinal velocities of the fragmentation residues from the 3rd degree polynomial fit to the measured data as the function of the mass of the fragmentation residue.

4.4 The reacceleration phenomenon and its implications

Although the first attempt to interpret the observed reacceleration phenomenon has been already performed in [Ric03], the variety and completeness of the current data allows us to extend the qualitative understanding of the whole process. With respect to the above presented data we can summarize ***the experimental facts***:

I. The reacceleration of the fragmentation residues appears to be a common feature of the relativistic heavy-ion collisions.

II. The velocities of the fragmentation residues with masses close to the projectile follow the Morrissey systematic but deviate from it above a certain mass loss.

III. The reacceleration of the fragmentation residues depends on the incident beam energy.

[*] the term statistical is used in the sense that these uncertainties of the different data points are not correlated

IV. The reacceleration of the fragmentation residues depends on the size of the target nuclei.

V. The widths of the velocity distributions of the reaccelerated fragmentation residues do not depend on the energy and vary only weakly with the geometry of the reaction system.

The first point may sound trivial, but it surely is not, since in order not to violate the conservation laws, the energy causing the fragments to reaccelerate has to come at the expense of something that is by no means experimentally obvious. However, the reacceleration of the fragmentation residues observed previously in several different systems [Enq99, Ric03] has been confirmed, thus proving to be a rather general feature of relativistic heavy-ion collisions, not accounting for plentiful data showing clear deviation from the Morrissey systematic already in [Mor89].

The second point describes the observation of a sudden deviation from a completely linear dependence meaning that the reacceleration should be a threshold effect.

The other two points summarize the newly gained qualitative knowledge. Their content may look qualitatively straight-forward, since with delivery of more energy, in terms of the higher incident beam energy or more nucleons to collide with in the heavier target, a larger dynamical effect can be expected. But the results have to be quantitatively understood keeping in mind the fifth point, which basically says that the energy delivered to the projectile remnant in the direct reaction is in all three systems just the same, otherwise the widths of the velocity distributions would not match (neglecting for a while the slight deviation for low fragment masses in the reaction with the aluminum target).

It now seems that the key for understanding the reacceleration phenomenon is the localization of the source of the momentum that is delivered to the projectile remnant. Unfortunately, the measurements alone do not give any direct answer, and the solution of the problem may be possible only with the help of theoretical models. But before advancing to a more complex analysis, it is desirable to assess also the semi-quantitative features of the results that go beyond the Morrissey systematic, which is taken as a reference:

VI. With respect to the Morrissey systematic, the magnitude of the reacceleration of the fragmentation residues in ^{197}Au+^{197}Au at 500 *A* MeV is similar to that of the fragments from the system with twice as much incident-beam energy.

VII. The net difference of mean longitudinal velocities $\Delta\langle v_z\rangle$ between the ^{197}Au+^{197}Au systems at varying beam energy stays in the mass region $A_{frag}\approx$80-130 practically independent from the mass of the final fragment.

VIII. With respect to the Morrissey systematic, the magnitude of the reacceleration of the fragmentation residues in ^{197}Au+^{27}Al at 500 *A* MeV is similar to that of the fragments from the symmetric system at the same incident-beam energy, despite the fact that the gold nucleus is as the target more than seven times heavier and has a radius almost two times larger than the aluminum nucleus.

IX. The pace of reacceleration of the fragmentation residues in ^{197}Au+^{27}Al, with the decreasing residue mass, is slightly slower than in the gold system with the same projectile energy.

Evaluating the meaning of the points above is not possible without adopting at least a simple model of the reaction evolution. The natural choice is the spectator-participant approach, leading to the excitation of the projectile remnant by the abrasion of nucleons in the initial phase through a basically geometrical cut-off by the overlapping zone, and formation of the participant fireball from the nucleons of a projectile and a target colliding with one

another. In this simplified picture there are two possible sources of momentum which can induce the reacceleration of the fragmentation residue.

The first one stems from the spectator itself, since the excitation energy gained in the abrasion process is released by the evaporation of individual nucleons or complex clusters. Any non-isotropic emission would cause the average relative momentum of the surviving projectile remnant to change in the direction opposite to that of the emission, in the same way as a jet engine induces the acceleration of a rocket. The second momentum source is the fireball of the participants, which after the initial compression phase violently explodes. Considering the spectator matter moving undisturbed in the original direction, the participant blast occurs behind its back, thus a hit by any piece of ejected participant matter, which would have to be faster, would cause an increase of the relative spectator momentum.

Turning the attention back to the presented semi-quantitative features of the results, it is puzzling why, according to point VI, the magnitude of the reacceleration itself is almost insensitive to the energy of the projectile. When considering this point, we have to remember that it is the excitation energy of the projectile remnant which should be the same in both systems since it is caused to a great part by the holes due to the abraded nucleons in the single-particle levels [Gai91]. The interpretation of the point VII alone is rather ambiguous. Generally speaking, it means that with decreasing mass of the final fragment the increase of energy somehow available for the reacceleration is the same despite its different amount delivered to the participants zone with presumably decreasing impact parameter, as demonstrated in **Fig.4.9**. We discuss this again later, but having it on mind, we can try to extrapolate the experimental data for the lower incident-beam energy of gold-on-gold toward the Morrissey systematic. The suspected point of the encounter then seems to lie in area of the same or slightly lower masses than in the higher energy system, what is better visible if the mean longitudinal velocities are recalculated into the laboratory mean recoil momenta using the following expression [Mor89]:

$$\left\langle P_z^* \right\rangle = \Delta m \left\langle \beta_z \right\rangle \frac{\beta\gamma}{\gamma + 1} \tag{4.1}$$

where Δm is the mass difference of the fragment and the projectile, β_z is the longitudinal velocity of the fragment in units of velocity of light c, β is the analogical velocity of the projectile, and γ is the relativistic kinematical factor of the projectile. In this frame, the Morrissey systematic looses its dependence on projectile energy and becomes universal, as can be seen in the right subset of Fig.4.9. While we consider the excitation energy of the spectator as also being the same despite the different beam energies, this would implicate that the reacceleration can be at best only triggered by the amount of the energy delivered to the participants. This would not be so surprising, since there is still twice as much energy available than in the case of the system with the 500 A MeV beam. Concerning Fig.4.9, one should not get intrigued by the mass-dependent difference of the recoil momenta, since this is due to the kinematical factor applied in eq.4.1. However, for comparison of the effect of the reaction, we prefer the reference frame of the projectile as being the most transparent. On the other hand, in the limiting case of the reacceleration onset for the same mass loss it also allows a possibility of the reacceleration threshold being reached by the amount of the excitation energy induced purely by the abrasion, denying the participant blast to play any role at all.

Looking again at the left plot of Fig.4.9, turning the attention to the $A_{frag} \leq 80$, we can observe that the difference in the longitudinal momentum change between the symmetric systems with different projectile energy and between the systems differing only by reaction geometry displays a very similar magnitude as well as the trend, again pointing to the energy

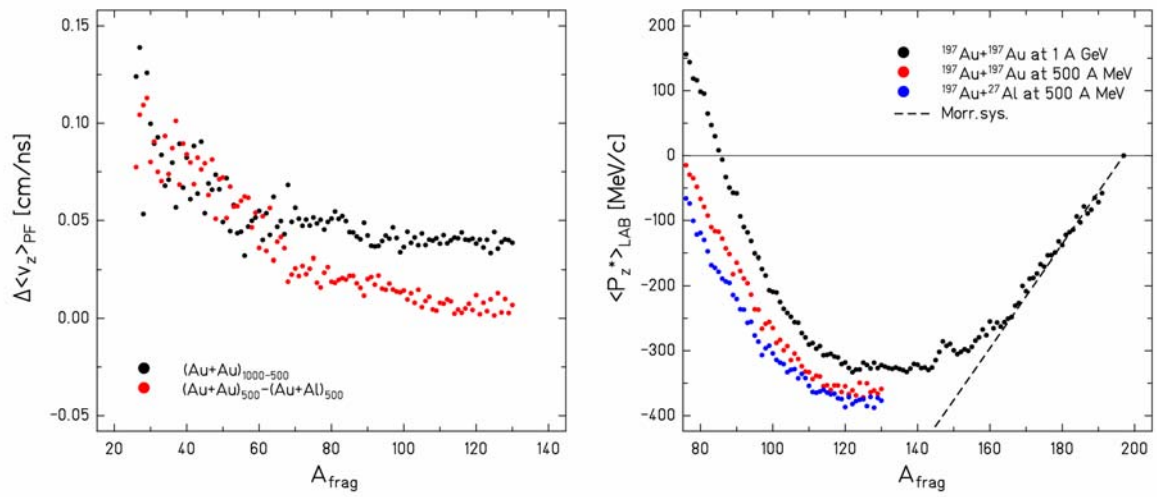

Fig. 4.9: *Left:* The difference of the measured mean longitudinal velocities in the projectile frame as the function of the mass of the fragment for systems with either the same collision geometry (black points) or the same incident beam energy (red points). *Right:* The measured average longitudinal momentum transfer as a function of the mass of the fragmentation residue in the laboratory frame. The black dashed line represents the Morrissey systematic [Mor91].

delivered to the participant zone as the key quantity determining the magnitude of reacceleration.

Also the fact stated in point VIII that the system with the smaller target nucleus reaccelerates almost in the same way as the other two systems speaks rather against a direct relation of this phenomenon to the energy delivered to the participant zone, since with smaller aluminum nuclei the same abrasion wound to the gold projectile is caused by less participating target nucleons. This of course means a smaller accumulation of the energy in the subsequent fireball. In fact this abrasion wound may be a key to understand the last presented point, since if the energy of the fireball would be set aside, it is effectively the only difference between the two systems with the same lower beam energy. Moreover, just in terms of the geometrical considerations, the surface of the conical scar is the only difference between the two systems which increases with increasing violence of the collision. If that would be true, it also extends the meaning of the point VII, and may indicate the reason why the difference in reacceleration in both Au+Au systems is, once fully established, kept in the above mentioned mass range the same.

Summarizing the above discussion the qualitative as well as the semi-quantitative features of the experimental results direct the attention more to the spectator itself than to the participant blast as the main source of the reacceleration phenomenon, but still considering the second process as playing a possible role at least in kind of a ignition of a hypothetical "*rocket engine*" [Dan05].

Of course, one can argue that this very simple analysis neglected several significant aspects of heavy-ion collisions at relativistic energy, but the main idea was just to sketch the most profound aspects of the experimental data and their mutual relationship.

For example, in a more elaborate analysis, one would have to account the effects of the lower velocity in the experiments with lower beam energy implicating the possible longer exposition of the spectator remnant to the effects of the blast, which on the other side due to the relativistic effects does not scale with the incident beam velocity. Furthermore the evolution of the participant region is ruled by a complex interplay of nuclear forces, resulting in pressure gradients depending on the cross sections of the nucleon-nucleon scattering which however may also vary with energy and density, modified by the influence of the surrounding nuclear medium. Also the composition of the particles ejected by the fireball and their collective flow may influence the response of the spectator in several ways. It can be

speculated about the influence of pions, for their mean-free path in the nuclear medium is several times shorter than the typical nuclear radii, thus possibly causing the preferential excitation of the near-side of the escaping spectator. In the above recital one should not forget the arguments for a rather fast equilibration of the hot spectator remnant effectively preventing any preferential emission, shutting the possible source of energy for reacceleration completely down.

The intention of the last paragraph was not to account for all possible aspects of the nuclear reaction dynamics, but rather just to mention a few examples of various diverse aspects which would be needed to be evaluated in order to achieve a fully consistent description. This of course goes beyond the capabilities of any simple and intuitive model and requires the involvement of a very elaborate theoretical description. But the advantage in interpretation gained by the possibilities of a developed model is limited by its inner hypotheses, assumptions and approximations, shifting the reliability of the conclusions from the reliability of the experimental data to that of the model itself.

Therefore, we would like to make a clear distinction between these two approaches, from which the first one has been presented within this chapter and which tries to put emphasis on the pure experimental observations, and the second is adopted in Chapter 7 fully dedicated to the comparison of the experimental data with the results obtained predominantly with a dynamical model based on the Boltzmann-Uehling-Uhlenbeck equation [Dan00].

5. Determination of the impact parameter

The impact parameter is indeed the key quantity determining the dynamical evolution of the reaction of two relativistic heavy-ions. It is defined as the distance of the closest approach of two nuclei if they had continued in their original direction of motion at their original speed. In such relativistic heavy-ion collisions, i.e. in the projectile-energy range of few hundreds up to few thousands MeV per projectile nucleon, one can adopt an abrasion-ablation description of the collision process [Gai91] adopting the concept of participants and spectators [Bow73, Wes76] (see **Fig.5.1.**). Thus, the impact parameter determines the number of nucleons abraded from the projectile, which being slammed against their target counterparts form the fire streak of the so-called participant zone.

In a typical mid-peripheral collision ($b \approx b_{max}/2$), after an initial compression phase, the participant zone violently explodes, resulting in a flow of individual particles and light clusters, potentially hitting the escaping spectator matter and affecting its dynamical evolution.

On the other hand, in very peripheral collisions the number of nucleons in the overlapping zone can be so low, that after undergoing few scatterings on one another, the nucleons of the projectile basically pass through the ones of the target nucleus without any significant density build-up, thus preventing the spectator from being influenced by any participants blast. Such spectator leaves the place of the collision slightly slowed down by the friction during the abrasion process and is excited proportionally to the number of the lost nucleons. The excitation energy is subsequently released in form of eventual break-up and evaporated nucleons or light clusters, leaving a cold residue which enters the detection device.

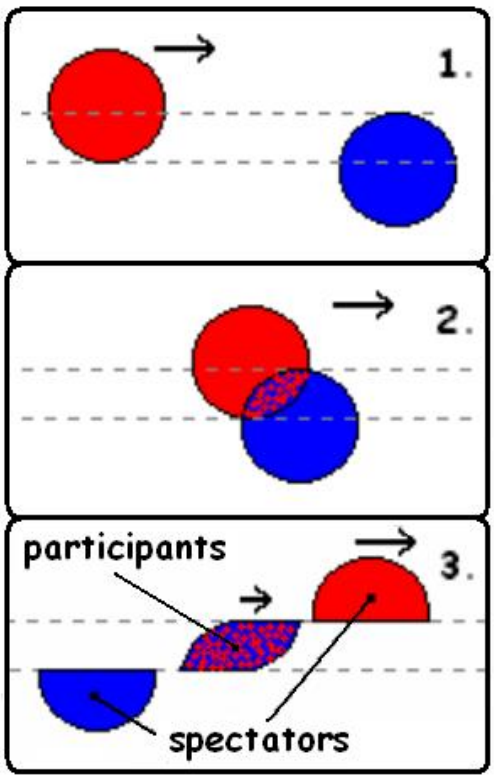

Fig.5.1: Schematic concept of the spectator and participant matter in a heavy-ion collision in the relativistic energy domain.

The exact distinction, with respect to the number of participating nucleons, which is ruled by the impact parameter of the collision, between the events when participant's fire streak fully develops and can, if at all, affect the spectator, and the events when the spectator leaves collision place undisturbed, cannot be yet clearly made. It is the main aim of this work to investigate the dependence of the possible spectator response on the participant blast and how the properties of the blast are ruled by the number and the energy of the participating nucleons, i.e. by the impact parameter and the energy of the nuclear collision.

Moreover, in order to extend our investigation, and to test different theoretical concepts and descriptions of the collision process, the knowledge of the impact parameter is the essential quantity providing the consistent link between the experimental observables and their theoretical predictions. Therefore this chapter is dedicated to the experimental determination of the impact parameter.

5.1. Impact parameter determination in exclusive measurements

The exclusivity of the experiment is defined as the ability to measure enough reaction products that the reaction kinematics can be fully reconstructed and the reaction plane determined in a single event.

5.1.1. Multiplicity of detected particles

The impact parameter characterizing the initial state of the heavy-ion reaction is not directly measurable. Therefore, it is necessary to search for an observable, which is strongly correlated with it. In the exclusive measurements, the simplest observable is the multiplicity of the detected particles. The hypothesis of the strong correlation of the multiplicity with the impact parameter b has been confirmed already by intranuclear-cascade calculations in the early 80's [Cug83]. Also the results of the Plastic Ball [Gut89] were presented in correlation with the multiplicity as the qualitative measure of the impact parameter. However, the first consistent method of transforming the qualitative estimate of the impact parameter into a quantitative one over the whole range of the multiplicity distribution came first with the approach of Cavata et al. [Cav90], extending thus the early work of Schroeder et al. [Schr78].

Within the approach of Cavata et al., it is assumed, that the multiplicity is monotonously correlated with the impact-parameter, and its dependence on the measured cross section is interpreted as an impact parameter dependence of the geometrical reaction cross-section.

At relativistic energies, the total nucleus-nucleus cross section can be, within the black-body hypothesis, approximated by the geometrical cross-section: $\sigma_g=\pi(R_t+R_p)^2$, where R_t and R_p are the equivalent hard-sphere radii of the target and projectile nuclei, respectively. As a function of the squared impact parameter, the derivative of the cross section is constant $d\sigma_g/d(b^2)=\pi$, up to the maximum value $(R_t+R_p)^2$ of b^2, and is zero beyond this value. To any value m of the multiplicity it is possible to associate the integral S of the measured cross section $\sigma(M)$, from m to infinity.

$$S = \sum_{M=m}^{\infty} \sigma(M)\,. \tag{5.1}$$

Since the mean value of the multiplicity decreases monotonously with the impact parameter b, it is also possible to associate to m the impact parameter B such that

$$\int_0^{B^2} d(b^2)\frac{d\sigma_g}{d(b^2)} = S\,, \tag{5.2}$$

thus $B^2=S/\pi$. This procedure can be used step by step in order to calculate the average value of b^2 corresponding to any multiplicity integral $[m_i,m_j]$ as $b_{ij}^2 = (B_i^2 + B_j^2)/2$, as illustrated in **Fig.5.2**. In absence of any dispersion in the correlation between multiplicity and impact parameter the method is rigorous. However, in reality there is always a finite dispersion given by the statistical nature of the reaction process, but as long as the correlation is large enough in comparison to the dispersion, the method remains valid.

In principle, this method may be used with any variable that any available theoretical models could show to be reasonably well correlated with the impact parameter of the collision. In the range of intermediate energies this seems to be true for example also for the multiplicity of the light charge particles, transverse energy, zero degree energy or the total bound charge, i.e. Z_{bound}, as will be discussed in the next section.

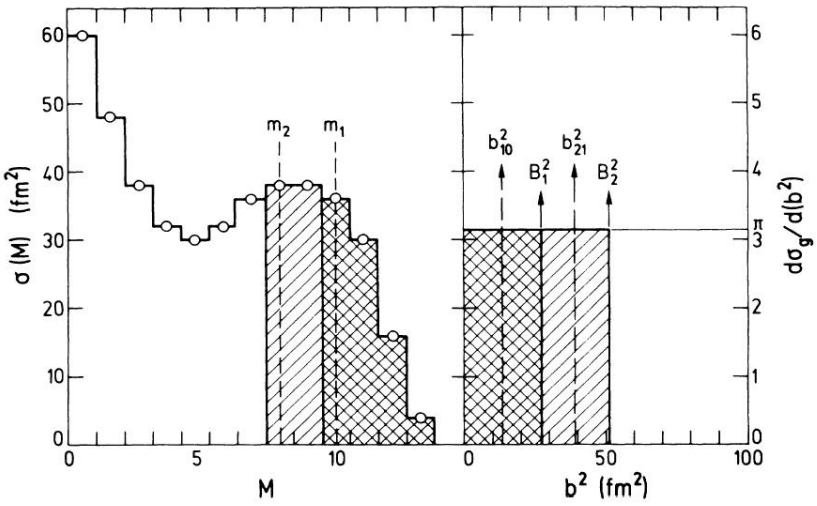

Fig.5.2: Principle of the method: measured cross-section versus multiplicity (*left*) and geometrical cross section vs b^2, the square of the impact parameter (*right*). The hatched areas correspond to equal integrated cross section on both diagrams, with three multiplicity limits $m_0=\infty$, m_1, and m_2 (reprinted from the ref. [Cav90]).

5.1.2. Z_{bound} as the measure of the impact parameter

Among several observables which were found to be correlated with the impact parameter, the one based on the quantity called Z_{bound} deserves a special attention, since, as will be shown, it allows the extension of the impact parameter determination also into the measurements of inclusive nature, such as those which are the object of this thesis.

The quantity Z_{bound} has been first introduced by Hubele et al. [Hub91] in order to measure the number of charges contained in projectile fragments, measured in the exclusive experiments of the ALADIN collaboration. Z_{bound} is defined as the sum of all charges of all complex fragments with $Z\geq 2$, and thus it gives the atomic number of the excited projectile spectator reduced by the number of hydrogen nuclei emitted from it. Therefore, it depends on the primary abrasion and the secondary deexcitation stages and reflects the violence of the collision. Moreover, while the multiplicity of light particles is sensitive to both the projectile and the target nucleus, Z_{bound} is related only to the size of the projectile spectator.

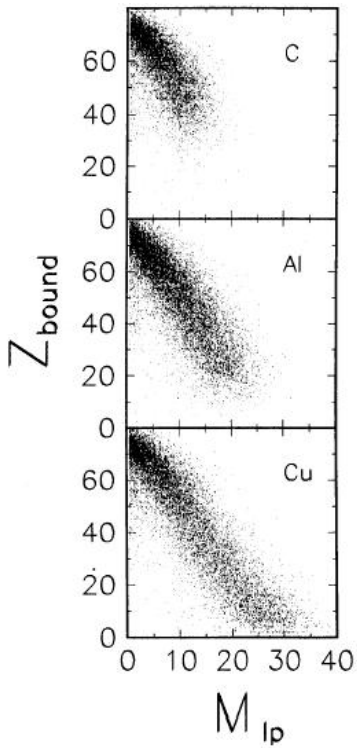

Fig.5.3: Correlation between the multiplicity M_{lp} of light charged particles and Z_{bound} for Au+C,Al,Cu at 600 A MeV (reprinted from [Hub91]).

As revealed in **Fig.5.3**, the nearly linear correlation between the light particle multiplicity $\langle M_{lp}\rangle$ and the Z_{bound} suggest that either of them can be used for the impact parameter selection. The reconstruction of the impact parameter from Z_{bound} can be then performed with use of the geometric cross section decomposition with respect to Z_{bound} in the same way as it was introduced in the Chap.5.1 for the multiplicity of the detected particles. Additionally, according to the mentioned study of Hubele et al. [Hub91], Z_{bound} seems to be even better impact parameter selector in case of very peripheral collisions than the $\langle M_{lp}\rangle$.

5.2. Impact parameter determination in inclusive measurements

An inclusive experiment does not provide the information which allows deducing neither the multiplicity of light charged particles nor the sum of bound charges. Thus in this case the impact-parameter selectors introduced in the last chapter cannot be used.

This limitation is also present in the case of the FRS, since one can profit from the high resolution in mass and velocity only at the expense of the limited angular and momentum acceptance of the detection device, corresponding to 15mrad around the beam axis and 3% in momentum, respectively. For example, in case of the system ^{197}Au+^{197}Au at 1 *A* GeV, this angular acceptance corresponds to 100% transmission for fragments of mass above *A*~110, 75% transmission for fragments with mass *A*~70 and transmission decreasing down to app. 40% for masses *A*~25, and even much less for light-charged particles, as discussed in chap.3.4.4.

Therefore, due to the limited acceptance, only one fragment per reaction can be measured, thus not allowing for the complete information on the reaction kinematics, neither the multiplicity nor Z_{bound} based determination of the impact parameter [Hub91].

However, as suggested already by the results of the QMD calculations in the study of Aichelin et al. [Aich88], also the charge and/or mass of the greatest fragments produced in the inclusive experiments can serve as an impact-parameter selector. This requires an ability to determine the order of the detected fragment, i.e. whether it has been the fragment with the greatest mass and/or charge produced in the reaction, or whether it has been the second fragment or even the fragment of the lower rank.

For all fragments with mass greater than half of the mass of the original projectile this condition is indeed true, since any other partner produced in the reaction has to be smaller by default. But the information allowing an extension of the classification of the detected fragments below this limit is not directly available from the inclusive data, but can be deduced from the results of experiments performed at full-acceptance devices.

Yet, in reactions involving large projectiles, even very small excitations of the spectator produced in high impact parameter collisions may lead to fission, producing fragments of similar size as a true fragmentation process following abrasion and subsequent evaporation resulting from the collision with significantly lower impact parameter. Therefore, the unambiguous determination of the mean impact parameter is possible only for the largest residues produced in the fragmentation process, provided we can separate them from the fragments produced by fission.

In the following section, it will be shown, how one can profit from the complementarity of the information from the full-acceptance experiments in order to determine the order of the fragments detected by the Fragment Separator and how the quantitative relation between the mass of the largest residue and the mean impact parameter can be established.

5.2.1. Order of the fragmentation residue

Full-acceptance experiments, such as the ALADIN spectrometer [ALA] can profit from the detection of all fragments produced within one reaction event. However due to the limited mass resolution, the size of individual fragments can be evaluated only in terms of the charge, which is on the other hand directly correlated to the mass (see Chap.4).

Taking the direct advantage of the data measured by the ALADIN group in the experiment ^{197}Au+^{197}Au at 1 *A* GeV which were provided to the authorby the ALADIN collaboration, it is possible to construct a correlation between the charges of the largest (Z_{max}) and the second largest (Z_{max2}) fragment produced in one reaction event, as displayed in **Fig.5.4**. The

triangular shape of the correlation reflects the trivial conditions that the sum of the largest and the second largest charge cannot be greater than the charge of the projectile.

While the top of the triangle in the left subset of Fig.5.4 can be associated with the fission process, producing two large almost equally sized fragments, the ridge at the triangle base represents the fragmentation events, characterized by either a large residue accompanied by several small-sized fragments (right side of the ridge) or a multifragmentation event resulting in several intermediate-mass fragments (left side of the ridge).

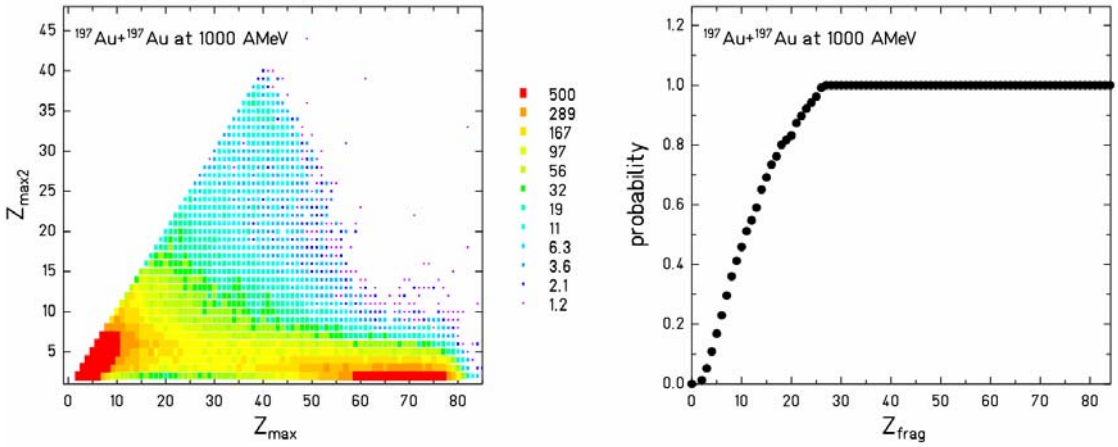

Fig.5.4: *left:* Correlation of the highest (Z_{max}) and the 2nd highest (Z_{max2}) charge produced in the reaction of ^{197}Au+^{197}Au at 1 *A* GeV. The top of the triangle corresponds to fission events, the ridge at the bottom to the fragmentation; *right:* Probability that the charge of the measured fragment is the highest charge produced in an individual reaction of ^{197}Au+^{197}Au at 1 *A* GeV (fission events excluded) [source data provided by ALADIN [ALA]]

The clear distinction between different reaction processes allows excluding fission events from the further analysis and thus directly evaluating the probability, that the detected charge is the greatest charge produced in one fragmentation event. Results of this evaluation are displayed in the **Fig.5.4**, where one observes that every residue with charge $Z \geq 27$ is the fragment with the greatest charge produced in the reaction (Z_{max}). In comparison with the data measured in this study, where charge as well as mass resolution is possible, $Z=27$ corresponds to average mass $A \sim 60$ (see chap.4). The probability being the greatest fragment drops to 50% for charge $Z=11$, which corresponds to mass $A \sim 25$.

5.2.2. Z_{max} as an impact-parameter selector

The same ALADIN study as discussed above shows, that Z_{bound} (which can be used as a measure of the impact parameter in peripheral collisions [Hub91]) is clearly correlated with Z_{max}, the fragment with the greatest charge, for $\sim 25 \leq Z_{max} \leq Z_{proj}$ (=79), as displayed in **Fig.5.5**. This is then the experimental evidence for the predicted behavior of the greatest fragmentation residues with respect to the impact parameter as discussed already by [Aich88]. Contrary to that, the correlation of the 2nd greatest fragment produced in the reaction Z_{max2} with Z_{bound} is qualitatively worse and quantitatively different (Fig.5.5). Therefore only Z_{max} can serve as a measure of the impact parameter in the similar way as Z_{bound}. If one then takes into account that fragments with charge $Z \geq 27$ ($A \geq 60$) measured by the FRS are for sure the greatest fragments produced in the reactions, it can be concluded that these ***fragments carry the unambiguous information on the mean reaction impact parameter themselves***, even though they have been measured using inclusive experimental technique. The remaining task is the calibration of our impact parameter selector (i.e. charge *Z* or mass *A* of the largest detected fragments), which is addressed in the following section.

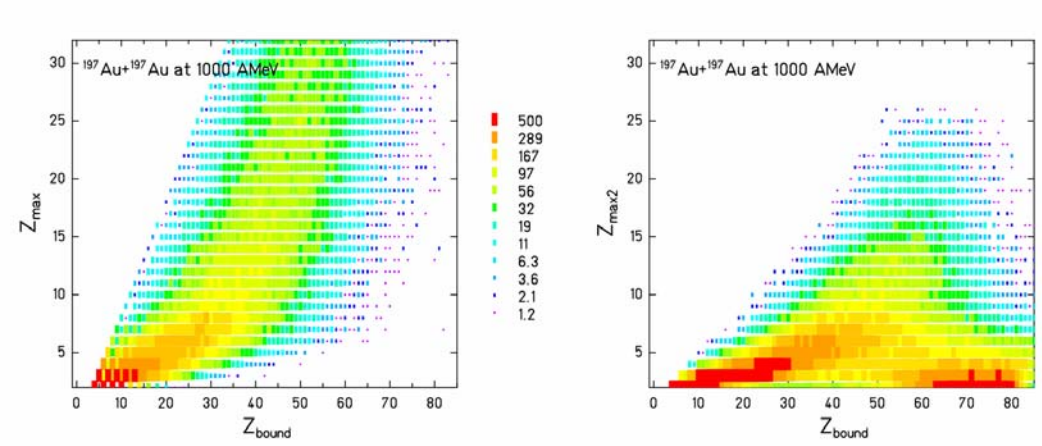

Fig.5.5: *left:* Correlation of the highest charge (Z_{max}) and the sum off all bound charges (Z_{bound}) produced in the reaction of ^{197}Au+^{197}Au at 1 *A* GeV. The full line indicates the mean value of Z_{bound} with respect to $Z_{max.}$; *right* Correlation of the 2nd highest charge (Z_{max2}) and the sum of all bound charges (Z_{bound}) produced in the reaction of ^{197}Au+^{197}Au at 1 *A* GeV [source data provided by ALADIN]

A similar evaluation of the range of nuclear charge for which the nuclear charge of the observed fragment is for sure the greatest one produced in the reaction, thus applicable for the correct impact parameter determination, has to be performed also for the other two experiments analyzed within this study, i.e. ^{197}Au+^{197}Au/^{27}Al at 500 *A* MeV. However, in this case the nearest projectile energy with which ALADIN collaboration performed its experiments investigating the same reaction systems is 600 *A* MeV. On the other hand, as revealed by the complex analysis of the ALADIN data [Schut96], the spectator fragmentation is basically universal in the relativistic energy regime between 400-1000 *A* MeV and thus also results of the FRS experiments are compatible with the ALADIN ones, although the beam energy differs by 100 *A* MeV.

The figures displaying the correlation of the Z_{max} and Z_{max2}, and probability of being the greatest detected charge in the reaction event for the systems ^{197}Au+^{197}Au/^{27}Al at 600 *A* MeV reconstructed from the original data provided to the author by the ALADIN collaboration can be found in App. C. On this place we limit ourselves by stating that the range of the residue charges (masses), for which an unambiguous mean impact parameter determination can be performed is practically the same as in the case of the system ^{197}Au+^{197}Au at 1 *A* GeV.

5.3. Impact parameter as a function of the residue mass in Au+Au/Al systems

The observation of a direct correlation between Z_{max} and Z_{bound} in a wide range of charges (Z~25-80) [Hub91], gives us a possibility to deduce the impact parameter even in inclusive measurements such as those performed with the FRS.

In the present work we first take advantage of the previously determined correlation of Z_{max} and the impact parameter b, which was performed by the ALADIN colaboration [Schut96b] in two steps via the correlation with Z_{bound}. Although the results presented in their work refer to Au+Au at somewhat lower incident beam energy, i.e. 600 *A* MeV, the universality of the Z_{max} dependency on Z_{bound} within wide incident energy range as shown in [8] assures the applicability in both of our systems ^{197}Au+^{197}Au, i.e. at 500 and 1000 *A* MeV.

In the work of the ALADIN collaboration [Schut96b], first the dependence of the impact parameter on the sum of all produced bound charges Z_{bound} was established, utilizing the

method of decomposition of the total reaction cross section with respect to the Z_{bound}, similarly as described in section 5.1.2. Then using the correlation of Z_{max} with Z_{bound} as is done in Fig.5.2, one can determine the direct dependence of Z_{max} on the impact parameter.

Due to the unambiguous identification of all detected fragments in charge Z as well as in mass A in the FRS experiments within this study, we can transform this correlation into the dependence of the mean impact parameter $\langle b \rangle$ on the mass of the final residue A_{res}. Following the argumentation concerning the correlation of Z_{max2} (Fig.5.5.b)) given above, we set as the lower limit of the charge of the fragments for which we determine the impact parameter as Z=27, i.e. A=60. The upper limit is the charge (mass) of the projectile. The mean impact parameter $\langle b \rangle$ as a function of the final residue mass as deduced with the help of the results by the ALADIN group is displayed in **Fig. 5.6** as a red dashed curve.

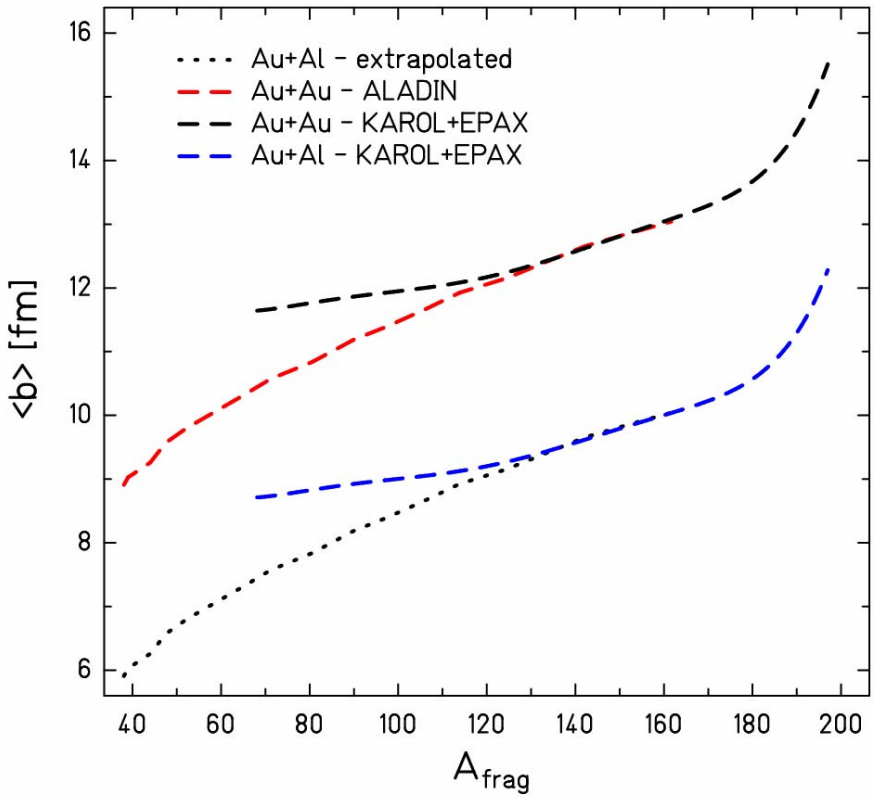

Fig.5.6: Mean impact parameter as a function of the projectile residue mass determined by the decomposition of the total reaction cross section with respect to the mass of the final residue A_{res}. Red dashed line indicates the impact parameter obtained from the data of ALADIN for Au+Au at 600 A MeV [Schut96b], black and blue dashed line indicate results obtained by utilizing calculated total differential reaction cross section with model of Karol [Kar75] and production cross section by EPAX2 [Sue00]. The black dotted line indicates the extrapolation of the ALADIN data for the Au+Al system; for details see text.

However, it should be stated, that the approach to determine the impact parameter with use of Z_{bound} performed by Huebele et al. [Hub91] uses the geometrical cross section and the method of [Schr78]. But since our interest lies also in the investigation of very peripheral collisions leading to rather small mass losses, the approximation of the nuclear density by a sharp geometrical cut-off seems to be inappropriate. Moreover the model to which the experimental data are compared in chap.7 uses nuclear densities with diffuse profile. Therefore, we consider as necessary to also account for the diffuse profile of the nuclear density.

As a complementary, and to certain extend also an alternative approach we use the analogical method of decomposition of the total reaction cross section with respect to the mass of the final residue A_{res}. Yet this time for calculating the total reaction cross section we utilize the model of Karol [Kar75] with empirical density profiles [Mye74, Mye76] and an empirical parameterization EPAX2 [Sue00] for calculating the absolute cross section with respect to the mass of the final residue. Results of this procedure are also displayed in Fig.5.6 as a black dashed curve.

Comparison of both dependencies of A_{res} on the impact parameters in Fig.5.6 reveals clearly the difference for very peripheral collisions in the range of $\langle b \rangle \approx$13.5-16 fm, corresponding to mass $A_{res} \approx$180-197, caused by the sharp cut-off in the density profile of the geometrical cross-section method. In this mass region we will prefer the result obtained with use of the more realistic nuclear density profiles and reliable differential cross sections calculated by EPAX2. On the other hand, following the region of remarkable agreement between $\langle b \rangle \approx$12.0-13.5 ($A_{res} \approx$110-180), the correlation from the KAROL+EPAX tends to yield too high impact parameters with respect to the result provided by ALADIN using geometrical cross sections and measured yield of Z_{bound}. In this region of masses $A_{res} \approx$62-110, we follow the experimentally measured data of ALADIN, since EPAX2 is predominantly based on a parameterization of the fragmentation data where less than half of the projectile mass has been lost.

Unfortunately, at the time of writing this thesis, the experimentally determined impact parameters as the function of the nuclear-charge of the final residue for the system ^{197}Au+^{27}Al were not available. For the larger impact parameters, the relation between impact parameter b and residue mass A can still be estimated by the combination of the models of Karol and EPAX. Comparing the results for the systems Au+Au and Au+Al, we observe a shift of $\Delta\langle b \rangle$=3.0±0.1 fm, meaning that a fragment of the same mass was in case of Au+Al reaction produced on average at impact parameter that is by 3 fm lower than in the case of the Au+Au reaction. Therefore, we assumed that it is justified to expect a similar impact parameter dependence on A_{frag} in the system Au+Al as was observed in case of the ALADIN data for Au+Au at 600 A MeV with the same shift of 3fm. This parameterization of the impact parameter as a function of A_{frag} is displayed in Fig.5.6 as a black dotted line.

6. Model calculations

It has been a common feature of many experimental observables arising from investigations of very complex processes such as heavy ion collision, that without the link to the results of theoretical predictions no intuitive understanding would be possible. Retrospectively, we can admit that this as well may have been the fate of the reacceleration phenomenon clearly observed already in the work of [Enq99], if there would not had been the independent theoretical survey of the spectator properties by the use of a dynamical model based on the Boltzmann-Uehling-Uhlenbeck equation (BUU) by Shi et al [Shi01].

It is then natural that also in this study the very same model is used to guide our understanding of the experimentally observed phenomenon. This chapter is therefore dedicated to the description of the model, which was provided by and is being developed at Michigan State University, USA, by the group of Pawel Danielewicz [Dan00].

6.1. BUU model – historical and general remarks

The BUU equation is based on the Boltzmann equation, a classical kinetic equation for dilute gases first formulated by Boltzmann in 1872:

$$\frac{\partial}{\partial t} f + \mathbf{v}\frac{\partial}{\partial \mathbf{r}} f + \mathbf{F}\frac{\partial}{\partial \mathbf{v}} f = \Omega(f)\,. \tag{6.1}$$

It describes the distribution function of a dilute gas $f(\mathbf{r},\mathbf{v},t)$, which is defined such that $f(\mathbf{r},\mathbf{v},t)d\mathbf{r}d\mathbf{v}$ is the number of molecules at time t positioned between $\mathbf{r}$ and $\mathbf{r}+d\mathbf{r}$ having velocities in the range $\mathbf{v}\rightarrow\mathbf{v}+d\mathbf{v}$. It is assumed that the particles move under the influence of an external force per unit mass $\mathbf{F}$, except when they collide with each other in which case it is also assumed that only two particles take part in the collision, described by the collision operator $\Omega(f)$.

In 1933 the Boltzmann equation was modified by Uehling and Uhlenbeck to include Pauli blocking [UU33].

$$\frac{\partial}{\partial t} f + \mathbf{v}\frac{\partial}{\partial \mathbf{r}} f + \mathbf{F}\frac{\partial}{\partial \mathbf{v}} f = \int d\phi_1 \int g w(\vartheta g) d\Omega \left\{ f f_1' (1+\theta f)(1+\theta f_1) - f f_1 (1+\theta f')(1+\theta f_1') \right\} \tag{6.2}$$

The function $w(\vartheta g)d\Omega$ represents the effective cross section for a collision which changes the direction of the relative velocity g of two molecules by the angle ϑ, such that this velocity after collision g' lies within an element of solid angle $d\Omega = \sin\vartheta d\vartheta d\varphi$, where φ is the azimuthal angle about g. The subscript 1 denotes functions and variables pertaining to the second molecule in the collision, over which the integration takes place, and the primes denote functions and variables, which are taken after the collision. The differential $d\varphi$ has the form:

$$d\varphi = VG(m/h)^3 d\mathbf{r} \tag{6.3}$$

where G is an eventual weight-factor, and V is included for dimensional reasons, but is to be considered as having the value unity to agree with the meaning of f as giving the number of particles per phase cell in coordinate-momenta space of which space part has unit volume.
The factor θ accounts for the different features of the Bose-Einstein (θ=+1) and Fermi-Dirac (θ=-1) statistics. For the later it represents the Pauli principle, when two fermions cannot

occupy the same quantum-mechanical state, thus effectively lowering the collision probability. When taking $\theta = 0$ and slightly modifying the collision term [UU33], it is possible to recover the Boltzmann equation of the classical Maxwell statistics.

This extended Boltzmann equation is therefore usually known as Boltzmann-Uehling-Uhlenbeck equation (BUU), but also often referred as Vlasov-Uehling-Uhlenbeck equation (VUU). Its relativistic versions are then often known as Landau-Vlasov equation (LV) or Boltzmann-Nordheim-Vlasov equation (BNV).

The first functional BUU model was developed at Michigan State University by Bertsch, Kruse and Stöcker in order to test the conjecture that in relativistic heavy-ion collisions the pions can serve as a measure for the compressional energy and hence of the nuclear equation of state [Ber84]. Since that time different approaches became more and more refined as a result of constructive competition among different groups and many physical questions have been addressed and answered.

6.2. BUU at MSU

The model [Dan00] follows the dynamics of heavy nuclei within the Landau quasiparticle theory with its relativistic formulation [Bay76]. In this approximation, the state of a system is completely specified when the phase-space distributions $f_X = f_X(\mathbf{p},\mathbf{r},t)$ for all particles are given. The distributions satisfy the Bolzmann equation

$$\frac{\partial f_X}{\partial t} + \frac{\partial \varepsilon_X}{\partial \mathbf{p}}\frac{\partial f_X}{\partial \mathbf{r}} - \frac{\partial \varepsilon_X}{\partial \mathbf{r}}\frac{\partial f_X}{\partial \mathbf{p}} = \kappa_X^{<}\left(1 \mp f_X\right) - \kappa_X^{>} f_X \tag{6.4}$$

The l.h.s. accounts for the motion of particles in the MF, while the r.h.s. accounts for collisions. The single-particle energies ε_X are derivatives of the net energy E of a system, with respect to the particle number X:

$$\varepsilon_X(\mathbf{p},\mathbf{r},t) = \frac{(2\pi)^3}{g_X}\frac{\delta E}{\delta f(\mathbf{p},\mathbf{r},t)}, \tag{6.5}$$

where g_X is the spin degeneracy. The vector $\mathbf{v}_X = \partial\varepsilon_X/\partial\mathbf{p}$ is the velocity, while $-\partial\varepsilon_X/\partial\mathbf{r}$ is the force. The degrees of freedom in the description are nucleons, pions, deltas and N* resonances, and optionally light ($A \le 3$) clusters. The factors $\kappa^{<}$ and $\kappa^{>}$ on the r.h.s of (6.4) are the feeding and removal rates, resp..

Consistently with the Fermi Golden Rule and the requirements of covariance, the contribution of binary collisions of particle X to the removal rate in (6.4) is

$$\begin{aligned}
\kappa_X^{>}(\mathbf{p}_1) &= \frac{g_x}{\gamma_1}\int\frac{d\mathbf{p}_2}{(2\pi)^3\gamma_2}\int\frac{d\,\mathbf{p}_1^{'}}{(2\pi)^3\gamma_1^{'}}\int\frac{d\,\mathbf{p}_2^{'}}{(2\pi)^3\gamma_2^{'}}\frac{1}{2}\overline{\left|M_{2X\to 2X'}\right|^2} \\
&\times(2\pi)^3\delta(\mathbf{p}_1+\mathbf{p}_2-\mathbf{p}_1^{'}-\mathbf{p}_2^{'})2\pi\delta(\varepsilon_1+\varepsilon_2-\varepsilon_1^{'}-\varepsilon_2^{'})f_2(1-f_1^{'})(1-f_2^{'}) \\
&= \frac{g_x}{\gamma_1}\int\frac{d\mathbf{p}_2}{(2\pi)^3\gamma_2}\frac{1}{2}\int d\Omega^{*'}\frac{p^{*'2}}{4\pi^2\gamma_1^{*'}\gamma_2^{*'}v_{12}^{*'}}\overline{\left|M_{2X\to 2X'}\right|^2}f_2(1-f_1^{'})(1-f_2^{'}) \\
&= g_x\int\frac{d\mathbf{p}_2}{(2\pi)^3}\frac{1}{2}\int d\Omega^{*'}v_{12}\frac{d\sigma}{d\Omega^{*'}}f_2(1-f_1^{'})(1-f_2^{'})
\end{aligned} \tag{6.6}$$

In the above, $\overline{|M|}^2$ represents a squared invariant matrix element for scattering, averaged over initial and summed over final spin directions. The factors $\gamma = 1/\sqrt{1-v^2}$ are associated with the respective velocities and $d\mathbf{p}/\gamma$ is the invariant measure. The starred quantities in (6.6) refer to the 2-particle c.m.s. defined by vanishing of the three-momentum, $\mathbf{P}=0$, where $P=p_1+p_2$. The cross section is given by

$$\frac{d\sigma}{d\Omega^{*'}} = \frac{p^{*'2}}{4\pi^2 \gamma_1^* \gamma_2^* v_{12}^* \gamma_1^{*'} \gamma_2^{*'} v_{12}^{*'}} \overline{\left|M_{2X\to 2X'}\right|^2} \tag{6.7}$$

The relativistic relative velocity is defined through

$$\gamma_1\gamma_2 v_{12} = \left[-\frac{[(Pu_2)u_1 - (Pu_1)u_2]^2}{P^2} \right]^{1/2} \tag{6.8}$$

The above definitions ensure the standard form of the detailed-balance relation, i.e. here

$$p^{*2}\frac{d\sigma}{d\Omega^{*'}} = p^{*'2}\frac{d\sigma}{d\Omega^{*}}. \tag{6.9}$$

6.3. Most significant parameters of the model

Since this study aims at investigation of the fundamental properties of the nuclear mean field, from this perspective, the most relevant parameters of the model are those which may influence the dynamics of the mean field itself, or which may by means of accompanying processes lead to similar effects as if they would be produced solely by the virtue of the mean field.

The natural representative of the first group is the quality of the mean field, whether it is momentum dependent (i.e. nonlocal) or momentum independent (i.e. static). The second group contains the nuclear incompressibility and in-medium nucleon-nucleon cross-section, since their effects on experimental observables may be of comparable magnitude as that of mean fields nonlocality, as demonstrated for example in [Shi01].

Generally speaking, the MF dynamics follow from the dependence of the total energy on the phase-space distribution. The model adopts simple parameterizations of the net energy, such that they are sufficiently flexible with respect to the MF and the equation of state (EOS). In these parametrizations, the energy consists of the covariant volume term and the noncovariant gradient correction (E_1), isospin interaction (E_T) and Coulomb (E_{Coul}) term defined in the system frame:

$$\begin{aligned} E &= \int d\mathbf{r}\tilde{e} + E_1 + E_T + E_{Coul} \\ &= \int d\mathbf{r}\tilde{e} + \frac{a_1}{2\rho_0}\int d\mathbf{r}(\nabla\rho)^2 + \frac{a_T}{2\rho_0}\int d\mathbf{r}\rho_T^2 + \frac{1}{4\pi\varepsilon_0}\int d\mathbf{r}d\mathbf{r}'\frac{\rho_{ch}(\mathbf{r})\rho_{ch}(\mathbf{r}')}{|\mathbf{r}-\mathbf{r}'|} \end{aligned} \tag{6.10}$$

where $\tilde{e}$ is the energy density, ρ denotes the baryon density, ρ_0=0.160 fm^{-3} is the normal density and ρ_T represents the density of the third component of isospin. a_T the parameter of the isospin term, which contributes to the isospin asymmetry coefficient in the Weizsäcker

formula and gives rise to the isospin term in the optical potential. This model assumes a_I= 97 MeV, that it assures for reasonable results for the mass asymmetry and the asymmetry in the potential deduced from the scattering [Schwa82,Bec69]; a_1 is the parameter connected to the finite range of the nuclear forces and properties of the nuclear mean field and is therefore addressed in the following subsection.

6.3.1. Static and nonlocal Mean Field

As already addressed in the Section 1.1 of the Introduction to this thesis, the momentum dependence of the nuclear mean field is the essential quality necessary for proper understanding of the phenomena observed in the heavy-ion physics, with implications for astrophysics, and reaching even to the early phases of the evolution of the Universe.

Although the nonlocality of the nuclear potential has been long known since nucleon-nucleon elastic scattering experiments from late 50ties [Bet56, Wya60], its role on the evolution of the heavy-ion collision had not been well understood, or often even hoped for being negligible, since the calculations with self-consistent momentum-dependent mean field require significantly greater amount of computation time, not mentioning the obstacles of numerical solutions.

But after the critical analyses of the influence of the nonlocal mean field by Aichelin et al. [Aich87] it became obvious that honest analyses of emerging experimental results cannot neglect the effects of momentum dependence, although different observables do not necessarily yield the same sensitivity. In the present days, despite the steady progress [e.g. Dan02a], the issue of nonlocality of the nuclear mean field is not yet satisfactorily solved and the search for observables with selective sensitivity to MD properties of the nuclear mean field still continue, as is the example of this work.

Therefore also this BUU model allows for selective utilization of momentum-dependent, as well as momentum independent mean fields, so that sensitivity of chosen experimental observables can be tested.

In the energy functional E defined by eq.6.10 the quality of the MF affects the energy density $\tilde{e}$ and parameter of the gradient correction a_1.

The gradient term in the energy allows accounting for the effects of the finite range of the nuclear force together with the lowest-order quantal effects of the curvature in the wavefunctions. By the choice of MI MF the parameter a_1 is taken as a_1=21.4 MeV as corresponding to the finite range-correction from the Skyrme effective interaction and an additional Weizsäcker kinetic-energy term [Rin80]. In case of MD MF the parameter a_1 is taken as a_1=18.2 MeV, arising from the adjustment to the ground-state data performed by the code developer [Dan00].

Aside from the isospin component, the strong-interaction field from the covariant volume part is chosen as acting on baryons only, since pions or other mesons are infrequent in the energy regime where the comparison of model predictions to experiment is intended. With respect to the calculation convenience, the fields within this model are chosen such that they can be easily identified as either vector or scalar [Pan93]. Thus the nonrelativistic reduction of the energy density in the case of the ***momentum-independent fields*** is [Dan98]:

$$\tilde{e} = \sum_X g_X \int \frac{dp}{(2\pi)^3} f_X(\mathbf{p}) \sqrt{p^2 + m_X(\rho_s)} + \int_0^{\rho_s} d\rho_s' U(\rho_s') - \rho_s U(\rho_s) \tag{6.11}$$

where $m_X(\rho_s) = m_X + A_X U(\rho_s)$, A_X is the baryon number and

$$\rho_s = \sum_X g_X A_X \int \frac{d\mathbf{p}}{(2\pi)^3} \frac{m_X(\rho_s)}{\sqrt{p^2 + m_X^2(\rho_s)}} f_X(\mathbf{p}) \tag{6.12}$$

the energy density $\widetilde{e}$ (6.11) alone gives rise to single-particle energies

$$\widetilde{\varepsilon}_X(p, \rho_s) = \sqrt{p^2 + m_X^2(\rho_s)} \tag{6.12}$$

The potential

$$U(\xi) = \frac{-a\xi + b\xi^{\upsilon}}{1 + (\xi / 2.5)^{\upsilon - 1}} \tag{6.13}$$

is taken with $\xi=\rho_s/\rho_0$ and a, b and υ are adjusted to reproduce average nuclear ground-state properties. The role of the denominator in eq. (6.13) is to prevent supraluminous behavior at high densities. To energies eq. (6.12) the gradient, isospin and Coulomb corrections are added in the system frame, but they are dropped out from collision integrals and velocities,

$$\varepsilon_X = \varepsilon_X + A_X U_1 + t_{3X} U_T + Z_X \Phi \tag{6.14}$$

where $U_1=-a_1\nabla^2(\rho/\rho_0)$, $U_T=a_T\rho_T/\rho_0$, and Φ is the Coulomb potential.

The parameters of the nuclear potential a,b and v depend on the choice of the EoS, i.e. the incompressibility of the nuclear matter and are thus discussed in the next subsection 6.3.2.

Contrary to the above case, in the case the ***momentum-dependent MFs*** in their nonrelativistic reduction, is the energy density parameterized in the local frame where baryon flux vanishes [Pan93,Dan98,Hom99]:

$$\widetilde{e} = \sum_X g_X \int \frac{d\mathbf{p}}{(2\pi)^3} f_X(\mathbf{p}) \left(m_X + \int_0^p dp' v_X^*(p', \rho) \right) + \int_0^{\rho} d\rho' U(\rho') \tag{6.15}$$

where U is of the form expressed by eq. (6.13) with $\xi= \rho/\rho_0$ and the local particle velocity v_X^* depends on kinematic momentum and density

$$v_X^*(p, \xi) = \frac{p}{\sqrt{p^2 + m_X / (1 + c \frac{m_N}{m_X} \frac{A_X \xi}{(1 + \lambda p^2 / m_X^2)^2})^2}} \tag{6.16}$$

The energy (6.15) alone gives rise to the local single-particle energies

$$\widetilde{e}_X = (p, \rho) = m_X + \int_0^p dp' v_X^* + A_X \left[\rho \left\langle \int_0^{p_1} dp' \frac{\partial v}{\partial \rho} \right\rangle + U(\rho) \right] \tag{6.17}$$

where

$$\rho \left\langle \int_0^{p_1} dp' \frac{\partial v}{\partial \rho} \right\rangle = \sum_Y g_Y \int \frac{d\mathbf{p}_1}{(2\pi)^3} f_Y(\mathbf{p}_1) \int_0^{p_1} dp' \frac{\partial v_Y^*}{\partial \rho}. \tag{6.18}$$

Generally the set of parameters of (6.15) can acquire different values according to the value of the group effective mass [Jam89] in normal matter at the Fermi surface ($m^*=p^F/v^F$) and for different the incompressibility. Therefore they are discussed within the frame of the following subsection.

6.3.2. Soft and hard Equation of State

The stiffness of the equation of state of nuclear matter, ruling how volume changes with temperature and pressure, has been already for decades in the center point of the heavy-ion research. This quantity plays the crucial role in many astrophysical processes such as stability of the neutron stars, supernovae explosions or the evolution of the early Universe. The numerical value of the nuclear incompressibility K, has undergone a complicated evolution from early estimates of up to 800 MeV [Gle88] at the late seventies down to nowadays commonly accepted range of 210-380 MeV [Dan02a]. However this interval is still uncomfortably large and a common effort to further constrain this quantity continues.

In the search for more exact value of K, similar to momentum dependent case, one first usually tests the sensitivity of the chosen observable to the most extreme values of the stiffness. This is also the case of this BUU model, which takes advantage of the above described approach with very controlled Equation of State. Since two out of three parameters of eq. (6.13) are generally fixed by the requirement that in nuclear matter the total energy has a minimum at $\rho=\rho_0$ with a binding energy of app. 16 MeV/n. The "only" free parameter is hence determined by requiring a specific incompressibility. Rather than extracting the EoS from the ab initio calculation, this approach offers the opportunity to test how stiff the EoS has to be in order to reproduce the experimental data. Hence the compressibility is treated as a free parameter of the theory.

In the case of the momentum independent MFs the parameters a,b and v are determined from the requirements that $\rho=\rho_0$ at the value of e/ρ-$m_N\approx$ -16.0 MeV for incompressibility K = 210 MeV (***soft EoS***), and -17.0 MeV for K = 380 MeV (***hard EoS***).

The parameter sets resulting from adjustments are: a=187.24 MeV, b=102.62 MeV and v=1.6339 for K =210 MeV, and a=121.26 MeV, b=52.10 MeV and v=2.4624 for K =380 MeV**.**

In case of the momentum-dependent MFs, except the parameters a,b and v of eq. (6.13) one also has to evaluate the parameters c, λ, m^*/m of eq.(6.16) and fix the height of the optical potential U_{opt}^{∞} in the asymptotic case at ρ_0 when momentum $p\rightarrow\infty$, and the momentum p_0 for which the optical potential vanishes at the normal density, i.e.$U_{opt}(p_0,\rho_0)$ = 0. For more detailed discussion on how to deduce the numerical values of these parameters see [Dan98]. The values of the above parameters as used in the calculations within this work, with respect to the chosen nuclear matter EoS stiffness K, are summarized in the **Tab.6.1**.

Tab.6.1: Parameter values for the momentum-dependent mean fields.

a (MeV)	b (MeV)	v	c	λ	m^*/m (MeV)	p_0 (MeV)	U_{opt}^{∞} (MeV)	K (MeV)
209.79	69.757	1.4623	0.64570	0.95460	0.70	680	40	210
122.79	20.427	2.7059	0.64570	0.95460	0.70	685	40	380

6.3.3. In-medium reduced and free nucleon-nucleon cross sections

It is often expected, that due to fermionic nature of the nucleons, in case of the increased density during the collision the Pauli blocking may prevent scattering into already occupied state. This would effectively lower the in-medium scattering cross-sections and would cause a decrease in the collision rate [Dan00]. For this case there seems to be a supportive evidence from experiments focusing on the stopping observables, such as linear-momentum transfer, balance energy and $ERAT=E_{\perp}/E_{\parallel}$ (ratio of transverse and longitudinal energy, respectively) [Col98, Schu97, and Schn98]. However for perturbative processes, matrix elements in the cross-sections would be expected to be similar in medium to those in free-space.

On the other hand, based on specific theoretical considerations, the pion polarization effect may even enhance the in-medium cross section [Ber88, Bro89, DeJ89] and thus cause an increase of the collision rate.

Within the utilized code, it is possible to explore two types of cross sections in the medium: the free cross-sections and the cross-sections reduced in such a manner that their radii are limited by the interparticle distance,

$$\sigma = \sigma_0 \tanh(\sigma_{free} / \sigma_0) \tag{6.19}$$

where $\sigma_0=\rho^{-2/3}$. The reduction is only applied to the elastic cross sections, in order to maintain the detailed-balance relations in the medium.

6.3.4. Definition of the spectator

The important concept of spectators and participants in heavy-ion collisions was first introduced by Bowman et al. [Bow73] and later employed for the description of a wide-angle energetic particle emission by Westfall et al. [Wes76]. The two nuclei slamming against one another can be viewed as producing cylindrical cuts through each other. The swept-out nucleons or participants from projectile and target undergo a violent collision process. The remnants of the projectile and target, the spectators, continue in the meantime with almost undisturbed velocities, and are much less affected by the collision process than the participant nucleons. This picture is supported by features of the experimental data as well as by results of dynamic calculations [Gos77, Dan92, Dan95, Gait00].

In this work we adopt the original operational definition of spectator matter as introduced by Shi in [Shi01]. As a spectator is considered the matter of which the magnitude of the local longitudinal velocity exceeds half of the velocity in the initial state and of which the local density exceeds one-tenth of the normal density.

Since this definition is rather arbitrary, it may lead in some extend to an improper determination of the spectator and participating nucleons during the most violent stage of the reaction. However after the time of several tens of fm/c, when the projectile and target nuclei are already well separated, this definition assures for unambiguous identification of the greatest surviving spectator piece and comfortably allows following its subsequent dynamical evolution.

7. Experiment vs. simulations

The subject of this chapter is the direct comparison of the experimentally determined mean longitudinal velocities of the fragmentation residues with the theoretically predicted spectator response to the participant blast.

The experimental results are summarized in chapter 4, where we have intended to understand the observed features of the reacceleration of the fragmentation residues without the involvement of any prior idea or model, which would give a direct prediction of the present phenomenon, in order to identify or learn about the basic properties of the potentially responsible mechanism. The approach of chapter 7 is exactly the opposite.

The model which yielded the first prediction of the spectator response to the participants blast [Shi01, Dan00] is utilized to study the evolution of the kinematical properties of the spectator matter in the reaction systems identical to those experimentally investigated. We start with the presumption that the participants blast is responsible for any changes in the kinematical behavior of the spectator, and we use the capabilities and selected free parameters of the model to test the likelihood of the blast-response explanation under the conditions of varying incident-beam energy and the geometry of the colliding system. The aim is to reconstruct the properties of the spectator response, which would correspond to the observed features of the reacceleration. The criteria judging the authenticity of the theoretical concept are set by the experimental results.

While the BUU model is able to describe the highly non-equilibrium stages of the heavy-ion collisions, it is still limited in its single-particle description meaning that the evaporation stage of the equilibrated projectile-like fragment (i.e. the spectator) cannot be properly addressed. In other words, such model can describe the evaporation of complex clusters only in a very limited way. In connection with similar models this leads to frequent application of various coalescence approaches in order to simulate the cluster production and evaporation. Within these approaches it is assumed that the individual particles, which come together within a certain distance in the phase-space, form a cluster, and since this time on they are propagated with common space-time trajectory. But in this way the coalescence procedures do not affect the residue decay rates, and thus the limitation of such concept prevents it from being used in our case, where we want to investigate the phenomenon of a magnitude, for which any additional systematic uncertainty, brought in by a process following the one we wish to study, can have a detrimental influence.

On the other hand, evaporation from an equilibrated hot prefragment is considered to be isotropic, thus on average not influencing the kinematical properties of the cooling spectator in terms of its mean velocity or average momentum per nucleon $\langle \mathbf{p} \rangle / A$. We therefore assume, that the $\langle \mathbf{p} \rangle / A$ of the surviving spectator after the initial abrasion stage and pre-equilibrium emission will be the same as it would be after the evaporation. This makes the impact parameter, instead of the final residue mass, the relevant frame of reference, because the $\langle p_z/A \rangle$, after reaching the equilibrated stage (where the kinematical properties of the spectator do not change anymore with time), should depend only on the violence of the initial collision being ruled by the impact parameter, provided the incident-beam energy is fixed. This allows directly comparing $\langle p_z/A \rangle^{(*)}$ of the final residues measured in the experiment with the same quantity calculated for the kinematically and thermally stabilized hot prefragment, where the impact parameter provides the necessary frame of reference.

But the exact time when the hot fragment reaches the stage of complete equilibration and freeze-out may not be always easily identifiable. Gaitanos et al. [Gait00] and Shi et al. [Shi01]

(*) The quantity measured in the experiment is in fact $\langle p_z \rangle / A$, which is assumed to be equal to the quantity $\langle p_z/A \rangle$ that is calculated by the BUU model.

argue that the effective end of the collision for the system Au+Au at 600 *A* MeV for *b*=4.5 fm, resp. Sn+Sn at 800 *A* MeV for *b*=5 fm occurs around 50-60 fm/c. Even with a safe guard, the time 100 fm/c would be enough for a good separation of the spectators from the participants. However, it is desirable to follow the evolution of the spectator properties up to longer time scales (app. up to 200 fm/c) in order to see if the resulting momentum balance is sustained in the later dynamical evolution, especially with respect to the developing blast of the participating nucleons. If the whole spectator does not absorb the exchanged momentum, the spectator may lose part of its momentum and mass quickly after the collision. This would correspond to an increase and subsequent decrease in the mass and the momentum of the spectator during their time evolution, following the initial stage of the collision, i.e. for t>~50 fm/c. To a good extent, in our systems this is not the case, as can be observed in **Fig.7.1**, where both the mean mass and the net mean longitudinal momentum change per nucleon of the spectator matter decrease significantly in later stages of their time evolutions. In other words, the results of the simulations indicate that the exchanged momentum was completely assimilated by the spectators.

As an example, Fig.7.1 displays the time evolution of the mass and the change of longitudinal momentum per nucleon of the spectator produced in the reaction ^{197}Au+^{197}Au at 1 *A* GeV at various impact parameters calculated with a soft EoS, momentum-dependent mean field and in-medium reduced nucleon-nucleon elastic-scattering cross sections $\sigma_{in\text{-}med.}$.

During the initial violent stage of the reaction (t≈0-60 fm/c) the spectator matter is significantly slowed down and subsequently bounced-off. As a consequence, the net relative longitudinal momentum change generally reaches a rather stable level determined by the reaction impact parameter. On a smaller scale, one can observe that $\Delta|\langle p_z/A\rangle|$ does not fully stabilize, but also that within the considered time scale of 100-200 fm/c the deviations from the constant value play a minor role, and do not significantly influence the overall ordering of the $\Delta|\langle p_z/A\rangle|$ with respect to the impact parameter.

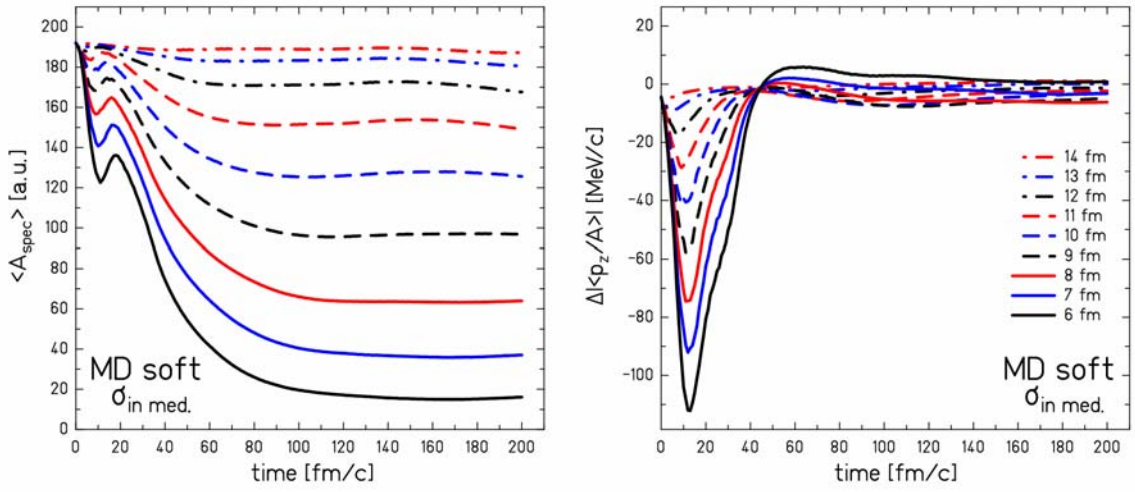

Fig.7.1: Time evolution of the mean mass $\langle A_{spec}\rangle$ (*left*) and the net mean longitudinal momentum change per nucleon (*right*) of the projectile spectator for different impact parameters in the system ^{197}Au+^{197}Au at 1 *A* GeV as calculated within the BUU model for a soft EoS with momentum-dependent mean field and in-medium reduced NN cross sections. $\Delta|\langle p_z/A\rangle|$ is given in the C.M. system.

Similar observations can be made for the case of the spectator mass and its evolution during the collision. After the initial abrasion phase, resulting in a fast mass loss and the time of spatial coexistence of both target and projectile, where the arbitrary rule of distinction between spectator and participant region is not well applicable (t≈10-30 fm/c), the spectator gradually looses mass even until the times t≈100 fm/c. This can be understood, as the

consequence of the abrasion process and the participant blast, when the strength of the explosion can practically blow away outer parts of the formed, not yet dynamically stabilized spectator matter.

As a consequence, we have decided for a direct comparison with the experiment to use the calculated values of $\Delta|\langle p_z/A\rangle|$ averaged over the time t=100-150 fm/c, which reflects the average properties of the spectator matter after the dynamical stabilization and damping out of the blast.

The figures displaying the time evolution of $\Delta|\langle p_z/A\rangle|$ and the mean mass of the spectator matter $\langle A_{spec}\rangle$ and their dependence on the impact parameter for all different equations of state can be found in the App.D.

7.1. ^{197}Au+^{197}Au at 1 *A* GeV

Fig.7.2 displays the measured net mean longitudinal-momentum change per nucleon $\Delta|\langle p_z/A\rangle|$ of the spectator residues, and its calculated analog for the surviving spectator matter in the reaction ^{197}Au+^{197}Au at 1 *A* GeV, as the function of the impact parameter in the center-of-mass reference frame, which in case of the experimental data is the best estimate of the reaction impact parameter as discussed in chap.5. The calculated results were obtained using a soft and hard EoS with a static potential and a soft and hard EoS with a momentum-dependent mean field (MD) combined with either in-medium reduced (*left*) or free nucleon-nucleon elastic cross sections (*right*).

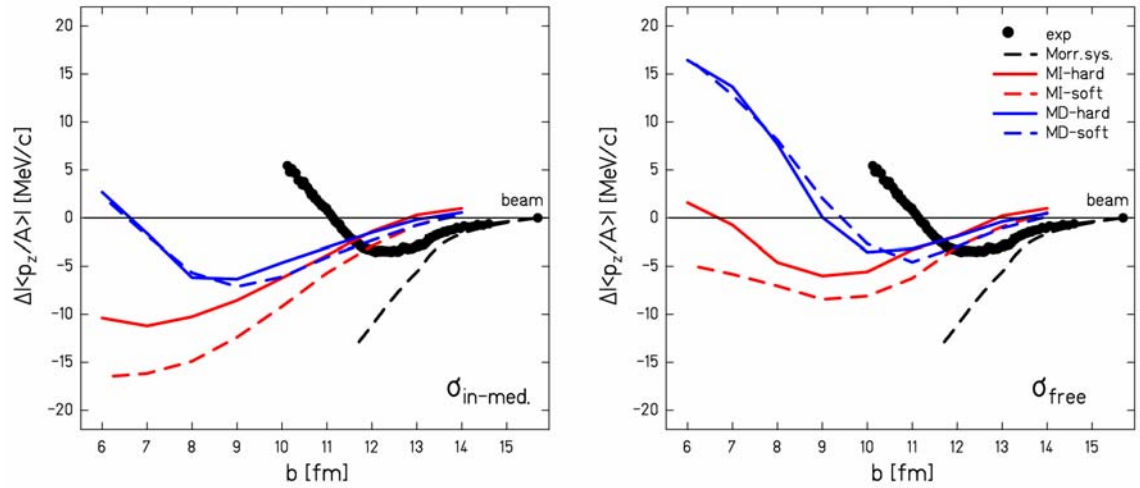

Fig.7.2: Comparison of the experimental and the calculated $\Delta|\langle p_z/A\rangle|$ of projectile-like residues with respect to the impact parameter in the system ^{197}Au+^{197}Au at 1 *A* GeV. $\Delta|\langle p_z/A\rangle|$ is given in the C.M. system. The calculated values were obtained with the BUU model [Dan00] with use of a soft and a hard EoS with a static (MI) or momentum dependent (MD) mean field, and in-medium reduced (*left*) or free (*right*) nucleon-nucleon elastic cross sections. In case of the experimental data the impact parameter *b* is the best estimate of the reaction impact parameter as discussed in chap.5.

7.1.1. Data comparison to calculations with $\sigma_{in\text{-}med}$

Comparing the experimental data with the results of the calculations, we first focus on the left plot of Fig.7.2 and the experimental results. Given by the correlation of the impact parameter and the final residue mass deduced in chap.5, we see that the considered fragments within the mass range A_{res}=60-197 are produced in the mean impact parameter range of $\langle b\rangle$≈10-16 fm. This gives evidence of, indeed, very peripheral collisions. In terms of the

simple geometrical abrasion picture this means that at $b \approx 10$ fm the average number of the abraded nucleons is about 30 (other are subsequently lost, presumably due to the evaporation or break-up), producing the participant zone of only about 60 nucleons, as displayed in **Fig.7.3**. The slowest fragments with mass $A_{res} \approx 135$ are produced on average at $\langle b \rangle \approx 12.5$ fm. This in terms of the simple geometrical abrasion picture means about 5 abraded nucleons producing a participant zone of app. 10 nucleons.

Investigating now the results of the theoretical calculations in Fig.7.2 (*left*), one immediately sees the splitting of the results according to the utilized mean field, i.e. whether momentum-dependent or momentum-independent MF has been used. The stiffness of the EoS does not play such a significant role. Also in case of these particular calculations, which are an extension of the original work of Shi et al. [Shi01], only the use of the momentum-dependent mean field can yield such a recovery of the spectator-residue momentum per nucleon, that the values greater than those before the collision are reached. This fact served as the main argument for interpreting the reacceleration of fragmentation residues in [Ric03] as the spectator response to the participant blast in [Shi01].

However, the current possibility to directly compare the experimental results and the theoretical predictions as a function of the impact parameter sheds new light on this physical phenomenon. Looking at the left part of the Fig.7.2, although the overall shape and magnitude of the spectator response seem to yield significant similarities, the disagreement with respect to the impact parameter is rather surprising. One observes a significant discrepancy in terms of the magnitude of the effect with respect to the impact parameter. The recovery of the velocities starts in the experiment on the average in reactions with around 4 fm larger impact parameter than in the simulations.

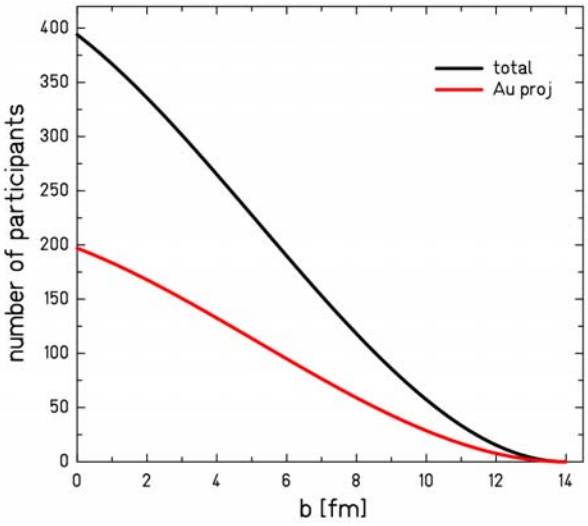

Fig.7.3: Total number of participants and those arising from the projectile as a function of the impact parameter in the reaction ^{197}Au+^{197}Au as calculated by the geometrical model [Mor78].

Certainly one can argue that the method applied only determines the mean impact parameter, while a specific residue with a certain mass can be produced in a wide range of impact parameters. But according to the investigation of the possible systematic error of this method carried out in [Hub91] and already discussed in chap.5, the results point to the spread of app. ± 1 fm, which is far less than the observed discrepancy. Also, despite the high number of test particles and independent runs, the statistical fluctuations of the calculations contribute with a statistical error of the order of 1-3 MeV/c depending on the impact. An additional systematic error is introduced by averaging $\Delta|\langle p_z/A \rangle|$ over a time period of 50 fm as discussed above and demonstrated in Fig.7.1.

However, this altogether cannot explain the significant deviation of the trends of the experimental and the calculated results, and rather points to the used physical assumptions as a source of the disagreement. Therefore, in the spirit of the interpretation of the spectator response in [Shi01], where the increase in relative momentum with the impact parameter for MD calculations is attributed to the "*strong enough explosion, when the ordered push may overcome the friction effects, producing a net longitudinal acceleration*", we have to search for the key parameters of the model responsible for the strength of the response in order to explore possible uncertainties of the theoretical description.

7.1.2. Data comparison to calculations with σ_{free}

A natural candidate for a parameter which may result in a significant enhancement of the strength of the participant's explosion arises already from the original work of Shi [Shi01], namely the free nucleon-nucleon elastic-scattering cross sections σ_{free}. Although the first calculations with σ_{free} by Shi were carried out only for b=5 fm, they revealed a significant increase in the spectator response. This has been understood in a way, that "… *because of higher cross sections, the equilibration is faster, which allows the participant to explode more violently when the spectators are still nearby.*" [Shi01].

Therefore, we performed identical calculations using MI and MD mean fields in combination with hard and soft EoS but this time with σ_{free}. The results of these calculations compared to the experimental values are displayed in the right subset of **Fig.7.2**.

It can immediately be seen that the theoretically predicted spectator response keeps similar features as for the case of $\sigma_{in\text{-}med.}$, especially with respect to a rather weak sensitivity to the stiffness of the EoS. But, the condition that a MD mean field is necessary to induce recovery of relative longitudinal momentum and producing net acceleration effect does not seem to be valid anymore. It is observed that even MI MFs can, for low impact parameters, lead to the net acceleration, producing the effect of the similar magnitude as MD MFs with $\sigma_{in\text{-}med.}$. This means that momentum dependence itself is not the exclusive cause of the effect responsible for the reacceleration of the fragmentation residues, but rather significantly contributes to conditions allowing for such process.

Generally the spectator response is significantly stronger with the σ_{free}, and comes much closer to the data than with $\sigma_{in\text{-}med.}$. In the case of σ_{free} and MD MFs the net relative longitudinal momentum change reaches its minimum at $\langle b \rangle \approx$ 10-11 fm and the region of the positive values at $\langle b \rangle \approx$ 9-9.5 fm, where it basically copies the trend of the data with a negative offset of $\approx$ 2 fm. But even though it is considerably smaller, the discrepancy of data and theory with respect to the impact parameter still prevails.

Before coming to any conclusions concerning the spectator response to the participants blast in the system ^{197}Au+^{197}Au at 1 A GeV, let us briefly discuss arguments for the use of in-medium reduced or free NN cross sections

It is often expected, that due to fermionic nature of the nucleons, in case of the increased density during the collision the Pauli blocking may prevent scattering into already occupied state. This would effectively lower the in-medium scattering cross-sections and would cause a decrease in the collision rate [Dan00]. For this case there seems to be a supportive evidence from experiments focusing on the stopping observables, such as linear-momentum transfer, balance energy and $ERAT=E_{\perp}/E_{\parallel}$ (ratio of transverse and longitudinal energy, respectively) [Col98, Schu97, and Schn98].

On the other hand, based on specific theoretical considerations, the medium modification of exchange virtual pions may even enhance the in-medium cross section [Ber88, Bro89, DeJ89] and thus cause an increase of the collision rate. Such an increase of $\sigma_{in\text{-}med.}$ could conceivably yield a better description of the data presented in the current work.

In case of low densities and high beam energies, $\sigma_{in\text{-}med.}$ should be very similar to σ_{free} [Dan00]. Taking into account the high impact parameter in which the fragments, studied in our work, seem to be produced and consequently the low number of directly abraded nucleons, one would not expect such a density build-up as in the central or semi-central collisions.

In order to better demonstrate the effects of the different NN cross sections, the left subset of **Fig. 7.4** displays the difference of the mean spectator mass calculated for the soft MD EoS with $\sigma_{in\text{-}med.}$ and σ_{free} for the system ^{197}Au+^{197}Au at 1 A GeV.

During the initial phase of the reaction (t≈10-30 fm/c), the abrasion results in slightly more abraded nucleons for σ_{free} than for the case calculated with $\sigma_{in\text{-}med.}$. As seen from the figure, projectile (as well as target) nuclei loose up to 5 nucleons more in favor of the participant region, when σ_{free} is assumed. This on one hand leads to proportionally higher excitation energy of the projectile remnant (i.e. spectator), and on the other to an increased number of the participating nucleons, allowing for a stronger participant blast.

Following the evolution of the mass difference to later times, one can observe gradually increasing difference of the spectator masses produced by either of two NN cross sections used, which saturates around t≈150 fm/c. This mass difference scales with the impact parameter, however reaches its maximum for b = 9 fm. This is understandable, since if the impact parameter is too low, the dynamic effects of the collision are so destructive, that in case of both kinds of cross sections, it is sufficient to lead to a survival of only a minor spectator piece (see also Fig.7.1 right). However, the slope of the mass difference in the early time t≈50 fm/c increases monotonically with the decreasing impact parameter, indicating generally faster and more violent evolution of the collision process.

The situation is similar in the case of hard MD Eos or when MI mean field is used. However, the momentum dependence enhances the effects of σ_{free} with respect to the momentum independent calculations (see App. D).

The question remains, whether the greater mass loss in case of σ_{free} calculations is the direct result of the stronger participant blast blowing away the outer parts of the spectator, or is it the consequence of generally more extensive abrasion, leading to higher excitation energies, thus allowing for a rapid emission of some outer nucleons, before reaching thermal equilibration?

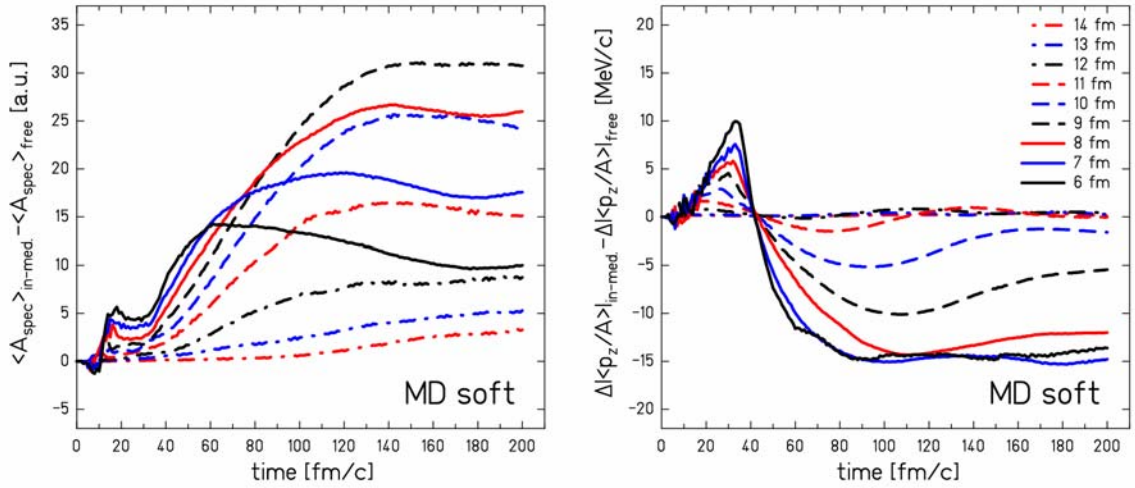

Fig.7.4: *Left:* Time evolution of the difference of the mean mass of the spectator matter and its dependence on the impact parameter calculated for soft MD EoS same system as in the left figure. with $\sigma_{in\text{-}med}$ and σ_{free} for the system ^{197}Au+^{197}Au at 1 A GeV. *Right:* Time evolution of the difference of mean $\Delta|\langle p_z/A\rangle|$ and its dependence on the impact parameter calculated for soft MD EoS with $\sigma_{in\text{-}med}$ and σ_{free} for the same system as in the left plot.

Some additional insight can be brought in by investigating the difference of $\Delta|\langle p_z/A\rangle|$ calculated for soft MD EoS with c, and how this difference evolves during the course of the reaction as displayed in right subset of Fig. 7.4.

When comparing the calculations for $\sigma_{in\text{-}med}$ and σ_{free}, one can observe that within the statistical fluctuations the results above $\langle b\rangle$=11 fm are practically the same, which is however not the case when comparing the masses of the hot spectator in the left plot. In other words, above $\langle b\rangle$=11 the momentum of the surviving spectator does not depend on the magnitude of

the cross sections used, but its mass does. For the case of b=11 fm, although the momentum difference is negligible, the mass difference at times $t \geq 100$ fm/c is around 15 units, which is hard to imagine as being the consequence of abrasion of only one more nucleon, at times $t \approx$10-30 fm/c, with respect to the in-medium reduced NN cross section scenario, as can be seen in the left plot of Fig.7.4. Contrary to that, for b=9 fm, the mass difference of the surviving spectator is around 30 nucleons, while 2 of them were directly abraded, and the difference in $\Delta|\langle p_z/A \rangle|$ is already by 10 MeV/c higher for the calculations with σ_{free}.

Therefore, it seems that the higher mass loss in the case of the calculations with σ_{free} is not monotonously related to a higher relative momentum gain. Also the difference of $\Delta|\langle p_z/A \rangle|$ seems to be independent from the choice of the cross sections below a certain value of the impact parameter, in this case for $b \leq$ 8fm. This points to two qualitatively different processes in the range of 8 fm $\leq b \leq$ 11 fm, implicating that generally higher σ_{free} allow for the onset of the process responsible for a spectator relative momentum recovery at higher impact parameters (already for $b \leq$11 fm) while $\sigma_{in\text{-}med}$ first at $b \leq$ 8fm. At this place it is worth to remind that according to the geometrical model (see Fig.7.3), the participant region should in the system ^{197}Au+^{197}Au colliding at an impact parameter b=8 fm, resp. b=11 fm, consist of app. 120 nucleons, resp. app. 30 nucleons, while at the mean impact parameter $\langle b \rangle$=12.5 where the experimental momenta start to recover it's only 10 nucleons.

The more general features of the results in Fig.7.4 can be within the frame of the used BUU model interpreted that, for $b >$ 11 fm a density at which the Pauli blocking could effectively prevent any nucleon-nucleon scattering was not reached, and the participants blast, if developed at all, remains effectively the same in calculations with both kinds of NN cross sections. However, the course of the calculated $\Delta|\langle p_z/A \rangle|$ at lower impact parameters signals, that the magnitude of the nucleon-nucleon cross-sections plays a significant role in the evolution of the whole colliding system.

Also the low sensitivity of the results with respect to the stiffness of the EoS for all investigated impact parameters supports the idea that the densities reached in our experiments were not high enough, to create a chance for different compressibilities to manifest themselves.

The fact, that heavy fragmentation residues are produced in collisions with rather low density build-up may seem as a drawback for the results which aim at contributing to the understanding of the properties of nuclear matter under extreme conditions. However, in contrast to experiments where high densities and temperatures are reached, the conditions ruling the reacceleration phenomenon seem to be purer and from this point of view also well controlled. According to the utilized model, to a great extent they do not yield, in the experimentally accessible impact parameter range, any additional strong dependence on problematically evaluable quantities such as density and compressibility, however, the extrapolation to region of lower b may still guide our understanding of the involved processes.

On the other hand, a new sensitivity to the magnitude of the NN cross-sections arose. This then means a shift of our main attention from disentangling the stiffness of the EoS from the nonlocal features of the nuclear potential rather to the separation of the latter from the effects of the magnitude of the NN cross section. This then affects our ability to draw more conclusive results concerning eventually specific aspects of the nonlocality of the nuclear mean field or the process in which it is revealed, which may be possible, if at all, only with additional experimental as well as theoretical investigation, e.g. exploring the dependence of the spectator response on the incident-beam energy or geometry of the colliding system.

7.2. ^{197}Au+^{197}Au at 500 *A* MeV

The investigation of the spectator response with respect to the incident beam energy is a natural evolution of this study. It is the most fundamental property of the nonlocality of the nuclear potential (and thus nuclear mean field) to "adapt" its depth according to the momentum of the incoming particle. As a consequence, the strength of the repulsiveness or attractiveness of the mean field seen by the entering particle varies with respect to its momentum. Thus, during the heavy-ion collision the forces acting against the compression of the nuclei and ruling the explosion of the participant zone may be different for different beam energies.

In the case of system ^{197}Au+^{197}Au at 500 *A* MeV one would expect less repulsive mean field. This may result in a generally greater density build up which, however, should not fully compensate the limitation by the smaller energy brought to the collision zone by the projectile. On the other hand, the smaller momentum means also smaller relative velocity of the colliding ions, meaning longer time of exposition of the spectator to the developing blast, thus possibly being able to acquire a greater push. However, with less energy the resulting blast should still be generally weaker than in the case of the 1 *A* GeV system.

Fig.7.5 displays the measured net mean longitudinal momentum change per nucleon of the fragmentation residues $\Delta|\langle p_z/A\rangle|$, and its calculated analog for the surviving spectator matter in the reaction ^{197}Au+^{197}Au at 500 *A* MeV, as the function of the impact parameter, which in case of the experimental data is the best estimate of the reaction impact parameter as discussed in chap.5. The calculated results were obtained using soft and hard EoS with a static potential and soft and hard EoS with a momentum-dependent mean field (MD) combined with either in-medium reduced (left subset of Fig.7.5) or free nucleon-nucleon elastic-scattering cross sections (right subset of Fig.7.5).

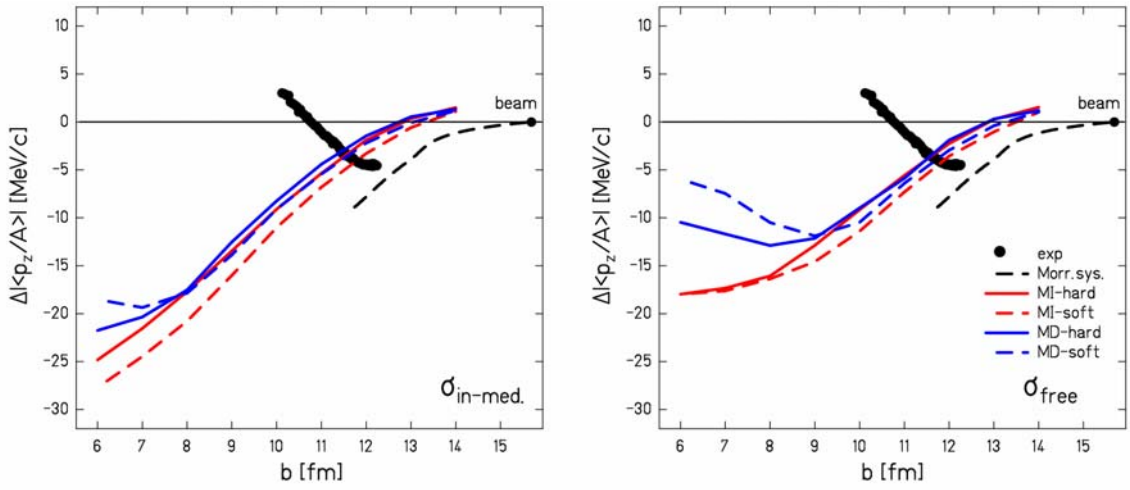

Fig.7.5: Comparison of the experimental and calculated mean longitudinal momentum change of the projectile-like residues with respect to impact parameter in the system ^{197}Au+^{197}Au at 500 *A* GeV. The longitudinal-momentum change is given in the C.M. system. The calculated values were obtained with the BUU model [Dan00] using soft and hard EoS with static (MI) or momentum dependent (MD) mean field, and in-medium reduced (left) or free (right) nucleon-nucleon cross sections. In case of the experimental data the impact parameter *b* is the best estimate of the reaction impact parameter as discussed in chap.5.

7.2.1. Data comparison to calculations with $\sigma_{in\text{-}med}$

Also in case of the system ^{197}Au+^{197}Au at 500 *A* GeV the attention will be first directed to the comparison of the experimental data with the results of the calculations obtained with $\sigma_{in\text{-}med}$ as displayed in the left subset of Fig.7.6. The used correlation of the fragment mass A_{frag} and the mean impact parameter $\langle b \rangle$ is the same as for the higher-energy system, but, with respect to the previous one, the mass range with available data is limited to A_{frag}=60-130 for reasons discussed in Chap.4. The extrapolation of the data to the higher masses, i.e. higher impact parameters, is expected follow the displayed Morrissey systematic as also arises from the discussion in the same chapter.

Since the measured mean net longitudinal-momentum change per nucleon $\Delta|\langle p_z/A \rangle|$of the fragmentation residue is in absolute scale very similar to the one measured in the experiment with the higher energy, the location of the minimum and the cross-over to the positive values is, with respect to the impact parameter, practically the same in both experiments. Therefore, the estimates of the number of the participating nucleons based on the simple geometrical model presented at the beginning of chap.7.1.1 and in Fig.7.3 are valid also for this reaction system.

However, in a great contrast to the almost identical course of the experimental data are the results of the BUU calculations, which significantly deviate from the data both in the absolute scale as in the overall trend for all four equations of state used. It seems like if the calculated results simply follow the extrapolated course of the Morrissey systematic with a constant offset, which on the other hand is only several MeV/c and thus still within the systematic error. Moreover, most of the pronounced features of the calculations for the higher-energy system seem to be lost. The results do not yield any significant sensitivity to the stiffness of the EoS neither to the choice of the MF. Only for the smallest impact parameters one can observe some signs of a possible recovery, yet in its magnitude far away from the one observed in Fig.7.2 (*left*).

The process or quality of the nuclear matter responsible in the model for reacceleration of the projectile remnants significantly depends on the incident energy, which is in strong contrast to the experimental observations summarized in chap.4.3, where only a small dependence on the energy brought to the participant zone is observed.

In order to try to learn more about the differences in the dynamical evolution of the two identical systems differing only by the incident-beam energy, the time evolution of the projectile remnant mass and its net longitudinal momentum change per nucleon for both systems is compared in **Fig.7.6**, where the results of the calculations with soft EoS and MD MF are shown for various impact parameters.

It follows from the left subset of Fig.7.6 that the collision of the two identical systems at the same impact parameter leads to a significantly lower mass loss in case of the lower incident beam energy. The highest pace of the growing mass-loss difference is in the initial phase of the reaction (t≈20-40 fm/c), but to a certain extent still evolves at later times. Particularly interesting is the evolution of this difference for the lowest considered impact parameters, where the lower-energy system even seems to catch-up with the mass loss suffered in the higher-energy system. This means that although the process responsible for losing the mass of the spectator can yield a comparably similar effect in both systems, for the lowest impact parameters in the higher incident-beam energy system it develops much faster. It may be interesting to recall that this concerns exactly those impact parameters for which in the calculations with 1 *A* GeV beam a recovery of the relative longitudinal momentum is observed.

In any case a very important revelation seems to be the fact that the calculations do not fully support the concept of the spectator-participant model of the reaction as being independent from the energy, and, according to the calculations, the deviation from such ideal

case in the range of the impact parameters accessible by means of the heavy fragmentation products investigated in the experiment is not negligible. For the impact parameter of 11 fm it accounts for approximately 15 nucleons, which with the help of Fig.4.7 can be around mass $A_{frag}\approx 80$ roughly translated into the difference of $\langle v_z\rangle\approx 0.07$ cm/ns what is even a bit more than the observed difference between the measured mean velocities. If that were acceptable for explaining the difference in the experimental data, there would not be many possibilities for any influence of the varying energy invested to the participant zone.

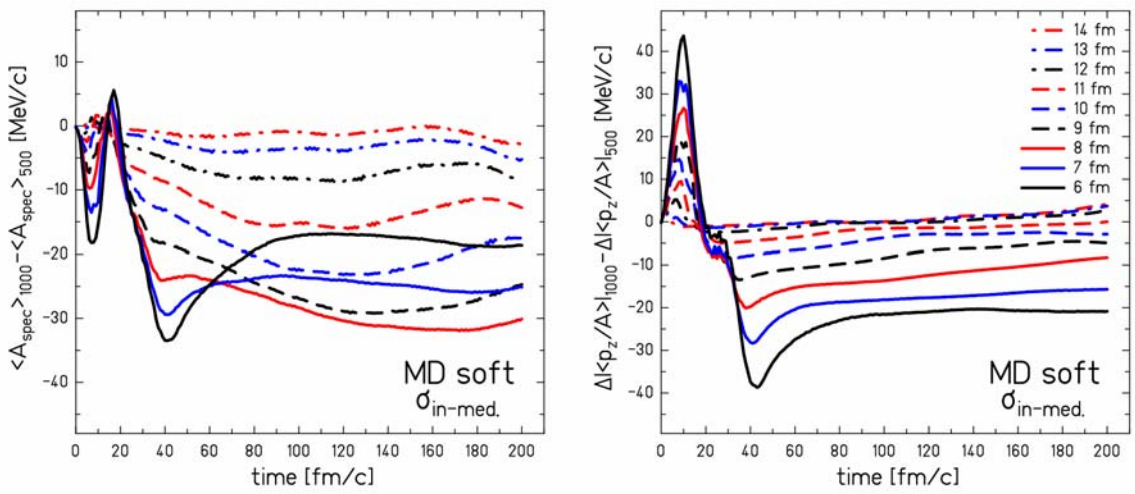

Fig.7.6: *Left:* Time evolution of the difference of the mean mass of the spectator matter and its dependence on the impact parameter calculated for soft MD EoS with $\sigma_{in\text{-}med}$ for the systems ^{197}Au+^{197}Au at 1 A GeV and ^{197}Au+^{197}Au at 500 A MeV. *Right:* Time evolution of the difference of $\Delta|\langle p_z/A\rangle|$ and its dependence on the impact parameter calculated for the same two systems as the left figure.

However, the calculations show a significant difference in $\Delta|\langle p_z/A\rangle|$ between the two considered systems. Most of it is a direct result of the initial collision phase, but while it, to some extent, evolves in the later times as well, it still stabilizes earlier than the difference of the masses. Moreover, the difference in $\Delta|\langle p_z/A\rangle|$ grows monotonically with decreasing impact parameter in contrary to the difference in spectator mass. This once more suggests that the mass and the relative longitudinal momentum of the spectator matter are not directly coupled in the process.

The situation described above is similar for hard MD EoS or when MI mean field is used. But, while the different stiffness of the nuclear matter yields results differing in the same way, the difference in mass loss as well as in the relative longitudinal momentum change is twice as large with MD MFs then with the momentum-independent ones, as can be seen in the full set of figures in App.D.

7.2.2. Data comparison to calculations with σ_{free}

Looking at the right subset of Fig.7.5, we can observe that neither the calculations with the free nucleon-nucleon elastic-scattering cross sections result in any clearly visible agreement with the data. But, there is still a significant difference with respect to the calculations discussed in the previous section, i.e. those with the in-medium reduced nucleon-nucleon elastic-scattering cross-sections. In the present case, at least the results of calculations with the MD MFs are leading to a partial recovery of the relative longitudinal momentum. In this region of low impact parameters ($b\leq 9$) the sensitivity to the nonlocal properties of the nuclear mean field is restored. But for the higher impact parameters neither the stiffness nor

the choice of the mean field play any significant role, and all calculations give similar results, copying the trend of the Morrissey systematic with practically constant offset.

It seems that the role of the higher nucleon-nucleon cross sections for the onset of the spectator response which was observed for the system with 1 *A* GeV beam is preserved despite the drop in the energy which can be delivered to the participant region. In order to better evaluate the significance of the different cross sections in the collision with the lower incident-beam energy, **Fig.7.7** displays the comparison of the spectator mass and the net relative longitudinal momentum change in time calculated for system ^{197}Au+^{197}Au at 500 *A* MeV with soft equation of state and momentum-dependent mean field using both sets of discussed nucleon-nucleon cross-sections.

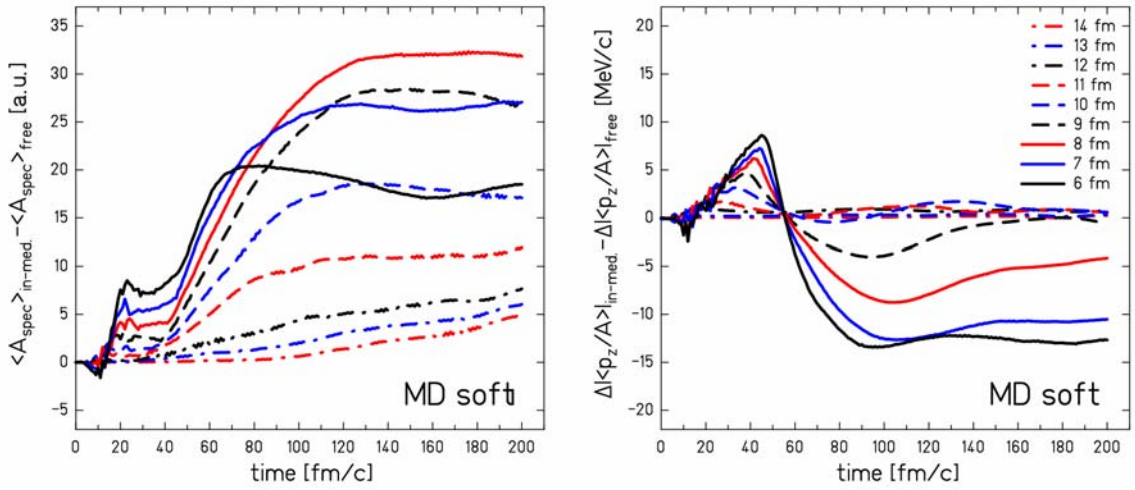

Fig.7.7: *Left:* Time evolution of the difference of the mean mass of the spectator matter and its dependence on the impact parameter calculated for soft MD EoS with $\sigma_{in\text{-}med}$ and σ_{free} for the system ^{197}Au+^{197}Au at 500 *A* MeV. *Right:* Time evolution of the difference of $\Delta|\langle p_z/A\rangle|$ and its dependence on the impact parameter calculated for soft MD EoS with $\sigma_{in\text{-}med}$ and σ_{free} for the same system as in the left figure.

The above figure is the analog of Fig.7.4 with the only difference being the incident-beam energy. Therefore, it is possible to analyze the features of the results in the lower-energy case in a similar way as of the higher-energy system in chap.7.1.2, and compare the mutual similarities of the two sets of results.

The left subset of Fig.7.7 again reveals that σ_{free} lead to a greater mass loss already during the abrasion phase of the reaction (t≈10-30 fm/c), yet this time the lower-beam energy slightly enhances the effect with respect to the higher-energy case (compare to Fig.7.4). This on the other hand should lead to an increased excitation energy caused by the abrasion, leading possibly in the end to a greater mass loss. The consequence of the more effective abrasion is an extra donation of nucleons to the participant zone enhancing the eventual blast.

But this does not seem to be the case, not with the respect to the higher-energy system. In case of the 500 *A* MeV beam the mass difference between two calculations with different cross sections increases rapidly after the initial abrasion phase, in favor calculations with σ_{free} saturating, in time t≈100-150 fm/c depending on the impact parameter. This is in qualitative agreement with calculations for 1 *A* GeV beam, but there is a quantitative difference (compare to Fig.7.4). Sorting the results by the impact parameter we observe that the greatest influence of the choice of the NN cross sections is for b=8 fm, while in the higher energy case it was already observed for b=9 fm. This corresponds to the result followed from discussion on Fig.7.6 which can be further extended, since the lower incident-beam energy leads generally to smaller mass loss, the region of partial "cross-section equivalency". Here the dynamic effects of the collision are so destructive, that in case of both kinds of NN cross sections, it is

enough to lead to a survival of only a minor piece, is reached in lower impact parameters, i.e. for b<8 fm where the difference in the spectator mass decreases with respect to the selection of the NN cross sections used.

This, however, means that the complete mass loss cannot be predetermined just by the abrasion phase, which is in case of σ_{free} more effective with respect to $\sigma_{in\text{-}med}$ in the lower incident-beam energy than in the system with 1 A GeV beam. This may again point to the role of the blast responsible for a great portion of the spectator mass-loss, probably by blowing parts of it away.

Shifting now the attention to the right subset of the Fig.7.7 we can observe the difference in evolution of the net longitudinal momentum change per nucleon as the result of the different NN cross-sections used in the calculations. Again in analogy to the results displayed in Fig.7.4 in case of the 1 A GeV system, the qualitative effects caused by the choice of the NN cross-sections is similar in the lower incident-beam energy, but a difference occurs when comparing the results quantitatively. The choice of the cross sections does not play any significant role until a certain impact parameter, this time it is b≈9 fm, while for the high-energy beam it is b≈11 fm, where the calculations with σ_{free} lead to a deviation from the trend set by the calculations with $\sigma_{in\text{-}med}$. However, the difference growing with the impact parameter saturates around b≈7 fm, while in the 1 A GeV case it was around b≈8 fm. Moreover, interestingly enough, it saturates at the same magnitude of the difference in $\Delta|\langle p_z/A\rangle|$ as in the higher-energy case, namely at ~ -15 MeV/c.

We can therefore speak again about two qualitatively different processes in the range of 7 fm ≤ b ≤ 9 fm, in which only the σ_{free} can induce some process leading to at least a partial recovery of the longitudinal spectator momentum per nucleon, while with $\sigma_{in\text{-}med}$ is the similar process induced first at b≈7 fm. Once this process is "turned on", it seems to have qualitatively and to great extent also quantitatively the same recovering influence on the longitudinal momentum per nucleon despite the different NN cross sections or the energy invested to the participant zone.

In other words, dynamical effects enhanced by the increase in invested energy in form of the higher incident-beam energy or by the more violent abrasion phase of the reaction due to the generally higher σ_{free} seem to influence only the onset of the relative-momentum recovering process, but not the process itself.

If the conclusion of the last paragraph is true, the naturally arising question is what can change the strength of the recovering process, and what and where is its source of energy if it can stay out of the reach, when varying the energy deposition to the participant zone by the change of the incident-beam energy, and even the dynamics of the blast through the choice of the NN cross sections?

In our opinion, this question points to the spectator itself, since it is the matter which is not directly "in-line of fire" in the initial reaction phase, thus not significantly influenced by the varying energy of the incident beam, neither by the magnitude of the NN cross-sections, since the slightly higher number of the abraded nucleons can be, with respect to the magnitude of the following mass-losses, probably neglected. In addition, it manages its own pool of energy acquired by the excitation during the abrasion and the initial interaction phase.

Provided the process responsible for the spectator longitudinal momentum per nucleon is basically only triggered faster by the choice of the different NN cross sections then the differences between the effects of the cross-section choice with respect to the varying incident-beam energy should be the same. The influence of $\sigma_{in\text{-}med}$ with respect to the changing incident-beam energy has been displayed in Fig.7.6 and discussed in the previous chapter. The influence of the beam energy in the case of σ_{free} is displayed in **Fig.7.8**.

At the first sight both figures look very similar. Especially the differences in $\Delta|\langle p_z/A\rangle|$ displayed in the right subsets look very much the same in Fig.7.6 as well as in Fig.7.8, despite

the significantly different behaviors and magnitudes of the individual $\Delta|\langle p_z/A\rangle|$ displayed for MD soft equation of state in Fig.7.2 and 7.5. We can just recall the results of the calculations for 500 *A* MeV system where with $\sigma_{in\text{-}med}$ almost no recovery of the relative momentum occurs at all, and that for σ_{free} and the 1 *A* GeV system the recovery and even reacceleration can be observed in quite different range of the impact parameters than in its counterpart with $\sigma_{in\text{-}med}$. This is an explicit support for the above statements concerning the independency of process responsible for the recovery of the net relative longitudinal momentum of the spectator on the magnitude of the NN cross-sections used in the calculations.

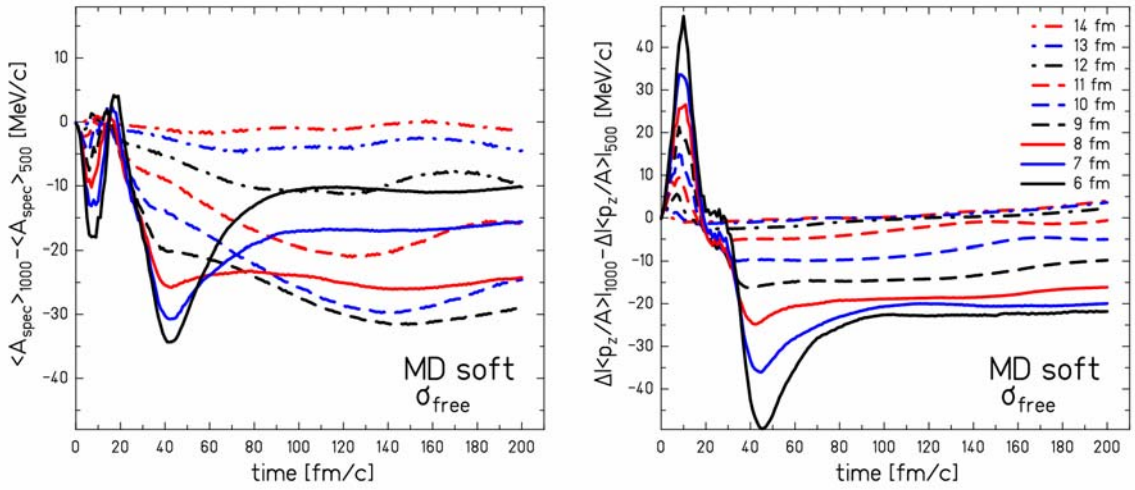

Fig.7.8: *Left:* Time evolution of the difference of the mean mass of the spectator matter and its dependence on the impact parameter calculated for soft MD EoS with σ_{free} for the systems ^{197}Au+^{197}Au at 1 *A* GeV and ^{197}Au+^{197}Au at 500 *A* MeV. *Right:* Time evolution of the difference of $\Delta|\langle p_z/A\rangle|$ and its dependence on the impact parameter calculated with σ_{free} for the same two systems as the left figure.

Concerning the difference in the spectator masses, the left subset of Fig.7.8 is also in qualitative agreement with its counterpart for $\sigma_{in\text{-}med}$ in Fig.7.6. But by quantitative measures the effect of σ_{free} leading to generally higher mass losses seems to be more enhanced by the increase of the incident-beam energy. This yet again points to at least partial independence of the pace of the spectator mass-loss and the evolution of its relative longitudinal momentum.

An immediately arising question is whether the observed spectator-mass dependency on energy invested to the participant zone and the magnitude of the NN cross-sections is in accord to the idea of the spectator being self-responsible for its own momentum recovery, although that still may be triggered by the impulse of the blast. In our opinion, the answer is yes, provided the additional mass-loss caused by either the higher incident-beam energy or the higher NN cross-sections does not change the relative energy of the spectator which may be available for the momentum-recovery process. This point will be discussed in more detail later.

Turning now the attention back to the beginning of this chapter and particularly to Fig.7.5 we realize, that even though the visible disagreement of the experiment and calculations was not very encouraging, the possibility to compare the results for the two identical systems with varying incident-beam energy made the true difference. As the result of the analyses of the BUU calculations for both systems using σ_{free} we could lay down the ground for a principally new concept of the spectator response to the participants blast which already yields first interesting qualitative similarities to the experimental features summarized in chap.4.3. However, before advancing to the final discussion, keeping also in mind the possible implications of the new concept of the spectator response for the nuclear equation of state, the

last investigated system will be revised and analyzed by means of the transport code calculations constrained by the experimental data.

7.3. ^{197}Au+^{27}Al at 500 *A* MeV

Fig.7.9 displays the measured net mean longitudinal momentum change per nucleon $\Delta|\langle p_z/A\rangle|$ of the fragmentation residue, and its calculated analog for the surviving spectator matter in the system ^{197}Au+^{27}Al at 500 *A* MeV, as the function of the impact parameter in the center-of-mass reference frame, which in case of the experimental data is the best estimate of the reaction impact parameter as discussed in chap.5. The calculated results were obtained with soft and hard EoS with static potential and soft and hard EoS with a momentum-dependent mean field (MD) combined with either in-medium reduced (*left*) or free nucleon-nucleon elastic-scattering cross sections (*right*).

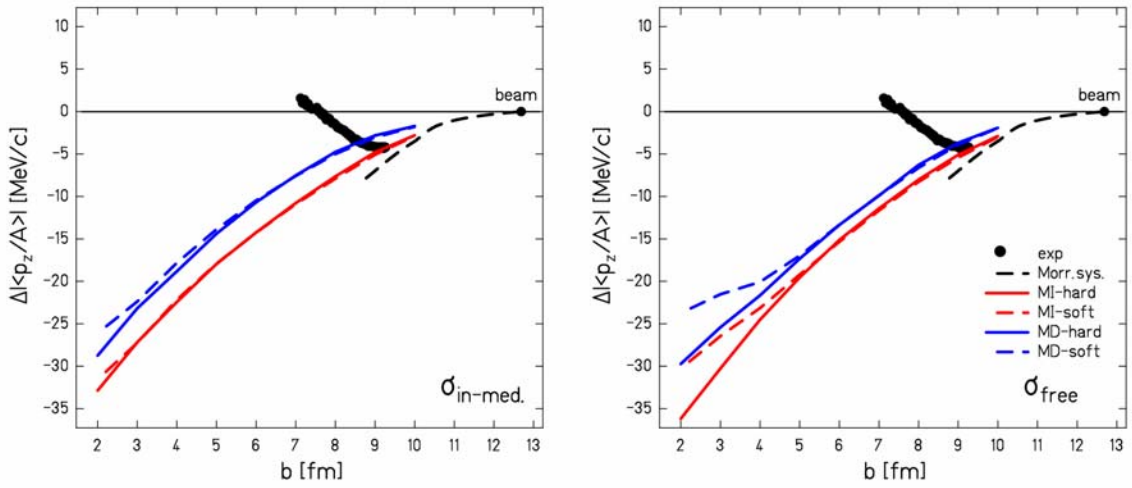

Fig.7.9: Comparison of the experimental and calculated $\Delta|\langle p_z/A\rangle|$ of the projectile like residues with respect to the impact parameter in the system ^{197}Au+^{27}Al at 500 *A* MeV. $\Delta|\langle p_z/A\rangle|$ is given in C.M. system. The calculated values were obtained with the BUU model [Dan00] using soft and hard EoS with static (MI) or momentum dependent (MD) mean field, and in-medium reduced (*left*) or free (*right*) nucleon-nucleon elastic-scattering cross sections. In case of the experimental data the impact parameter *b* is the best estimate of the reaction impact parameter as discussed in chap.5.

7.3.1. Data comparison to calculations with $\sigma_{in\text{-}med}$

In the comparison of the last experimental dataset with the results of the calculations we will follow the same line of discussion as for the two previous systems. Therefore the attention will be first devoted to the experimental results. It can be observed, that according to the utilized correlation of the mass of the fragmentation residue and the mean impact parameter determined and discussed in chap.5, the detected fragments with A_{frag}=60-145 were on average produced in the range of mean impact parameters $\langle b\rangle\approx$7.5-9.5 fm. With help of the Morrissey systematic it is possible to extrapolate the data even for the higher fragmentation residue masses and the higher impact parameters, as indicated by the dashed line and the representation of the beam projectile in the position of the maximum impact parameter, which was determined with the simple geometrical model [Mor78].

Thus, also in this system we observe that the fragments are produced in very peripheral collisions, though due to the size of the aluminum target nuclei it is possible to penetrate a bit deeper into the gold nucleus, reaching $\langle b_{A=65}\rangle/b_{max}$ ~ 58%, than if both the projectile and the

target nuclei are of the same size, reaching $\langle b_{A=65} \rangle / b_{max}$ ~ 66%. In terms of the simple geometrical abrasion picture this means that at $b \approx 7.5$ fm, i.e. at impact parameter where the mean longitudinal momenta first reach the positive values, the average number of the nucleons abraded from the gold projectile is around 14, while from the aluminum target nuclei it is only about 8 nucleons, forming thus the participant zone of 22 nucleons.

As can be deduced from **Fig.7.10**, even accounting a possible systematic error in the impact-parameter determination does not really increase the number of participating nucleons by a factor greater than two. Moreover, the number of nucleons abraded from the gold projectile is almost identical to the number of nucleons, namely 15, which would be abraded in the collision with $\langle b \rangle$~11 fm in case of the ^{197}Au+^{197}Au in order to just reach the positive values of the net relative longitudinal momentum change. In other words, according to the simple geometrical abrasion picture, the number of nucleons abraded from the gold projectile necessary for recovery of the measured relative longitudinal momentum on the same level as before the collision does not depend on the size of the target nuclei. Thus it does not seem to depend on the size of the participant zone and the strength of the potential blast.

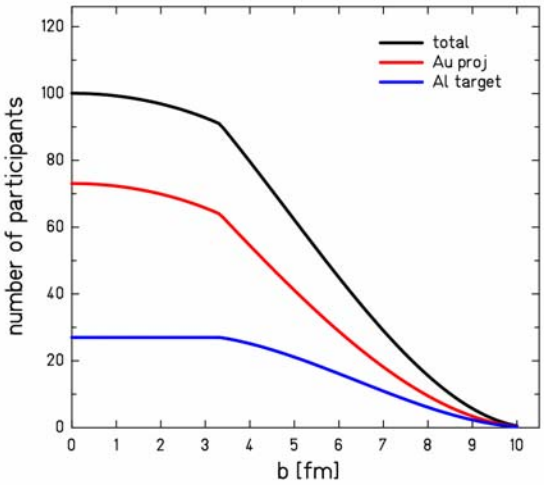

Fig.7.10: Total number of participants and those contributed by the gold projectile and aluminum target as the function of the impact parameter in the reaction ^{197}Au+^{27}Al as calculated by the geometrical model [Mor78].

The last conclusion is in agreement with the observations summarized in the chap.4.4, which were achieved without any direct quantification. But the way of deducing the impact parameter for the system with aluminum target is not fully independent of the gold-on-gold system (see chap.5.3); therefore, this particular result of the last paragraph should not be overestimated, but rather taken as yet another indication for in the meantime developed new concept of the spectator response.

In any case, due to results displayed in Fig.7.10 it is possible to get the feeling of the aluminum contribution to the participant zone, which accounts for ~30% at b=3 fm, ~35 % at b=6fm and ~40% at b=9fm despite its more than seven-times smaller mass and approximately two times smaller radius than the gold projectile. Under these circumstances, the energy delivered to the participant zone in collisions with impact parameters leading to the same final fragmentation residues is in aluminum target system only by few tens of percent smaller than in the gold target system with the same incident-beam energy. It is hard to imagine, that such a small difference would completely change the strength of the possible participant blast. But as will be shown below, at least the calculations indicate that it indeed does.

Turning the attention finally to the results of the calculations in the left subset of Fig.7.11, where for four various equations of state and with use of $\sigma_{in\text{-}med}$, no traces of any relative longitudinal momentum recovery are visible. In contrast to the experimental data the results of all calculations reveal a declining tendency of $\Delta|\langle p_z/A \rangle|$ of the spectator matter with the decreasing impact parameter. The slope of the decline gets even steeper towards the lowest impact parameters.

An unexpected feature of the calculated results is their quantitative sensitivity to the momentum-dependent properties of the nuclear mean field, while staying practically insensitive to the choice of the stiffness of the EoS. Moreover, this feature is observed in the full range of the studied impact parameters even without involvement of any momentum-recovering mechanism, which in both gold-on-gold systems seemed to be the process that,

when present, split the calculated predictions according to the (non)locality of the utilized MFs. If properly understood, this property of the calculated results would suggest the highly asymmetric reactions as also suitable candidates for testing the momentum-dependent properties of the nuclear mean field even in systems were no clear reacceleration nor any momentum-recovery is observed, extending the similar conclusion of [Shi01] made for a non-reaccelerating system ^{124}Sn+^{124}Sn.

In order to try to gain more insight into the patterns of calculated data in left subset of Fig.7.9, it is useful to compare them with the analogical results calculated for the symmetric system ^{197}Au+^{197}Au at the same incident-beam energy, i.e. 500 *A* MeV. However, since the impact parameter range of the considered collision in Au+Al system is not identical to the one in Au+Au system, an only approximate comparison is possible. With this respect, we utilize the finding of chap.5.3, namely that according to the predictions of the EPAX [Sue00] and model of Karol [Kar75] the fragmentation residues with the same mass are in both systems produced in reactions with impact parameters differing by ~3 fm in the whole mass range of the considered fragments. This approximation is for qualitative comparisons extrapolated also into the regions of lower impact parameters. (*Note: such impact parameters will be in the following comparisons depicted as the "corresponding impact parameters", meaning that for example b=3 fm in the reaction ^{197}Au+^{27}Al corresponds to b=6 fm in the reaction ^{197}Au+^{197}Au*).

Fig.7.11 then displays the time evolution of the difference between the mean masses of the spectator matter and between the net relative longitudinal momentum changes and their dependence on the "corresponding impact parameter" calculated for soft MD EoS with $\sigma_{in\text{-}med}$ for the systems ^{197}Au+^{197}Au and ^{197}Au+^{27}Al at 500 *A* MeV.

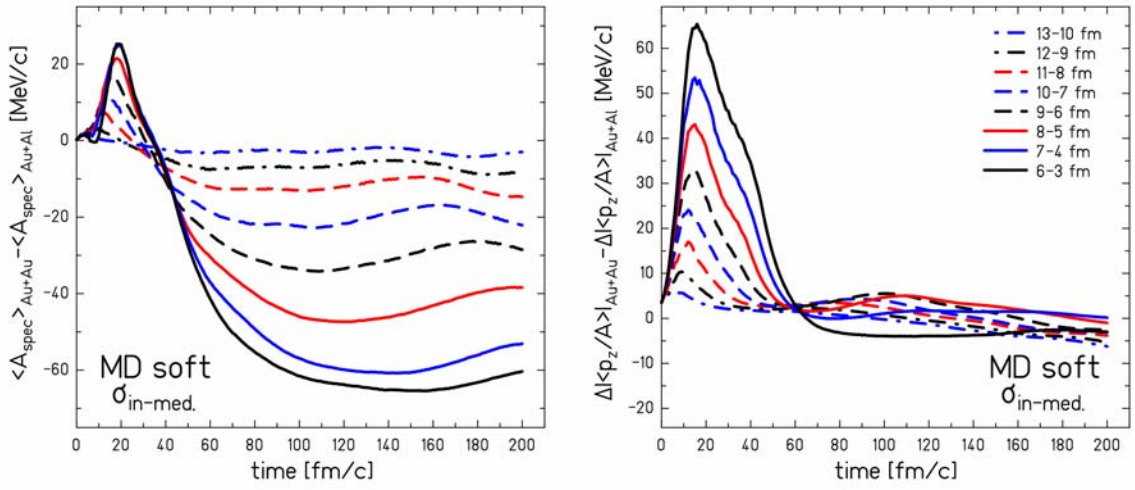

Fig.7.11: *Left:* time evolution of the difference of the mean mass of the spectator matter and its dependence on the "corresponding impact parameter" calculated for soft MD EoS with $\sigma_{in\text{-}med}$ for the systems ^{197}Au+^{197}Au and ^{197}Au+^{27}Al at 500 *A* MeV. *Right:* time evolution of $\Delta|\langle p_z/A\rangle|$ and its dependence on the "corresponding impact parameter" calculated for the same two systems as the left figure. For definition of the "corresponding impact parameters" see the text.

The left subset of Fig.7.11 demonstrates how significant influence the size of the target nucleus can have. It also reveals an interesting feature, which is important for completion of the newly constructed concept of the spectator response and indicates the answer to the question raised at the end of chap.7.2.2. Although the comparison of the simulations is limited by the compatibility of the "corresponding cross-sections", no reasonably assumed systematic error can reverse the trend observed in the evolution of the spectator mass difference in the left plot of Fig.7.11. During the initial abrasion phase of the collision the magnitude of the difference in the masses calculated for the two systems scales with the "corresponding impact

parameter" and more importantly it is in the absolute value positive. That means that abrasion process in the Au+Al system is more violent than in the Au+Au system. However, during the subsequent evolution with time the absolute value of the mass difference becomes clearly negative. This implicates that even though the gold projectile suffered significantly greater wound by the collision with the aluminum ion, at the end it did not loose as many nucleons as the gold projectile which experiences a milder encounter with another gold nucleus. In our understanding, the process responsible for this additional mass loss has to come from the outside of the spectator matter, in other words is caused by the blast. It is natural to view the possible blast caused by the collision of the gold with aluminum nucleus as weaker than the one developed in the correspondingly violent collision of two gold ions, provided the incident-beam energy in the laboratory frame is the same, as is the case of our experiments.

Turning now the attention to the right plot of Fig.7.11, right at the first sight, the difference in $\Delta|\langle p_z/A\rangle|$ reflects a very similar behavior of the two systems despite the size of the target nuclei, and despite the difference in the strength of the blast. Only the closer look reveals the changing order of the calculations for different "corresponding impact parameters". Since this effect appears only for the sufficiently low "corresponding impact parameters" we interpret this as the consequence of presence of the momentum recovering process in the calculations with the gold target, which seems to be almost completely missing in the calculations with the aluminum target.

The situation described above is similar for hard MD Eos or when MI mean field is used. Neither the stiffness, nor the momentum-dependence of the nuclear mean field change the difference in mass loss or the longitudinal momentum change, as can be seen in the full set of figures in App.D.

7.3.2. Data comparison to calculations with σ_{free}

While in the analysis of the previous two gold-on-gold systems we could see how significant effect the change of the used NN cross sections can have, looking at the right subset of Fig.7.9 we can observe that with the aluminum target the use of σ_{free} seem to have only a very limited effect.

As in the case of $\sigma_{in\text{-}med}$, also in this case the trends of the calculations are far away from reproducing the data, although the agreement in the area of coincidence of the data and the Morrissey systematic is quite promising. Also the qualitative feature of the insensitivity to the stiffness of the EoS and difference according to the choice of the nuclear mean field is preserved over a substantial part of the investigated impact parameter range. Yet this time the sensitivity to the momentum dependence is approximately half than what can be seen in the left plot of Fig.7.9.

Moreover, in the low impact parameters ($b \leq 5$) we can observe an interesting way of splitting the theoretical results, which for the only time in this analysis sorts relatively according to the stiffness for the utilized EoS. To be more specific, the calculations with soft EoS for static as well as for the nonlocal mean field seem to slow down in the drop of $\Delta|\langle p_z/A\rangle|$, yielding the signs of its possible recovery. This effect seems to have the same magnitude in both calculations.

In an effort to understand how the difference in the magnitude of the NN cross sections can affect the possible spectator response in such asymmetric system, **Fig.7.12** displays the difference of the spectator masses and $\Delta|\langle p_z/A\rangle|$ calculated again for soft MD EoS with $\sigma_{in\text{-}med}$ and σ_{free} for the system ^{197}Au+^{27}Al at 500 A MeV.

When investigating the right plot of Fig.7.12, it can be observed that also in this asymmetric system σ_{free} cause a greater damage to the gold projectile. First in the initial phase of the collision σ_{free} leads to the abrasion of more nucleons, which is overall much more

enhanced in this particular system, than in any of the symmetric gold-on-gold ones (compare to Fig.7.4 and 7.7). This can be understood in the way that the smaller aluminum nucleus has to penetrate deeper into the larger gold projectile in order to abrade the same number of nucleons from the gold projectile, when considering the geometrical picture, thus when increasing the overall magnitude of the reaction probability its abrasion effectiveness is enhanced according to surface of the scar caused by the penetration, which is larger than in case of the symmetric system. However, from the point of view of understanding the dynamical evolution of the system, a more interesting point is that the overall mass loss difference caused by σ_{free} is generally only 2-3 times greater than the mass loss difference caused by the abrasion when $\sigma_{in\text{-}med}$ and σ_{free} were compared in both Au+Au systems in times $t \geq 100$ fm/c. The ratio of the difference of the abraded mass and the total mass loss is app. 8-10, when considering only the calculations for the impact parameters where the mass loss difference does not saturate; e.g. for b=9 the number of nucleons abraded in time $t \approx 10$-30 fm/c due to the change of NN cross sections was only ~2-3 in both Au+Au systems, but the total difference in the mass, for $t \geq 100$ fm/c, due to the different cross sections is ~25-30 nucleons.

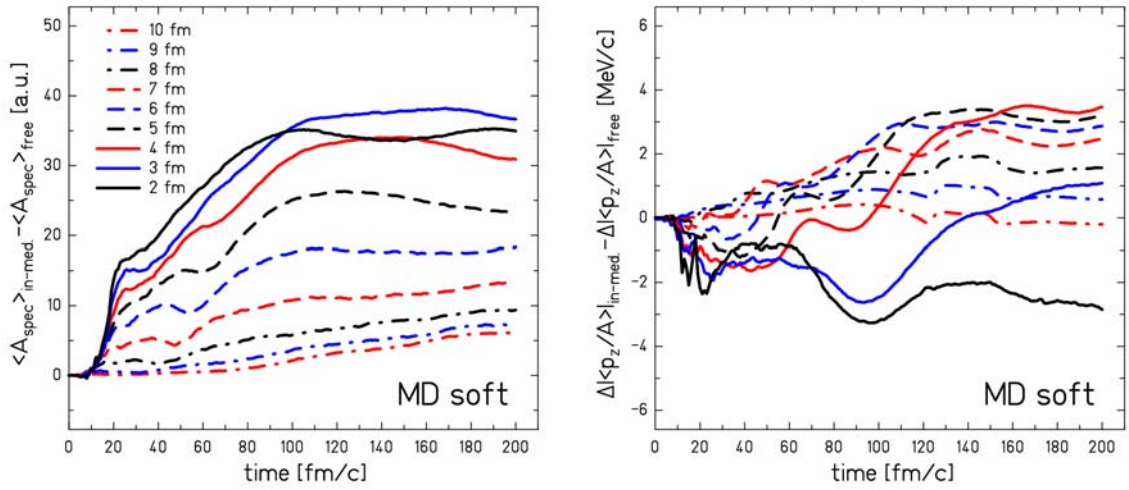

Fig.7.12: *Left:* Time evolution of the difference of the mean mass of the spectator matter and its dependence on the impact parameter calculated for soft MD EoS with $\sigma_{in\text{-}med}$ and σ_{free} for the system ^{197}Au+^{27}Al at 500 A MeV. *Right:* Time evolution of the difference of $\Delta|\langle p_z/A\rangle|$ and its dependence on the impact parameter calculated for soft MD EoS with $\sigma_{in\text{-}med}$ and σ_{free} for the same system as in the left figure.

In our opinion, this is the further evidence for the participants blast as being responsible for the additional mass loss in both symmetric systems, and that the strength of the blast significantly varies with the magnitude of the cross-sections. On the other hand, since the ratio of the differences in abraded masses and the total mass difference does not change that dramatically, the strength, or better formulated, the effect of the blast on the spectator does not vary so much with the incident-beam energy. This may not sound very intuitive, but we suspect that it reflects the longer exposition of the spectator to the developing blast, since with lower incident beam energy it is slower, and cannot escape from the explosion zone as fast as in the case of a 1 A GeV beam.

Reformulating the main point of the last paragraph, the left plot of Fig.7.12 in comparison to its analogs in Fig 7.4 and 7.6 indicates that the participant blast is able to blow away parts of the spectator. Moreover the blast in the Au+Al system seems to be particularly weak, at least with respect to both Au+Au systems. Yet recalling the experimental results, this does not seem to affect the mean longitudinal velocities, which yield in the magnitude a very similar reacceleration as in the other two investigated systems. This is in an accord to the conclusions based on the results in Fig.7.11.

With such an interpretation we can re-investigate our deductions concerning the findings based on the comparison of $\Delta|\langle p_z/A\rangle|$ when calculated with different NN cross-sections, such as displayed in the right subset of Fig.7.4, and Fig.7.6. These differences helped to identify the onsets of the momentum-recovering process and even to trace the impact parameter needed for its onset. Considering now the differing strength of the blast as indicated in the previous paragraph, we gained confirming support for the observation that the "threshold impact parameter" decreases with decreasing incident-beam energy and increases with higher NN cross sections.

Examining now also the right plot of the Fig.7.12, the qualitative difference to its counterparts from analogical comparisons in symmetric systems can be observed. Since in this case, only one threshold impact parameter can be found. Considering only times $t \geq 30$ fm/c, the difference $\Delta|\langle p_z/A\rangle|$ first slightly increases with the decreasing impact parameter until app. $b \approx 4$ fm, below which the absolute value of the difference declines. In the spirit of the earlier analyses, this is the consequence of the onset of the relative momentum-recovering process in the case of the calculations with σ_{free}. However, the difference in $\Delta|\langle p_z/A\rangle|$ does not saturate as in the previously investigated systems, which indicates that for $\sigma_{in\text{-}med}$ no process leading to any partial recovery of the momenta starts at all, just as follows also from the Fig.7.9, and as was cautiously interpreted in the discussion on the right subset of Fig.7.11. In other words, and with respect to the new concept of the spectator response developed in the chap.7.2, the blast was not strong enough to initiate the process leading to the recovery of $\Delta|\langle p_z/A\rangle|$.

Before advancing to the final discussion and summary of the observations made when investigating the spectator response in terms of the simulations restricted by the experimental data, the survey of the mutual comparisons will be completed by **Fig.7.13**. There the effects of the size of the target nucleus on the spectator mass and its $\Delta|\langle p_z/A\rangle|$ in calculations with σ_{free} is displayed, again with use of the "corresponding impact parameters" as introduced in chap.7.3.1.

.But Fig.7.13 does not reveal any qualitatively new information about the dynamical evolution of the investigated systems. The left subset of the figure displays the influence of the size of the target nucleus on the evolution of the spectator mass, which can be viewed as a consequence of the blast, that is considerably stronger in the Au+Au reaction than in the one with the aluminum target despite the larger cross-sections in both system. Recalling the results of the simple geometrical model displayed in Fig.7.3 and Fig.7.10, we can observe that the ratio in the number of abraded nucleons in Au+Au and Au+Al system, with respect to the "corresponding impact parameters", is app. ~2. We suspect this fact for being also the most detrimental factor in the strength of the blast revealed in the BUU calculations.

The right plot of Fig.7.13 then displays the difference in $\Delta|\langle p_z/A\rangle|$ calculated for the two systems. While for the higher "corresponding impact parameters" the difference in the calculations is practically negligible, the calculations for the lowest three ones yield already a visible difference. This can be understood when assuming the onset of the relative–momentum recovering process, which is in case of Au+Au already around b=9 fm, while for the system with aluminum it merely appears first at b=3 (see Fig.7.12 right). Therefore, due to the construction of the "corresponding impact parameters", which include the range of the true b for Au+Al system from b=3 to 10, the relative-momentum recovering process does not have chance to reveal itself in the right subset of Fig.7.13.

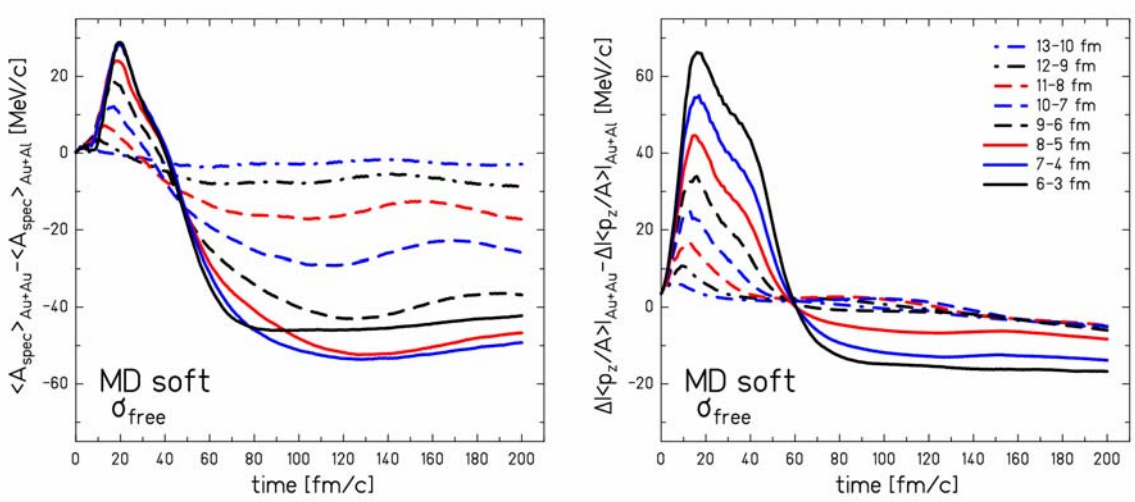

Fig.7.13: *Left:* Time evolution of the difference of the mean mass of the spectator matter and its dependence on the "corresponding impact parameter" calculated for soft MD EoS with σ_{free} for the systems ^{197}Au+^{197}Au and ^{197}Au+^{27}Au at 500 *A* MeV. *Right:* Time evolution of the difference of $\Delta|\langle p_z/A\rangle|$ and its dependence on the "corresponding impact parameter" calculated for the same two systems as the left figure.

7.4. The spectator response and its implications

Although the quantitative as well as qualitative comparison of the simulated and experimental results has shown important deviations, the long and tedious analyses of the theoretical results constrained by the experimental data resulted in a significant shift of the understanding of the spectator response to the participant blast. Moreover, it also revealed basic characteristics of the mechanism, which seem to be in the model responsible for the recovery of the relative momentum of the spectator, with explicit similarities to the features of the process observed in the experiment. The aim of this last chapter is therefore to summarize and highlight the individual indications and pieces of evidence without which the creation of the new spectator response concept would not be possible.

The analyses started with the comparison of the experimentally determined and theoretically calculated $\Delta|\langle p_z/A\rangle|$ of the spectator residues in the reaction ^{197}Au+^{197}Au at 1 *A* GeV. There we have learned that the simulations, with respect to the experiment, yield a significant recovery of the spectator relative momentum only for too low impact parameters and only for the momentum-dependent mean-field. Increase of the magnitude of the NN elastic scattering cross-sections by switching to σ_{free} instead of the initially used $\sigma_{in\text{-}med}$ increased also the relative-momentum recovery effect in the simulations. However, it caused a significant recovery of the spectator relative momenta also in the case of the calculations with momentum-independent MFs. Thus we learnt that the nonlocal quality of the nuclear potential is not the exclusive cause of the relative-momentum recovery, but seemed to lead to its significant enhancement.

The comparison of the influence of the NN cross-section choice on the mass and the $\Delta|\langle p_z/A\rangle|$ of the spectator (Fig.7.4) revealed how significant the effect on both quantities is, but on each of them in a different way. Moreover, the initial insensitivity, subsequent dependency and again saturation of the difference in $\Delta|\langle p_z/A\rangle|$ with respect to the impact parameter pointed to the onset of a relative-momentum recovery process of a similar strength in both sets of calculations, but at impact parameter depending on the choice of the NN cross-sections.

The true break-through came with the analysis of the second reaction system, i.e. ^{197}Au+^{197}Au at 500 *A* MeV. The overall disagreement of the calculations and the experiment is even more pronounced than at the higher incident-beam energy, and, thus, the strength of the relative-momentum recovery process in the simulations seemed to be at first dependent on

the energy invested to the participant zone (compare Fig.7.2 and Fig.7.5). Additional to this, the comparison of the spectator mass as a function of the incident-beam energy showed how detrimental effect the higher energy of the incident beam can have on the spectator in terms of its mass (Fig.7.6). Then the relative comparison of the influence of the NN cross-section choice on $\Delta|\langle p_z/A\rangle|$ in this lower incident-beam energy system revealed a similar feature as for its higher-energy analog, allowing us to determine the onsets of the relative-momentum recovery process also in our second investigated system. But, while the values of the "threshold impact parameters" were again depending on the magnitude of the cross-sections, they were also generally lower than in the 1 *A* GeV system. However, the most significant observation was that in the both systems (Fig.7.4 and 7.7), the recovery process was of the same strength, meaning that it effectively does not depend on the amount of the energy invested to the participant zone, neither the different values of the used cross-sections nor the impact parameters when it sets on. Moreover, its strength was the same despite the generally very different magnitude of the recovery of the spectator relative longitudinal-momentum (Fig.7.2 and 7.5).

This all pointed to the process which source cannot reside in the collision zone preventing it from being directly affected by the different strength of the collision being ruled by the incident-beam energy. It suggests that the spectator itself is responsible for its own momentum-recovery and the energy, which is for that used is acquired in the abrasion phase of the reaction, thus remaining generally the same even in reactions with different incident-beam energy. However, the process itself, in terms of being present at all, seems to be correlated well with the energy of the beam which reduction may be partially substituted by a higher magnitude of the NN cross sections or the inclusion of the momentum-dependent properties of the nuclear mean field into the calculations. In other words, the onset, but only the onset, of the momentum recovery process seems to depend on the strength of the blast.

The role of the blast in the initiation of the relative-momentum recovery process became more transparent in the analyses of the third system, i.e. ^{197}Au+^{27}Al at 500 *A* MeV, even though almost no effect of any relative-momentum recovery is in the simulations with $\sigma_{in\text{-}med}$ visible, in a strong contrast to the experimental data which reaccelerate in similar manner as the fragmentation residues in ^{197}Au+^{197}Au at the same incident beam energy. From the simple geometrical model applied to the experimental results, we have additionally learned that the same number of nucleons needs to be abraded in order to yield at the end the residue with the same reacceleration as in the case of the gold-on-gold system at the same incident-beam energy. But after introducing the "corresponding impact parameters" in order to directly compare the evolution of the spectator mass between the systems with aluminum and gold target, we observed that while the abrasion process is, in the compared impact parameters, much stronger with aluminum as the target nucleus, at the end the overall spectator mass loss is much greater in the calculations with the gold-on-gold system. Moreover the changes in $\Delta|\langle p_z/A\rangle|$ remained practically the same in both compared systems. In other words, in the calculations, despite the lower number of abraded nucleons in the reaction with gold target, the blast was much stronger and could simply blow away greater portions of the spectator, yet the most importantly, without affecting its momentum per nucleon.

Looking retrospectively at the relative power of the blast "newly revealed" also in Fig.7.4 and Fig.7.8 we could see its correlation with the threshold impact parameter necessary for the onset of the relative-momentum recovery mechanism, which contributed as the last piece to the new understanding of the spectator response.

In conclusion, guided by the results of the above differential analyses, the understanding of the net longitudinal-momentum recovery per nucleon observed in the calculations and interpreted as the spectator response to the participant blast has undergone a systematic evolution. From the view of the net relative longitudinal-momentum recovery as being the direct consequence of the ordered push provided by the participant blast, we have arrived at

the concept of the spectator having its own power and resources to induce the recovery of its relative longitudinal-momentum. However, it seems that still a sufficiently strong blast is needed at least for the ignition of this additional engine, which is ruled by the energy input, number of participating nucleons, reaction geometry and the properties of nuclear matter in terms of its stiffness, quality of the mean field and the magnitude of the NN scattering cross-sections. But once the relative longitudinal-momentum recovery process is turned on, it does not significantly depend on the properties of the blast, but rather only on the amount of the available energy presumably acquired in the abrasion stage of the reaction.

While it is possible in the simulations to trace the properties of the relative longitudinal-momentum recovering process, there is unfortunately no direct answer to the question how this mechanism actually works. In our opinion, it is not so unreasonable to presume that it may be a slightly enhanced backward emission of individual nucleons or complex clusters, which by their recoil donate the spectator a little extra push forward. An unanswered question then remains why only certain strength of the blast can force the spectator to release anything backwards beyond the level allowed by the emission isotropy. However, advancing further with the speculative element of the new concept, it can be suggested that the necessary condition for an onset of the process responsible for the recovery of the spectator momentum is that the blast reaches the spectator on time, i.e. before it fully equilibrates. The supportive argument for this hypothesis may be the fact that the strength of the blast implicates the time it effectively reaches the spectator as also indicated by the pace of the spectator-mass evolution. Then, when the particles of the blast reaching the nucleons of the spectator, the excitation energy of the individual nucleons on the near-side, with respect to the blast, is on the average higher than when the spectator is already fully equilibrated. Thus the relatively same impact of the blast can, in case of the not-fully-equilibrated spectator, yield an additional and sufficiently large increase of the local excitation, which would result in ejection of a particle or a cluster, supporting with its recoil the recovery of the spectator relative momentum.

The effect of the relative momentum recovery would grow with the size and especially the nuclear charge of the emitted fragment, since the Coulomb force would enhance its recoil. Such a consideration may be taken as a hint why the BUU code does not properly reproduce the magnitude of the momentum recovery, since as mentioned in the introductory part of this chapter, it's by default limited in the description of the cluster production. On the other hand it surely does not have to be the only reason. As we could see the important role of the blast, it should not be forgotten that the reliability of its description by the model is limited by our knowledge of the nuclear equation of state. And this is not yet complete.

But more important than the deficiencies of the quantitative predictions is just the fact that the model contains the elements of the process, which yields the relative longitudinal-momentum recovery. Reviewing now the main characteristics of this process, determined by the analyses of the theoretical results guided by the experimental data, we can compare it with the qualitative behavior of the reacceleration phenomenon analyzed in the chapter 4. The result is a striking similarity of the both processes suggesting that it can be indeed the very same mechanism, which yields the reacceleration of the fragmentation residues in the experiment as well as the recovery of the relative longitudinal momentum of the spectator matter in the simulations.

8. Conclusions

This study has been motivated by an experimental observation of a fascinating phenomenon of the reacceleration of the fragmentation residues [Enq99, Ric03] and the theoretical prediction of the spectator response to the participant blast [Shi01]. While the theoretical work of [Shi01] implicates the use of the net relative longitudinal momentum change of the spectator residue during a heavy-ion collision as a new observable sensitive to the various aspects of the nuclear equation of state, the work of [Ric03] interprets the experimentally observed reacceleration as the theoretically predicted spectator response. But the limited amount of the experimentally investigated systems and the missing direct information on the impact parameter prevented the reacceleration from being explicitly used for any quantitative assessments with respect to the extraction of information on the nuclear equation of state.

Therefore, we decided to provide the absent bridge by experimental investigation of a reaction system were the reacceleration of the fragmentation residues would be quantitatively comparable with the model predictions mediated by the impact parameter. In addition, we intended to extend the study also with respect to the incident-beam energy and the geometry of the colliding system, both presumably affecting the dynamical evolution of the system, testing thus the reliability of the model and possibilities of extracting any specific information related to the properties of nuclear matter under extreme conditions described by the equation of state.

We performed a sequel of experiments in which the reaction system ^{197}Au+^{197}Au was investigated at laboratory incident-beam energies of 0.5 and 1 *A* GeV, complemented by a study of the system ^{197}Au+^{27}Au at 0.5 *A* GeV. All three experiments were performed utilizing the high-resolution magnetic spectrometer, the Fragment Separator, at GSI-Darmstadt, Germany. The main results of these experiments have been the mean longitudinal velocities of the fragmentation residues as the function of their masses, which can be to a great extent related to a specific impact parameter.

The experimental results revealed a clear reacceleration of the fragmentation residues with a very similar magnitude in all the studied systems. However, the differences in the actual reacceleration observed for the fragments with the same mass, or with the minimum mass-loss needed to cause the fragment velocity to deviate from the Morrissey systematic, for different systems provided valuable information on the source and the properties of the mechanism responsible for the reacceleration. The analysis pointed to the spectator remnant as being responsible for its own reacceleration, which seems to be in its strength independent from the energy invested, which on the other hand appears to rule what is the minimum impact parameter at which the relative longitudinal-momentum process sets on. Moreover the geometry of the system turned out in the experiment to be of no relevance for the onset of the reacceleration, but to slightly influence its overall magnitude. The discussion of experimental results was concluded by introducing a novel concept of the reacceleration which from the original version of an effect of the "*strong enough explosion, when the ordered push may overcome the friction effects, producing a net longitudinal acceleration*" [Shi01] changed to the spectator reaccelerated by the recoil of particles or clusters emitted in a slightly enhanced backward emission initiated possibly by a strong enough blast, which besides that seems to have only a limited function.

Parallel to the experimental analysis, we also used the theoretical model, which yielded the first predictions of the spectator response to the participant blast. We used four different equations of state with varying stiffness of the nuclear matter and the momentum-dependent quality of the nuclear mean field, and with two different sets of the NN scattering cross sections we calculated the time evolution of the physical quantities analogical to those measured in the experiment for all three experimentally investigated systems. However, the

direct quantitative comparison of the calculated results and the experimental data yielded significant discrepancies, which could even cause doubts whether the experimentally observed and theoretically predicted effects are a consequence of the same process. But the differential analyses of the theoretical results allowed extracting the information on the mechanism, which is in the model responsible for at least a partial recovery of the relative longitudinal momentum of the spectator. While trying to stay unbiased by the interpretation of the experimental findings, also the analysis of the calculated results pointed to the spectator as being self-responsible for the recovery of its own longitudinal momentum per nucleon, practically independent on the strength of the blast, which, however, still seems to influence at least the conditions for its onset.

The very similar properties of the process recovering the spectator relative longitudinal momentum in the theoretical results and those of the mechanism identified when investigating the features of the experimentally observed reacceleration phenomenon indicate that the both processes can be of an identical nature, completing thus our contemporary understanding of the spectator response to the participant blast.

Having in mind the shift from the original to the new concept of the spectator response to the participant blast, we have to recall once more the pioneering works of Shi, Ricciardi and their collaborators. Since while the experiment and the theory were correctly interconnected, it may now seem that the original pretext of this work, aiming to contribute to the possible extraction of new information on the nuclear equation of state, was based on an incomplete understanding of the involved process. One can therefore question whether the spectator response, understood by the means of the new concept, can still contribute to the common effort of searching for the correct equation of state of the nuclear matter. We are convinced that the answer is yes, since it is still the blast that is ruled by the very most properties of the nuclear matter, therefore also any role of the blast in the spectator response is determined by these properties. Thus, the investigation of the conditions under which the spectator response is possible, and how it evolves with change of various reaction parameters, can reveal the information on the behavior of the nuclear matter under extreme conditions. The proper understanding of the process which can transmit such information is then necessary but still only one of the very first steps leading to the deepening of our insight into the peculiar nature of the nuclear matter.

Appendix A

Fig.A.1: *Left:* Review of correlation of the highest (Z_{max}) and the 2nd highest (Z_{max2}) charge produced in the reactions ^{197}Au+^{197}Au at 600 *A* MeV and 1 *A* GeV and ^{197}Au+^{27}Al at 600 *A* MeV as measured by the ALADIN collaboration. The top of the triangle corresponds to fission events, the ridge at the bottom to the fragmentation. *Right:* Probability that the charge of the measured fragment is the highest charge produced in the corresponding reaction extracted from the data displayed in the left figures (fission events excluded) [source data provided by ALADIN [ALA]].

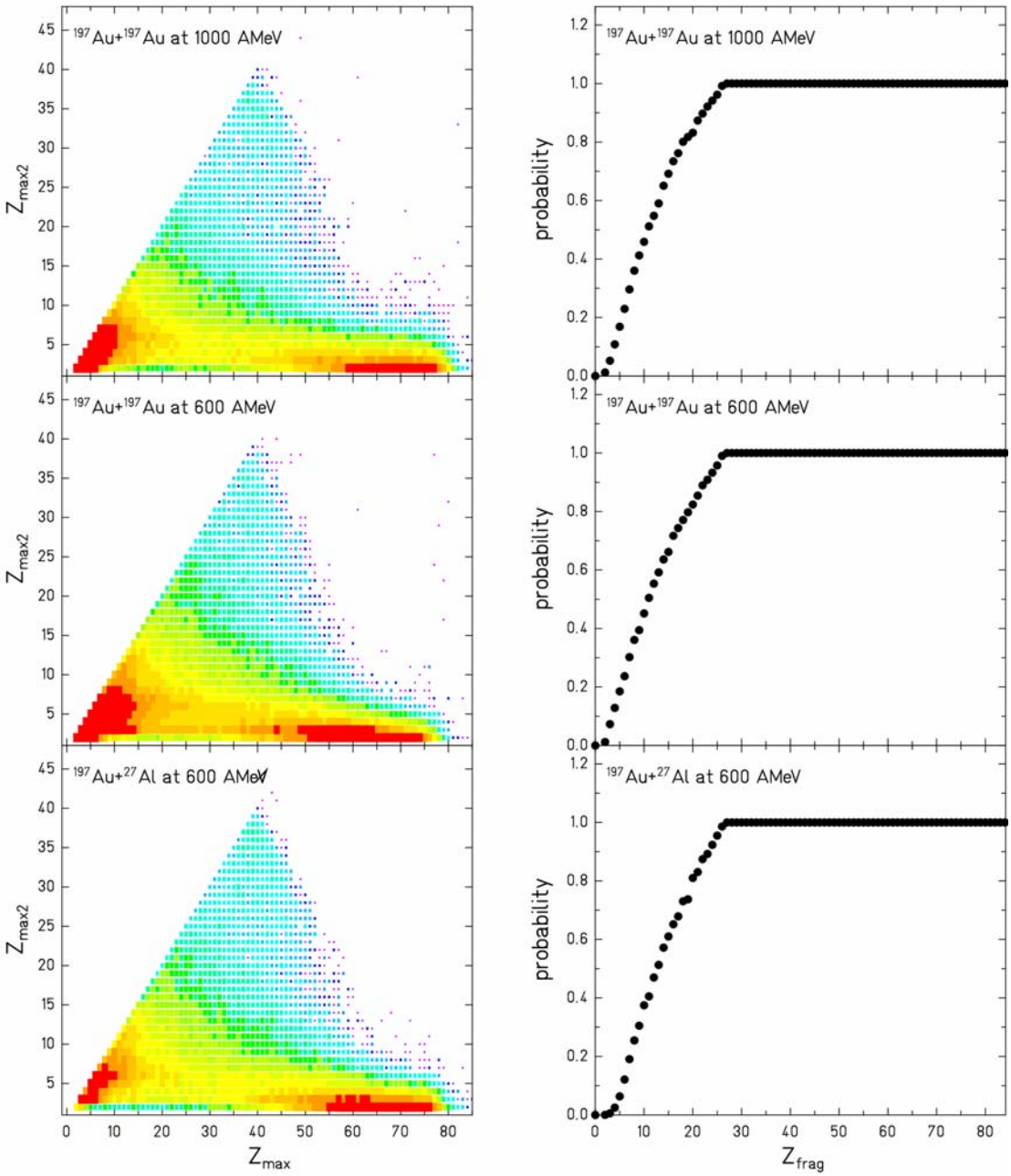

Appendix B1

Longitudinal velocity distributions of reaction residues with constant mass A_{res} in the reference frame of the primary beam measured in the experiment ^{197}Au+^{197}Au at 1 A GeV. The displayed differential yields are corrected for the dead-time, normalized to the same total beam intensity and corrected for the angular transmission dependence on the position at the intermediate and final focal plane. The longitudinal velocity distributions were reconstructed using the procedures described in chap.3.4. The staggering of the data in the region of low residue masses A_{res} and the sharp edges of the distributions in mass region close to the projectile are caused by the border effects, i.e. incomplete coverage of these distributions in the measurement.

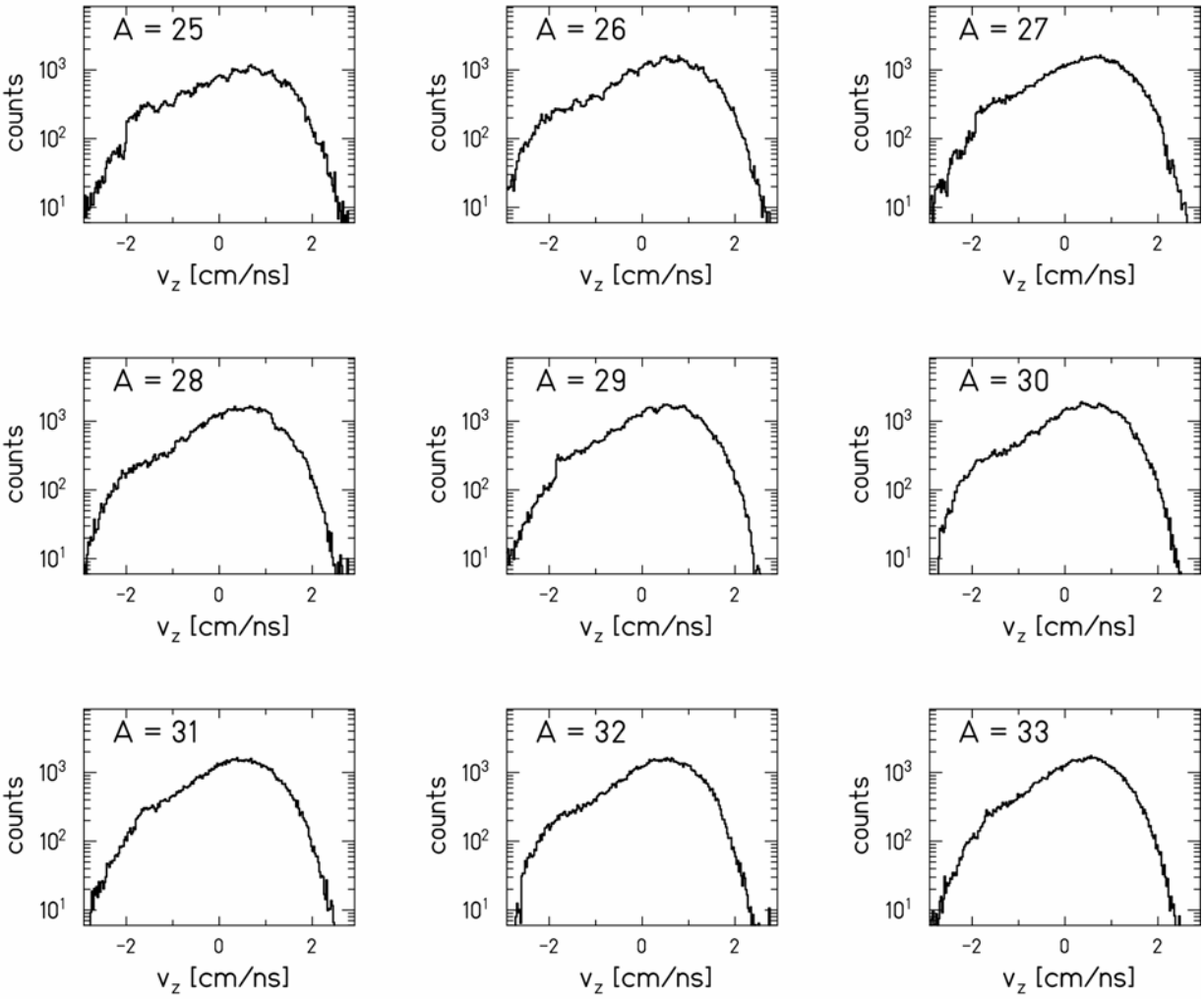

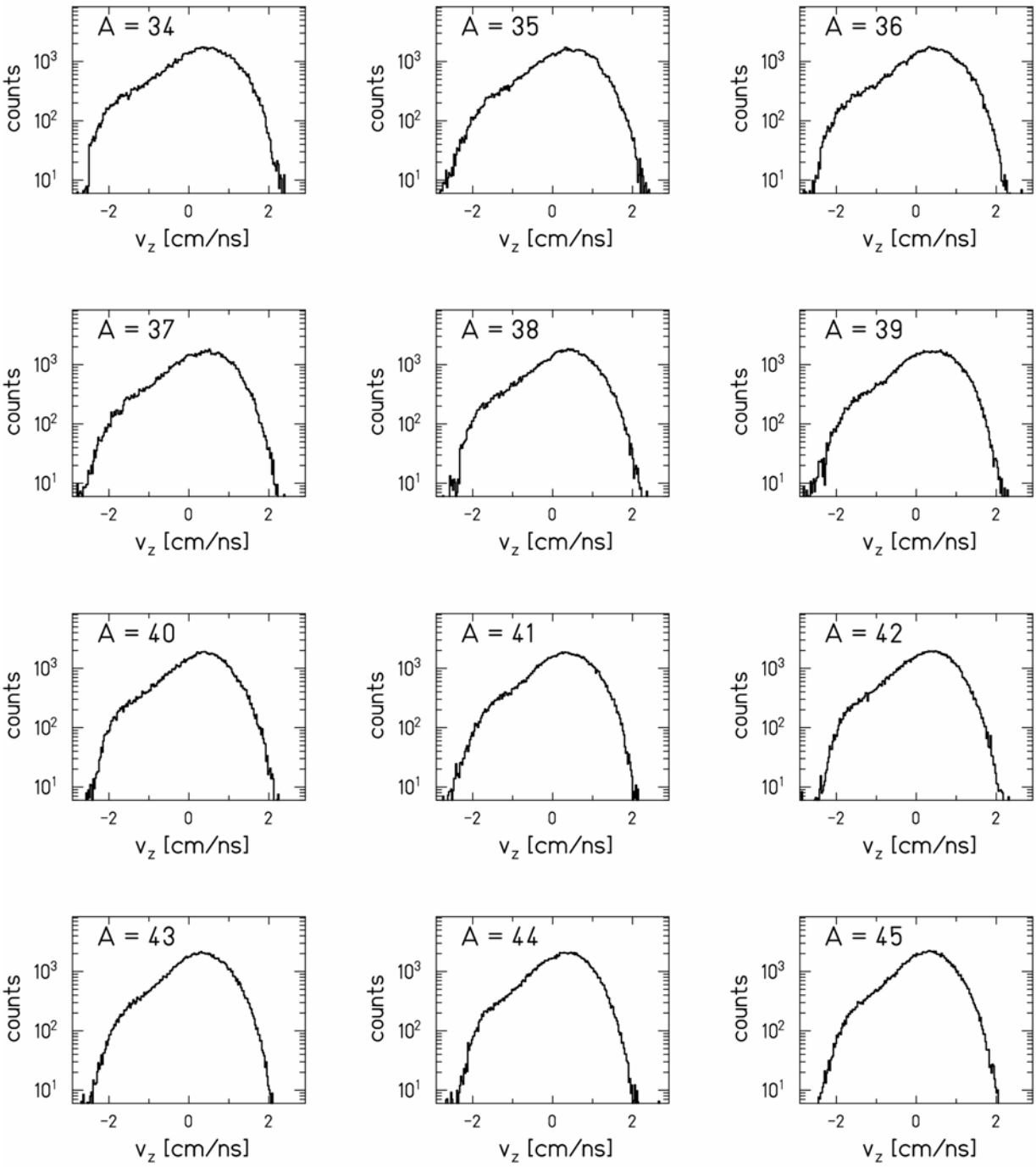
A = 34
A = 35
A = 36
A = 37
A = 38
A = 39
A = 40
A = 41
A = 42
A = 43
A = 44
A = 45
counts
v_z [cm/ns]

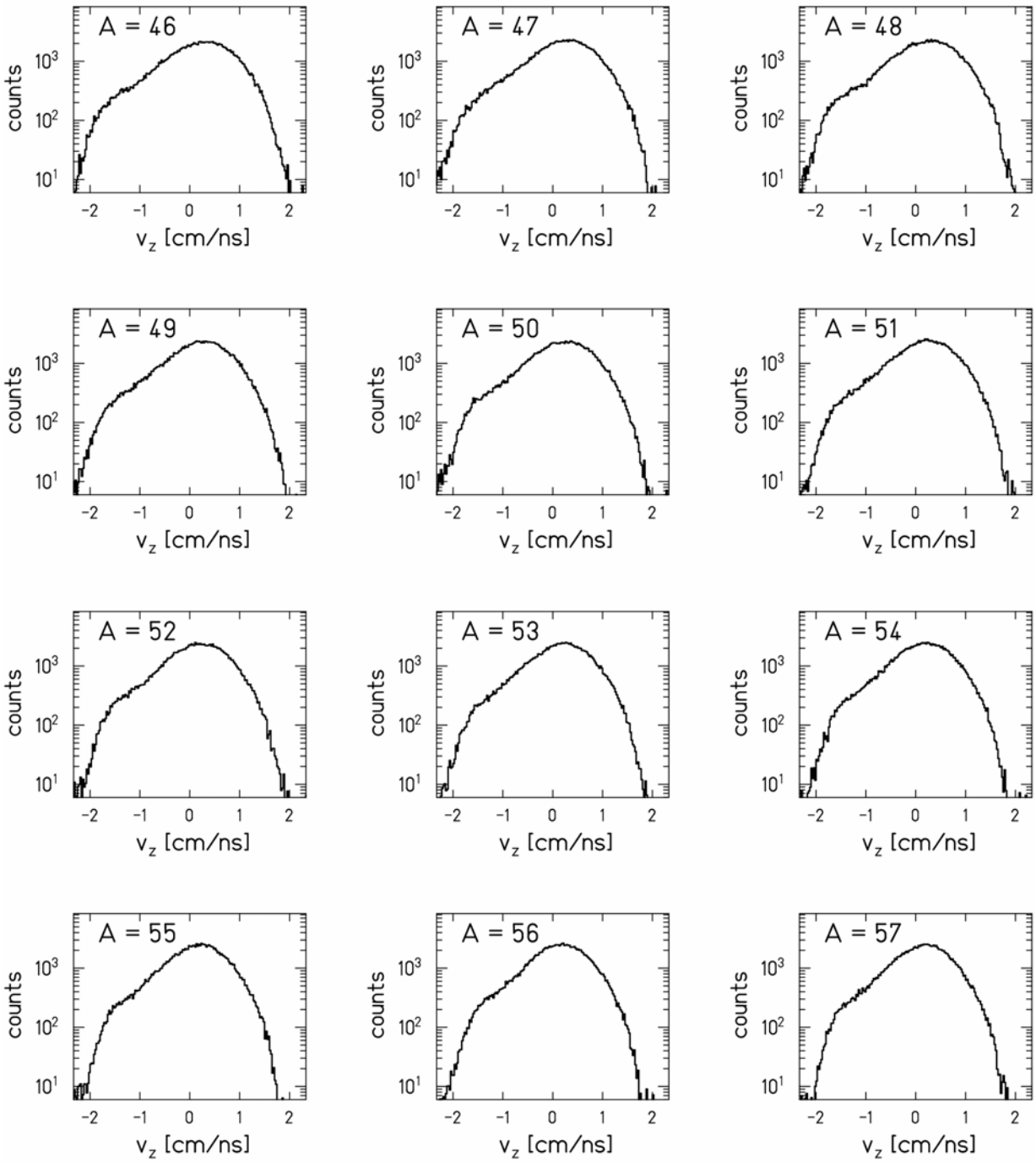
A = 46
A = 47
A = 48
A = 49
A = 50
A = 51
A = 52
A = 53
A = 54
A = 55
A = 56
A = 57
counts
v_z [cm/ns]

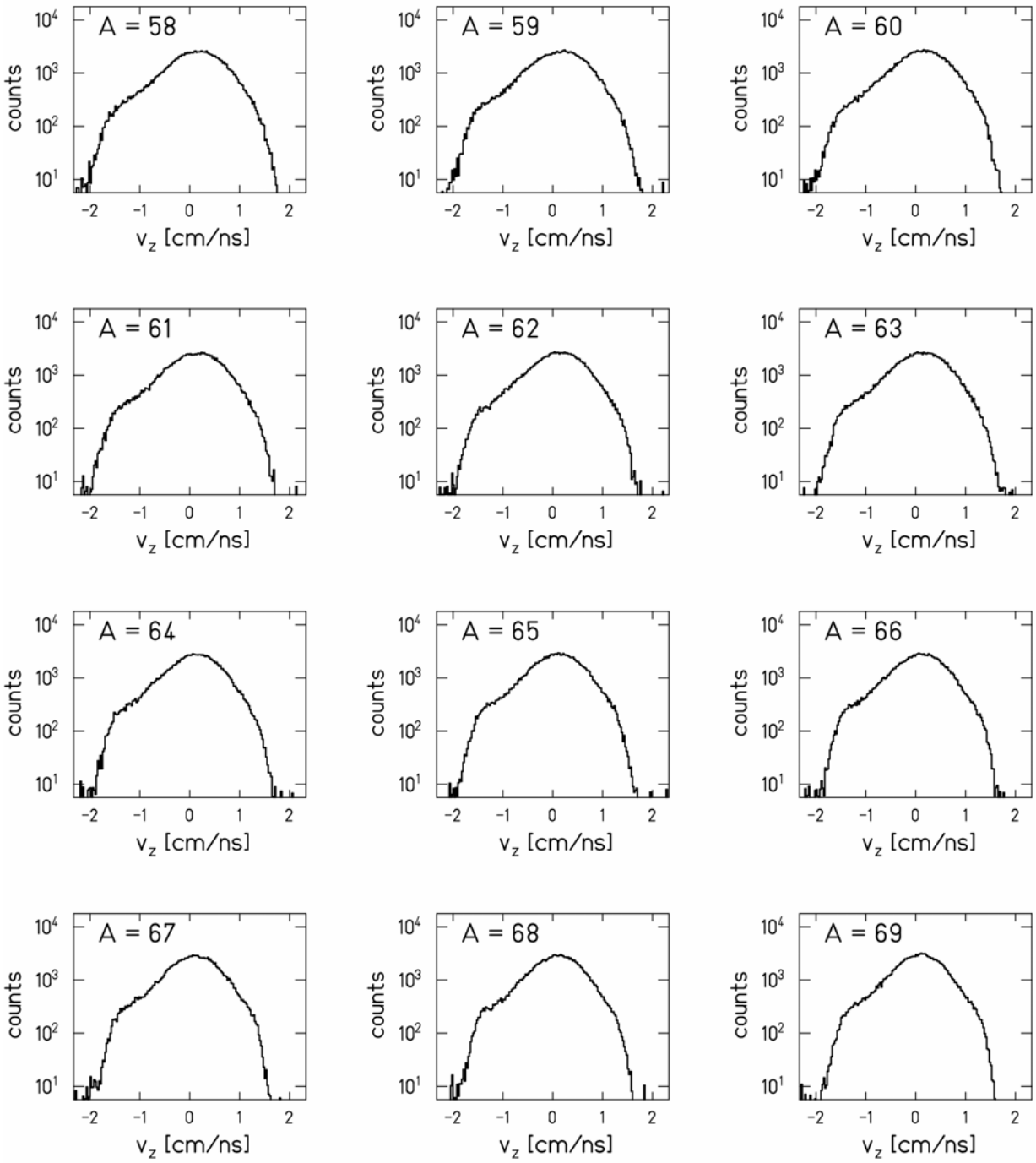
A = 58
A = 59
A = 60
A = 61
A = 62
A = 63
A = 64
A = 65
A = 66
A = 67
A = 68
A = 69
counts
v_z [cm/ns]

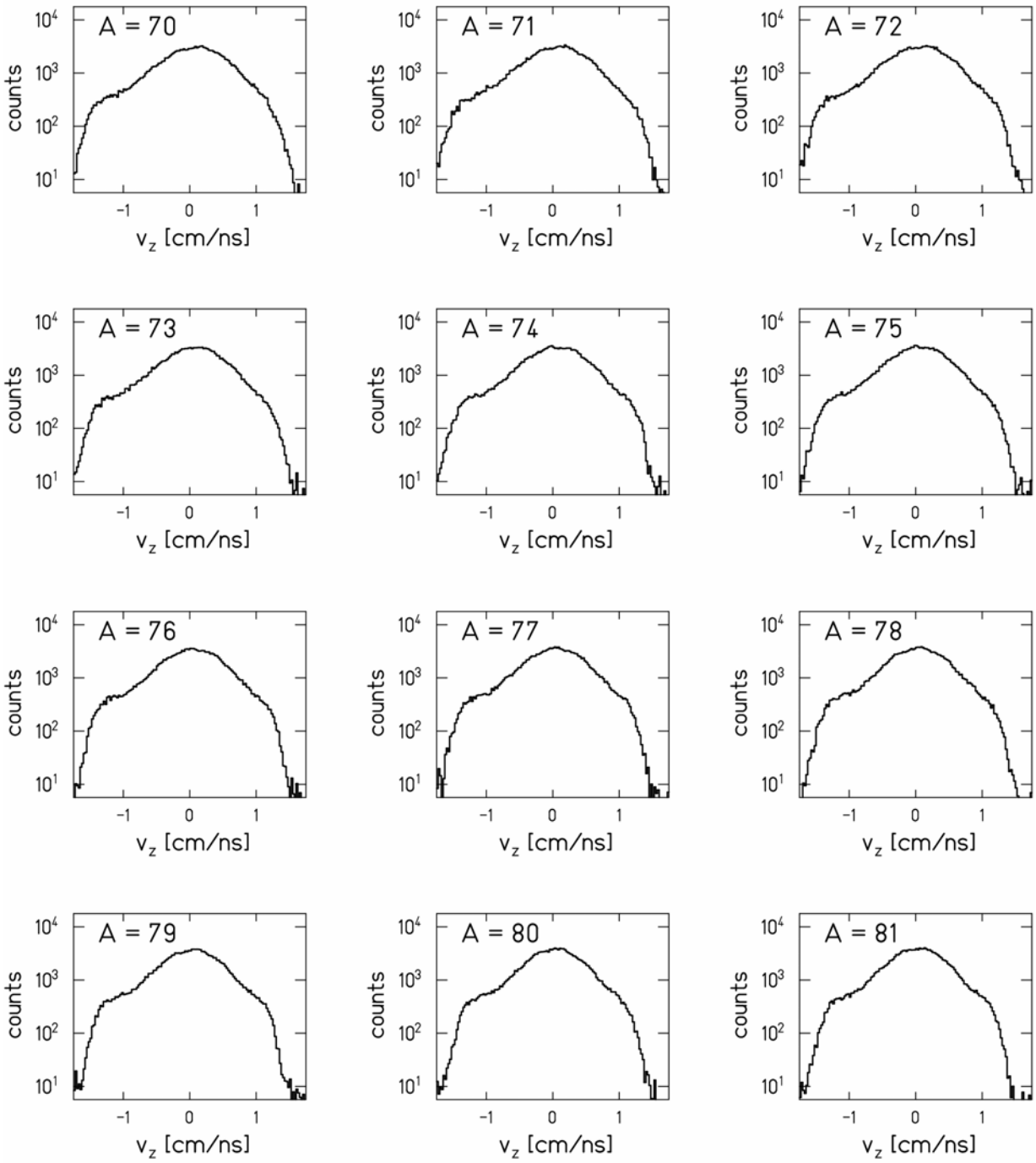
A = 70
A = 71
A = 72
A = 73
A = 74
A = 75
A = 76
A = 77
A = 78
A = 79
A = 80
A = 81
counts
v_z [cm/ns]

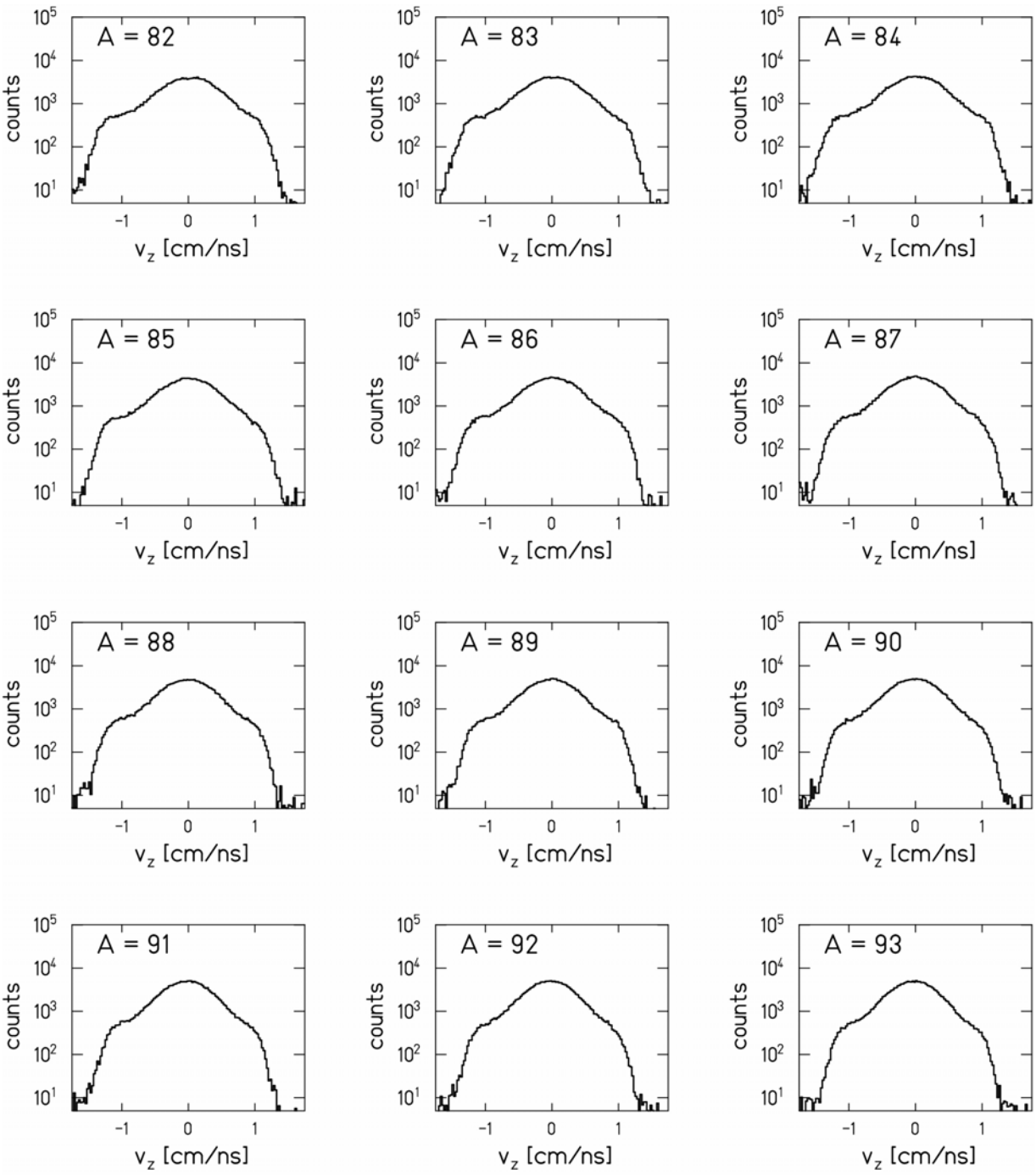
A = 82
A = 83
A = 84
A = 85
A = 86
A = 87
A = 88
A = 89
A = 90
A = 91
A = 92
A = 93
counts
v_z [cm/ns]

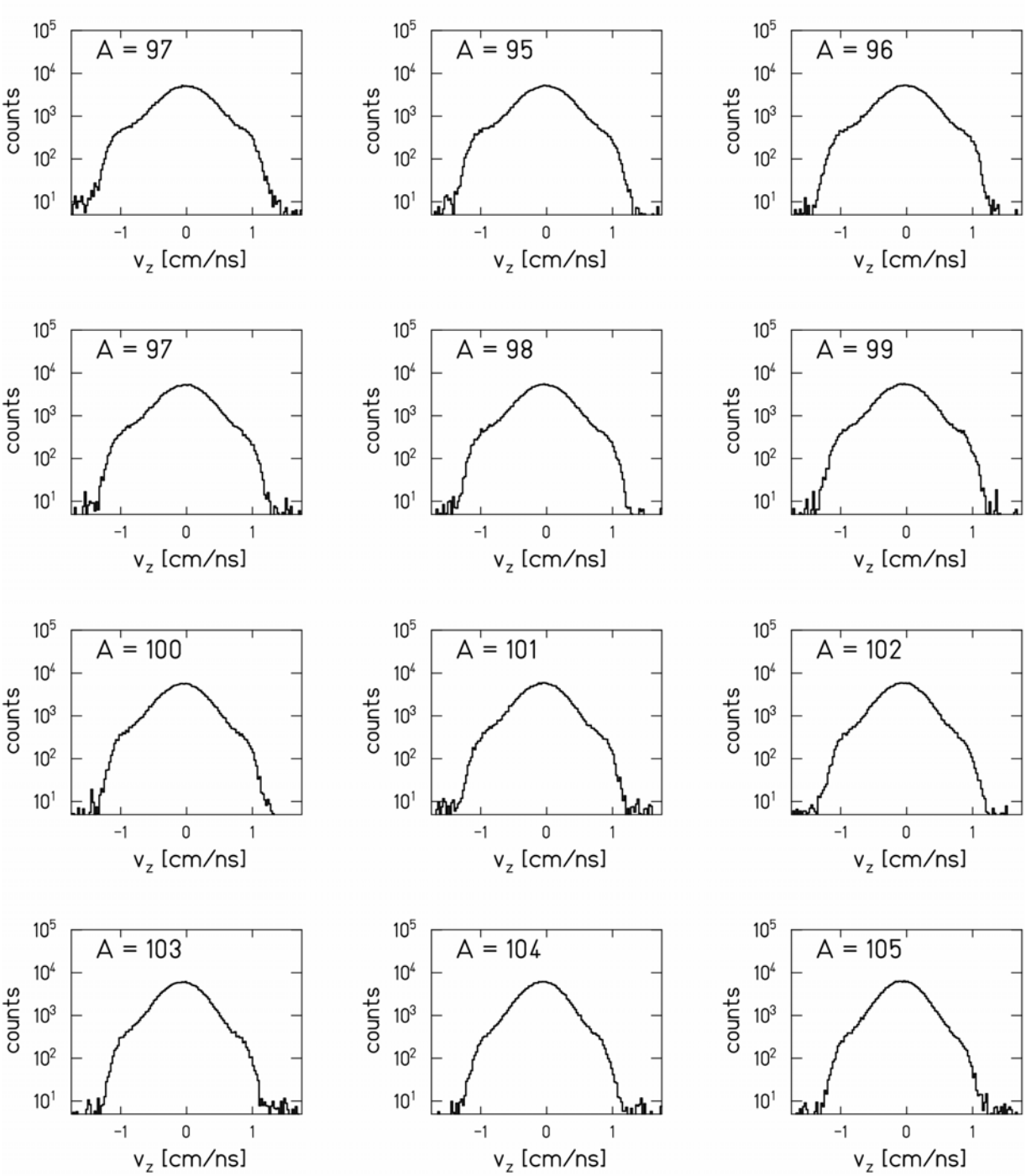
A = 97
A = 95
A = 96
A = 97
A = 98
A = 99
A = 100
A = 101
A = 102
A = 103
A = 104
A = 105
counts
v_z [cm/ns]

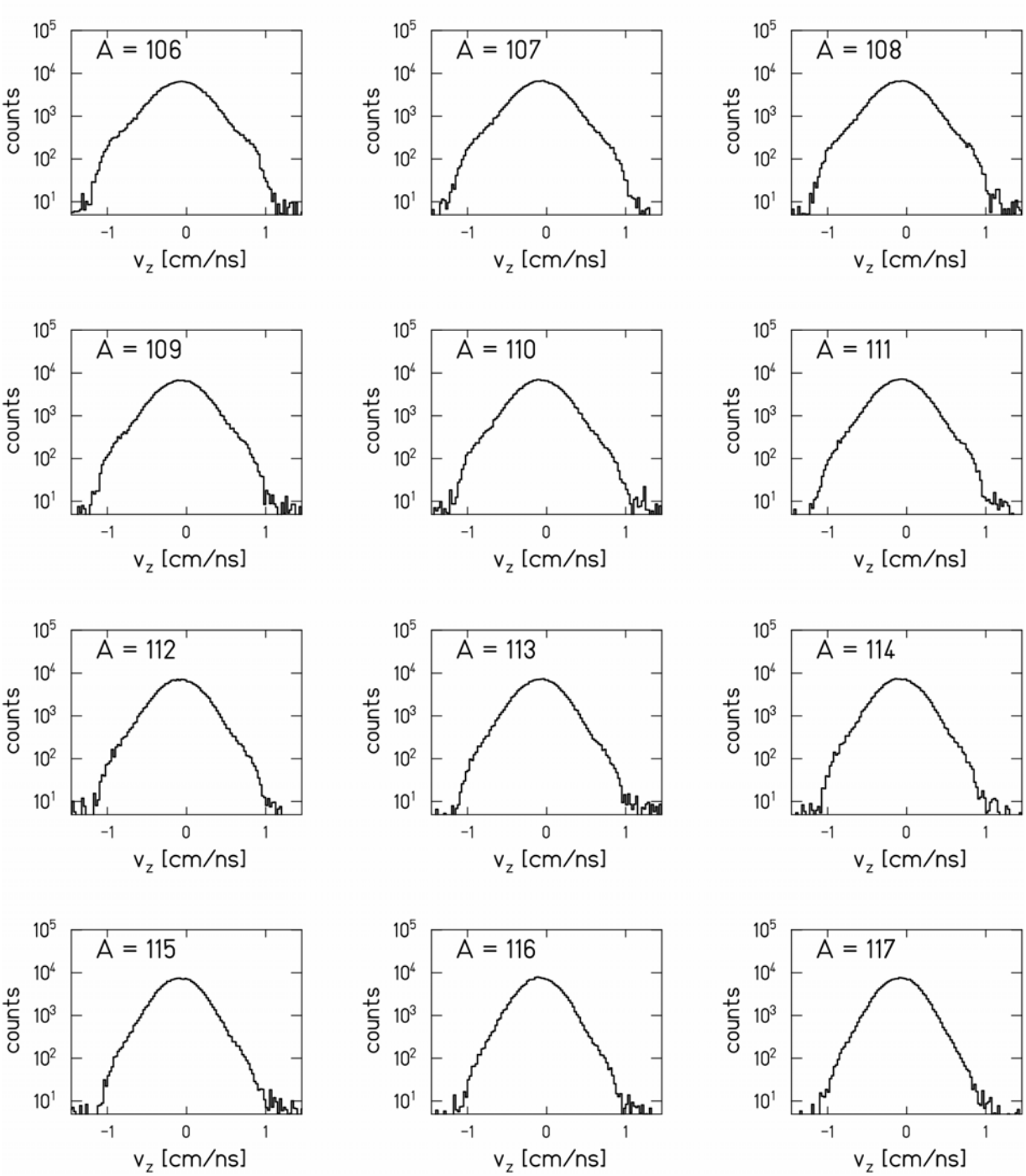
A = 106
A = 107
A = 108
A = 109
A = 110
A = 111
A = 112
A = 113
A = 114
A = 115
A = 116
A = 117
counts
v_z [cm/ns]

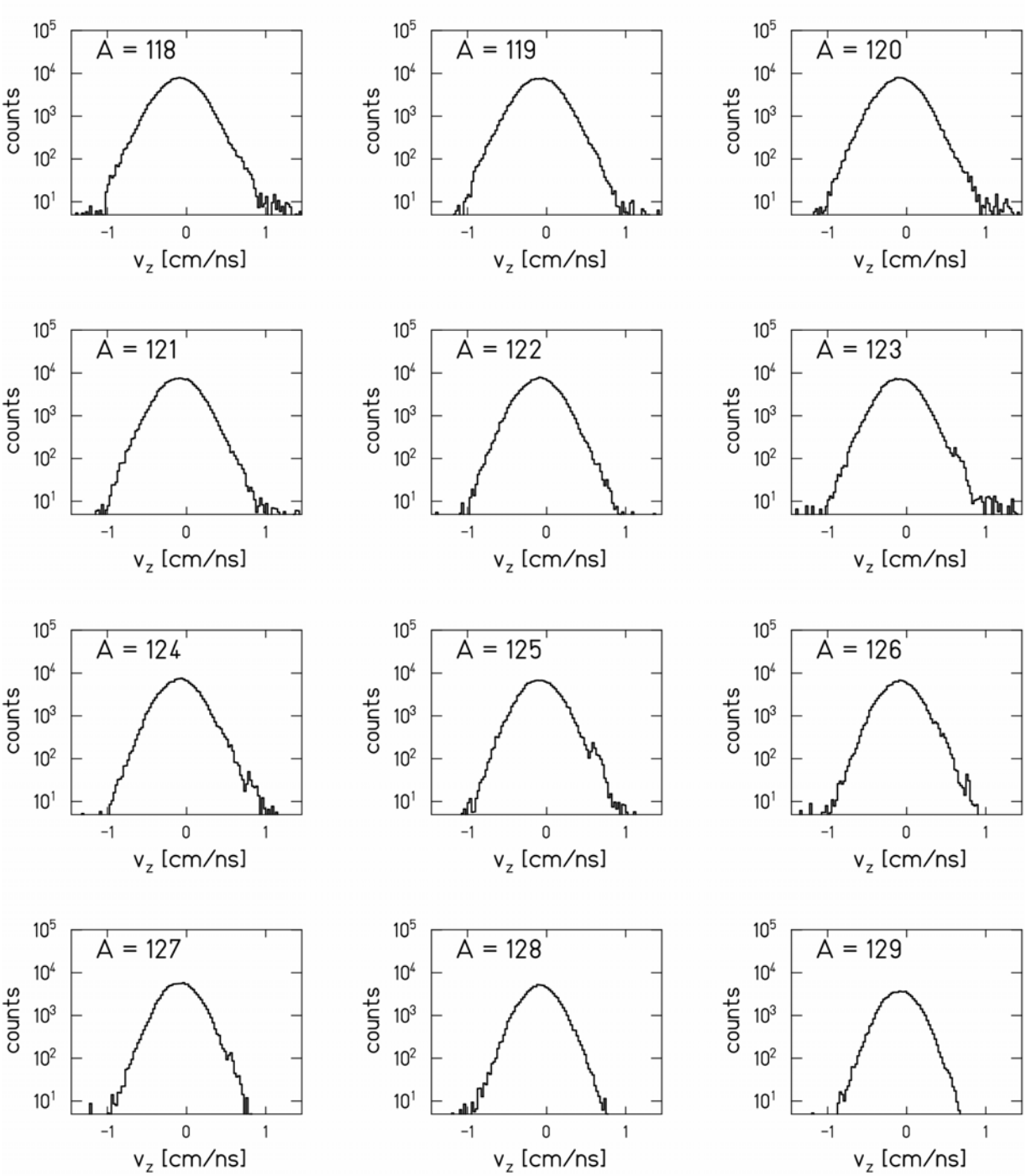
A = 118
A = 119
A = 120
A = 121
A = 122
A = 123
A = 124
A = 125
A = 126
A = 127
A = 128
A = 129
counts
v_z [cm/ns]

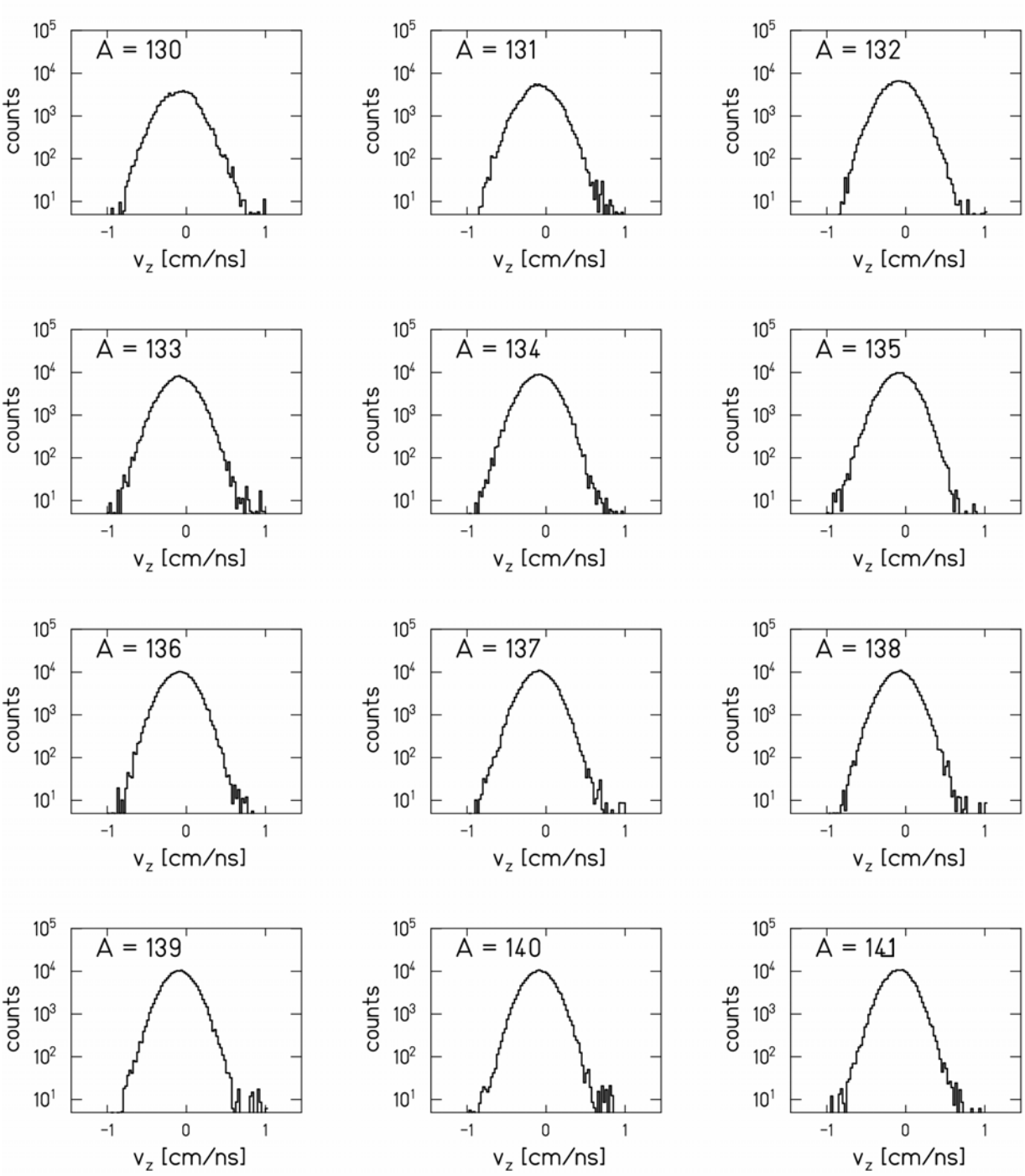
A = 130
A = 131
A = 132
A = 133
A = 134
A = 135
A = 136
A = 137
A = 138
A = 139
A = 140
A = 141
counts
v_z [cm/ns]

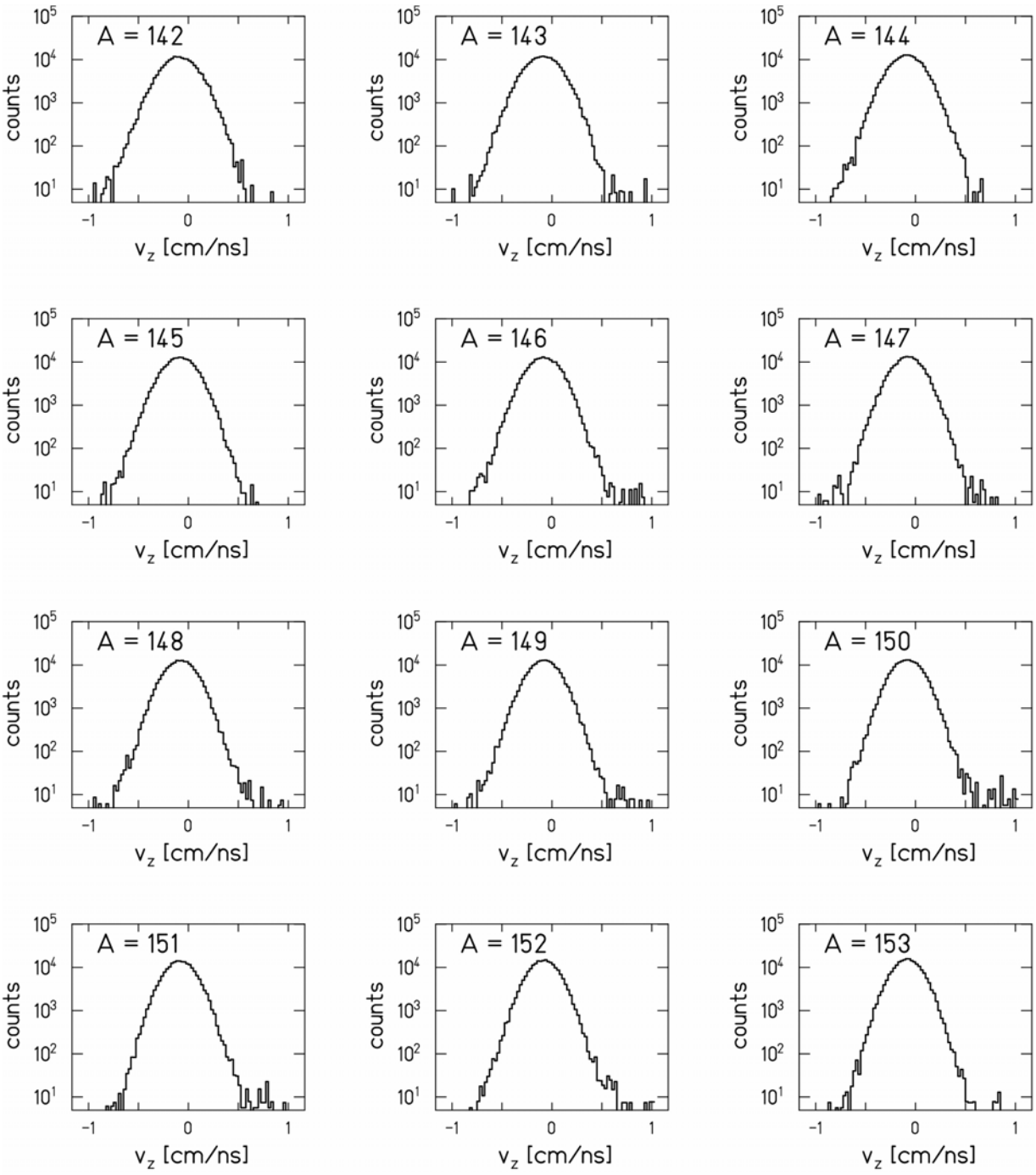
A = 142
A = 143
A = 144
A = 145
A = 146
A = 147
A = 148
A = 149
A = 150
A = 151
A = 152
A = 153
counts
v_z [cm/ns]

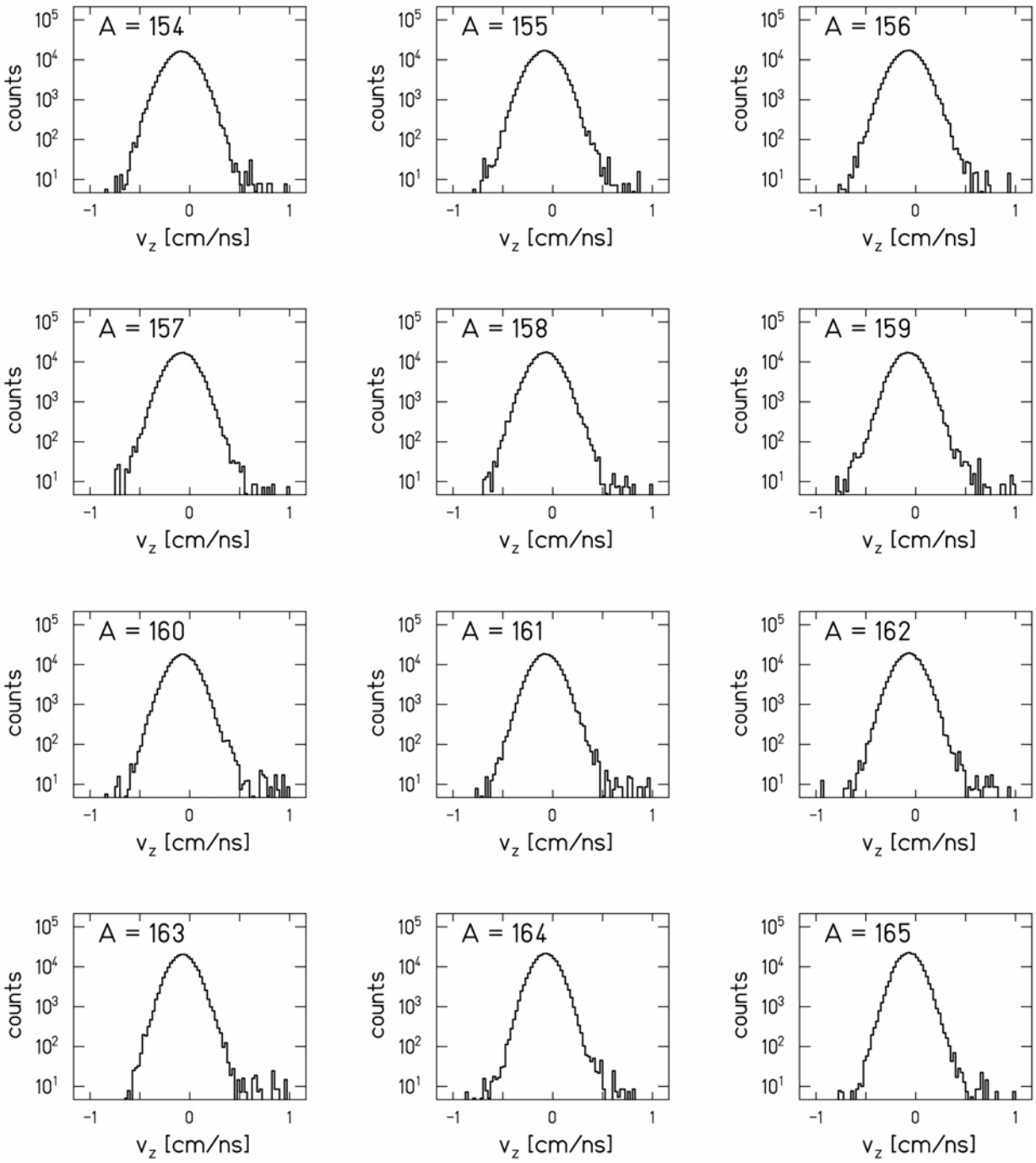
A = 154
A = 155
A = 156
A = 157
A = 158
A = 159
A = 160
A = 161
A = 162
A = 163
A = 164
A = 165
counts
v_z [cm/ns]

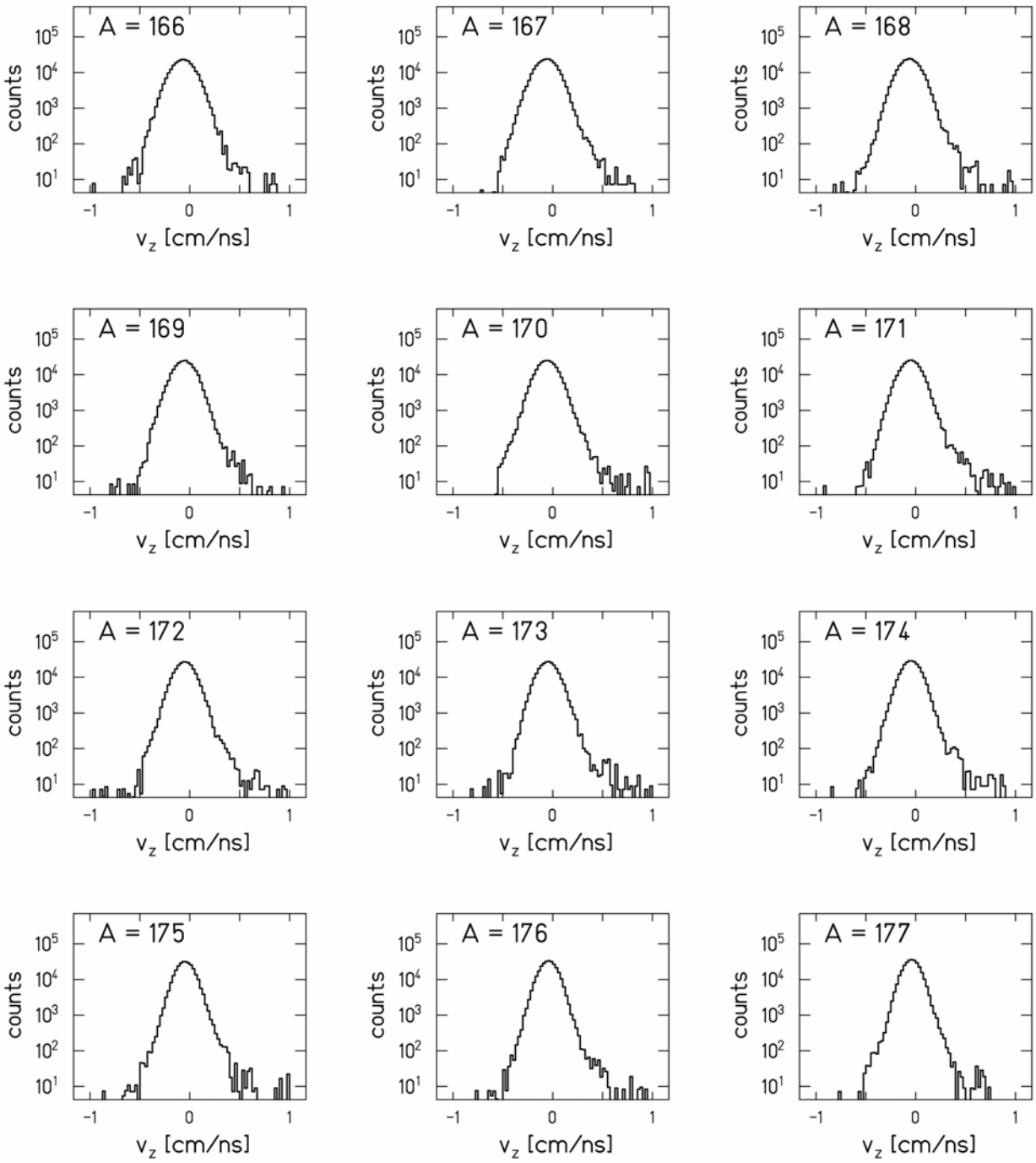
A = 166
A = 167
A = 168
A = 169
A = 170
A = 171
A = 172
A = 173
A = 174
A = 175
A = 176
A = 177
counts
v_z [cm/ns]

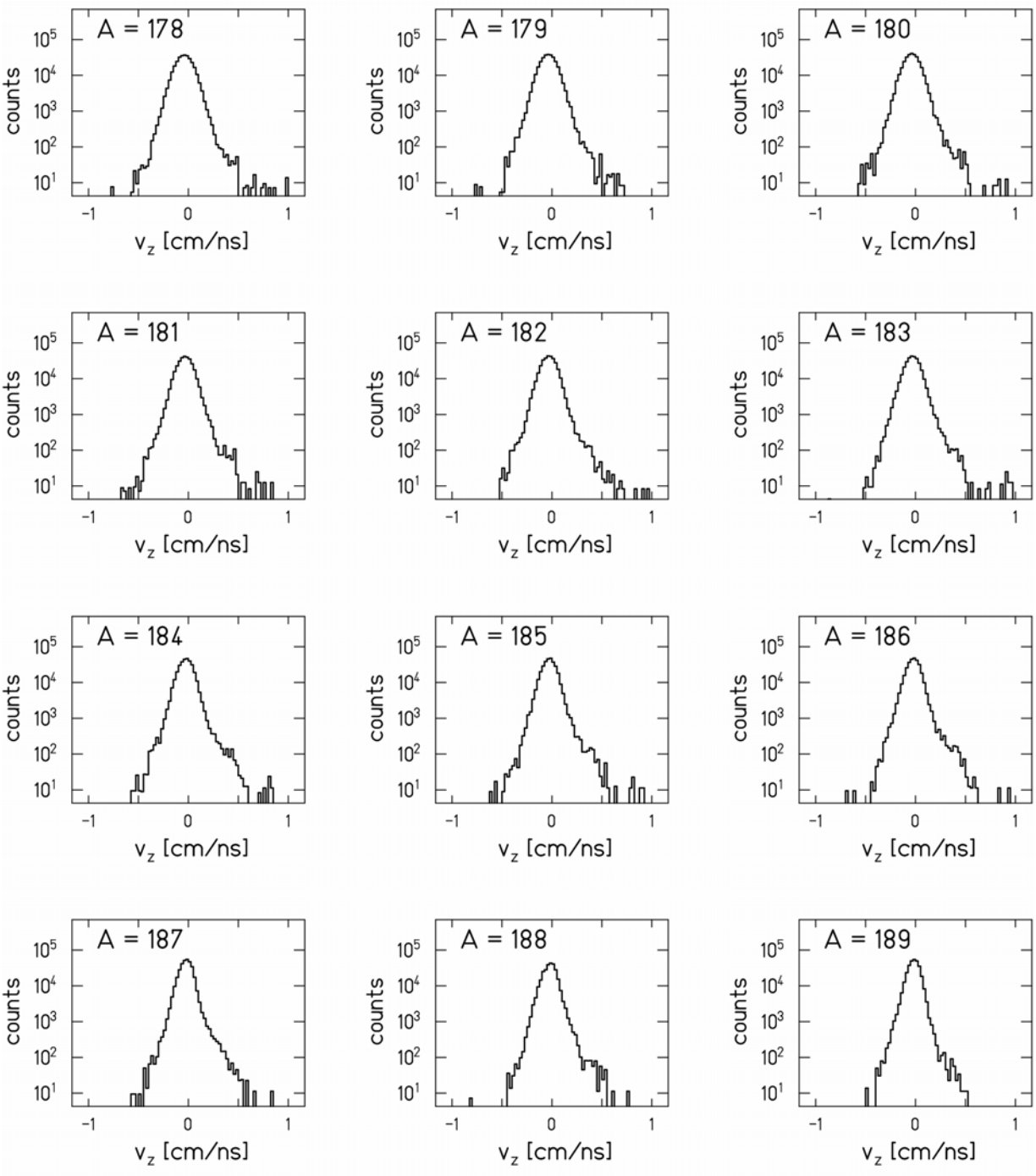
A = 178
A = 179
A = 180
A = 181
A = 182
A = 183
A = 184
A = 185
A = 186
A = 187
A = 188
A = 189
counts
v_z [cm/ns]

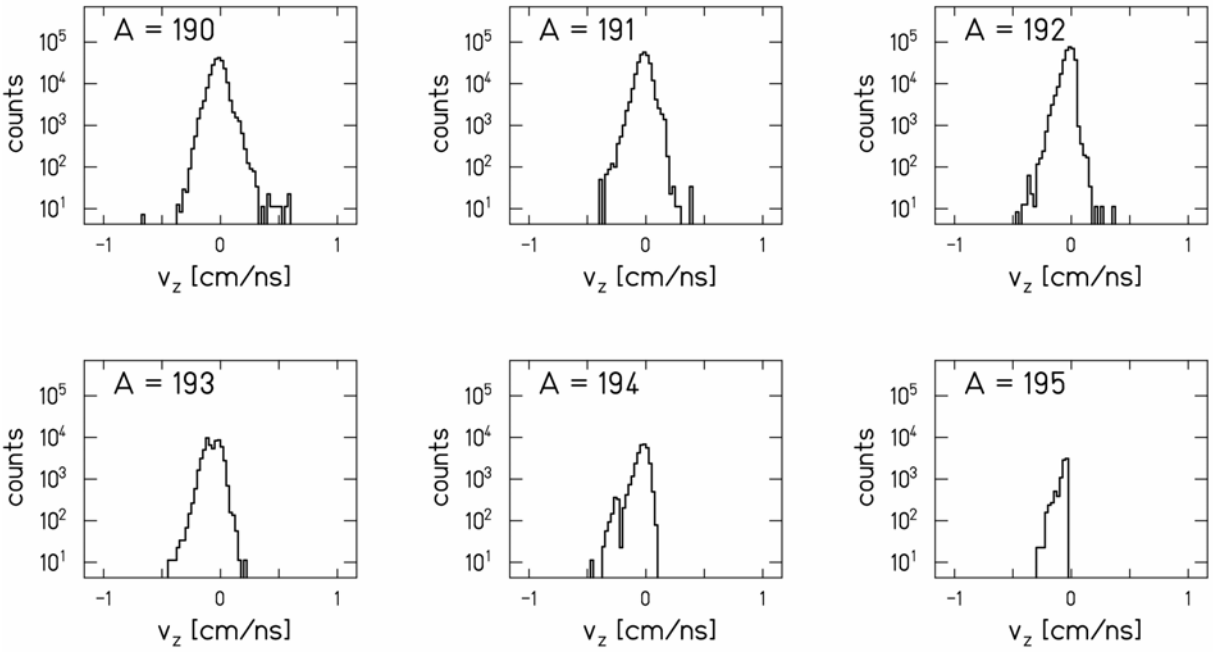
A = 190
A = 191
A = 192
A = 193
A = 194
A = 195
counts
v_z [cm/ns]

Appendix B2

Longitudinal velocity distributions of reaction residues with constant mass A_{res} in the reference frame of the primary beam measured in the experiment ^{197}Au+^{197}Au at 500 A MeV. The displayed differential yields are corrected for the dead-time, normalized to the same total beam intensity and corrected for the angular transmission dependence on the position at the intermediate and final focal plane. The longitudinal velocity distributions were reconstructed using the procedures described in chap.3.4. The staggering of the data in the region of low residue masses A_{res} and the asymmetry of the distributions in mass region around A_{res}~140 are caused by the border effects, i.e. incomplete coverage of these distributions in the measurement.

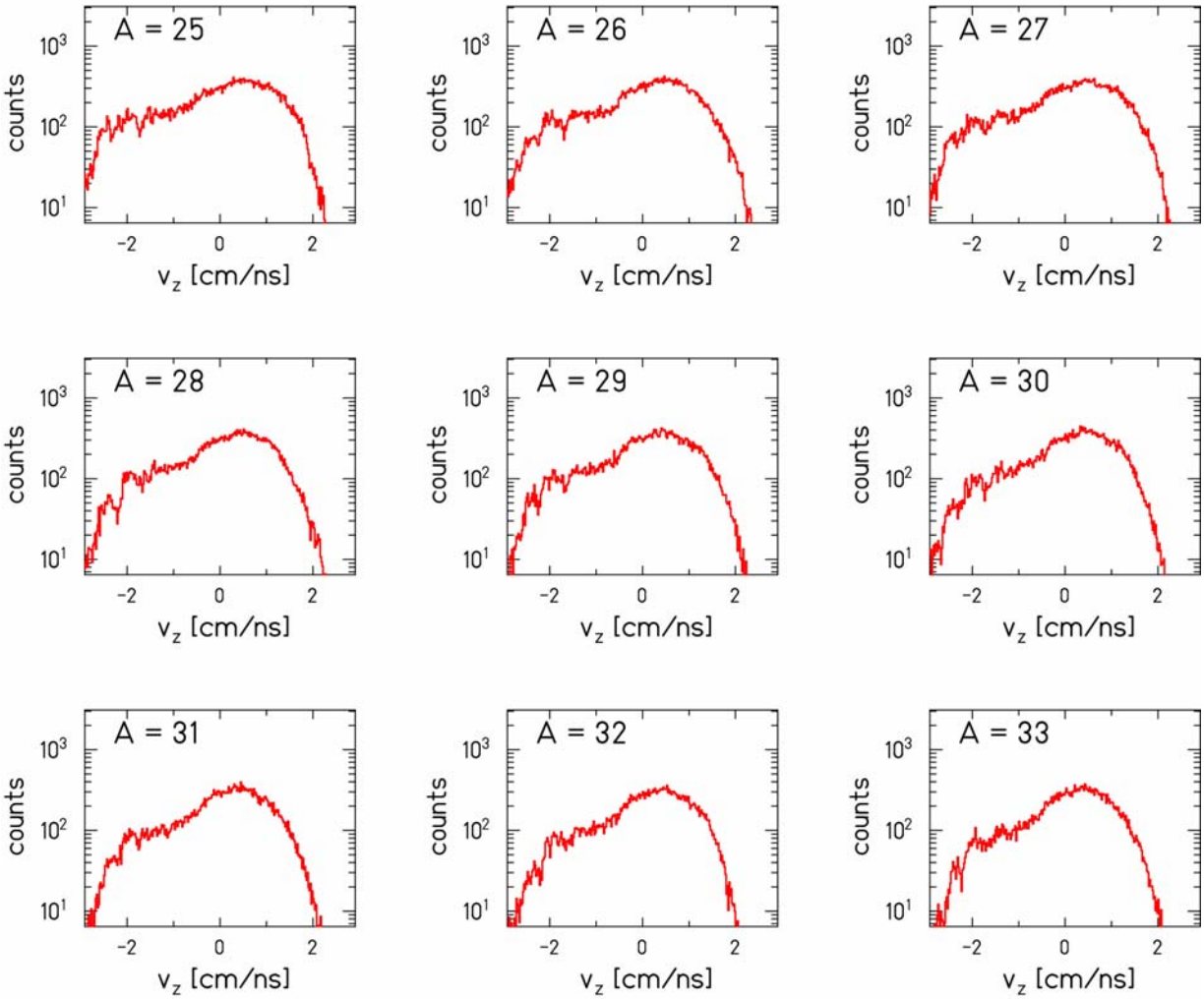

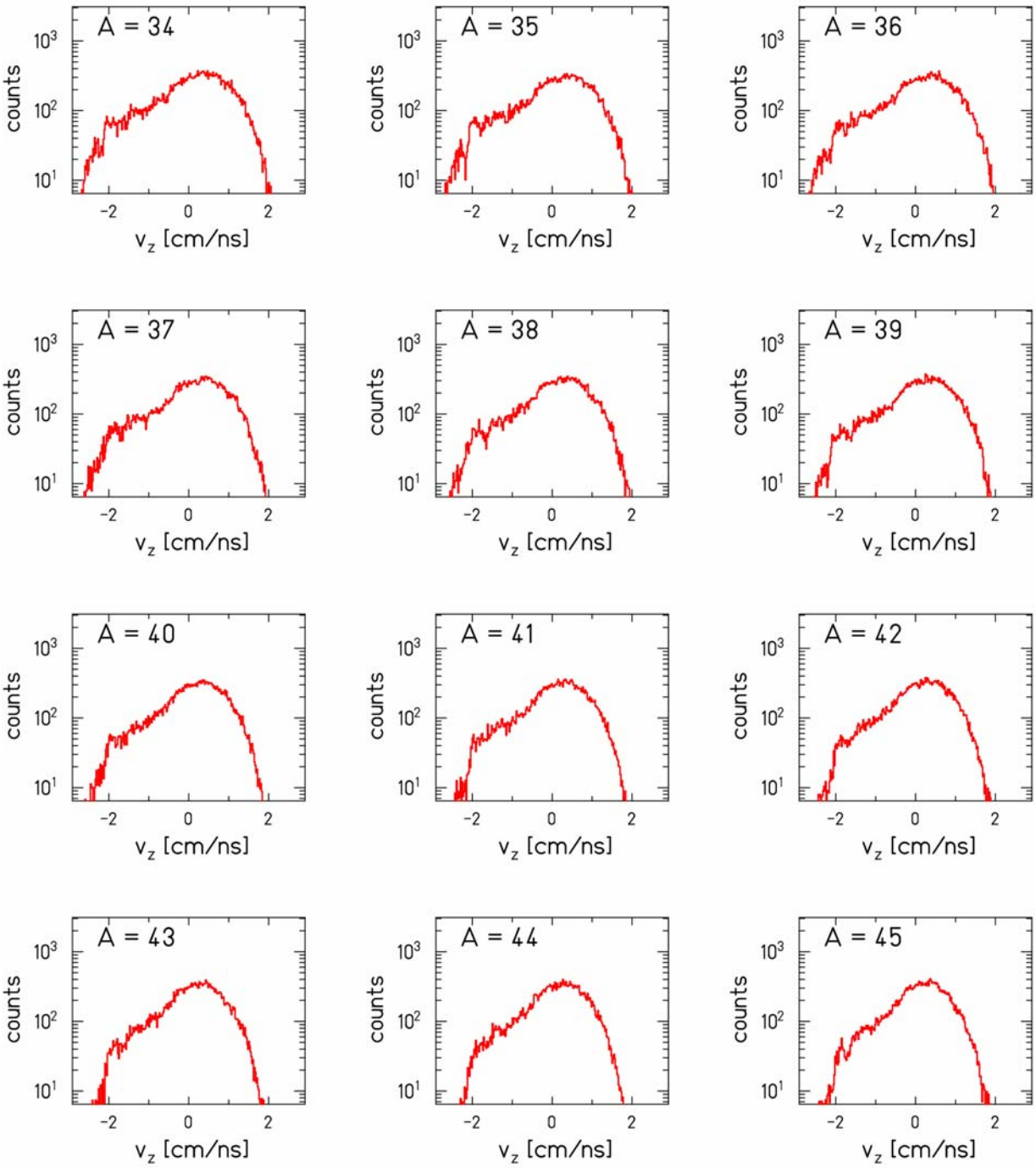
A = 34
A = 35
A = 36
A = 37
A = 38
A = 39
A = 40
A = 41
A = 42
A = 43
A = 44
A = 45
counts
v_z [cm/ns]

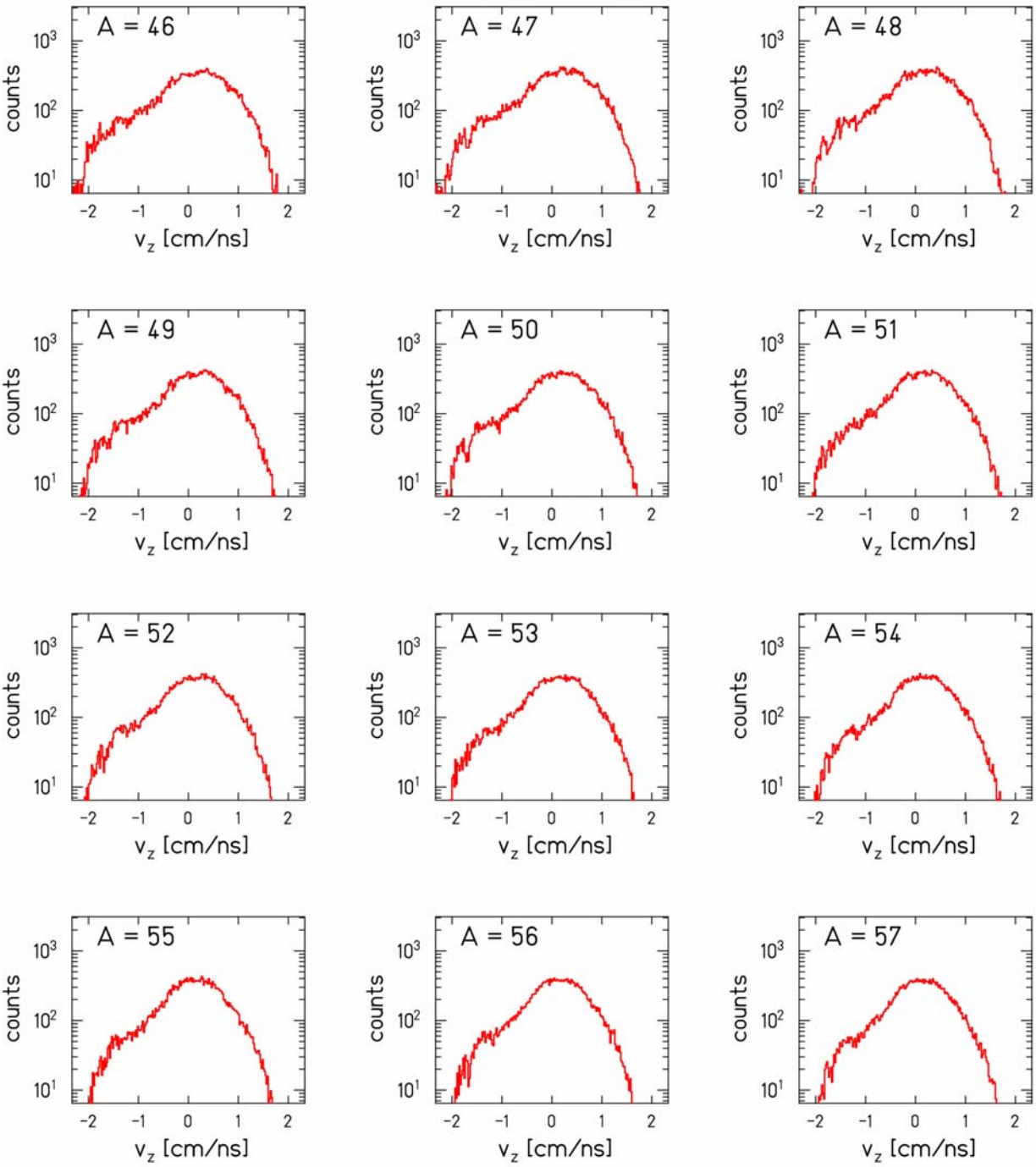
A = 46
A = 47
A = 48
A = 49
A = 50
A = 51
A = 52
A = 53
A = 54
A = 55
A = 56
A = 57
counts
v_z [cm/ns]

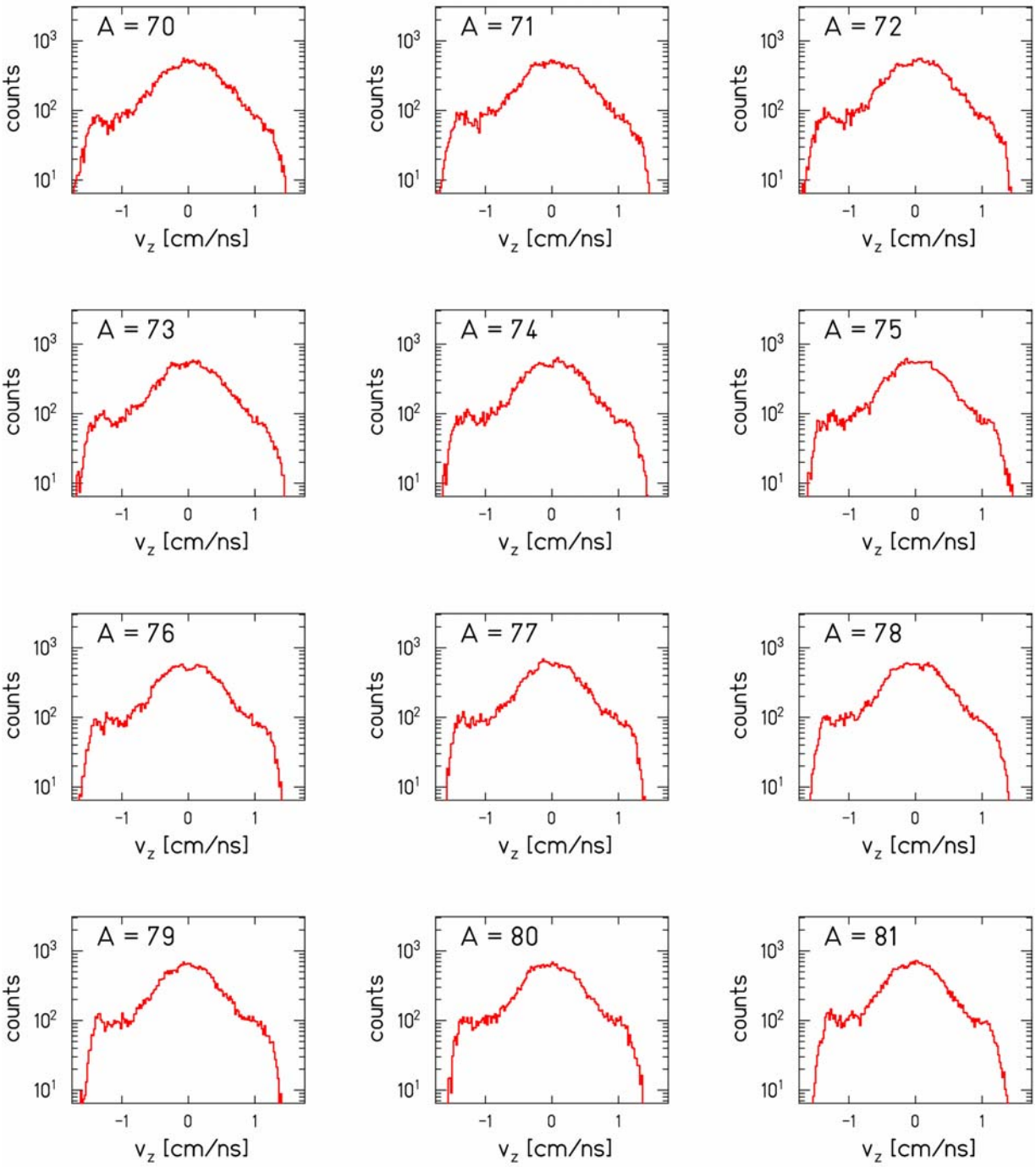
A = 70
A = 71
A = 72
A = 73
A = 74
A = 75
A = 76
A = 77
A = 78
A = 79
A = 80
A = 81
counts
v_z [cm/ns]

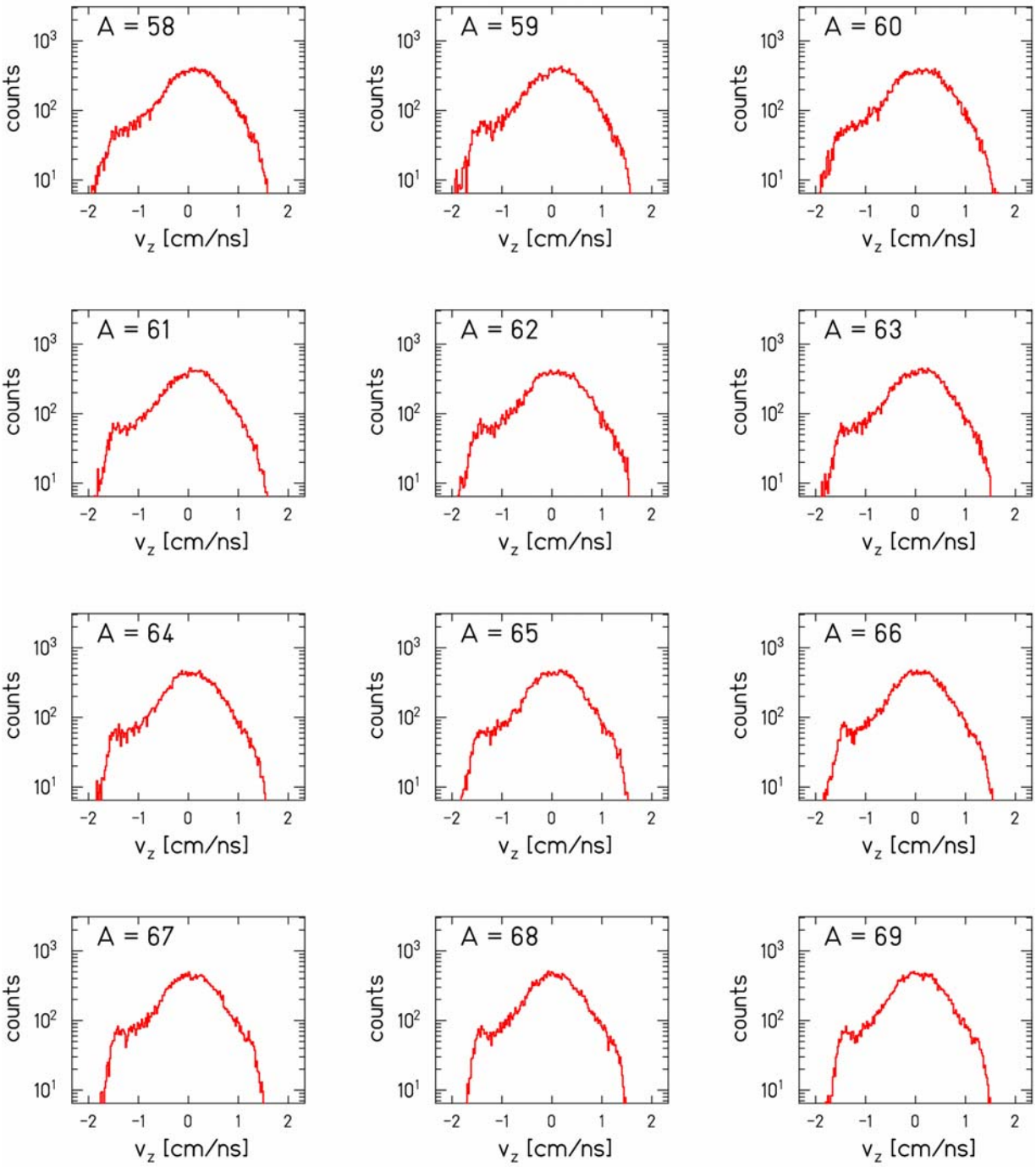
A = 58
A = 59
A = 60
A = 61
A = 62
A = 63
A = 64
A = 65
A = 66
A = 67
A = 68
A = 69
counts
v_z [cm/ns]

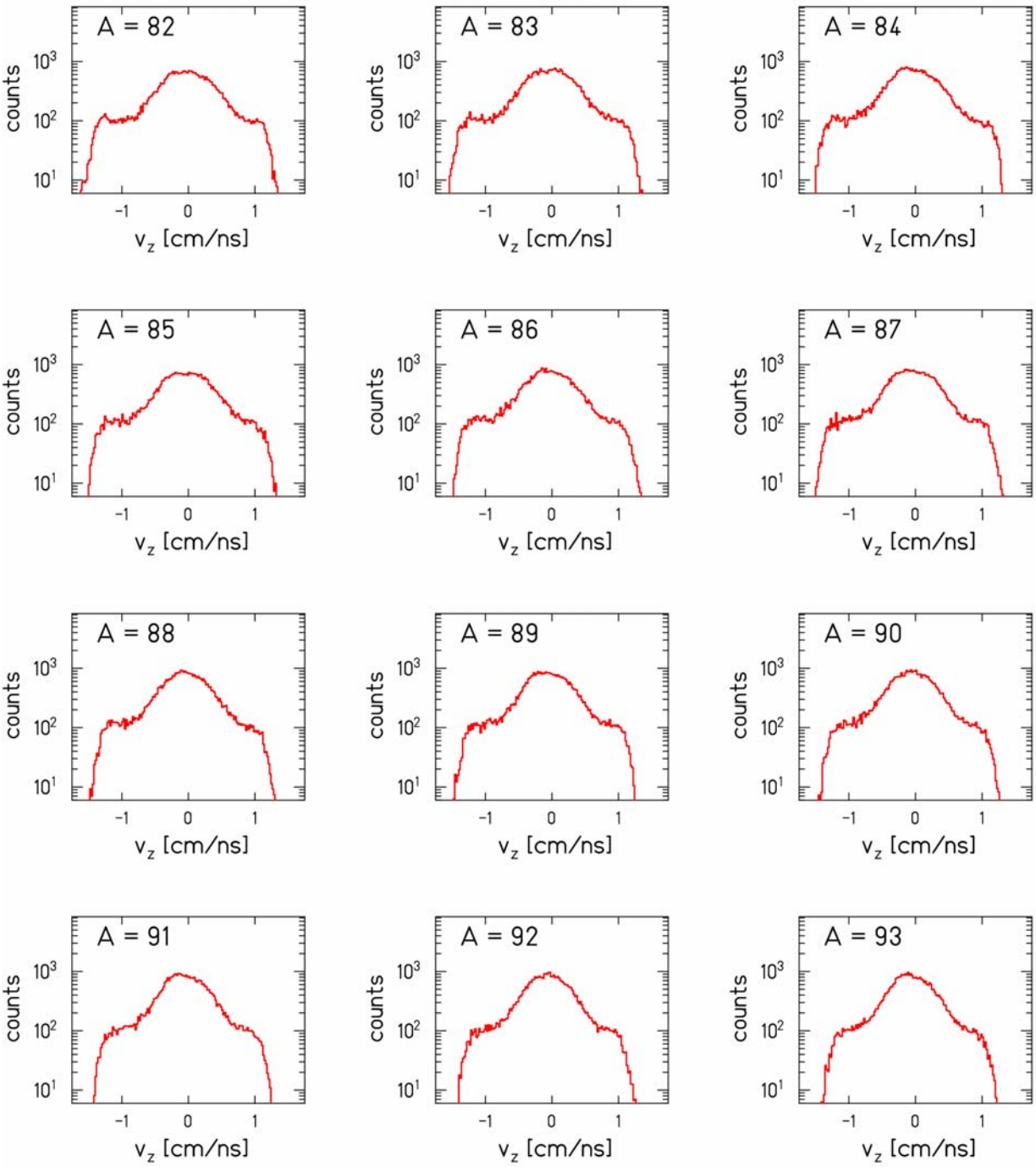
A = 82
A = 83
A = 84
A = 85
A = 86
A = 87
A = 88
A = 89
A = 90
A = 91
A = 92
A = 93
counts
10^3
10^2
10^1
−1
0
1
v_z [cm/ns]

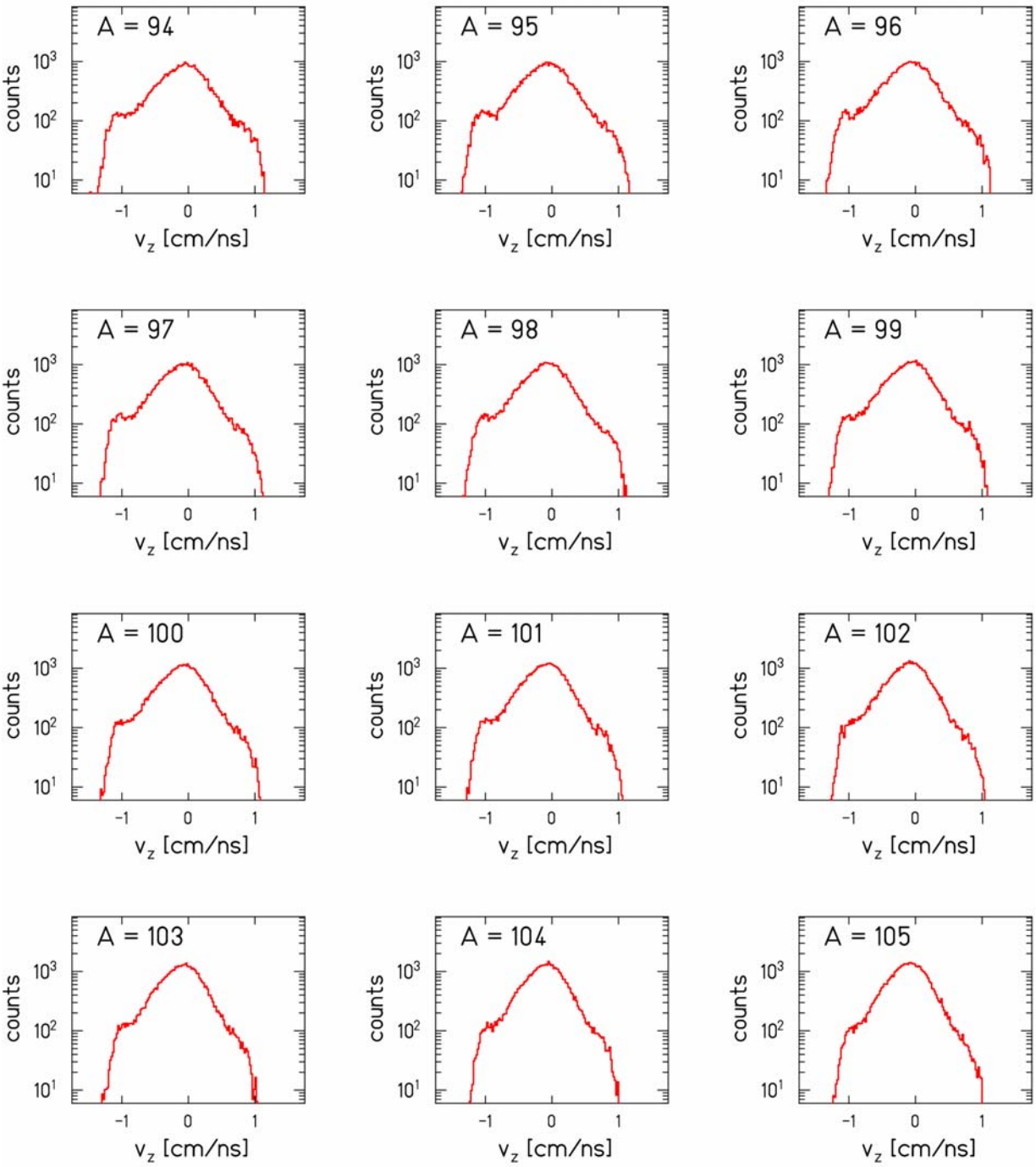
A = 94
A = 95
A = 96
A = 97
A = 98
A = 99
A = 100
A = 101
A = 102
A = 103
A = 104
A = 105
counts
10^3
10^2
10^1
−1
0
1
v_z [cm/ns]

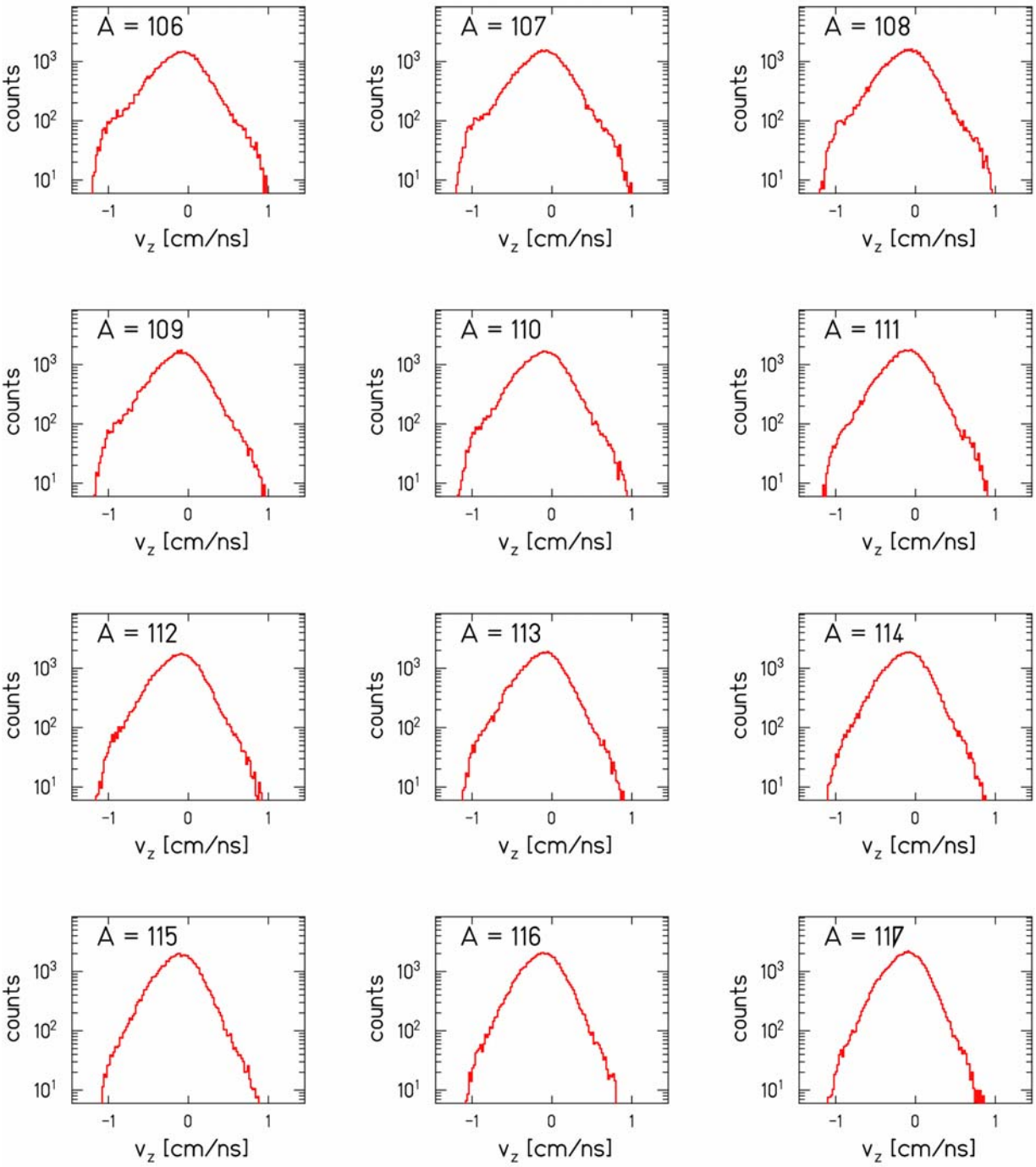
A = 106
A = 107
A = 108
A = 109
A = 110
A = 111
A = 112
A = 113
A = 114
A = 115
A = 116
A = 117
counts
v_z [cm/ns]

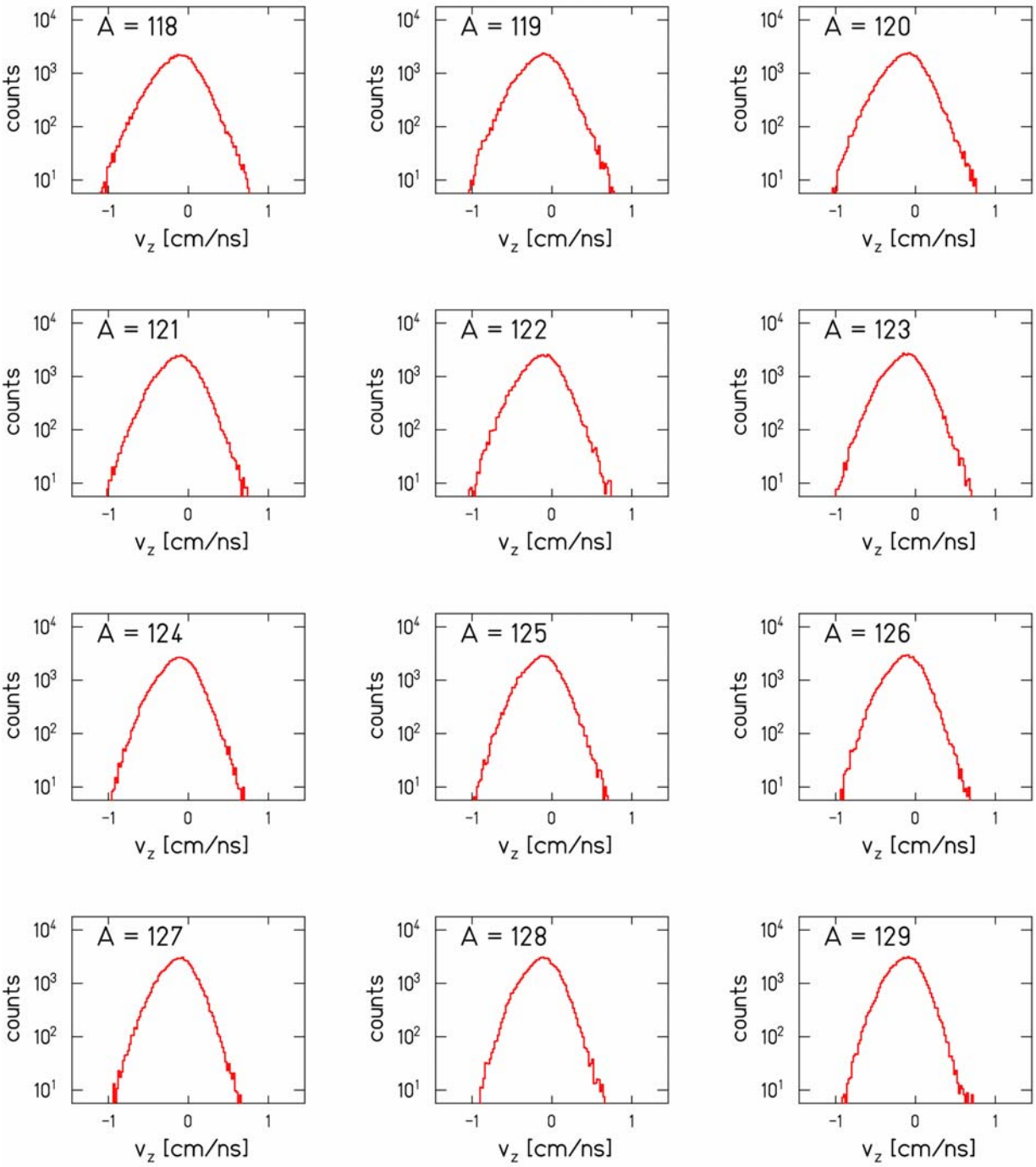
A = 118
A = 119
A = 120
A = 121
A = 122
A = 123
A = 124
A = 125
A = 126
A = 127
A = 128
A = 129
counts
v_z [cm/ns]

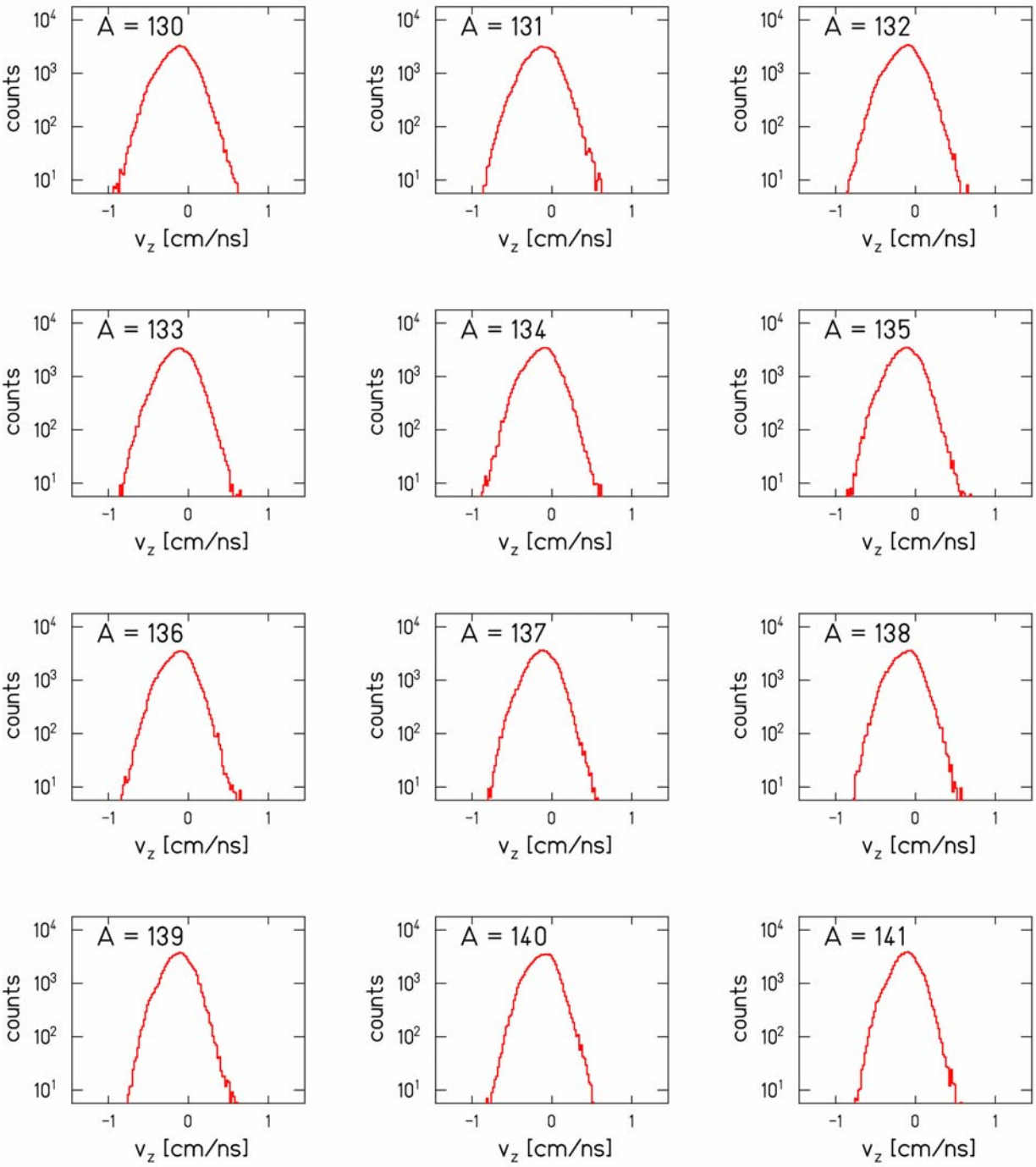
A = 130
A = 131
A = 132
A = 133
A = 134
A = 135
A = 136
A = 137
A = 138
A = 139
A = 140
A = 141
counts
v_z [cm/ns]

Appendix B3

Longitudinal velocity distributions of reaction residues with constant mass A_{res} in the reference frame of the primary beam measured in the experiment ^{197}Au+^{27}Al at 500 A MeV. The displayed differential yields are corrected for the dead-time, normalized to the same total beam intensity and corrected for the angular transmission dependence on the position at the intermediate and final focal plane. The longitudinal velocity distributions were reconstructed using the procedures described in chap.3.4. The staggering of the data in the region of low residue masses A_{res} and the asymmetry of the distributions in mass region around A_{res}~140 are caused by the border effects, i.e. incomplete coverage of these distributions in the measurement.

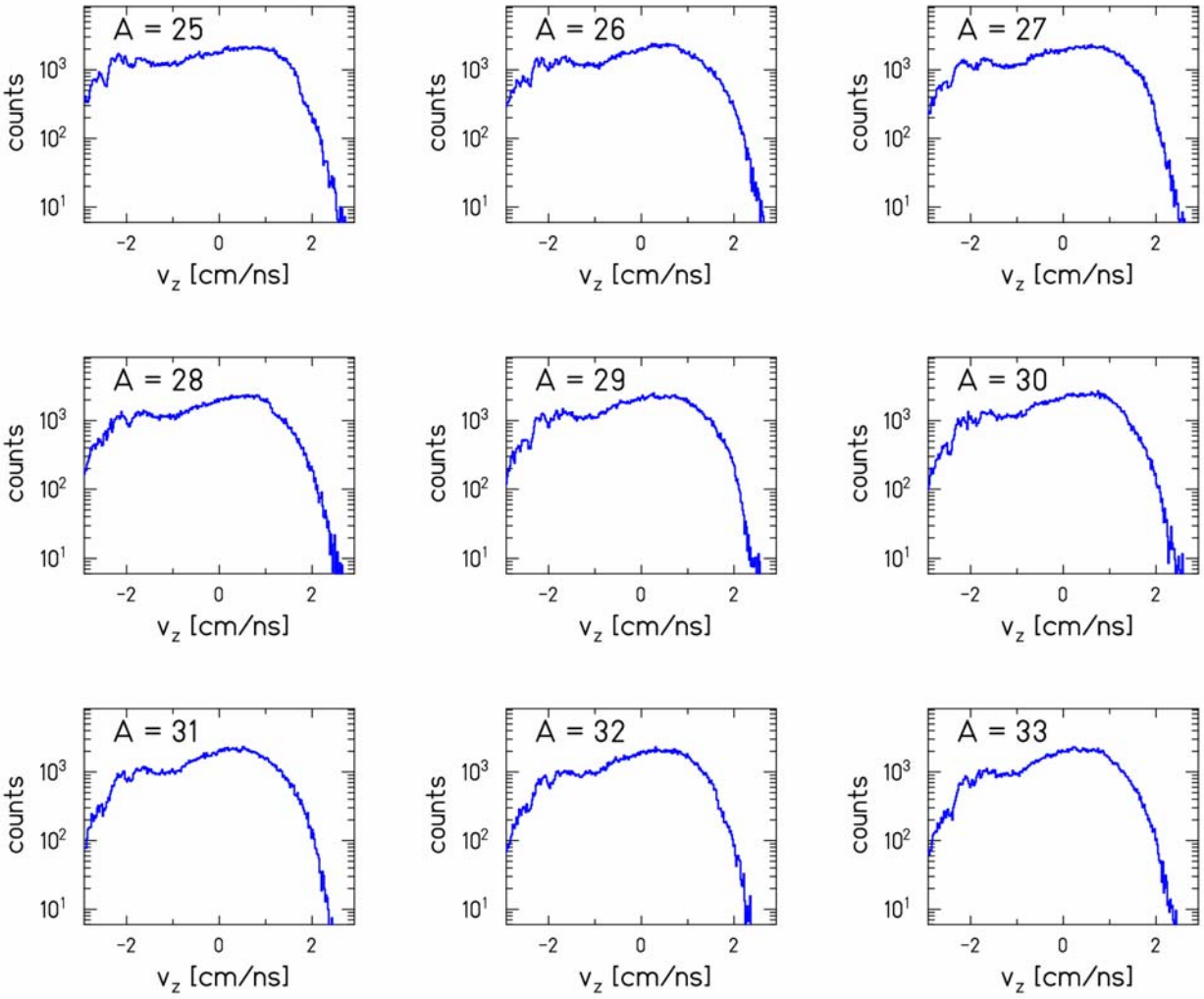

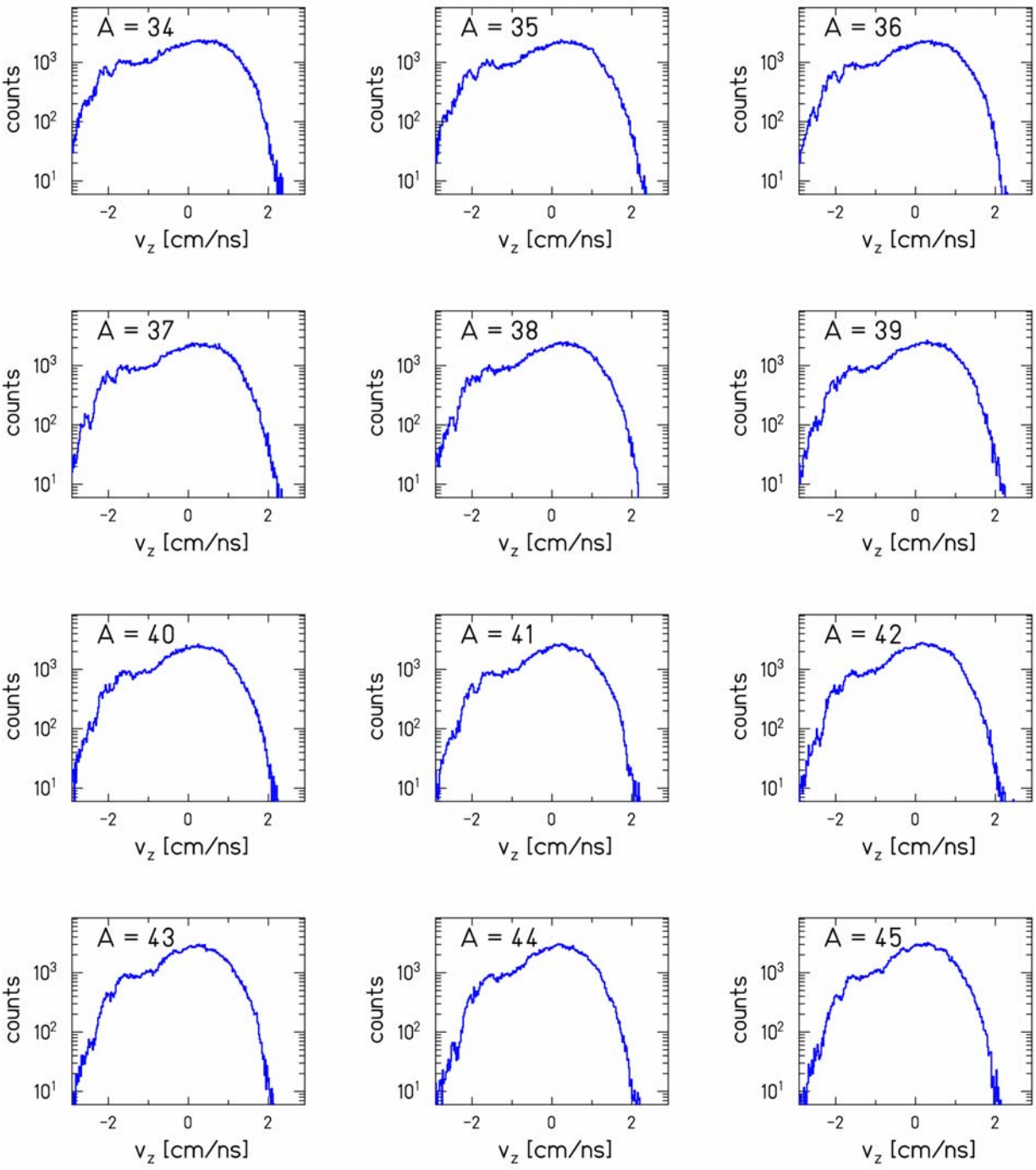
A = 34
A = 35
A = 36
A = 37
A = 38
A = 39
A = 40
A = 41
A = 42
A = 43
A = 44
A = 45
counts
v_z [cm/ns]

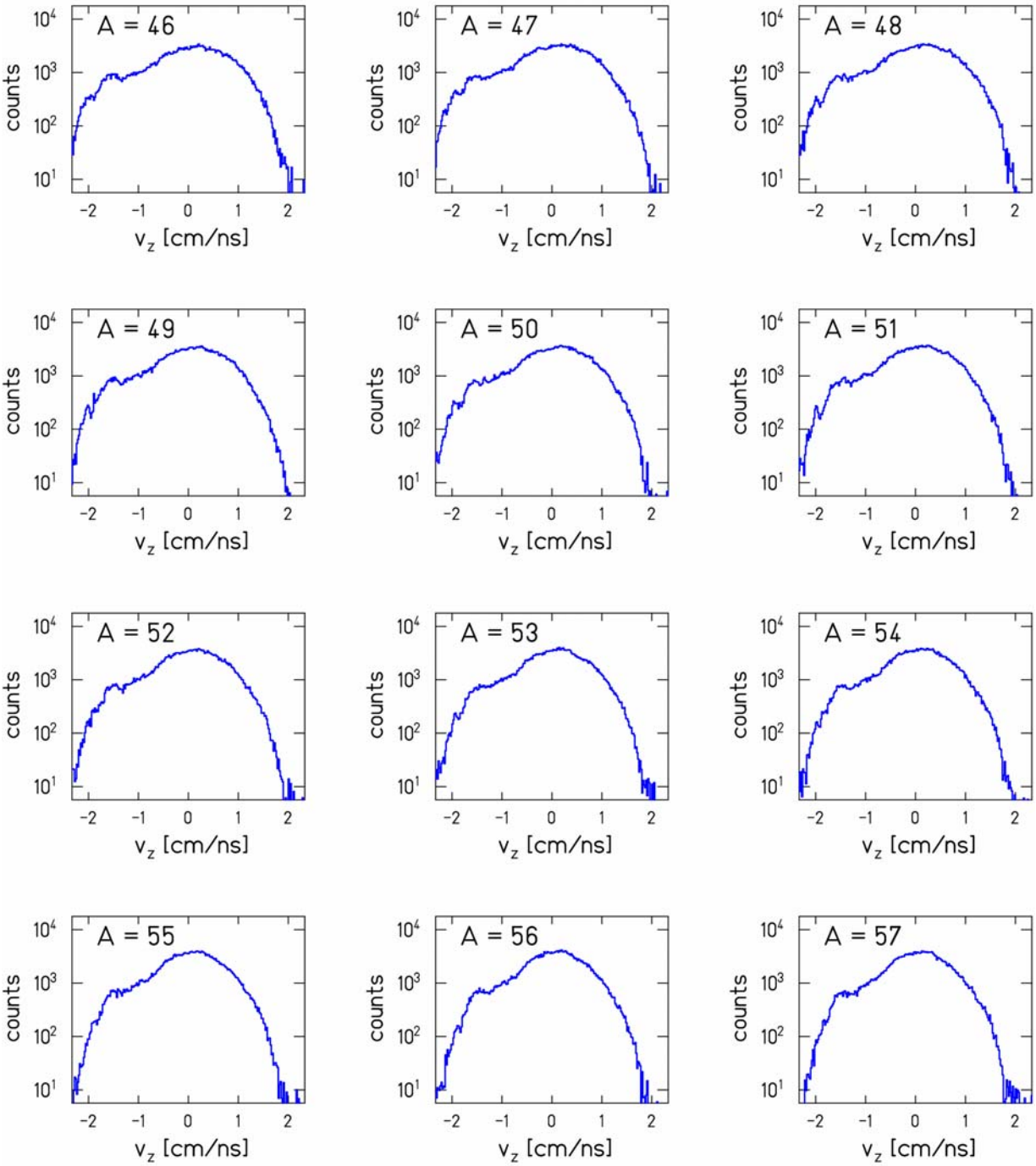
A = 46
A = 47
A = 48
A = 49
A = 50
A = 51
A = 52
A = 53
A = 54
A = 55
A = 56
A = 57
counts
v_z [cm/ns]

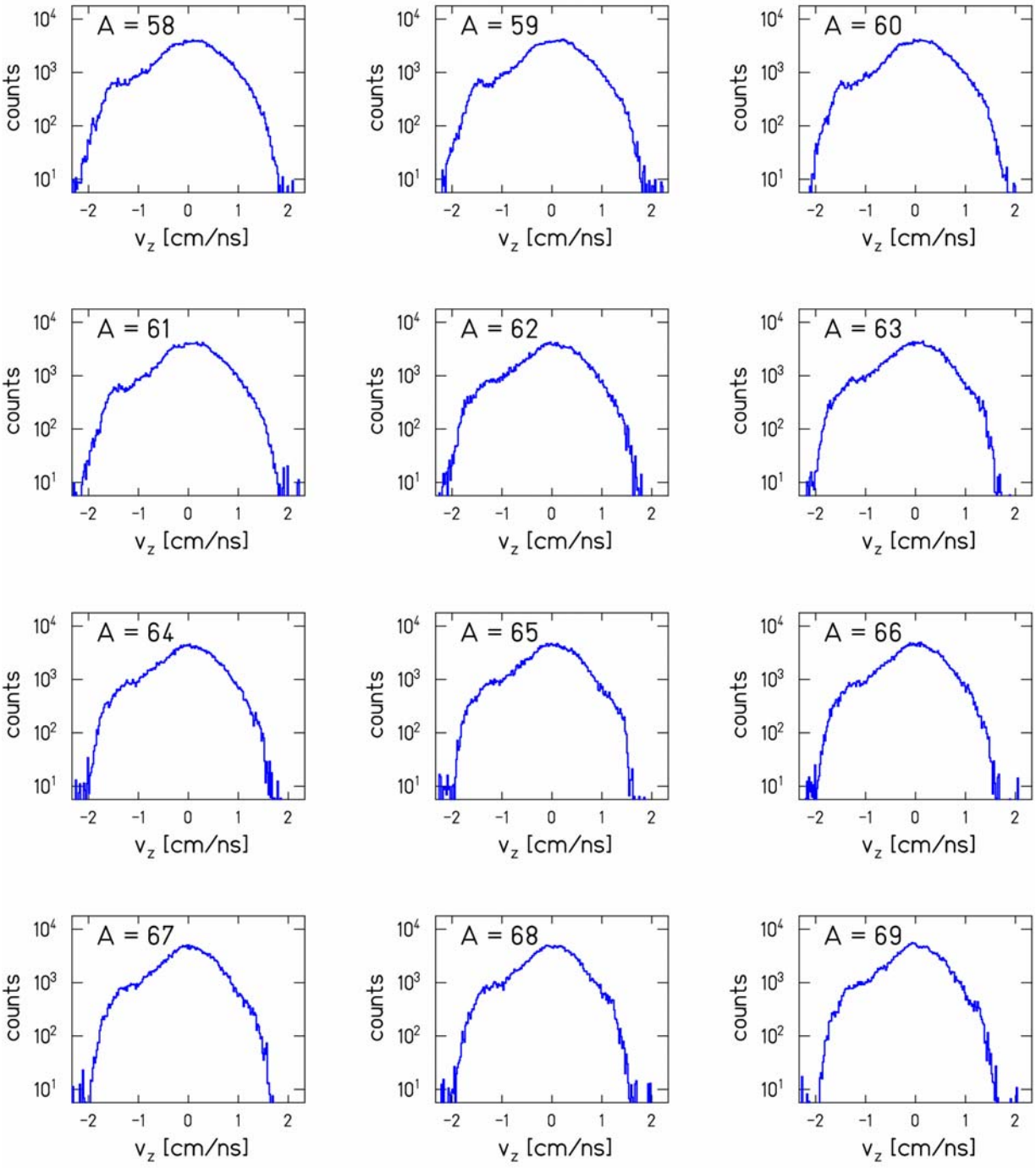
A = 58
A = 59
A = 60
A = 61
A = 62
A = 63
A = 64
A = 65
A = 66
A = 67
A = 68
A = 69
counts
v_z [cm/ns]

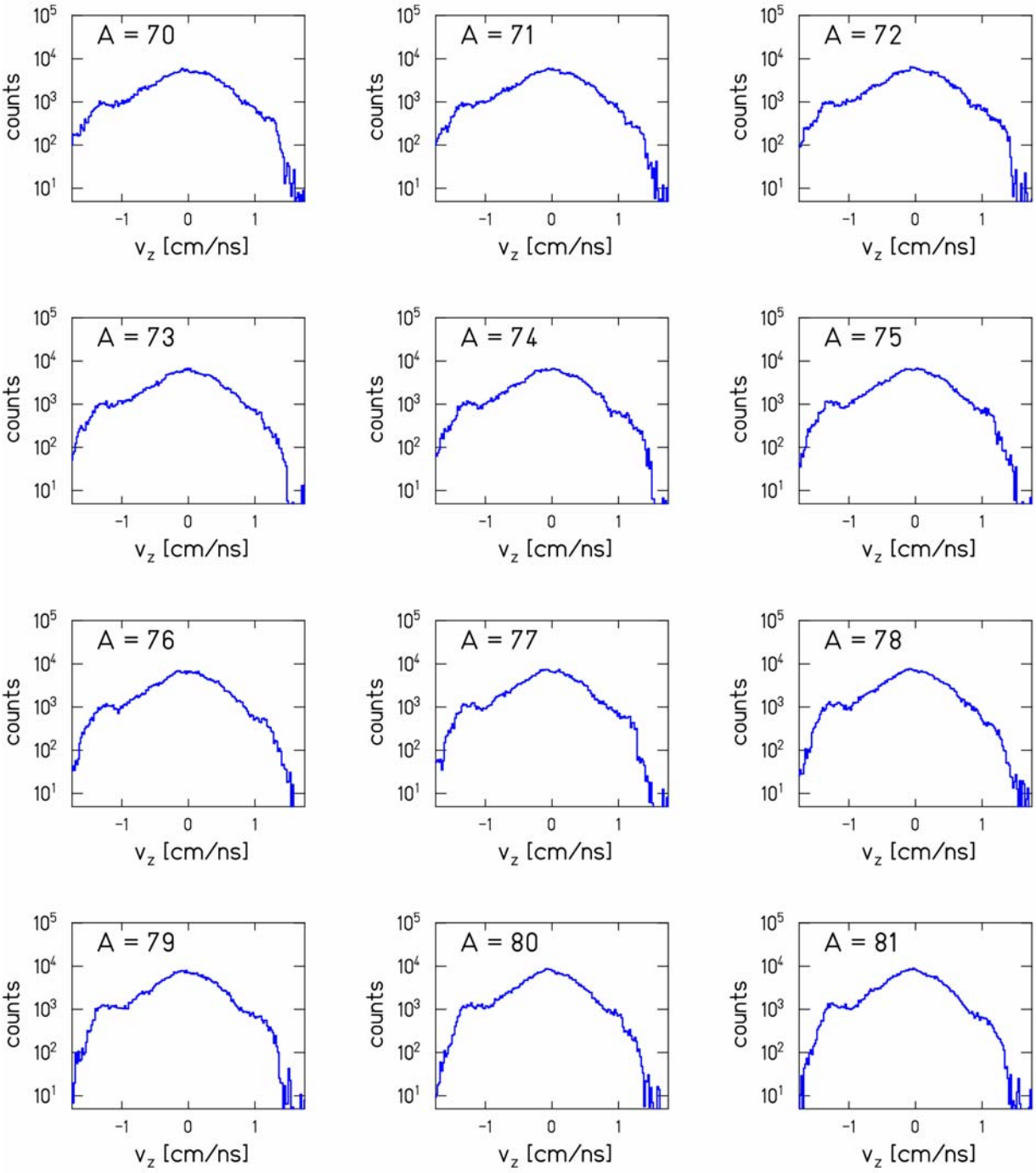
A = 70
A = 71
A = 72
A = 73
A = 74
A = 75
A = 76
A = 77
A = 78
A = 79
A = 80
A = 81
counts
v_z [cm/ns]

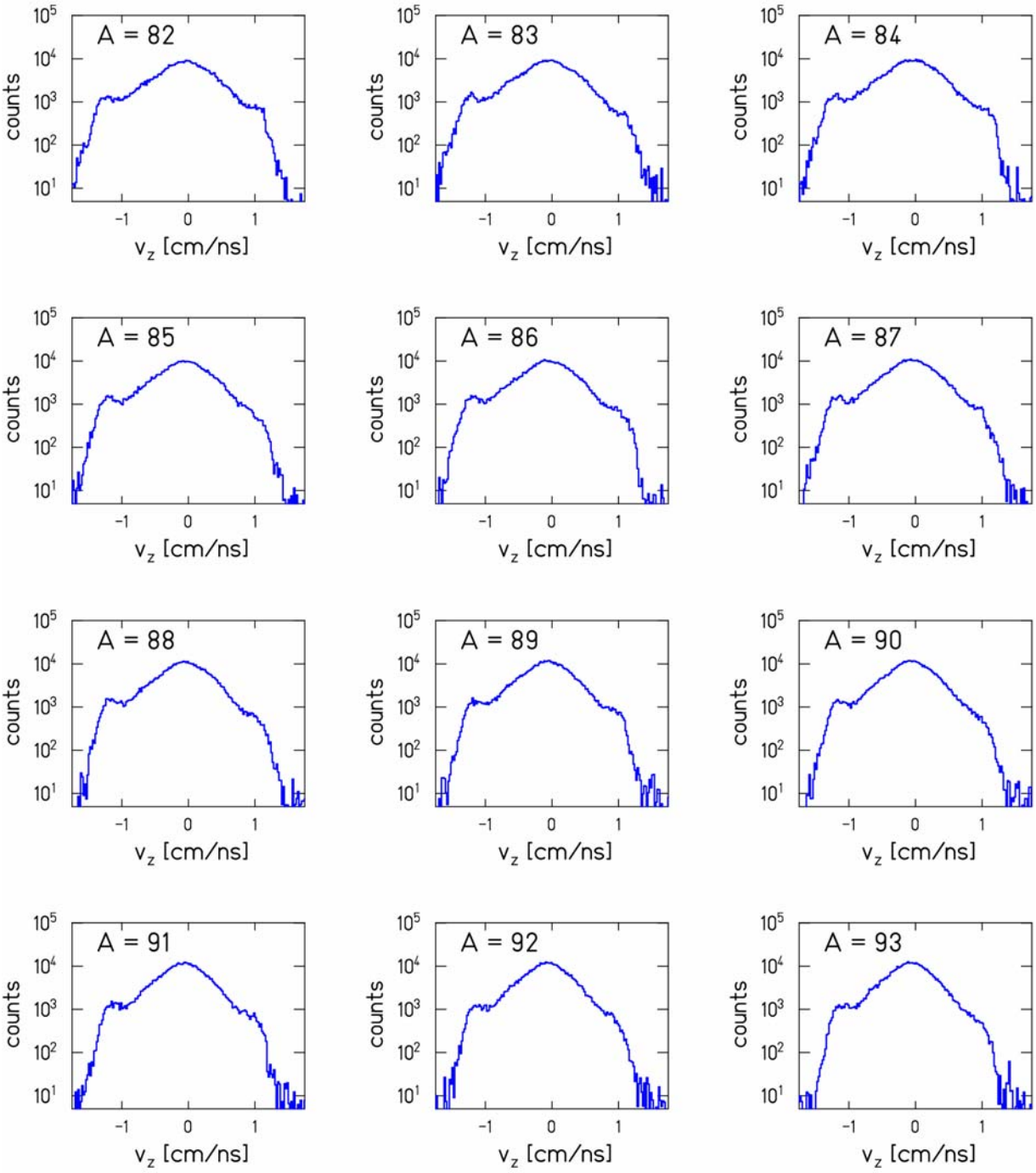
A = 82
A = 83
A = 84
A = 85
A = 86
A = 87
A = 88
A = 89
A = 90
A = 91
A = 92
A = 93
counts
v_z [cm/ns]

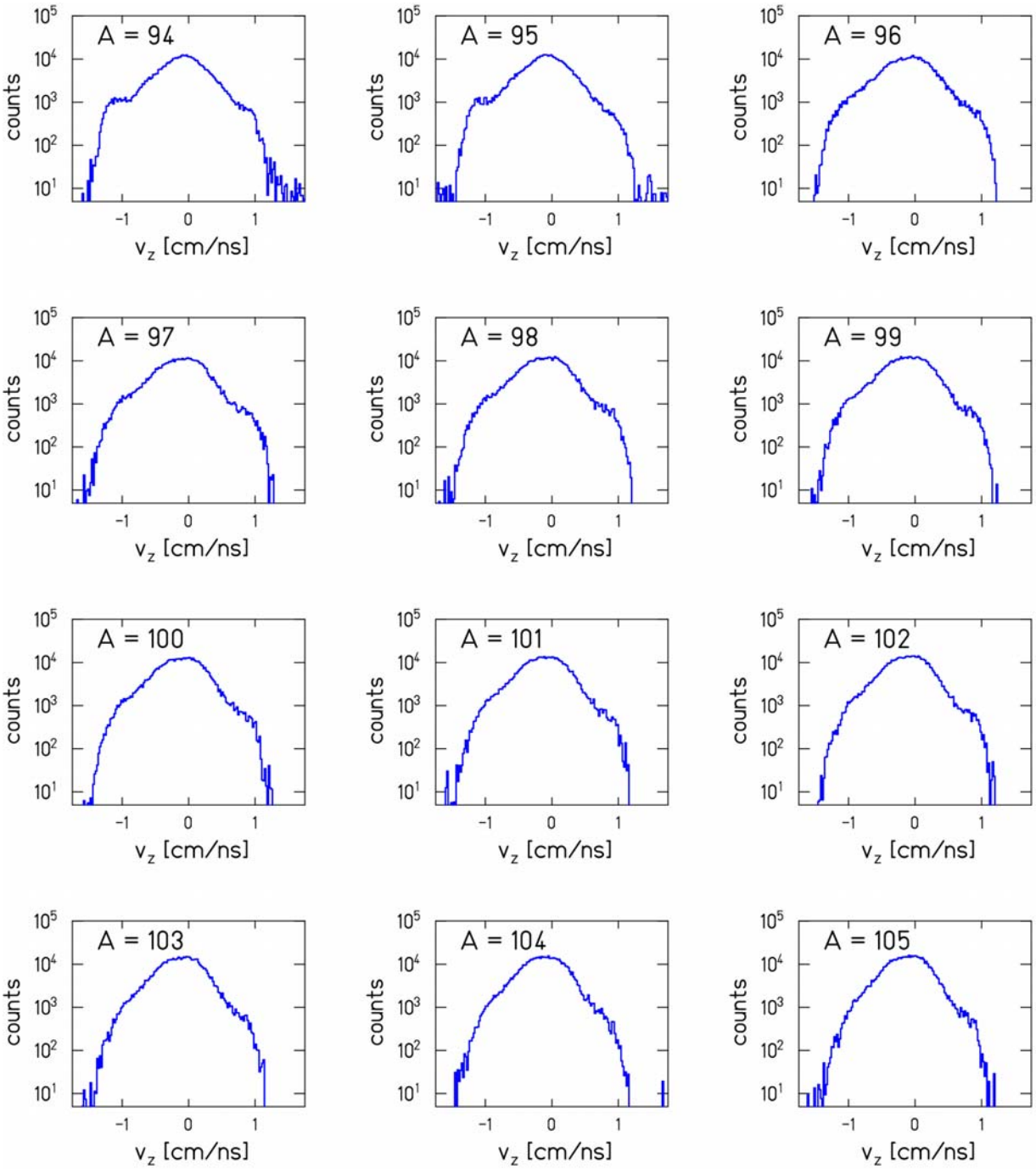
A = 94
A = 95
A = 96
A = 97
A = 98
A = 99
A = 100
A = 101
A = 102
A = 103
A = 104
A = 105
counts
v_z [cm/ns]

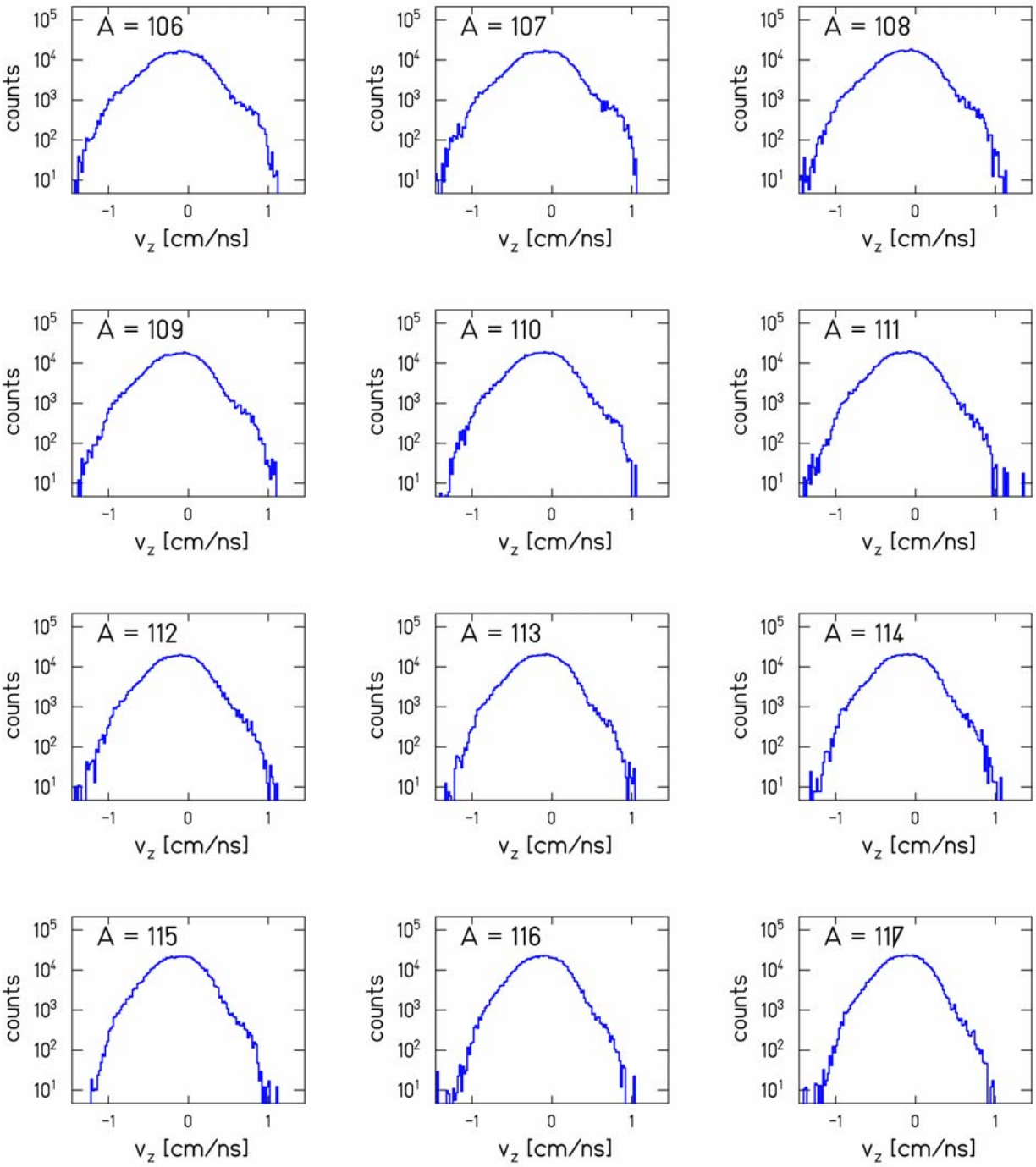
A = 106
A = 107
A = 108
A = 109
A = 110
A = 111
A = 112
A = 113
A = 114
A = 115
A = 116
A = 117
counts
v_z [cm/ns]

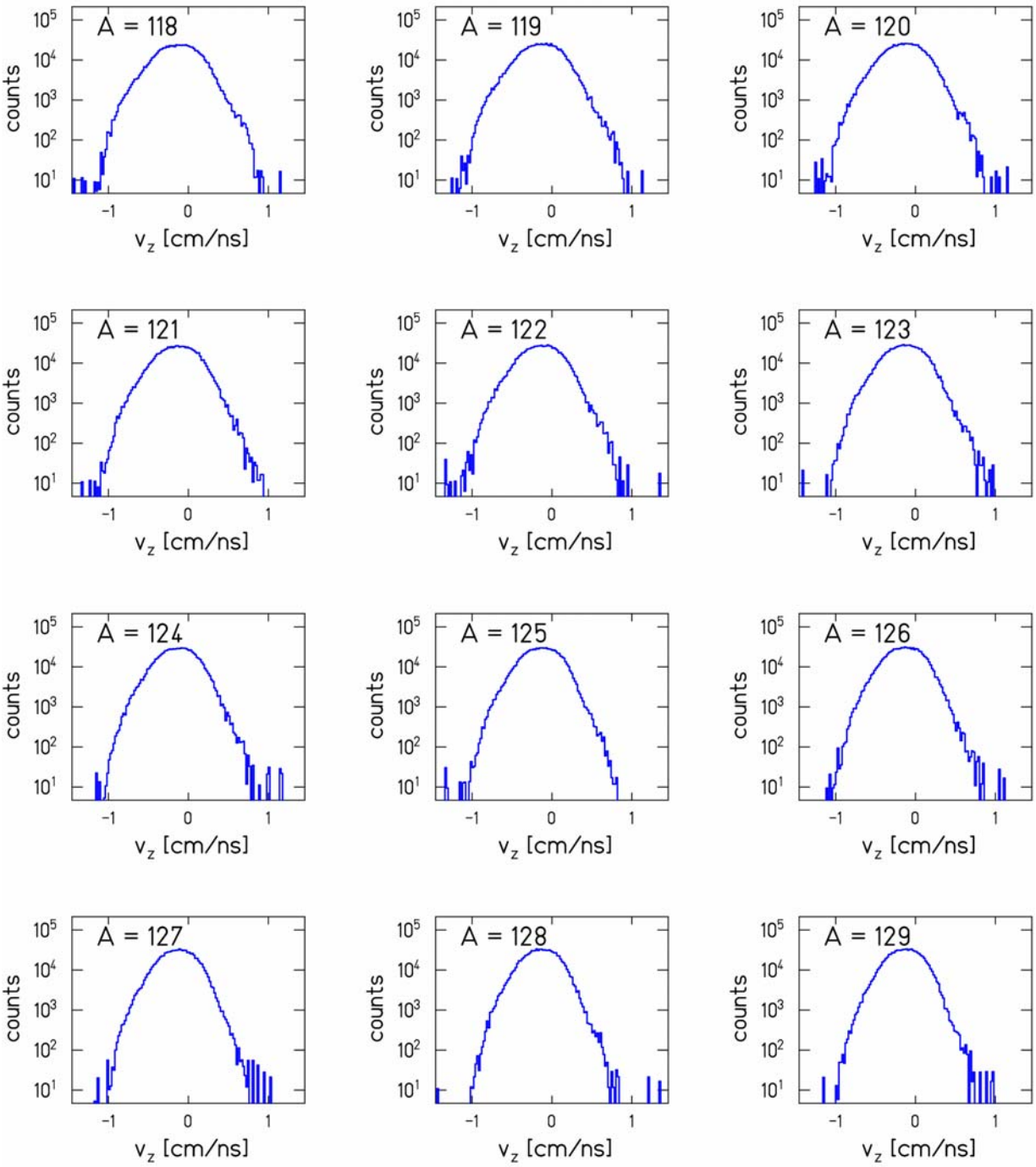
A = 118
A = 119
A = 120
A = 121
A = 122
A = 123
A = 124
A = 125
A = 126
A = 127
A = 128
A = 129
counts
v_z [cm/ns]

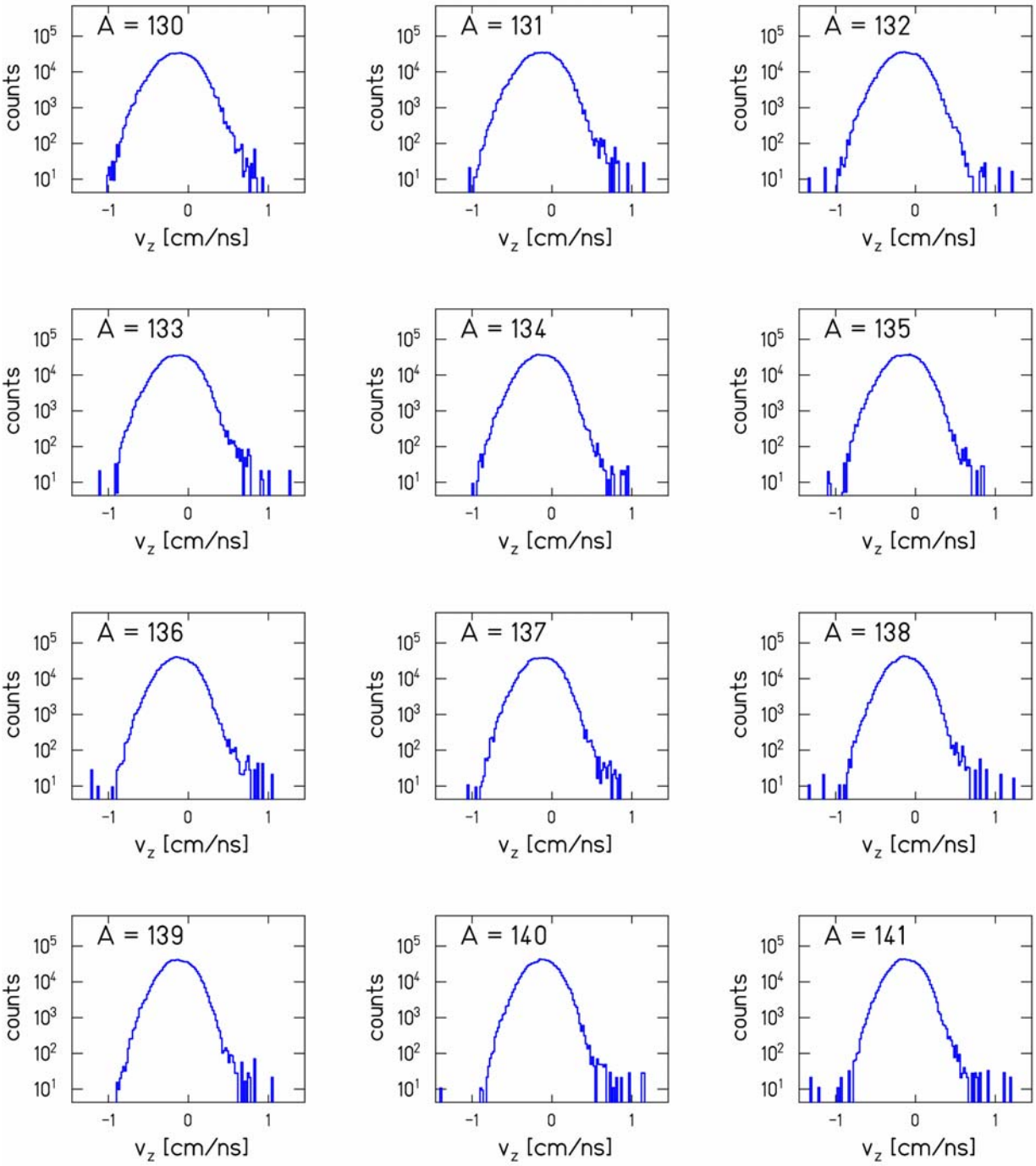
A = 130
A = 131
A = 132
A = 133
A = 134
A = 135
A = 136
A = 137
A = 138
A = 139
A = 140
A = 141
counts
v_z [cm/ns]

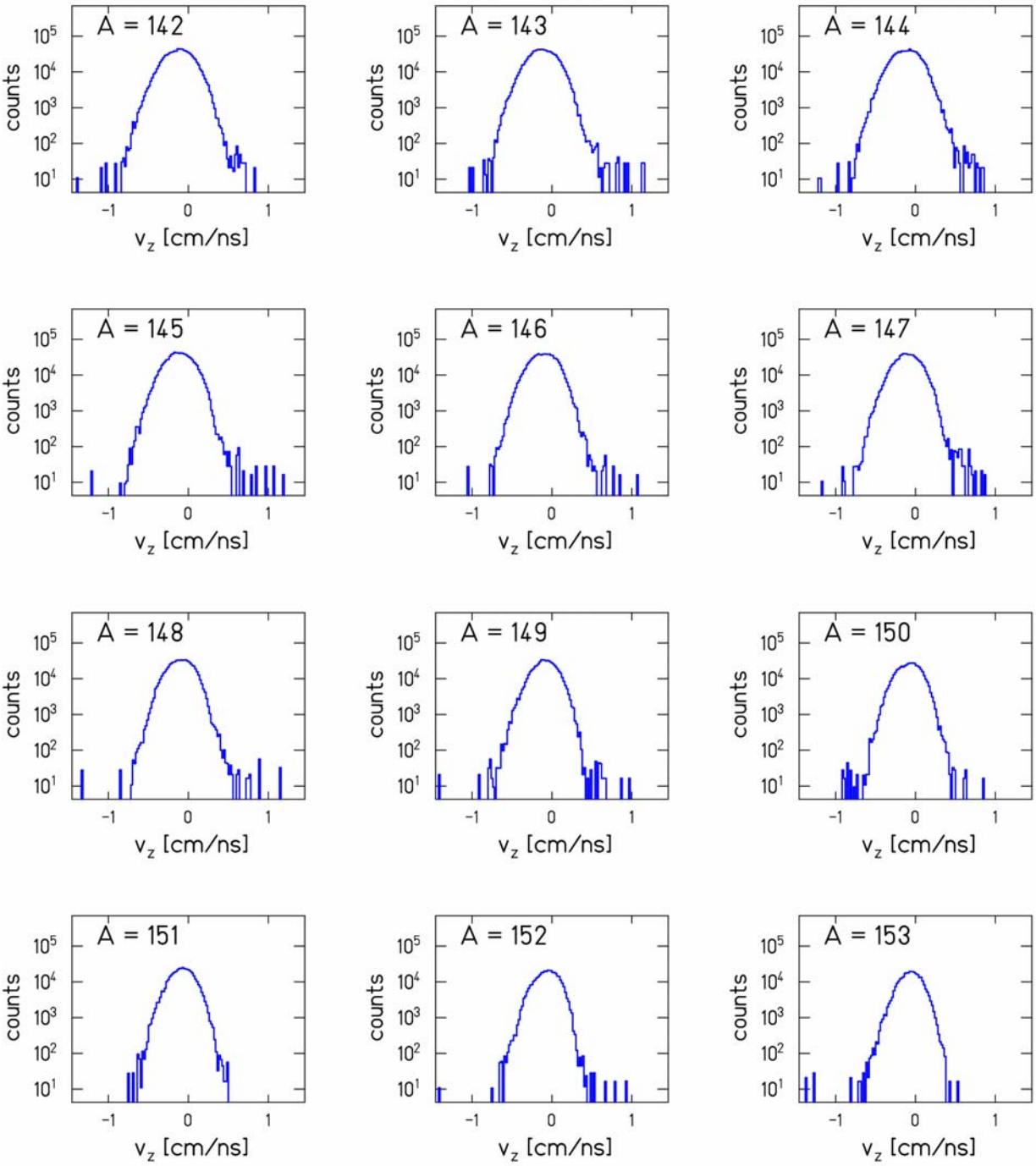
A = 142
A = 143
A = 144
A = 145
A = 146
A = 147
A = 148
A = 149
A = 150
A = 151
A = 152
A = 153
counts
v_z [cm/ns]

Appendix C

Fig.C1: Evaluation of the total transmission efficiency of the FRS as the function of the fragmentation residue mass A_{frag} and its dependence on the investigated reaction system. The displayed values are not applicable for fission or any fast break-up dominated by very asymmetric partitions of the disassembling system (for discussion of various types of reaction processes see chap.4.1.1).

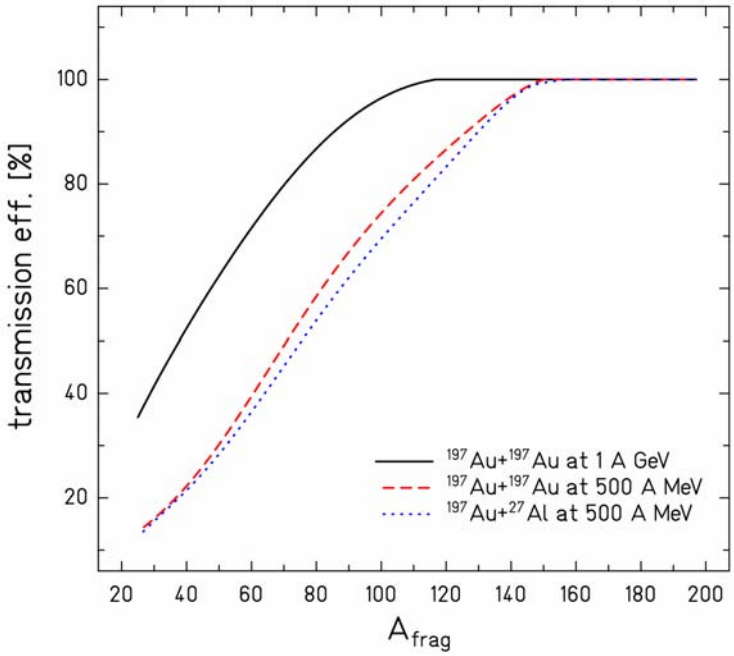

Fig.C2: Evaluation of the effect of the limited angular transmission of the FRS on the mean longitudinal velocity as the function of the fragmentation residue mass A_{frag} and its dependence on the investigated system. The consequence of the limited angular transmission is then a generally higher mean longitudinal velocity. The displayed values are not applicable for fission or any fast break-up dominated by very asymmetric partitions of the disassembling system (for discussion of various types of reaction processes see chap.4.1.1).

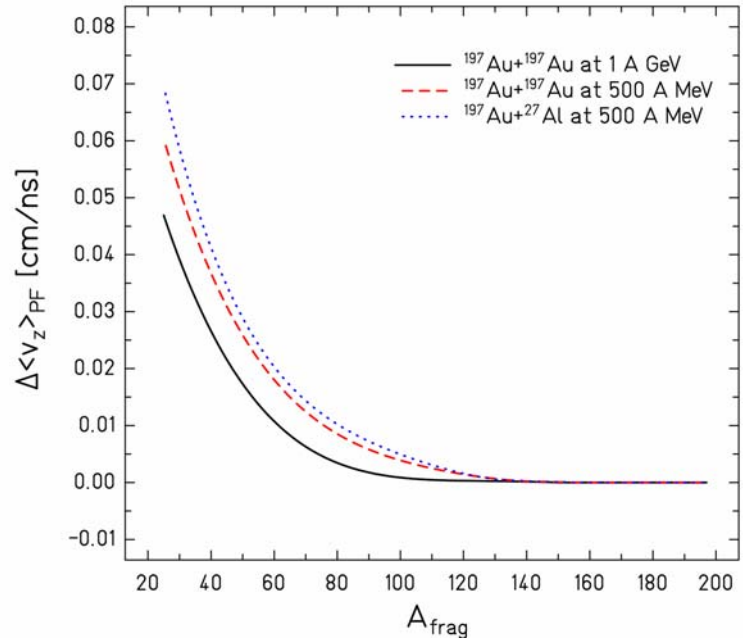

Appendix D

Review of results of the calculations performed within the BUU model for all three experimentally investigated systems complementing the discussion in the chap.7. The results are given for four different equations of state and two different parameterizations of the nucleon-nucleon elastic-scattering cross-sections as the function of the time for several different impact parameters. All displayed results were calculated in the center-of-mass reference frame. For description of the used BUU model see chap.6, for the definition of the "corresponding impact parameters" used for the comparison of Au+Au and Au+Al systems with incident beam energy of 500 *A* MeV see chap.7.3.

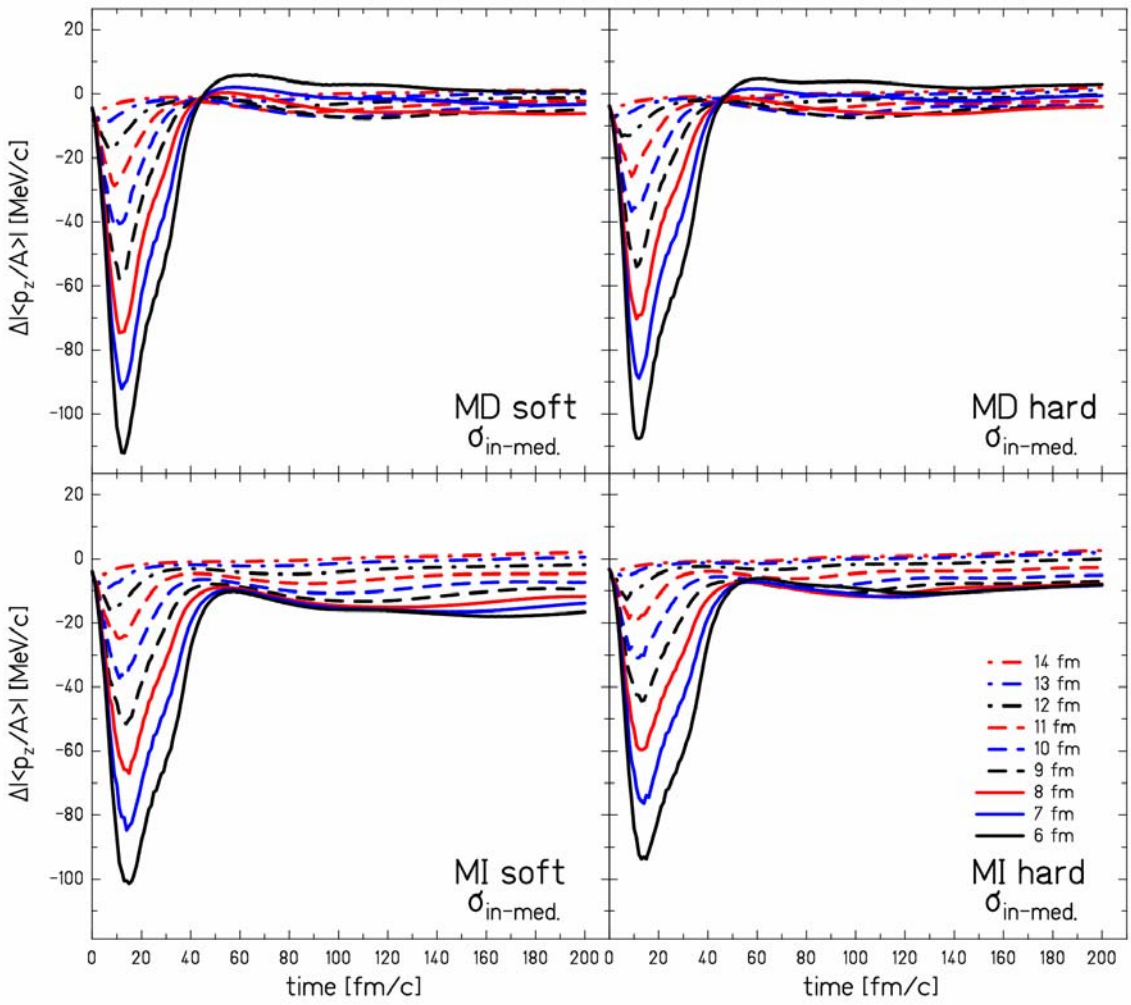

Fig.D.1: Time evolution of the net mean longitudinal momentum change per nucleon of the projectile spectator $\Delta|\langle p_z/A\rangle|$ for different impact parameters in the system ^{197}Au+^{197}Au at 1 *A* GeV as calculated within the BUU model for a soft and a hard EoS with a momentum-dependent (MD) nuclear mean field and for a soft and hard EoS with a momentum-independent (MI) nuclear mean field using in-medium reduced nucleon-nucleon elastic-scattering cross sections $\sigma_{in\text{-}med}$. $\Delta|\langle p_z/A\rangle|$ is calculated in the center-of-mass reference system.

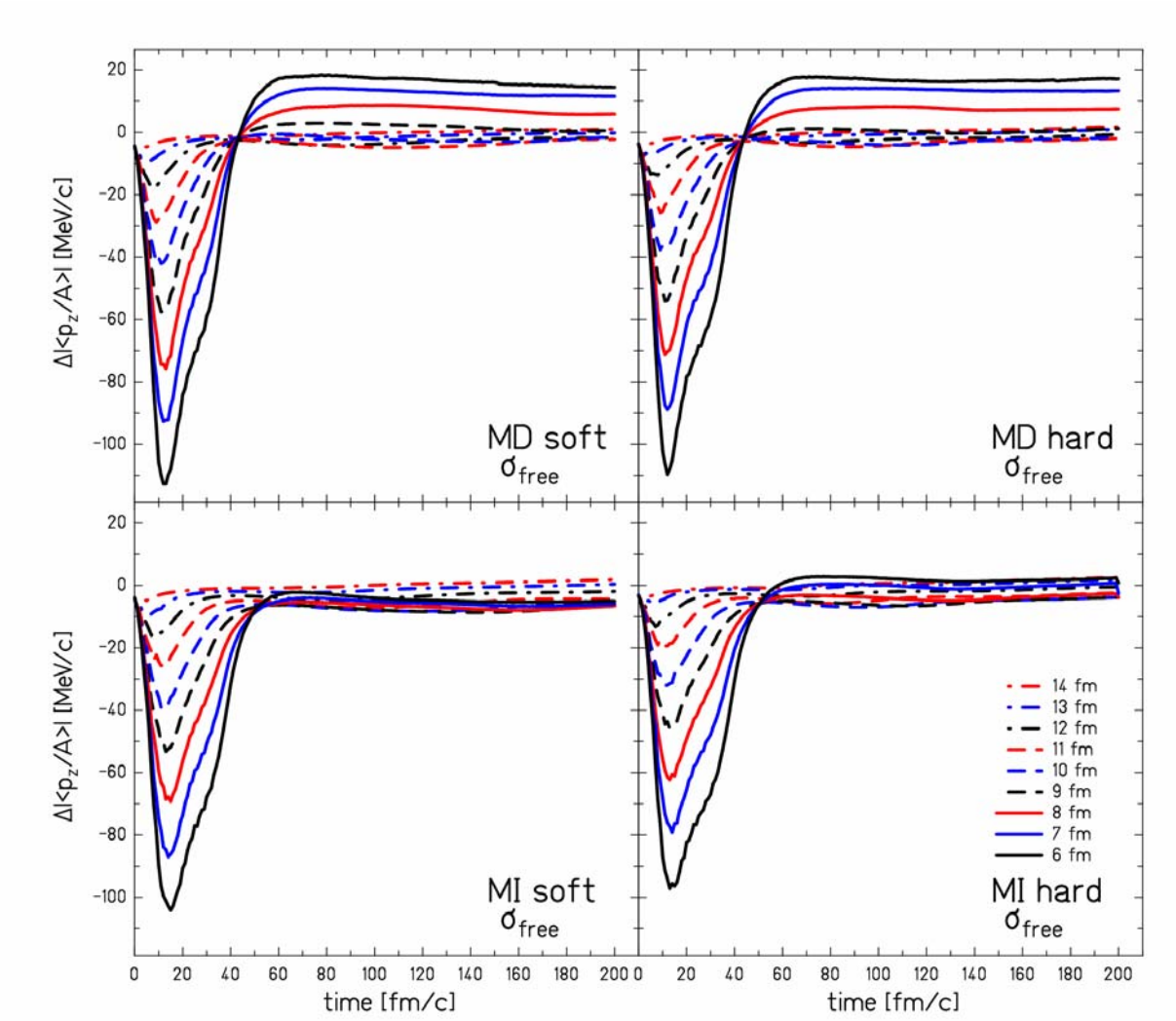

Fig.D.2: Time evolution of the net mean longitudinal momentum change per nucleon of the projectile spectator $\Delta|\langle p_z/A\rangle|$ for different impact parameters in the system ^{197}Au+^{197}Au at 1 *A* GeV as calculated within the BUU model for a soft and a hard EoS with a momentum-dependent (MD) nuclear mean field and for a soft and hard EoS with a momentum-independent (MI) nuclear mean field using free nucleon-nucleon elastic-scattering cross sections σ_{free}. $\Delta|\langle p_z/A\rangle|$ is calculated in the center-of-mass reference system.

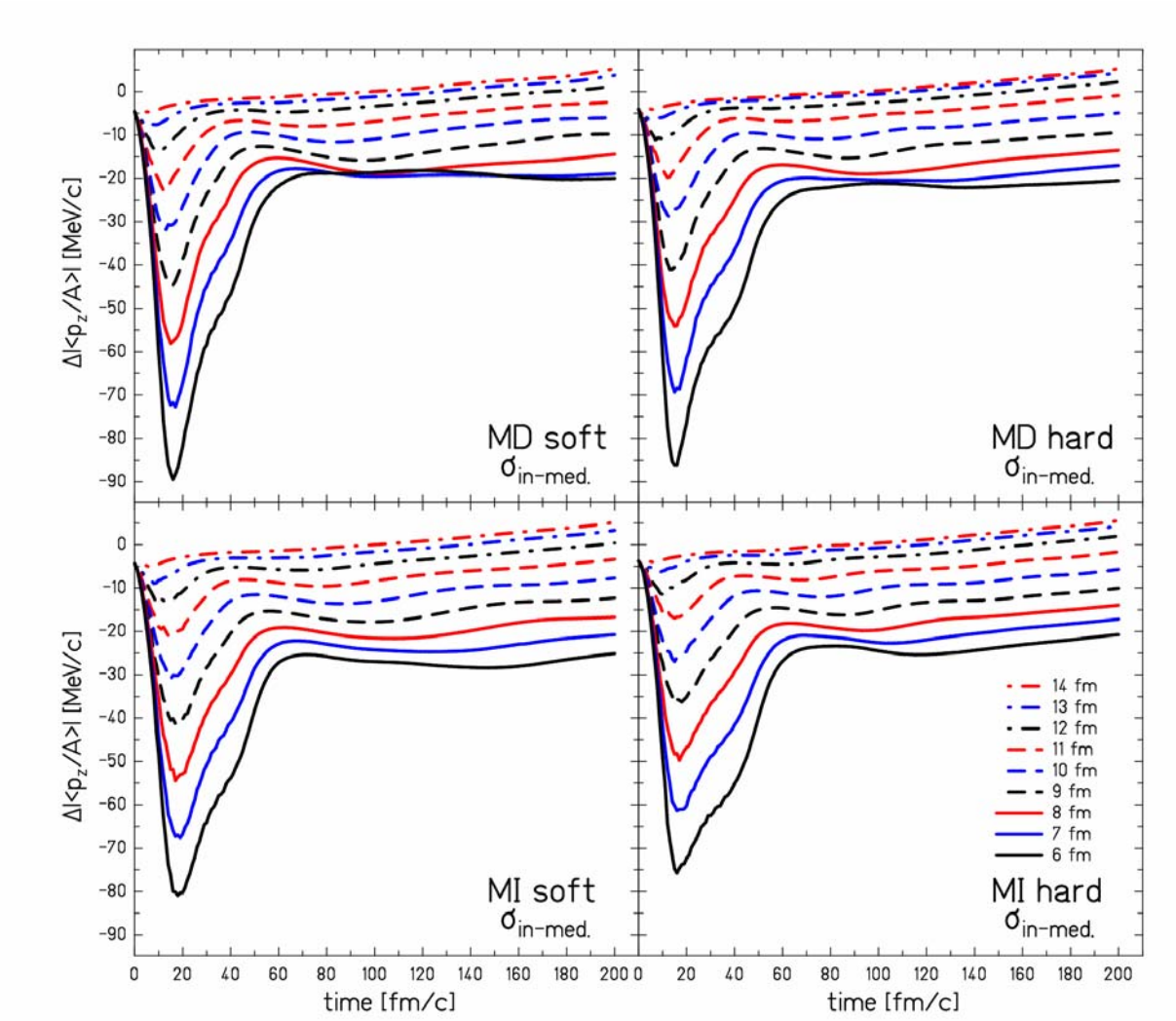

Fig.D.3: Time evolution of the net mean longitudinal momentum change per nucleon of the projectile spectator $\Delta|\langle p_z/A\rangle|$ for different impact parameters in the system ^{197}Au+^{197}Au at 500 A MeV as calculated within the BUU model for a soft and a hard EoS with a momentum-dependent (MD) nuclear mean field and for a soft and hard EoS with a momentum-independent (MI) nuclear mean field using in-medium reduced nucleon-nucleon elastic-scattering cross sections $\sigma_{in\text{-}med}$. $\Delta|\langle p_z/A\rangle|$ is calculated in the center-of-mass reference system.

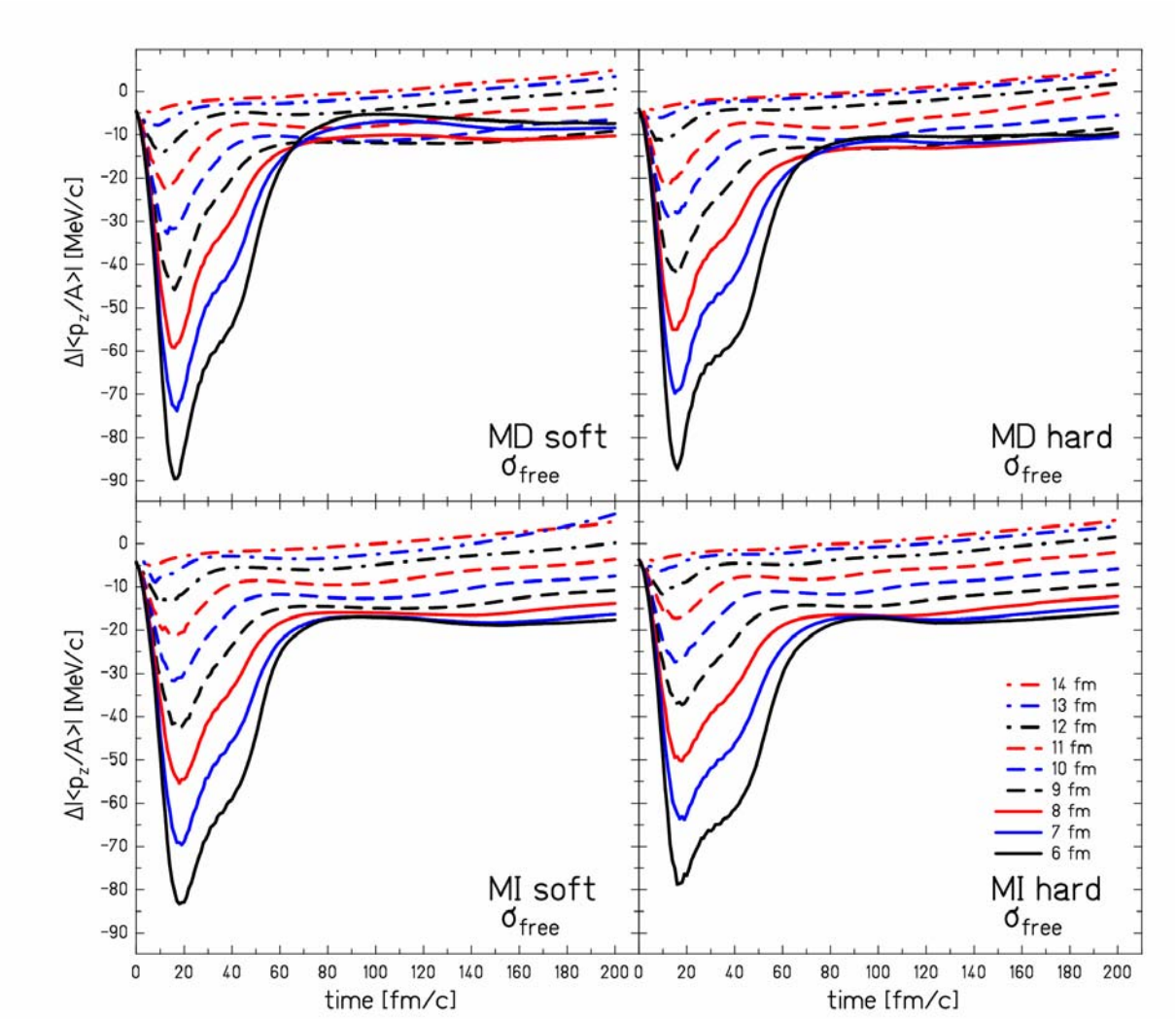

Fig.D.4: Time evolution of the net mean longitudinal momentum change per nucleon of the projectile spectator $\Delta|\langle p_z/A\rangle|$ for different impact parameters in the system ^{197}Au+^{197}Au at 1 *A* GeV as calculated within the BUU model for a soft and a hard EoS with a momentum-dependent (MD) nuclear mean field and for a soft and hard EoS with a momentum-independent (MI) nuclear mean field using free nucleon-nucleon elastic-scattering cross sections σ_{free}. $\Delta|\langle p_z/A\rangle|$ is calculated in the center-of-mass reference system.

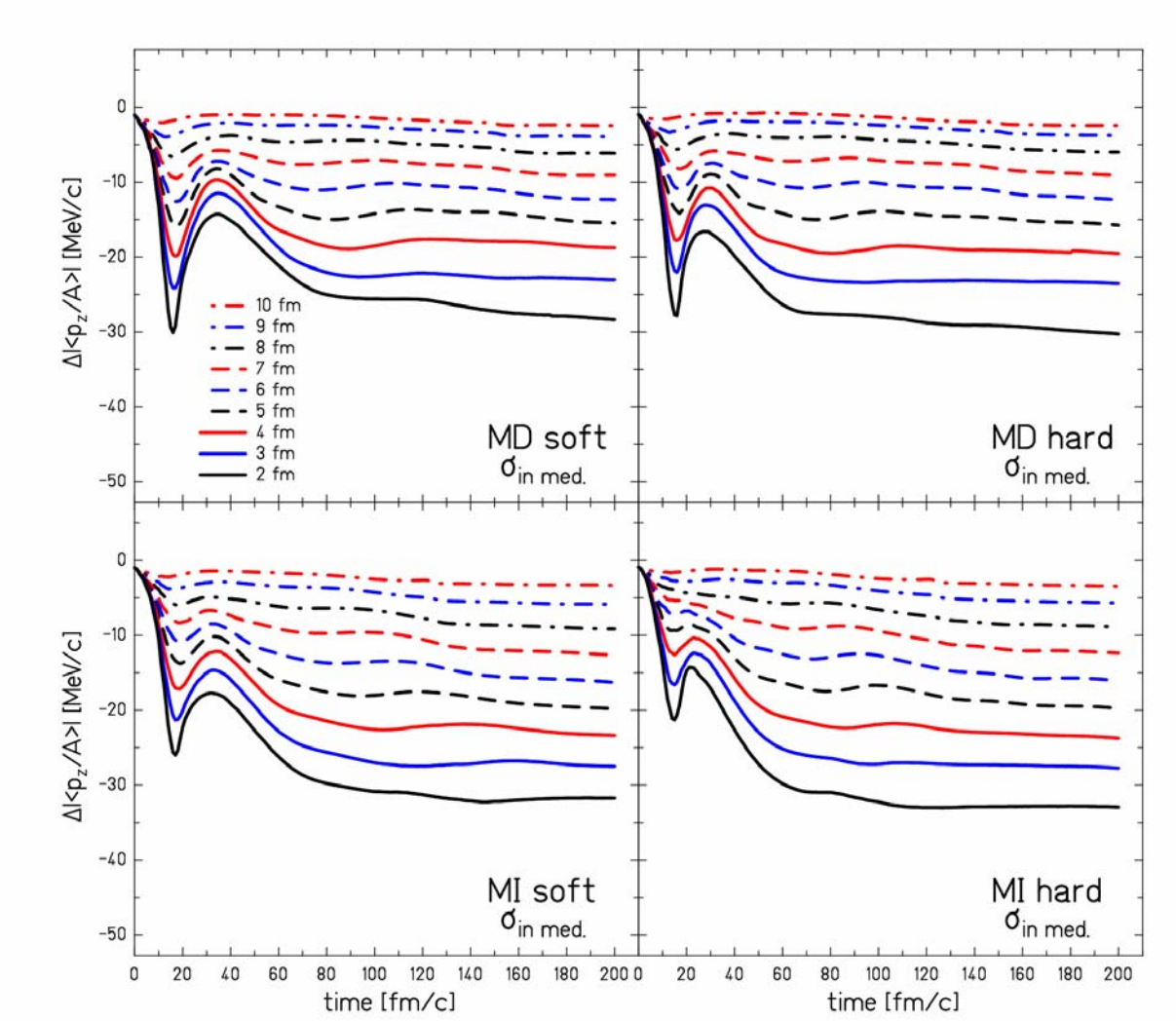

Fig.D.5: Time evolution of the net mean longitudinal momentum change per nucleon of the projectile spectator $\Delta|\langle p_z/A\rangle|$ for different impact parameters in the system ^{197}Au+^{27}Al at 500 A MeV as calculated within the BUU model for a soft and a hard EoS with a momentum-dependent (MD) nuclear mean field and for a soft and hard EoS with a momentum-independent (MI) nuclear mean field using in-medium reduced nucleon-nucleon elastic-scattering cross sections $\sigma_{in\text{-}med}$. $\Delta|\langle p_z/A\rangle|$ is calculated in the center-of-mass reference system.

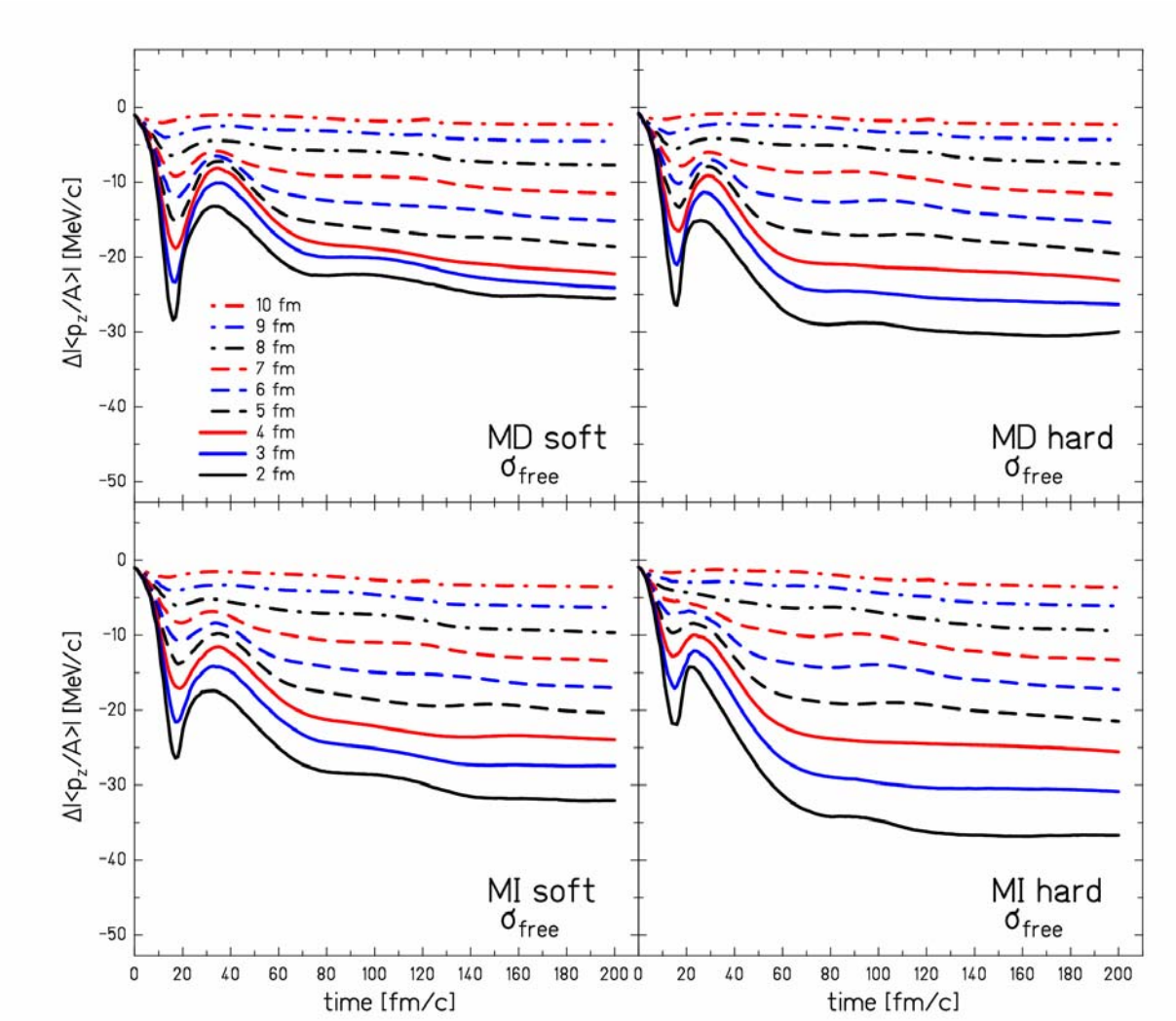

Fig.D.6: Time evolution of the net mean longitudinal momentum change per nucleon of the projectile spectator $\Delta|\langle p_z/A\rangle|$ for different impact parameters in the system ^{197}Au+^{27}Al at 500 A MeV as calculated within the BUU model for a soft and a hard EoS with a momentum-dependent (MD) nuclear mean field and for a soft and hard EoS with a momentum-independent (MI) nuclear mean field using free nucleon-nucleon elastic-scattering cross sections σ_{free}. $\Delta|\langle p_z/A\rangle|$ is calculated in the center-of-mass reference system.

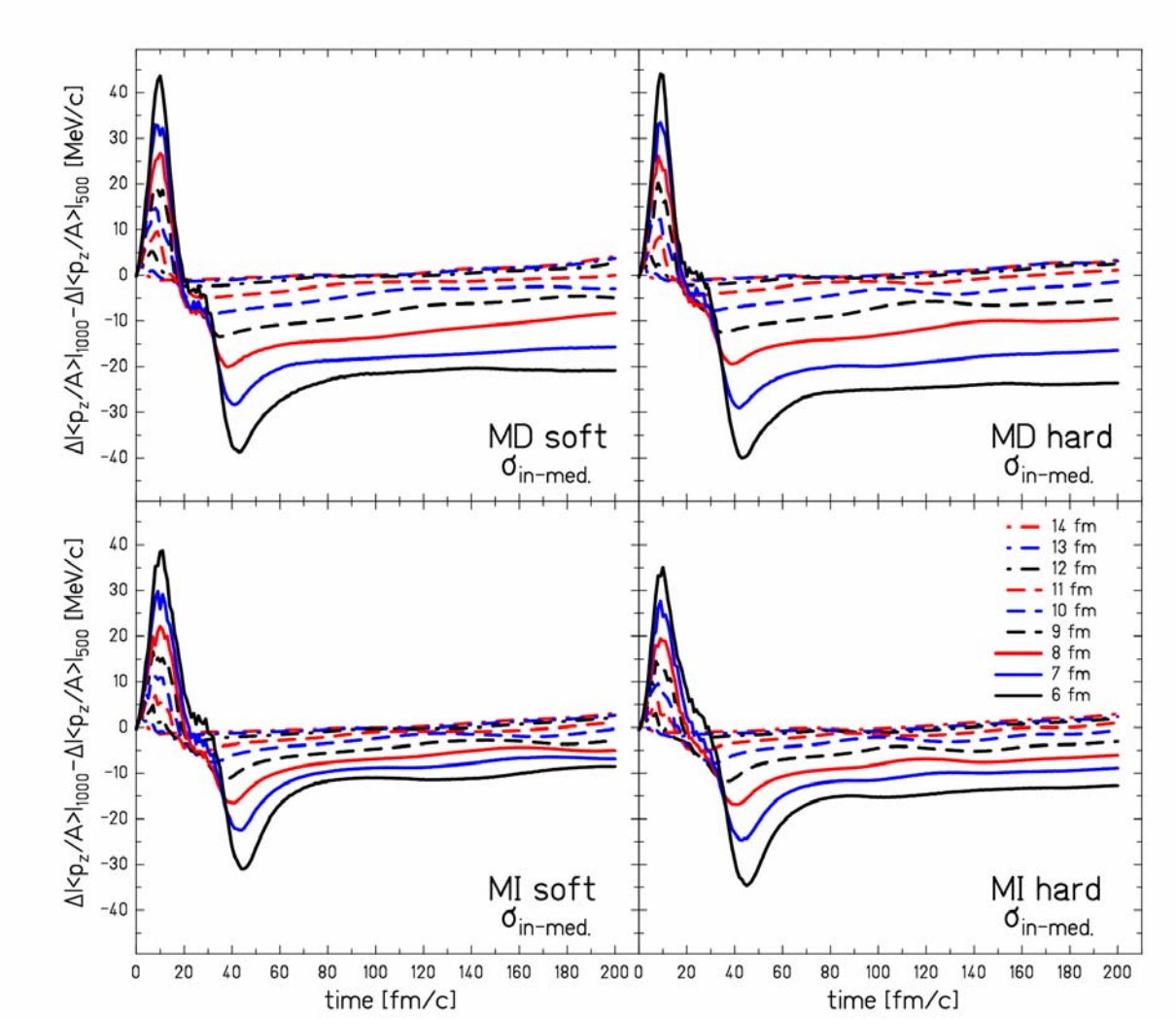

Fig.D.7: Time evolution of the difference of the net mean longitudinal momentum change per nucleon $\Delta|\langle p_z/A\rangle|$ of the spectator matter and its dependence on the impact parameter calculated within the BUU model for a soft and a hard EoS with a momentum-dependent (MD) nuclear mean field and for a soft and hard EoS with a momentum-independent (MI) nuclear mean field with in-medium reduced nucleon-nucleon elastic-scattering cross sections $\sigma_{in\text{-}med}$ for the systems ^{197}Au+^{197}Au at 1 A GeV and ^{197}Au+^{197}Au at 500 A MeV. $\Delta|\langle p_z/A\rangle|$ is calculated in the center-of-mass reference system.

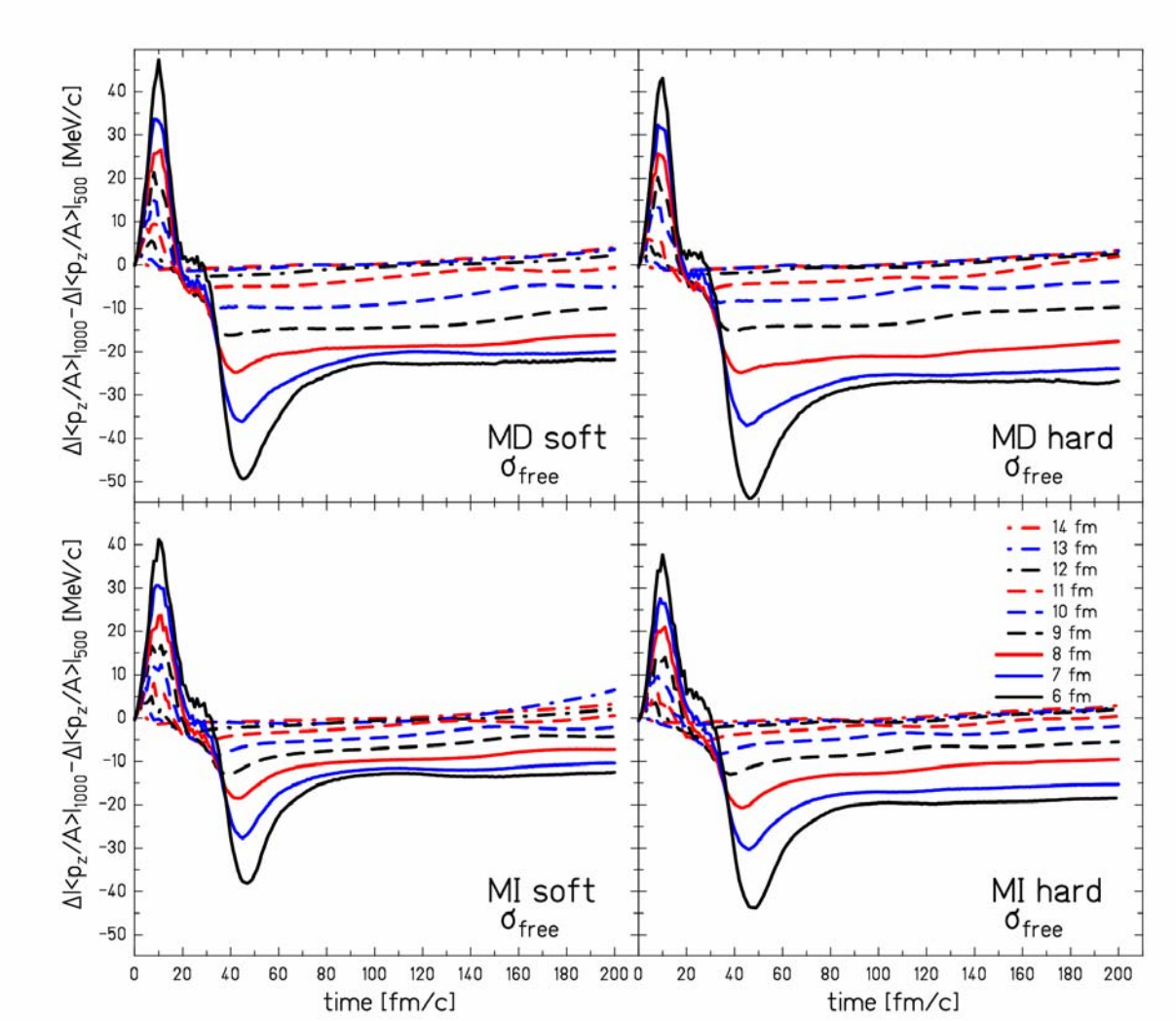

Fig.D.8: Time evolution of the difference of the net mean longitudinal momentum change per nucleon $\Delta|\langle p_z/A\rangle|$ of the spectator matter and its dependence on the impact parameter calculated within the BUU model for a soft and a hard EoS with a momentum-dependent (MD) nuclear mean field and for a soft and hard EoS with a momentum-independent (MI) nuclear mean field with free nucleon-nucleon elastic-scattering cross sections σ_{free} for the systems ^{197}Au+^{197}Au at 1 A GeV and ^{197}Au+^{197}Au at 500 A MeV. $\Delta|\langle p_z/A\rangle|$ is calculated in the center-of-mass reference system.

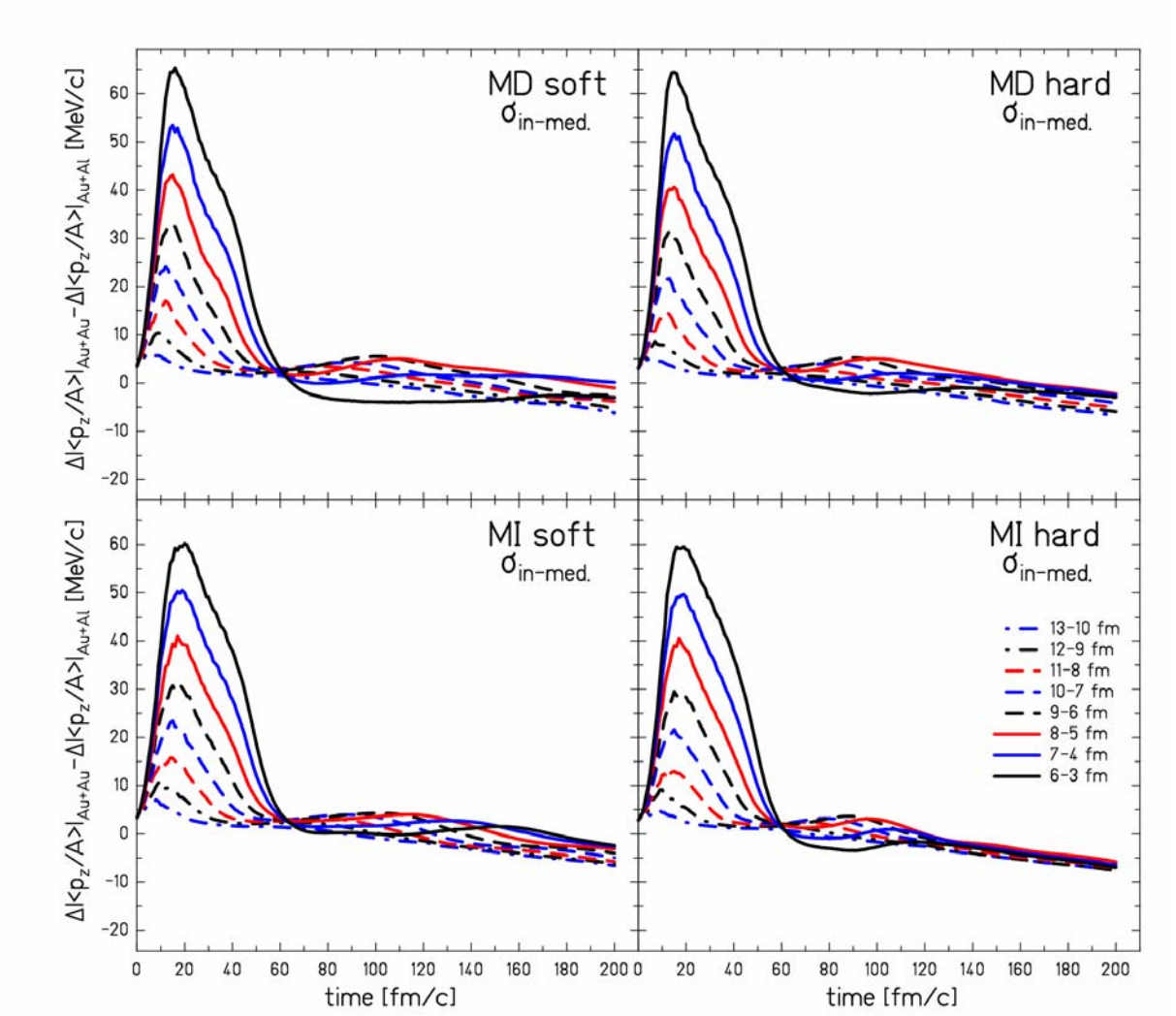

Fig.D.9: Time evolution of the difference of the net mean longitudinal momentum change per nucleon $\Delta|\langle p_z/A\rangle|$ of the spectator matter and its dependence on the "corresponding impact parameter" calculated within the BUU model for a soft and a hard EoS with a momentum-dependent (MD) nuclear mean field and for a soft and hard EoS with a momentum-independent (MI) nuclear mean field with in-medium reduced nucleon-nucleon elastic-scattering cross sections $\sigma_{in\text{-}med}$ for the systems ^{197}Au+^{197}Au at 500 A MeV and ^{197}Au+^{27}Al at 500 A MeV. $\Delta|\langle p_z/A\rangle|$ is calculated in the center-of-mass reference system.

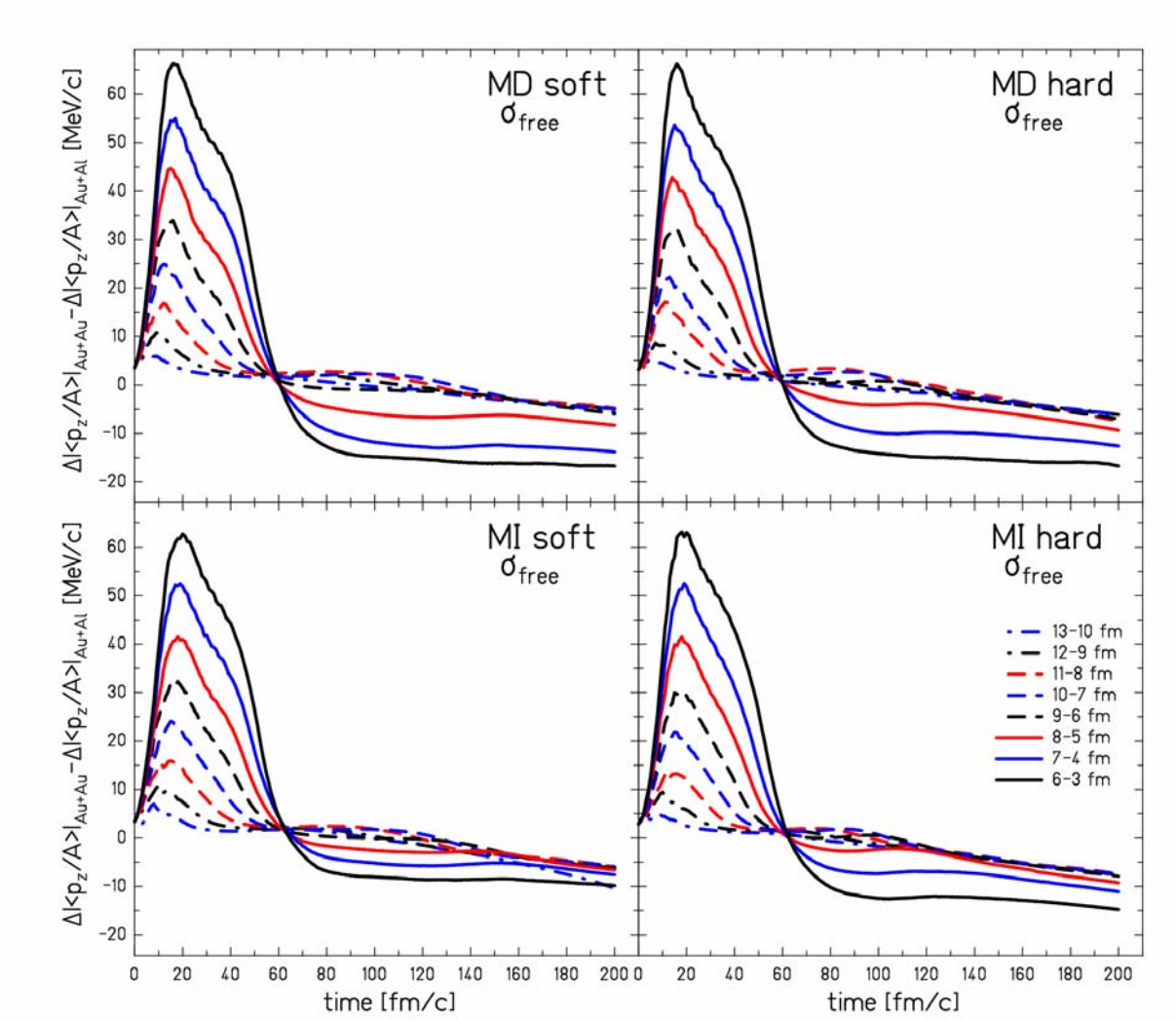

Fig.D.10: Time evolution of the difference of the net mean longitudinal momentum change per nucleon $\Delta|\langle p_z/A\rangle|$ of the spectator matter and its dependence on the "corresponding impact parameter" calculated within the BUU model for a soft and a hard EoS with a momentum-dependent (MD) nuclear mean field and for a soft and hard EoS with a momentum-independent (MI) nuclear mean field with free nucleon-nucleon elastic-scattering cross sections σ_{free} for the systems ^{197}Au+^{197}Au at 500 A MeV and ^{197}Au+^{27}Al at 500 A MeV. $\Delta|\langle p_z/A\rangle|$ is calculated in the center-of-mass reference system.

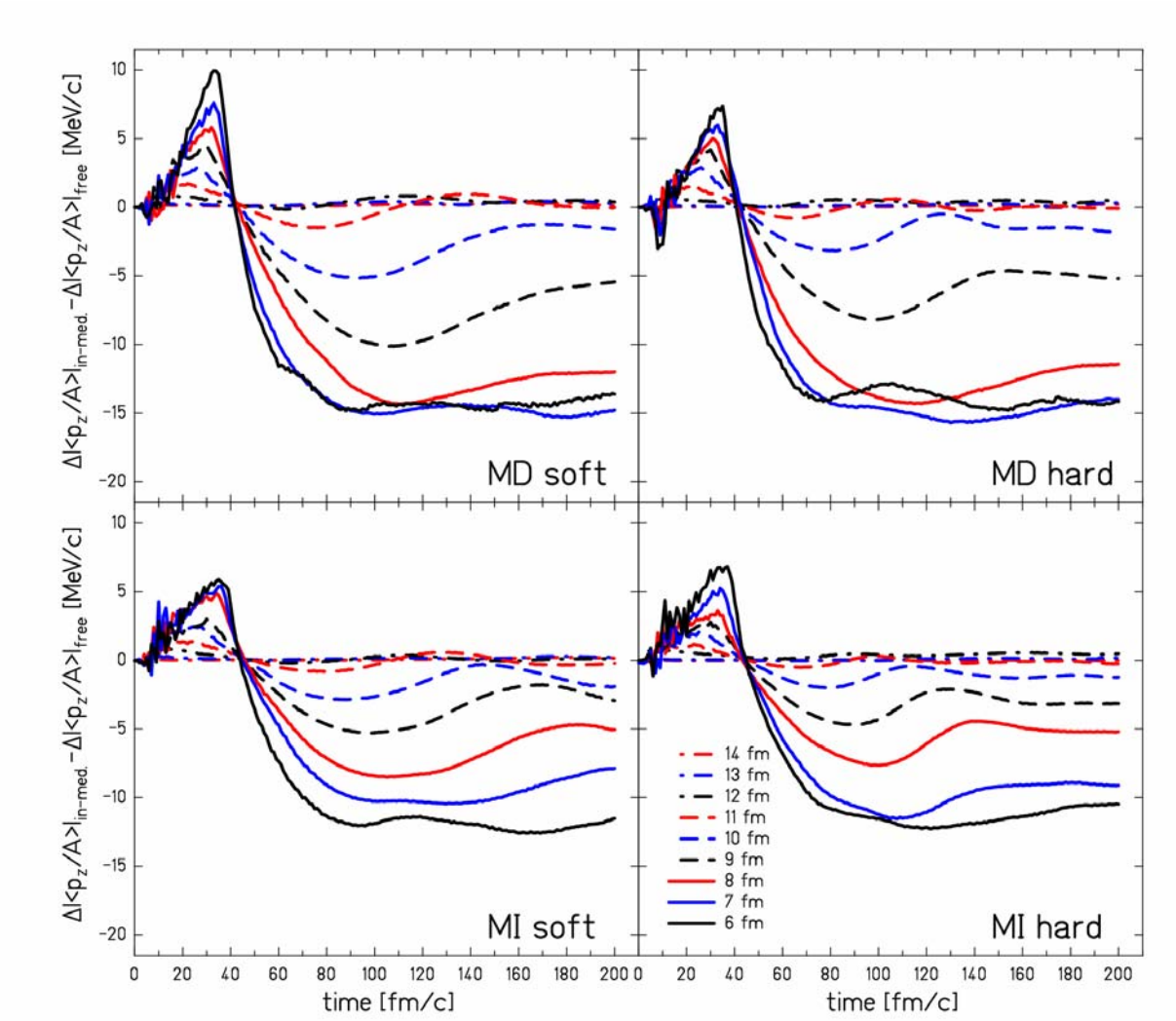

Fig.D.11: Time evolution of the difference of the net mean longitudinal momentum change per nucleon $\Delta|\langle p_z/A\rangle|$ of the spectator matter and its dependence on the impact parameter calculated within the BUU model for a soft and a hard EoS with a momentum-dependent (MD) nuclear mean field and for a soft and hard EoS with a momentum-independent (MI) nuclear mean field with in-medium reduced and free nucleon-nucleon elastic-scattering cross sections $\sigma_{in\text{-}med}$ and σ_{free}, respectively, for the system ^{197}Au+^{197}Au at 1 A GeV. $\Delta|\langle p_z/A\rangle|$ is calculated in the center-of-mass reference system.

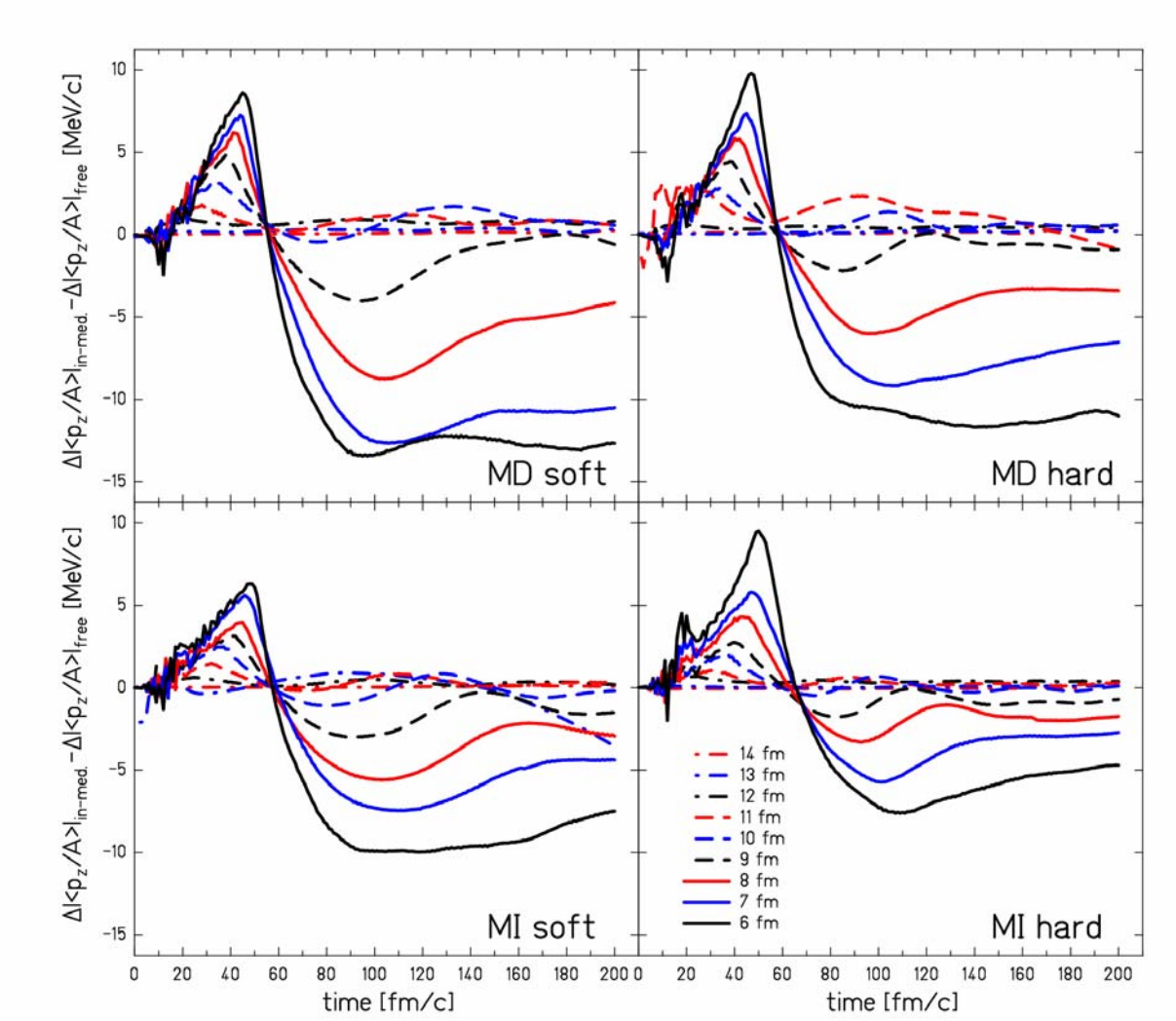

Fig.D.12: Time evolution of the difference of the net mean longitudinal momentum change per nucleon $\Delta|\langle p_z/A\rangle|$ of the spectator matter and its dependence on the impact parameter calculated within the BUU model for a soft and a hard EoS with a momentum-dependent (MD) nuclear mean field and for a soft and hard EoS with a momentum-independent (MI) nuclear mean field with in-medium reduced and free nucleon-nucleon elastic-scattering cross sections $\sigma_{in\text{-}med}$ and σ_{free}, respectively, for the system ^{197}Au+^{197}Au at 500 A MeV. $\Delta|\langle p_z/A\rangle|$ is calculated in the center-of-mass reference system.

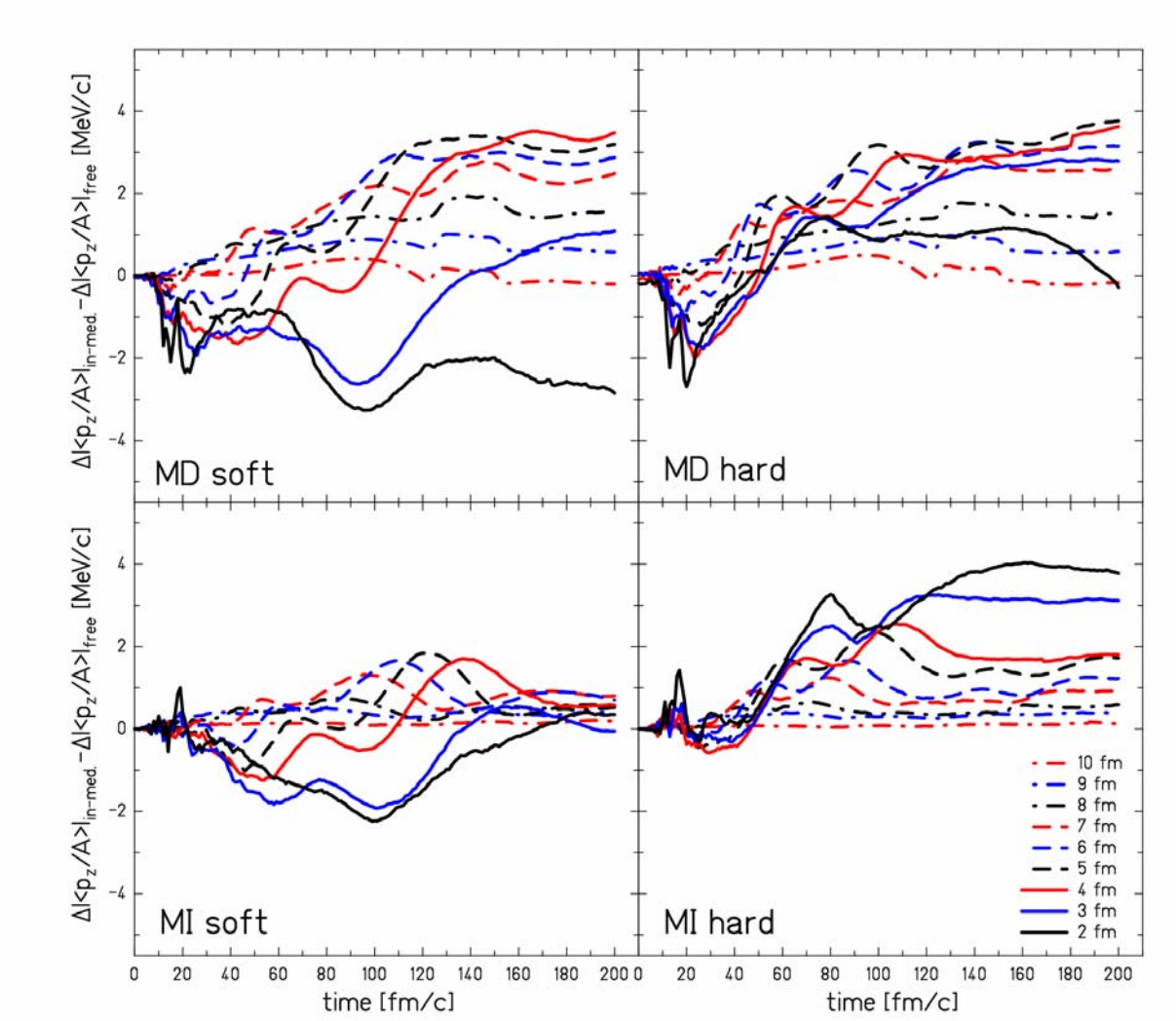

Fig.D.13: Time evolution of the difference of the net mean longitudinal momentum change per nucleon $\Delta|\langle p_z/A\rangle|$ of the spectator matter and its dependence on the impact parameter calculated within the BUU model for a soft and a hard EoS with a momentum-dependent (MD) nuclear mean field and for a soft and hard EoS with a momentum-independent (MI) nuclear mean field with in-medium reduced and free nucleon-nucleon elastic-scattering cross sections $\sigma_{in\text{-}med}$ and σ_{free}, respectively, for the system ^{197}Au+^{27}Al at 500 A MeV. $\Delta|\langle p_z/A\rangle|$ is calculated in the center-of-mass reference system.

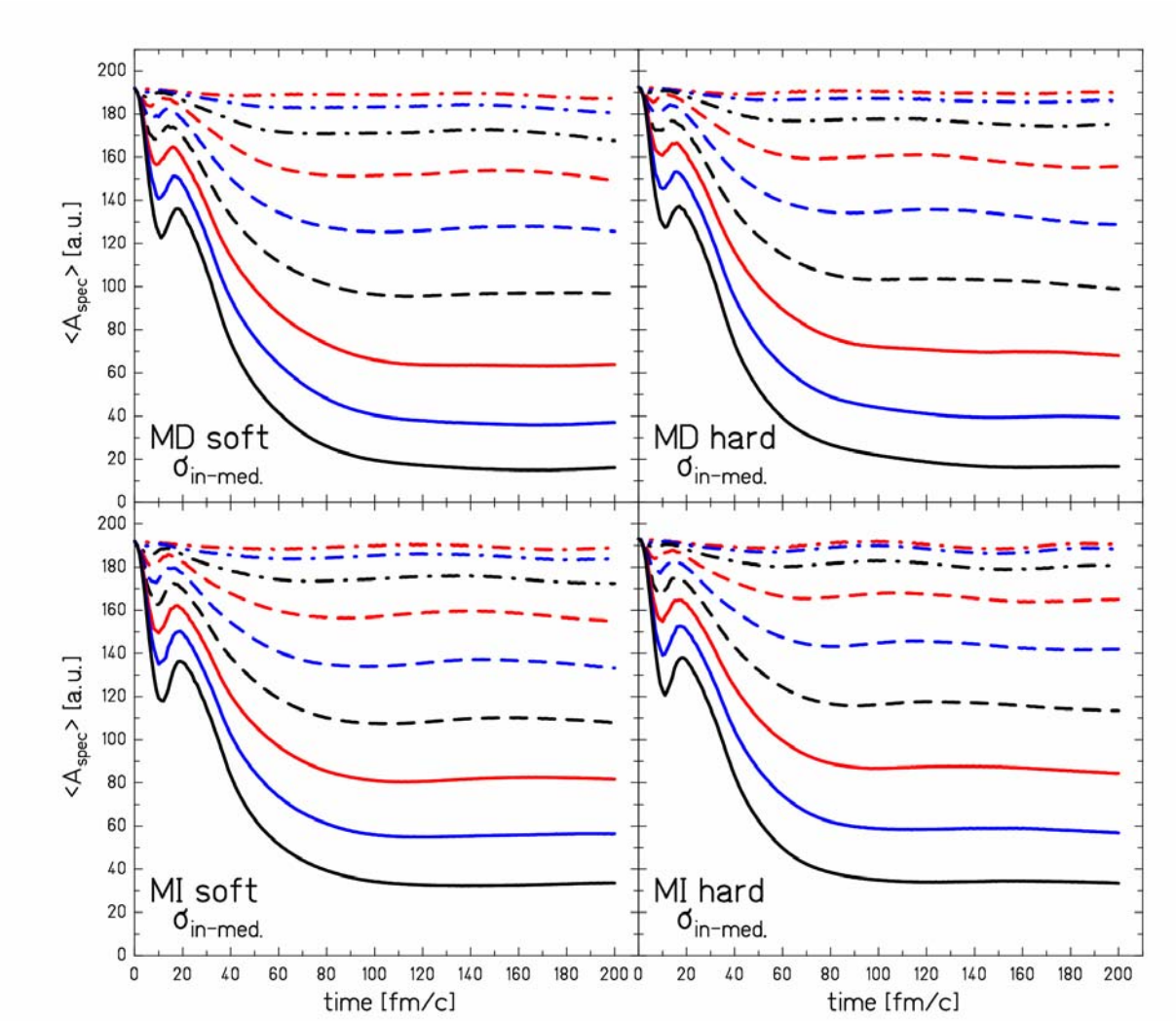

Fig.D.14: Time evolution of the mean spectator mass $\langle A_{spec} \rangle$ for different impact parameters in the system ^{197}Au+^{197}Au at 1 A GeV as calculated within the BUU model for a soft and a hard EoS with a momentum-dependent (MD) nuclear mean field and for a soft and hard EoS with a momentum-independent (MI) nuclear mean field using in-medium reduced nucleon-nucleon elastic-scattering cross sections $\sigma_{in\text{-}med}$. The lines of different style and color corresponding to different impact parameters, for which the particular calculation was performed, have the same meaning as in Fig.D.1.

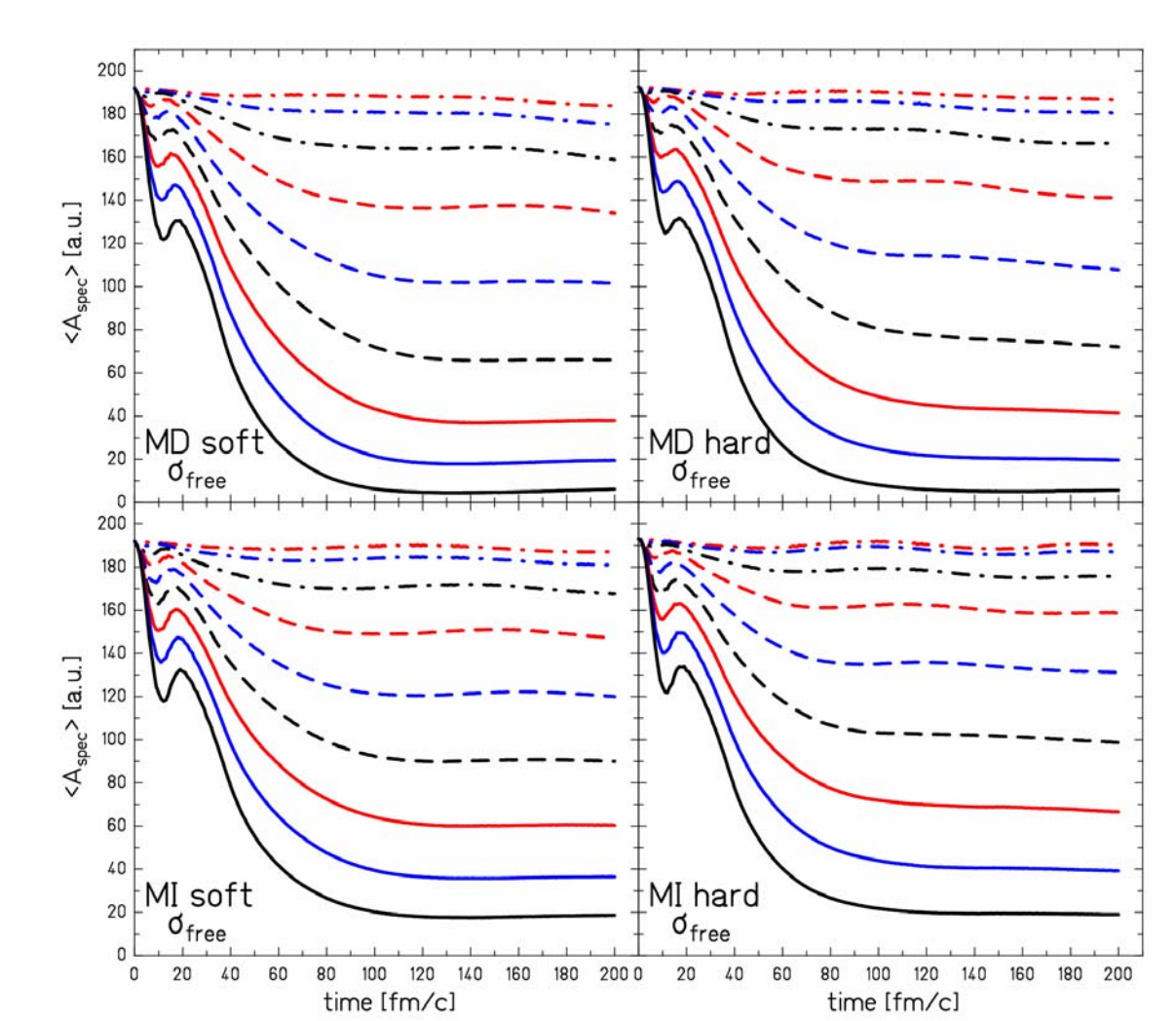

Fig.D.15: Time evolution of the mean spectator mass $\langle A_{spec} \rangle$ for different impact parameters in the system ^{197}Au+^{197}Au at 1 A GeV as calculated within the BUU model for a soft and a hard EoS with a momentum-dependent (MD) nuclear mean field and for a soft and hard EoS with a momentum-independent (MI) nuclear mean field using free nucleon-nucleon elastic-scattering cross sections σ_{free}. The lines of different style and color corresponding to different impact parameters, for which the particular calculation was performed, have the same meaning as in Fig.D.2.

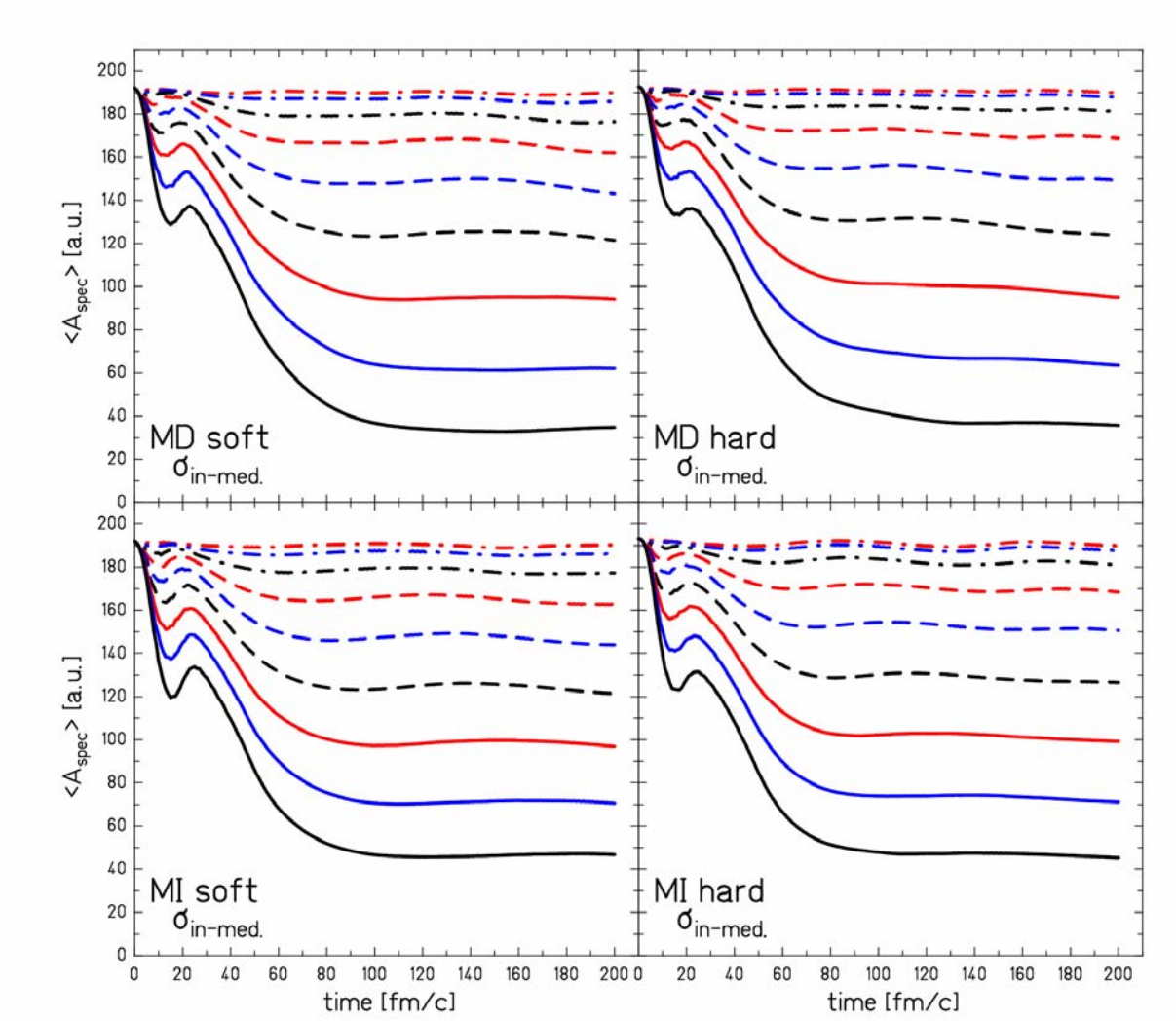

Fig.D.16: Time evolution of the mean spectator mass $\langle A_{spec} \rangle$ for different impact parameters in the system ^{197}Au+^{197}Au at 500 A MeV as calculated within the BUU model for a soft and a hard EoS with a momentum-dependent (MD) nuclear mean field and for a soft and hard EoS with a momentum-independent (MI) nuclear mean field using in-medium reduced nucleon-nucleon elastic-scattering cross sections $\sigma_{in\text{-}med}$. The lines of different style and color corresponding to different impact parameters, for which the particular calculation was performed, have the same meaning as in Fig.D.3.

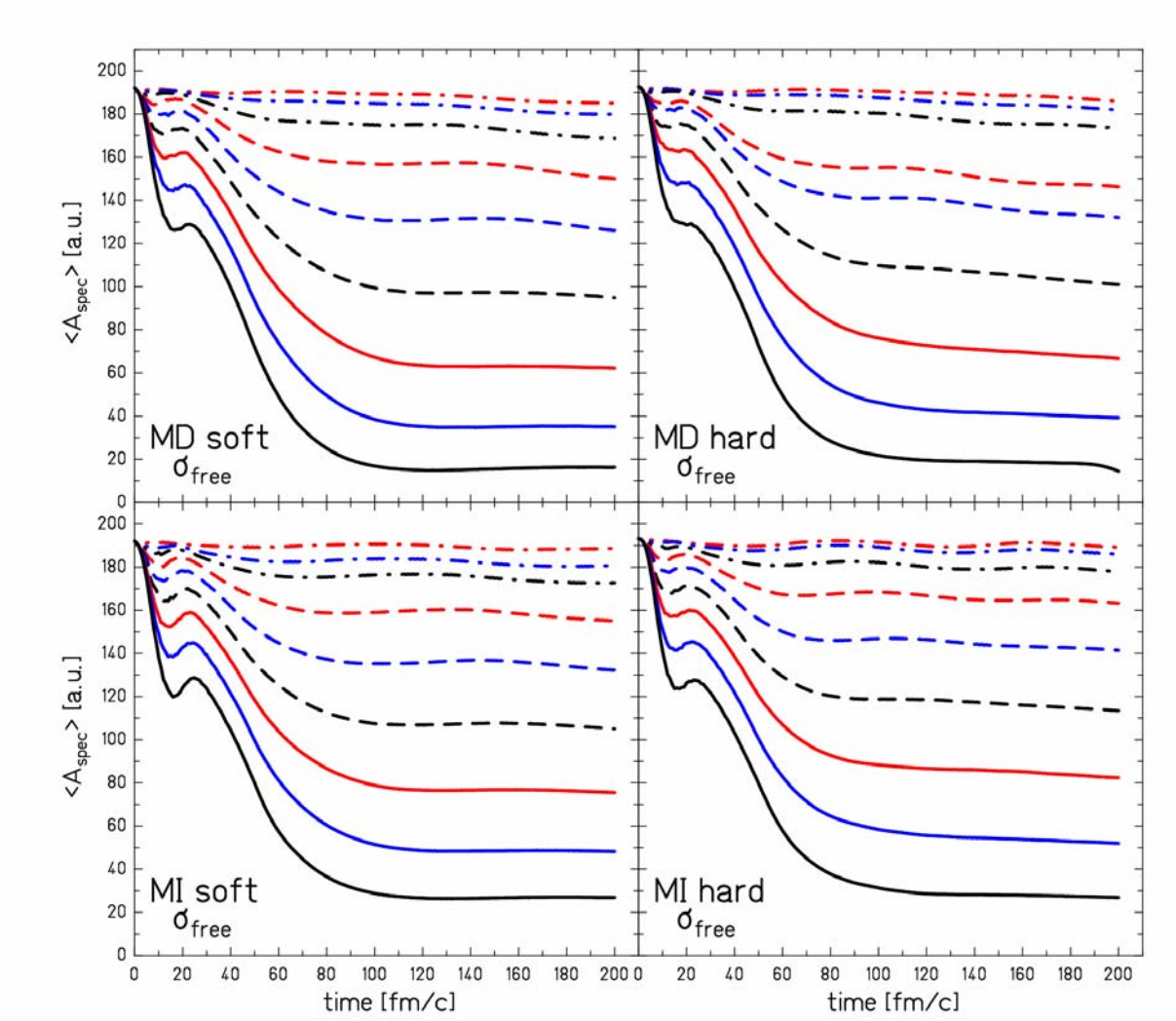

Fig.D.17: Time evolution of the mean spectator mass $\langle A_{spec} \rangle$ for different impact parameters in the system ^{197}Au+^{197}Au at 500 A MeV as calculated within the BUU model for a soft and a hard EoS with a momentum-dependent (MD) nuclear mean field and for a soft and hard EoS with a momentum-independent (MI) nuclear mean field using free nucleon-nucleon elastic-scattering cross sections σ_{free}. The lines of different style and color corresponding to different impact parameters, for which the particular calculation was performed, have the same meaning as in Fig.D.4.

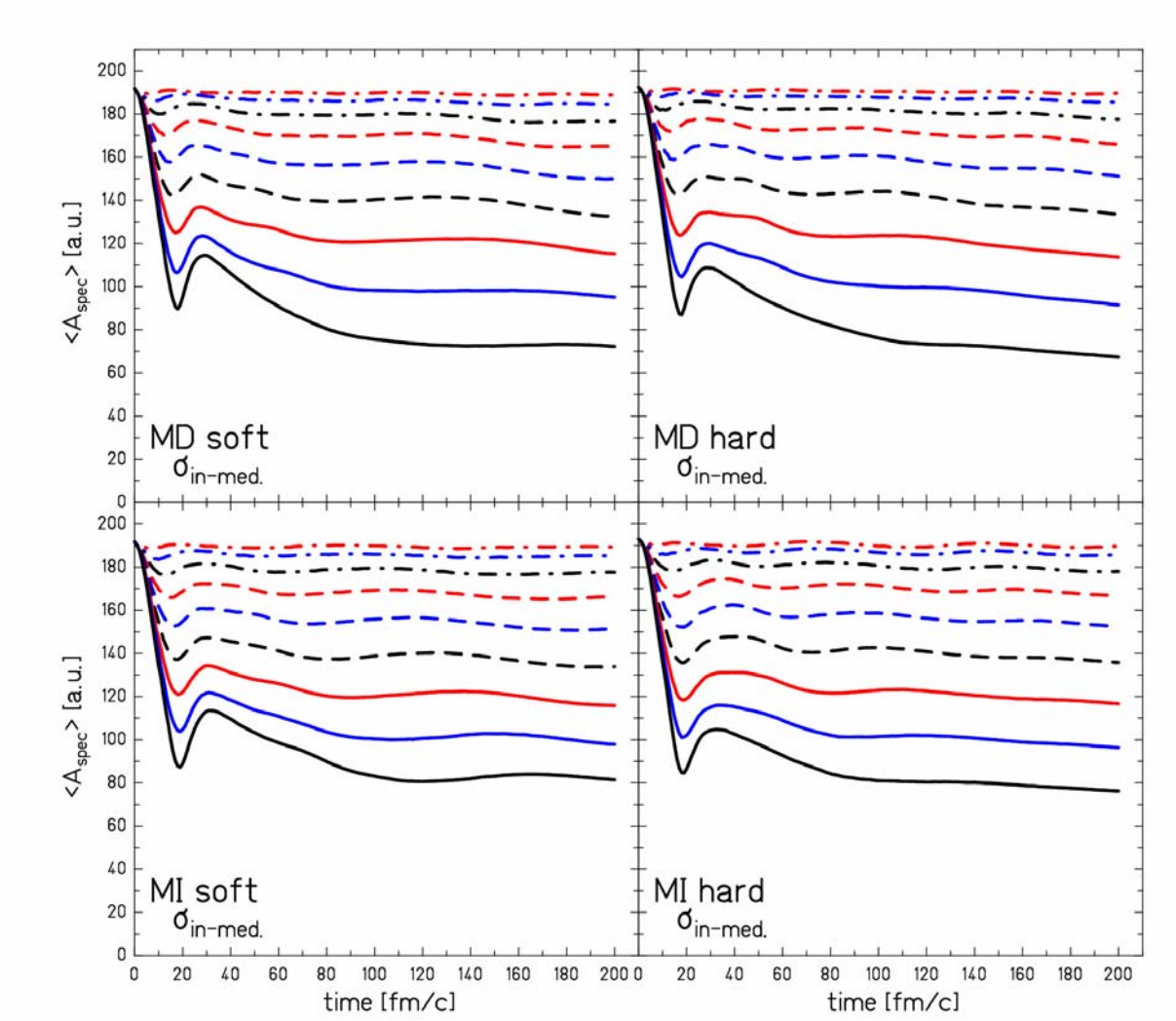

Fig.D.18: Time evolution of the mean spectator mass $\langle A_{spec} \rangle$ for different impact parameters in the system ^{197}Au+^{27}Al at 500 A MeV as calculated within the BUU model for a soft and a hard EoS with a momentum-dependent (MD) nuclear mean field and for a soft and hard EoS with a momentum-independent (MI) nuclear mean field using in-medium reduced nucleon-nucleon elastic-scattering cross sections $\sigma_{in\text{-}med}$. The lines of different style and color corresponding to different impact parameters, for which the particular calculation was performed, have the same meaning as in Fig.D.5.

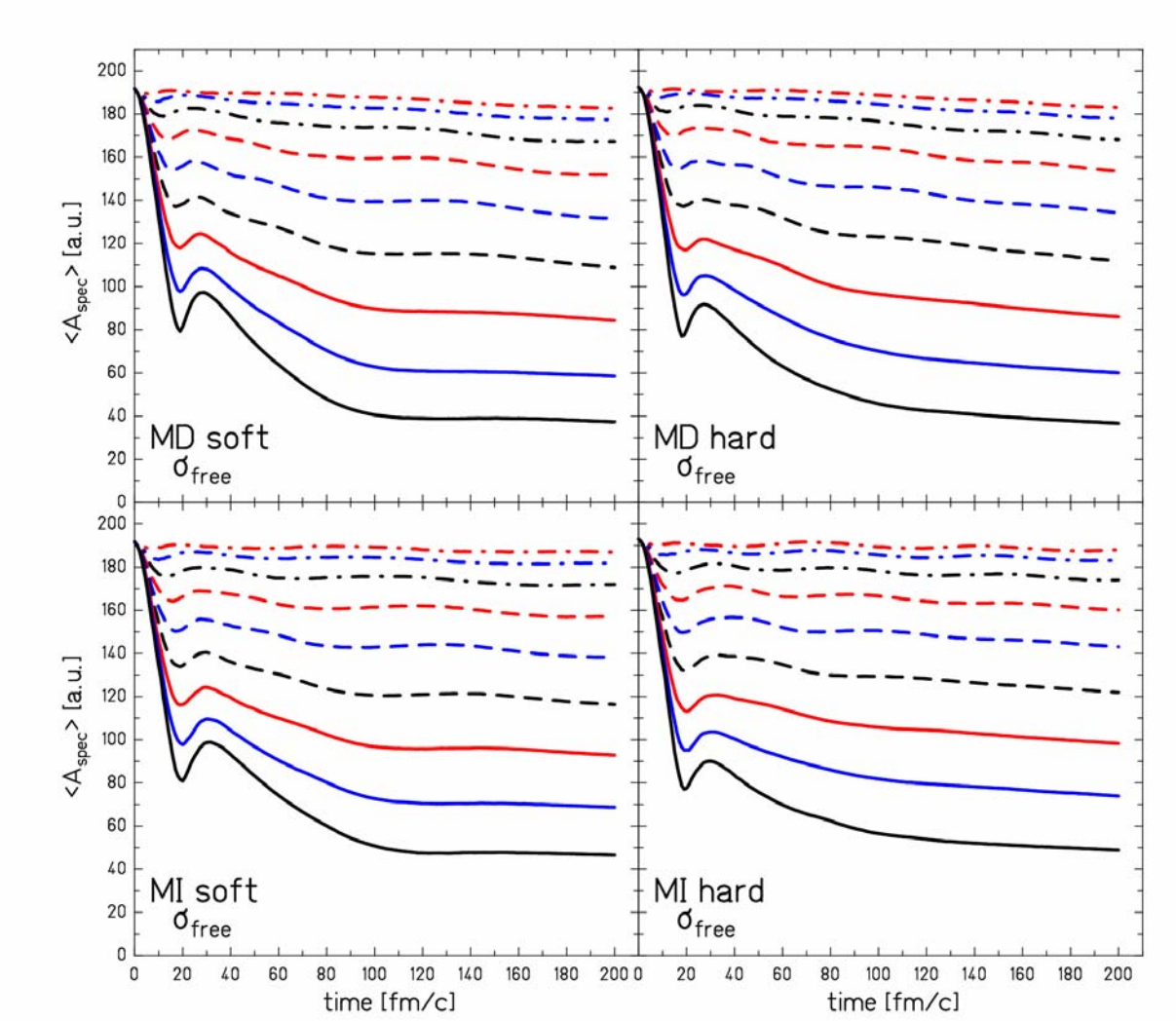

Fig.D.19: Time evolution of the mean spectator mass $\langle A_{spec} \rangle$ for different impact parameters in the system ^{197}Au+^{27}Al at 500 A MeV as calculated within the BUU model for a soft and a hard EoS with a momentum-dependent (MD) nuclear mean field and for a soft and hard EoS with a momentum-independent (MI) nuclear mean field using free nucleon-nucleon elastic-scattering cross sections σ_{free}. The lines of different style and color corresponding to different impact parameters, for which the particular calculation was performed, have the same meaning as in Fig.D.6.

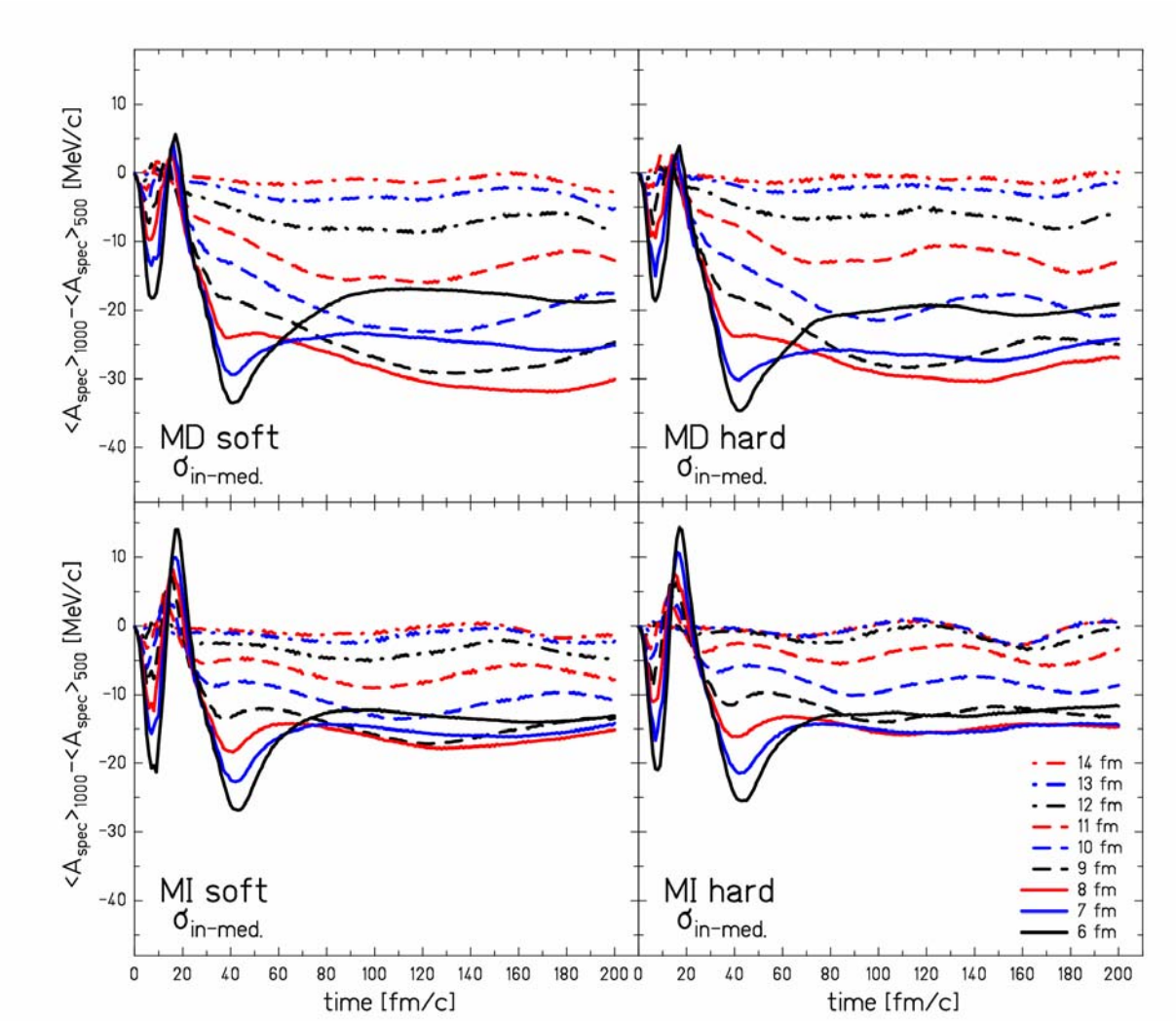

Fig.D.20: Time evolution of the difference of the mean spectator mass $\langle A_{spec} \rangle$ and its dependence on the impact parameter calculated within the BUU model for a soft and a hard EoS with a momentum-dependent (MD) nuclear mean field and for a soft and hard EoS with a momentum-independent (MI) nuclear mean field with in-medium reduced nucleon-nucleon elastic-scattering cross sections $\sigma_{in\text{-}med}$ for the systems ^{197}Au+^{197}Au at 1 A GeV and ^{197}Au+^{197}Au at 500 A MeV.

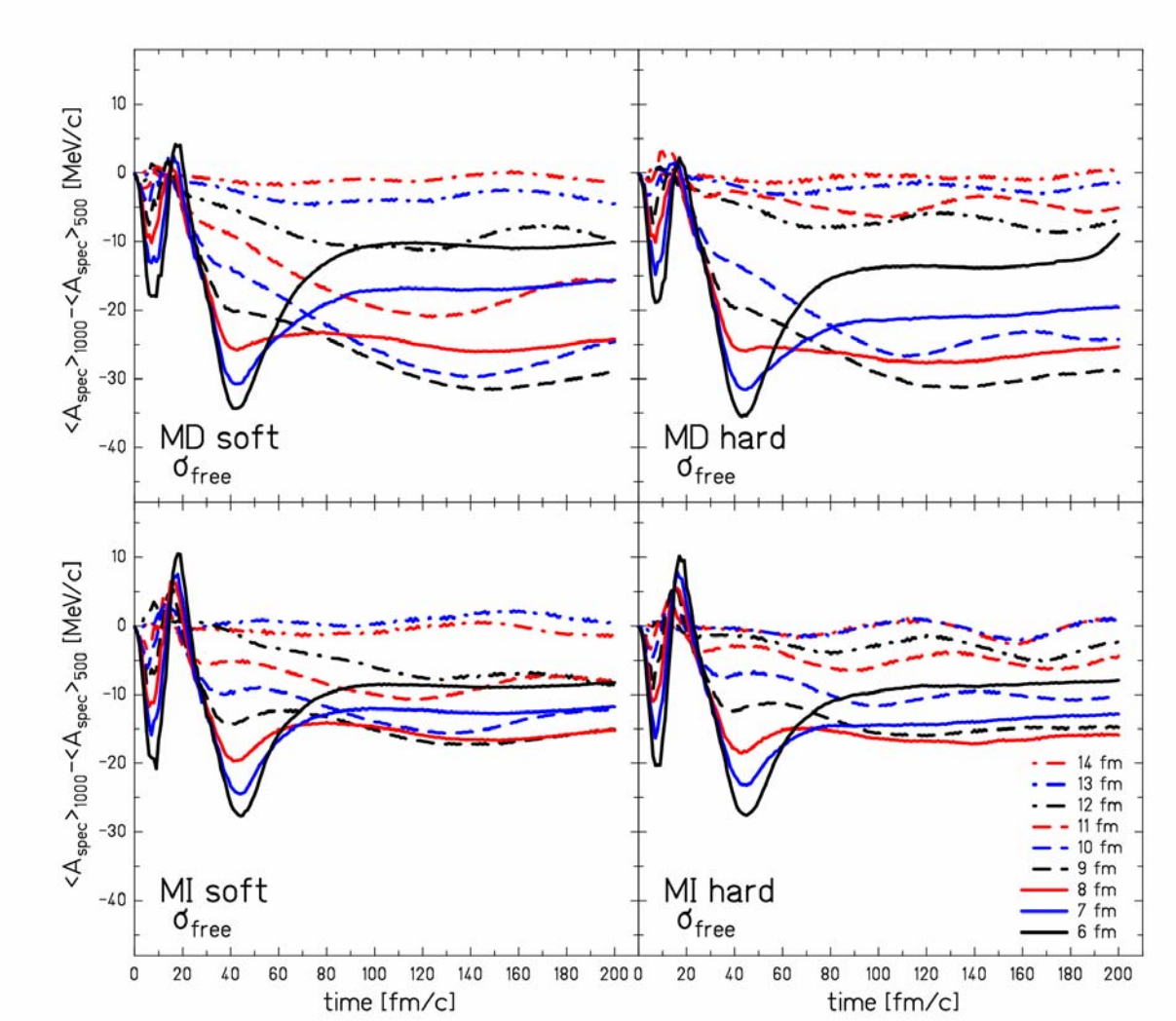

Fig.D.21: Time evolution of the difference of the mean spectator mass $\langle A_{spec} \rangle$ and its dependence on the impact parameter calculated within the BUU model for a soft and a hard EoS with a momentum-dependent (MD) nuclear mean field and for a soft and hard EoS with a momentum-independent (MI) nuclear mean field with free nucleon-nucleon elastic-scattering cross sections σ_{free} for the systems ^{197}Au+^{197}Au at 1 A GeV and ^{197}Au+^{197}Au at 500 A MeV.

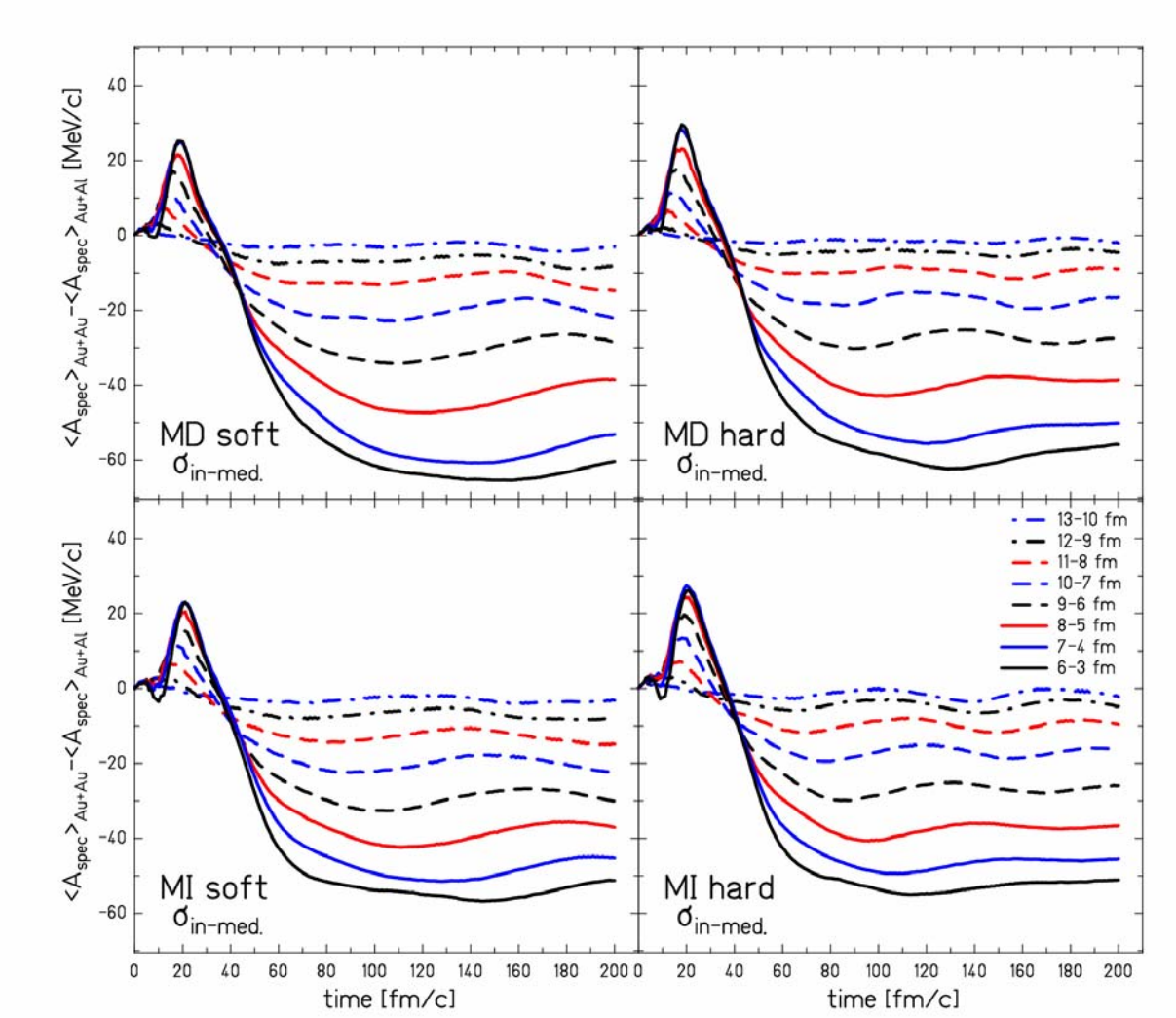

Fig.D.22: Time evolution of the difference of the mean spectator mass $\langle A_{spec} \rangle$ and its dependence on the "corresponding impact parameter" calculated within the BUU model for a soft and a hard EoS with a momentum-dependent (MD) nuclear mean field and for a soft and hard EoS with a momentum-independent (MI) nuclear mean field with in-medium reduced nucleon-nucleon elastic-scattering cross sections $\sigma_{in\text{-}med}$ for the systems ^{197}Au+^{197}Au at 500 A MeV and ^{197}Au+^{27}Al at 500 A MeV.

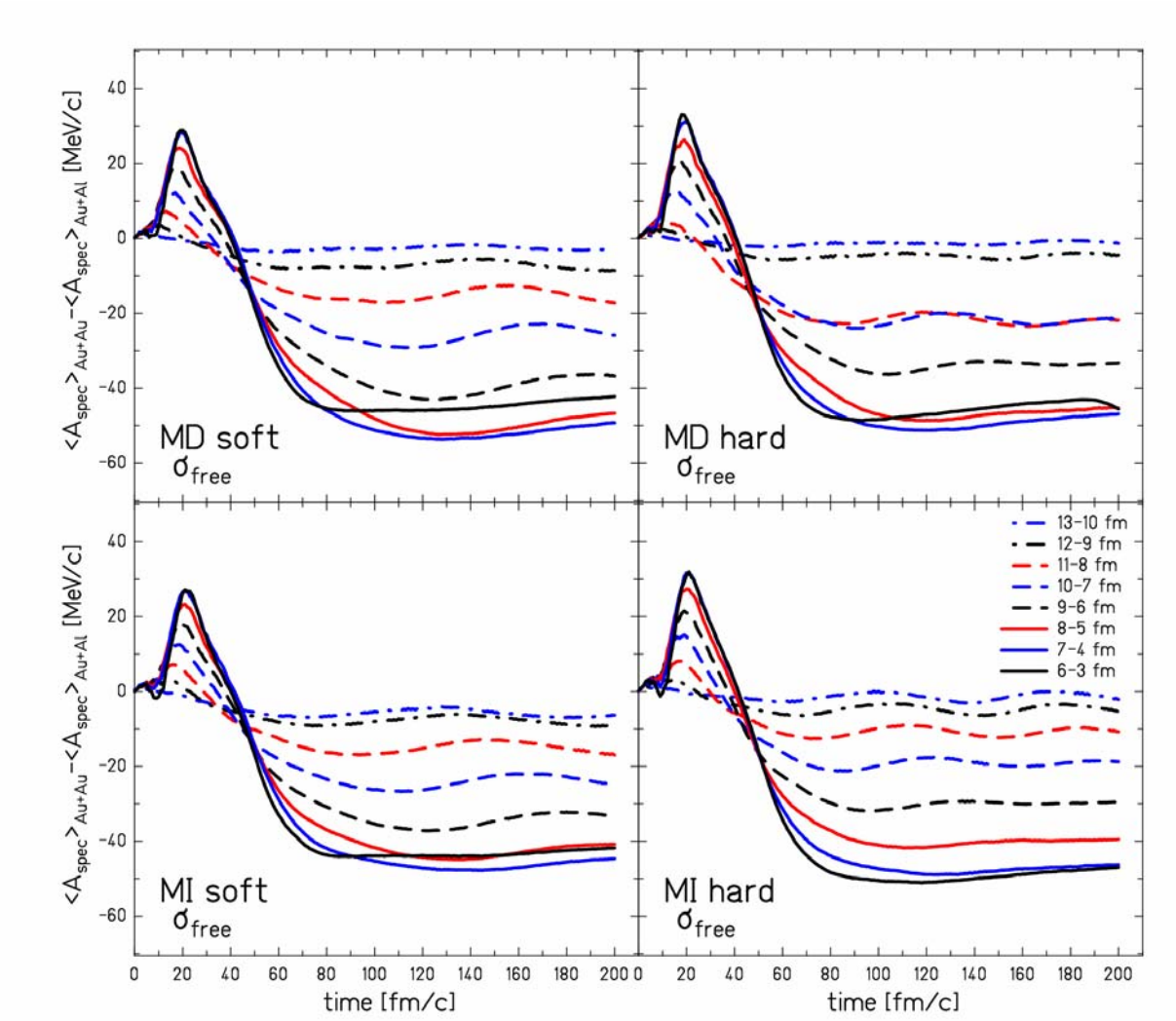

Fig.D.23: Time evolution of the difference of the mean spectator mass $\langle A_{spec} \rangle$ and its dependence on the "corresponding impact parameter" calculated within the BUU model for a soft and a hard EoS with a momentum-dependent (MD) nuclear mean field and for a soft and hard EoS with a momentum-independent (MI) nuclear mean field with free nucleon-nucleon elastic-scattering cross sections σ_{free} for the systems ^{197}Au+^{197}Au at 500 A MeV and ^{197}Au+^{27}Al at 500 A MeV.

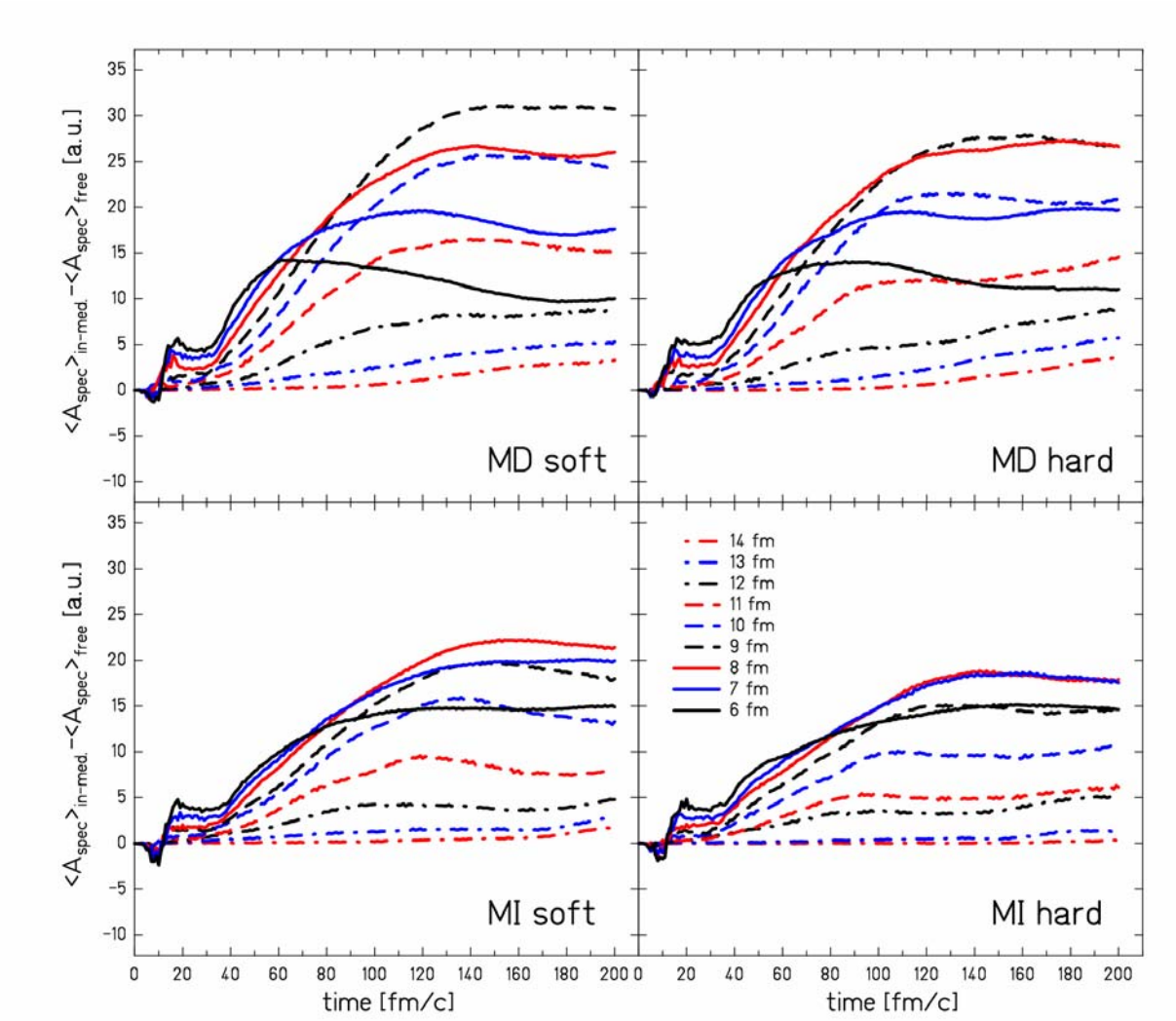

Fig.D.24: Time evolution of the difference of the mean spectator mass $\langle A_{spec} \rangle$ and its dependence on the impact parameter calculated within the BUU model for a soft and a hard EoS with a momentum-dependent (MD) nuclear mean field and for a soft and hard EoS with a momentum-independent (MI) nuclear mean field with in-medium reduced and free nucleon-nucleon elastic-scattering cross sections $\sigma_{in\text{-}med}$ and σ_{free}, respectively, for the system ^{197}Au+^{197}Au at 1 A GeV.

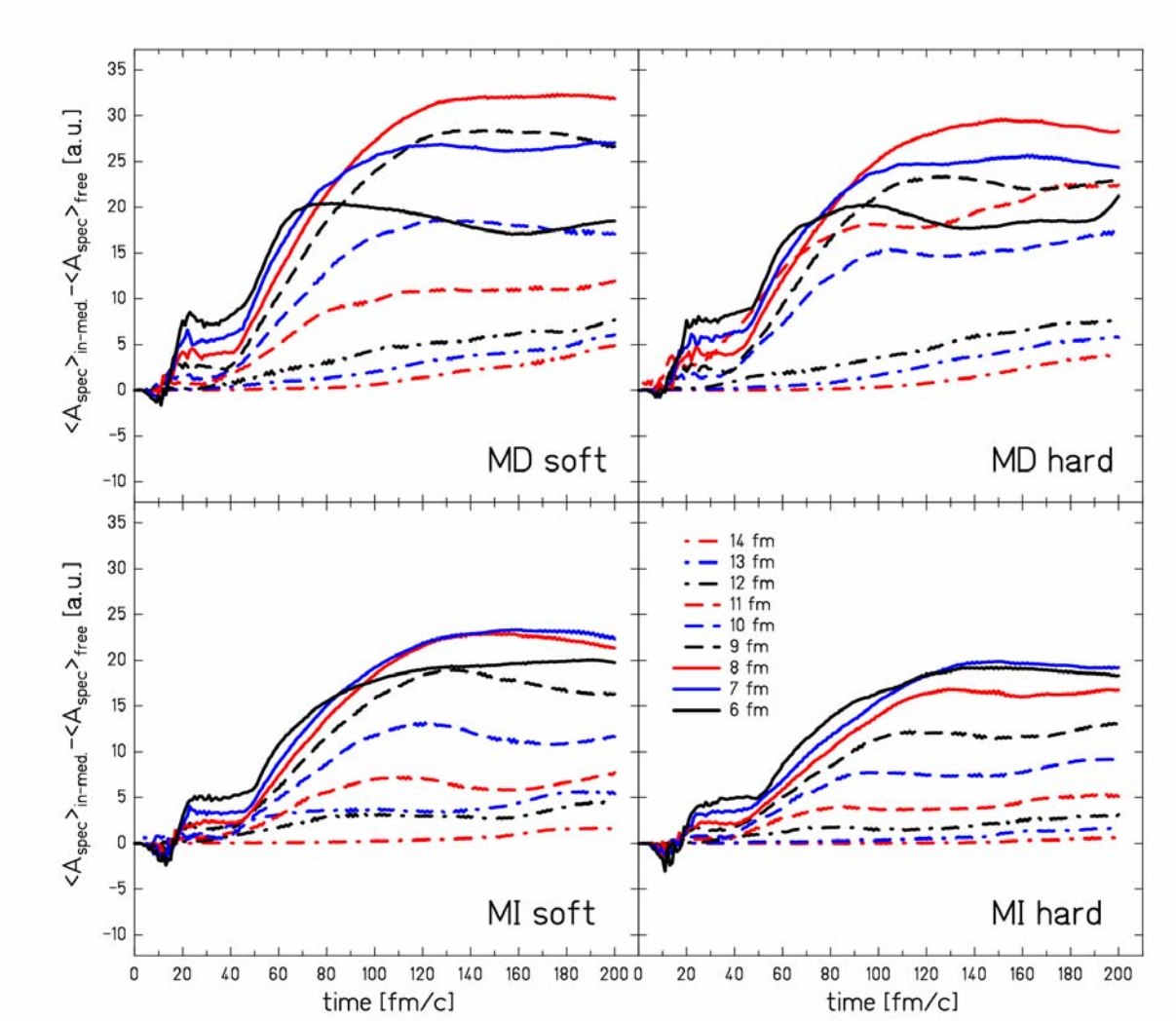

Fig.D.24: Time evolution of the difference of the mean spectator mass $\langle A_{spec} \rangle$ and its dependence on the impact parameter calculated within the BUU model for a soft and a hard EoS with a momentum-dependent (MD) nuclear mean field and for a soft and hard EoS with a momentum-independent (MI) nuclear mean field with in-medium reduced and free nucleon-nucleon elastic-scattering cross sections $\sigma_{in\text{-}med}$ and σ_{free}, respectively, for the system ^{197}Au+^{197}Au at 500 A MeV.

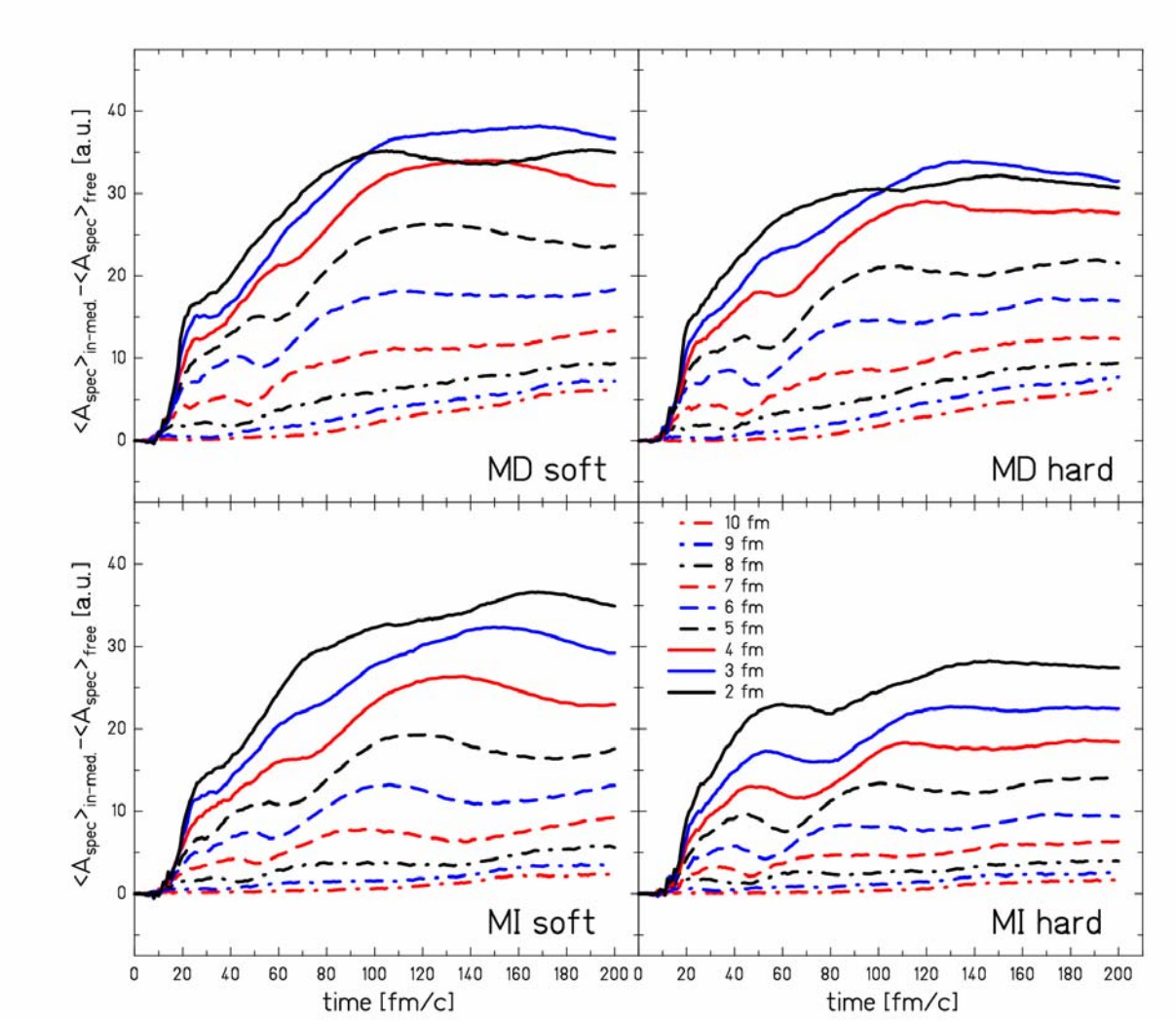

Fig.D.26: Time evolution of the difference of the mean spectator mass $\langle A_{spec} \rangle$ and its dependence on the impact parameter calculated within the BUU model for a soft and a hard EoS with a momentum-dependent (MD) nuclear mean field and for a soft and hard EoS with a momentum-independent (MI) nuclear mean field with in-medium reduced and free nucleon-nucleon elastic-scattering cross sections $\sigma_{in\text{-}med}$ and σ_{free}, respectively, for the system ^{197}Au+^{27}Al at 500 A MeV.

References

[Aich85] J.Aichelin and C.M.Ko, Phys. Rev. Lett. **55** (1985) 2661

[Aich87] J.Aichelin *et al.*, Phys. Rev. Lett. **58** (1987) 1926

[Aich88] J.Aichelin *et al.* Phys. Rev. **C37** (1988) 2451

[ALA] http://www-kp3.gsi.de/www/kp3/aladinhome.html

[AMA] http://www-w2k.gsi.de/charms/amadeus.htm

[Ain87] T.L.Ainsworth *et al.*, Nucl. Phys. **A464** (1987) 740

[Ann85] R. Anne and Y.Georget, Chambres a a circulation de gaz, etalonnage avec le faisceau GANIL, GANIL Report RA.YG.627.85 (1985) unpublished

[Bay76] G. Baym, S.U. Chin, Nucl. Phys. **A262** (1976) 527

[Baz84] D. Bazin and Y. Bouveret, Etude et mise au point d'une chambre multifits a ionisation pour la detection de faisceaux secondaires au GANIL, GANIL Report 84.03 (1984), unpublished

[Bec69] F.D. Becchetti, G.R. Greenlees, Phys. Rev. **182** (1969) 1190

[Ben02] J.Benlliure, J.Pereira-Conca, K.-H.Schmidt, Nucl. Instr. and Meth. **A478** (2002) 493

[Ber75] G.F.Bertsch, Phys. Rev. Lett. **34** (1975) 697

[Ber84] G.F.Bertsch, H. Kruse and S. DasGupta, Phys. Rev. **29** (1984) 673

[Ber88] G.F.Bertsch, G.E. Brown, V. Koch and B.Li, Nucl. Phys. **A490** (1988) 745

[Bet56] H.A. Bethe *et al.*, Phys. Rev. **103** (1956) 1353

[Bla80] J.P. Blaizot, Phys. Rep. **64** (1980) 172

[Bow73] J. D. Bowman, W. J. Swiatecki, and C.-F. Tsang, Lawrence Berkeley Laboratory Report No. LBL-2908, 1973 (unpublished!)

[Boy] D. Boyanovsky, hep-ph/0102120

[Bro89] G.E.Brown et al., Nucl. Phys. A505 (1989) 823

[Bro91] G.E.Brown et al., Phys. Rev. **C43** (1991) 1881

[Buch84] G.Buchwald *et al.*, Phys. Rev. Lett. **52** (1984) 1594

[Col98] E.Colin et al., Phys. Rev. **C57** (1998) R1032

[Cug81] J.Cugnon, Phys. Rev **C22** (1981) 1885

[Cum86] B.Cumming et al., Phys.Rev. **C33**, 926 (1986)

[Dan85] P.Danielewicz and G.Odyniec, Phys. Lett. **157B** (1985) 146

[Dan92] P.Danielewicz and Q.Pan, Phys. Rev. **C46** (1992) 2002

[Dan95] P.Danielewicz, Phys. Rev. **C51** (1995) 716

[Dan98] P.Danielewicz et al., Phys. Rev. Lett. **81** (1998) 2438

[Dan00] P.Danielewicz, Nucl. Phys. **A673** (2000) 375

[Dan02a] P.Danielewicz, Acta Phys. Pol. **B33** (2002) 45

[Dan02b] P.Danielewicz, R.Lacey and W.G.Lynch, Science **298** (2002) 1592

[Dan05] P.Danielewicz, private communications

[DeJ39] F.De Jong,B.Ter Haar and R.Malfliet, Phys. Lett. **B220** (1989) 485

[Dos85] K.G.R.Doss *et al.*, Phys. Rev. **C32** (1985) 116

[Dos86] K.G.R.Doss *et al.*, Phys. Rev. Lett. **57** (1986) 302

[Enq99] T.Enqvist *et al.*, Nucl. Phys. **A658** (1999) 47

[Fra83] B.Franczak – MIRKO - An Interactive Program for Beam , Lines and Synchrotrons, Computing in Accelerator Design and Operation, Proceedings, Berlin 1983

[Gai91] J.-J.Gaimard and K.-H.Schmidt, Nucl. Phys. **A531** (1991) 709

[Gait00] T.Gaitanos, H.H.Wolter, and C.Fuchs, Phys. Lett. **B478** (2000) 79

[Gal87] C.Gale, G.Bertsch and S.Das Gupta, Phys. Rev. **C35** (1987) 1666

[Gle88] N.K. Glendenning, Phys. Rev. **C37** (1988) 2733

[Gol74] A.S.Goldhaber, Phys. Lett. **B53** (1974) 306.

[Gos77] J. Gosset, H. H. Gotbrod, W. G. Meyer, A. M. Poskanzer, A. Sandoval, R. Stock, and G. D. Westfall, Phys. Rev. **C16** (1977) 629

[Gus84] H.A.Gustafsson *et al.*, Phys. Rev. Lett. **52** (1984) 1590

[Gut89] H.H. Gutbrod, A.M. Poskanzer, and H.G.Ritter, Rep. Prog. Phys. **52** (1989) 1267

[Had95] F.Haddad *et al.*, Phys. Rev. **C52** (1995) 2013

[Han93] E. Hanelt, A. Grewe, K.-H. Schmidt, T. Brohm, H.-G. Clerc, M. Dornik, M. Fauerbach, H. Geissel, A. Magel, G. Muenzenberg, F. Nickel, M. Pfuetzner, C. Scheidenberger, M. Steiner, K. Suemmerer, B. Voss, M. Weber, J. Weckenmann, C. Ziegler, Z. Phys. **A346** (1993) 43

[Hom99] A. Hombach, W. Cassing, S. Teis, U. Mosel, Eur. Phys. J. **A5** (1999) 157.

[Hub91] J.Hubele et al., Z. Phys. **A340** (1991) 263

[Jam89] M. Jaminon, C. Mahaux, Phys. Rev. C 40 (1989) 354.

[Jeu76] J.P.Jeukenne, A.Lejeune and C.Mahaux, Phys. Rep. **C25** (1976) 85

[Jia91] J.Jiang *et al.*, Phys. Rev. **C43** (1991) 2353

[Kar75] P. J. Karol, Phys. Rev. **C11** (1975) 1203

[Kau80] S.B.Kaufman et al., Phys. Rev. **C22** (1980) 1897

[Kru85] H.Kruse, B.V.Jacak and H.Stöcker, Phys. Rev. Lett. **54** (1985) 289

[Lie01] M.Liebendörfer *et al.*, Phys. Rev. **D63** (2001) 103004

[Lov88] W.Loveland et al., Phys. Rev. **C37** (1988) 1311

[Mol84] J.J.Molitoris *et al.*, Phys. Rev. Lett. **53** (1984) 899

[Mol85a] J.J.Molitoris and H.Stöcker, Phys. Rev. **C32** (1985) 346

[Mol85b] J.J.Molitoris and H.Stöcker, Phys. Lett. **162B** (1985) 47

[Mor78] D. J. Morrissey, W. R. Marsh, R. J. Otto, W. Loveland, G. T. Seaborg, Phys. Rev. **C18** (1978) 1267

[Mor89] D.J.Morrissey, Phys. Rev. **C39** (1989) 460

[Mye67] W.D.Myers and W.J.Swiatecki, Proceedings of the International Symposium on Nuclides far off the Stability Line, Lysekil, 1966, ed. W. Forsling, C.J. Herrlander and H. Ryde (Almqvist and Wiksell Boktryckeri AB, Uppsala), Arkiv foer Fysik 36 (1967) p 343.

[Mye74] W.D.Myers and W.J.Swiatecki, Ann. of Phys. **84** (1974) 186

[Mye76] W.D.Myers and Groote, Phys. Lett. **B61** (1976) 125

[Nap04] P.Napolitani, K.-H.Schmidt, A.S.Botvina, F.Rejmund, L.Tassan-Got, C.Villagrasa, Phys. Rev. C70 (2004) 054607

[Pak96] R.Pak et al., Phys. Rev. **C54** (1996) 1681

[Pan93] Q.Pan and P.Danielewicz, Phys. Rev. Lett. **70** (1993) 2062

[Per03] J.Pereira, *et al.*, contr. XLI International Winter Meeting on Nuclear Physics, January 26-February 2, 2003, Bormio, Italy

[Pra97] M.Prakash *et al.*, Phys. Rep. **280** (1997) 1

[Rei97] W.Reisdorf and H.G.Ritter, Annu. Rev. Nucl. Part. Sci. **47** (1997) 663

[Rei02] W.Reisdorf, Acta Phys. Pol. **B33** (2002) 107

[Ren84] R.E.Renfordt *et al.*, Phys. Rev. Lett. **53** (1984) 763

[Ric01] M.V.Ricciardi *et al.,* contr. XXXIX International Winter Meeting on Nuclear Physics, January 22-26, 2001, Bormio, Italy**;**

[Ric03] M.V.Ricciardi *et al.*, Phys. Rev. Lett. **90** (2003) 212302

[Ric05] M.V.Ricciardi, PhD thesis, Univesity of Santiago de Compostela, Spain 2005

[Rich01] J.Richert and P.Wagner, Phys. Rep. **350** (2001) 1

[Rin80] P. Ring, P. Schuck, The Nuclear Many-Body Problem, Springer-Verlag, New York, 1980.

[Scha97] Schaffner-Bielich *et al.*, Nucl. Phys. **A625** (1997) 325

[Sche74] W.Scheid, H.Müller and W.Greiner, Phys. Rev. Lett. **32** (1974) 741

[Schn98] A.Schnell *et al.*, Phys. Rev. **C57** (1998) 806

[Schr78] W.U.Schroeder, J.R.Birkelund, J.R. Huizenga, K.L.Wolf, V.E. Viola Jr., Phys. Rep. **45** (1978) 301

[Schu97] H.-J.Schulze *et al.*, Phys. Rev. **C55** (1997) 3006

[Schut96] A. Schüttauf et al., Nucl. Phys. **A607** (1996) 457

[Schut96b] A. Schüttauf, Untersuchung der Kernfragmentation, PhD-thesis, Frankfurt am Main 1996

[Schw98] W.Schwab, M.Bernas, P.Armbruster, S.Czajkowski, P.Dessagne, C.Donzaud, H.Geissel, A.Heinz, C.Kozhuharov, C. Miehe, G.Münzenberg, M.Pfützner, C.Stephan, K.-H.Schmidt, K. Sümmerer, L.Tassan-Got and B.Voss, Eur. Phys J. **A2** (1998) 179

[Schwa82] P. Schwandt, Phys. Rev. **C26** (1982) 55; AIP Conf. Proc. 97 (1983) 89

[Shi01] L.Shi, P.Danielewicz and R.Lacey, Phys. Rev. **C64** (2001) 034601

[Sue00] K.Suemmerer, B.Blank, Phys. Rev. **C61** (2000) 034607

[Ste92] M.Steiner, M.Blasche, H.-G.Clerc, H.Eickhoff, B.Franczak, H.Geissel, G.Münzenberg, K.-H. Schmidt, H. Stelzer and K. Summerer, Nucl. Instr. and Meth. **A312** (1992) 420

[Stö86] H.Stöcker and W.Greiner, Phys. Rep. **137** (1986) 278

[UU33] E.A.Uehling and G.E.Uhlenbeck, Phys. Rev. **43** (1933) 552

[Vos95] B.Voss, T.Brohm, H.-G.Clerq, A.Grewe, E.Hanelt, A.Heinz, M. de Jong, A.Junghans, W.Morawek, C.Röhl, S.Steinhäuser, C.Ziegler, K.-H.Schmidt, K.-H.Behr, H.Geissel, G.Münzenberg, F.Nickel, C.Scheidenberger, K.Sümmerer, A.Magel and M.Pfützner, Nucl. Instr. and Meth. **A364** (1995) 150

[Wes76] G. Westfall *et al.*, Phys. Rev. Lett. **18 (**1976**)** 1202

[Yar79] Y.Yariv and Z.Fraenkel, Phys. Rev. **C20** (1979) 2227

[You01] D.H.Youngblood, Nucl. Phys. **A687** (2001) 1c

[Wag00] A.Wagner *et al.*, Phys. Rev. Lett. **85** (2000) 18

[Wel88] G.M.Welke *et al.*, Phys. Rev. **C38** (1988) 2101

[Wir88] R.B.Wiringa, V.Fiks, A.Fabrocini, Phys. Rev. **C38** (1988) 1010

[Wya60] P.J.Wyatt, J.G.Wills and A.E.S.Green, Phys.Rev. **119** (1960) 1031

[Zie92] C. Ziegler, Diploma Thesis, Institut für Kernphysik, TH Darmstadt (1992).

Acknowledgments

This thesis is probably the greatest milestone I have so far passed on my scientific journey. It marks the end of one significant stage, not only of my professional carrier but also of my personal life. It also marks the beginning of another stage, exciting and thrilling at the same time, yet it is uneasy to foresee where the road may go. Although hesitating still eager, although tempted still worried I once again want to look back and see where I am coming from.

There, somewhere in the hazy past, hard to remember the exact occasion, but clearly hearing the words, I recall the tale of growing crystals. It was my physics teacher Charles Payne at Swain County High-School who caught my attention with this (for many maybe too boring) story from his scientific past, and how he tried to improve the quality and reliability of the growing method. Although I do not remember anymore what were these crystals supposed to be used for, somehow, that process of learning, asking, and searching for clues in order to better understand sounded too exciting, tempting and challenging. I think that was the moment when I really decided to become a physicist.

Next years, back in my home country, studying at Gymnasium Elišky Krásnohorské in Prague, two great physics teachers spotted my cautious interest, and started fuelling it with their gentle approach, keeping me motivated with dedicated support yet not allowing me to drop off because of a false satisfaction caused by ever growing, yet never complete knowledge. Therefore I would like to thank them both, Martina Kučerová and Miloslav Jireš, for guiding my very first steps.

The years of undergraduate studies were long and hard, but full of learning, gaining experience, first little successes and insights in and into the world of nuclear science. The most of the credit goes to my diploma thesis supervisor Dr. Andrej Kugler, whose support was extended also to this thesis. His involvement, often complicated by the distance, and support of my work at GSI-Darmstadt, resulting in this thesis, made many things much easier some even possible at all. I also appreciate his constructive criticism, which contributes to continuous improvement of my work and sorting the most important results. At this place I also would like to honestly thank Dr. Vladimir Wagner for all his engagement and great help in establishing and preserving the link to the Czech Technical University, which was due to the distance often very complicated.

I still do not fully comprehend how could have happened that, together with my wife, I was given such a great opportunity to come to GSI and especially to the group of Karl-Heinz Schmidt. His love for physics was simply infectious, turning an everyday work to a true passion. I thank him so much for his faith in me that he let me take the responsibility for the full scientific program investigating the spectator response, starting with the very first draft of the experimental proposal, and continuing through the analysis of the data, their interpretation and reaching even to the presentation of the main results in front of the scientific community. I often wonder how he could cope with my die-hard opposition when I was sometimes not convinced; even-though it turned out very soon that it is matter of my willing to understand rather than the matter of his explanation. I don't remember him ever loosing patience with me, but I do remember him always treating my objections (no matter how naive or emotional rather than scientific they might have been) with respect and dignity. I believe I have not learned from him just what it means to be a scientist, but moreover what it also means and takes to be a respectful and wise person. Well, I still have many things to improve, but reiterating it again, it is not the matter of the original, it is the matter of the copy.

When not present directly in person, Karl-Heinz's spirit was still around in form of his group, formed from the great people, each of them unique in his or her own way, but all together creating an ideal environment for scientific work. Therefore I want to thank

Aleksandra Kelic, for readiness to help in any situation. Sometimes I was even feeling a bit ashamed, since when I ran into troubles with relativistic calculations, I was sure that she will help, so my will to try first alone was often weakened, because unlike my own results, hers were always right. I will also never forget her engagement in my BUU calculations. Without her enthusiasm, and sacrifice of her CPU, I would give up long time ago and I would not be able to complete the full set of calculations as it is presented within this thesis.

At this place I also would like to thank to all other members of the CHARMS collaboration who allowed me to abuse their computers with my calculations. And this really meant a lot to me, and I was often having a bad conscience, since I sometimes felt like if they let me enter their homes so I can wash my dirty laundry, because my own washing machine is too small. Well its over now, but my great thanks go to all you guys – Antoine, Lydie, Radek, Strahinja and Vale.

This brings me to the borders of the peculiar world of theoretical physics. Originally I did not want to enter, just the idea of doing so has been scary enough. But driven by the burning desire to understand our observation of the reacceleration phenomenon, I found myself already one step too far. Therefore I would like to thank Prof. Pawel Danielewicz and Lijun Shi, for not casting me out as many theoreticians would do, but rather for their constant support, help and guidance in this, for me unknown, realm. Moreover, I am thankful for the given opportunity to work independently with their BUU code, and for all their patient discussions over the results, prepared publications and especially this thesis.

On the other side of the borders, in my own land of experimentalists, I would like to recall my encounter with Andreas Heinz. Before becoming a professor at Yale University, he spent almost half a year in the group of Karl-Heinz, which coincided with the first six month of my stay at GSI. During this time I took part in the first experiment with Andreas as my shift leader. Being a complete newcomer, I was thinking that it would not be a very comfortable feeling to work side by side with somebody with such a great experience like him. But it turned out to be exactly the opposite. Maybe he felt it is his personal mission, maybe he did not think about it at all, but his dedication and example has been for me the greatest inspiration. He never refused to answer any question, objection, comment or criticism, as well as he never refused to admit straightforwardly if he was not right. Well, this he did not have to do very often, but just the fact that he was able to admit that he is not perfect made him perfect in my eyes. And therefore, in my memories I keep him as an example of a true professionalism, which I would myself like to reach.

The list of the people who contributed to my thesis can never be complete. No matter how hard I will try, the number of people I have met during the past three years is simply too high. Some of them had a great impact on my work, such as those mentioned above, many other contributed just by a single advice or hint. Often these advices or hints were of essential importance, and without them the course of my work would be different or not as smooth as it was. This is especially valid for Darius Miskowiecz, my dearest beam-time coordinator who kept all his promises and who more than an opponent became a partner of our experimental effort. Another essential person has been Karl-Heinz Behr, the engineer of the Fragment Separator at GSI, who together with his team provided all the necessary technical assistance, no matter how challenging our demands sometimes were.

But no matter how great the technical support is, nor how brilliant can the scientific idea be, all the work together would not make any sense nor have any value without the support and appreciation from the people who are the closest to you. I am sure that some things, which I do, may be a mystery for a non-physicist, but the continuous and unconditional support from my family provides the necessary comfort, without which any intellectual activity is hard to imagine.

The last paragraph I have reserved for someone who deserves much more than just letters tagged together into few acknowledging words. In this case, I just feel I should write graffiti's

on every wall, I should scream out loud in the mountains so the echo can pass it farther, I should let it be published in the newspapers or tell everybody on the street how fortunate I am to have someone like you, my dearest love, … but it still would not be enough. Because no matter how great support or inspiration I get from the others, at the end it was always only my wife who stands by me under any circumstances, who stays even if everybody else is already gone home, who keeps me going even if I feel I cant any more, who never refuses to read what I write, honestly pointing out weak points which I don't want to see, discussing it all over and over again until I finally comprehend. And this all still while she is keeping her own work, and own project, moreover, somehow always at least one step ahead of me. I have been wondering already for a long time where does she take all that energy, why is she so disciplined and diligent. It's been a mystery for me, but I admire it and I am so much thankful for that. Working with you, my love, has not been only the most wonderful experience of my life; it has been its greatest blessing.